12-2015

TOWARDS A GREATER UNDERSTANDING OF HYDROTHERMALLY GROWN GARNETS AND SESQUIOXIDE CRYSTALS FOR LASER APPLICATIONS

Cheryl Moore
Clemson University, orionnebula66@yahoo.com

TOWARDS A GREATER UNDERSTANDING OF HYDROTHERMALLY GROWN GARNETS AND SESQUIOXIDE CRYSTALS FOR LASER APPLICATIONS

A Dissertation
Presented to
the Graduate School of
Clemson University

In Partial Fulfillment
of the Requirements for the Degree
Doctor of Philosophy
Chemistry

---

by
Cheryl Ann Moore
December 2015

Accepted by:
Joseph W. Kolis, Committee Chair
John Ballato
William T. Pennington
Andrew G. Tennyson

ABSTRACT

The hydrothermal method of crystal growth offers many benefits over traditional melt-based techniques such as lower temperature requirements relieving detrimental high temperature effects such as stress fracturing and a closed-environment, which limits impurities. The continued study of this type of growth including hydrothermal epitaxy is crucial in our world of constant miniaturization. Presented in this thesis is the hydrothermal growth of crystals of LuAG and Lu_2O_3 doped with a variety of dopants. Their room-temperature and cryogenic absorption spectra are also presented.

Much like Nature uses heat, pressure, water and a nutrient-rich feedstock we have used this hydrothermal technique to produce synthetic crystals of grossular, $Ca_3Al_2(SiO_4)_3$, a naturally occurring garnet as well as other aluminosilicates related to grossular, including a new type of vesuvianite. Other garnets important to the laser industry have also been grown using the hydrothermal technique, such as yttrium aluminum garnet (YAG), lutetium aluminum garnet (LuAG) and the related sesquioxide Lu_2O_3, (lutetia). The growth and characteristics of Yb-doped lutetia and LuAG, Nd-doped lutetia, and Dy-doped lutetia and YAG are presented herein. These laser crystals have been analyzed by high-resolution absorption spectroscopy at room temperature as well as 250K, 200K, 150K and 80K and absorption coefficients are presented.

A coprecipitation technique common in the ceramics field has been adapted for use creating precursors for hydrothermal crystal growth, including phase-pure

polycrystalline anorthite and phase-pure gehlenite. Coprecipitation has also been utilized to gain greater control of dopants to create pre-doped feedstocks used for the growth of laser crystal. The versatility of the hydrothermal growth method is also highlighted in a novel epitaxial technique, core growth, which coats the internal surfaces of a seed crystal as well as external surfaces. This can result in multifunctional, layered crystals with no additional size, suitable for applications in need of constant miniaturization demanded by today's industries.

DEDICATION

I would like to dedicate this work to the memory of Georgia Louise Thomas Jackley and Kenneth Rudolph Thomas. We did it!

ACKNOWLEDGMENTS

While writing a dissertation can be an extremely personal experience, to stop there would be to overlook so many people integral to the process and, without whom, this manuscript would not exist. First and foremost I must thank Clemson University, the Department of Chemistry, and specifically the Kolis research group for offering me the opportunity to study here. Chance may have ultimately landed me here, but I call it luck. Thank you to Dr. David C. Brown and everybody at Snake Creek Lasers, L.L.C. for taking me in and allowing me to walk beside you for this short time; you are some of the most amazing people I've ever met. Thank you especially to Lisa Vitali for helping me find my sanity when I almost lost it.

I would like to extend my deepest gratitude to the following people for their part in this work either directly or indirectly. To Kyle Fulle for being my right hand and sometimes my left hand, too. To Dr. Duminda Sanjeewa for opening to me a whole new world of lutetia and who has grown some of the most beautiful SN crystals I have seen. To Barbara Lewis for encouraging me when I was so ready to quit. You will never know what your kind words meant and mean to me still. To Craig Goodman for our countless hours of brainstorming. Ideas always seem to make more sense after they bounce off of you. To Dr. Colin D. McMillen. You taught me everything I know about crystal growth and reminded me of the importance of family when I really needed it. But most of all I'd like to thank Dr. Joseph Kolis for, among other things, guiding and supporting me when I

needed it most and giving me the latitude to stray from the beaten path occasionally. Who knows where in the world I would be without you. Literally.

TABLE OF CONTENTS

Page

Table of Contents (Continued)

Chapter Page

Table of Contents (Continued)

Chapter Page

Table of Contents (Continued)

Chapter Page

LIST OF TABLES

List of Tables (Continued)

Table Page

LIST OF FIGURES

List of Figures (Continued)

Figure Page

List of Figures (Continued)

Figure Page

List of Figures (Continued)

Figure Page

List of Figures (Continued)

Figure Page

List of Figures (Continued)

Figure Page

List of Figures (Continued)

Figure Page

List of Figures (Continued)

Figure Page

List of Figures (Continued)

Figure Page

List of Figures (Continued)

List of Figures (Continued)

List of Figures (Continued)

Figure Page

CHAPTER ONE

CRYSTALS, CRYSTAL GROWTH, AND LASERS

Left to herself, Nature has shown that she can produce a staggering array of different crystals in any part of the world from the humble snowflake to the jaw-dropping spectacle of the Crystal Caves in Naica, Mexico, home to some of the largest and arguably the most beautiful natural crystal displays in the world.[1] Over the course of half a million years the mineral-rich waters of the mine aided by temperatures approaching 115°C from a magma pocket deep below the earth's surface combined to create amazing crystals of $CaSO_4$ some of which have grown 30 feet or more.

A little easier to imagine, though not much less impressive, is a simple geode; a crystal cave that fits in the palm of our hand. Break open the drab, rock-like exterior and the beautiful purple points of amethyst inside remind us of nature's brilliance. Crystals are not only beautiful but useful. Quartz is found on all the beaches of the world and is used in everything from additives in asphalt to grinding slurry and even as the time keeping mechanism in quartz watches.

Gemstones like flawless diamond can take our breath away but are also very useful for polishing and grinding due to its extreme hardness but we would hardly want to mine these valuable crystals for polishing. So as with many things, man often sees something in nature and tries to synthesize it and reproduce it in the lab. Not only beautiful, useful and sometimes priceless, crystals of all types have found applications in all areas of industry.

The growth of synthetic crystals and their analysis lies at a unique junction of many different disciplines: physics, engineering, materials science and chemistry, to name just a few and scientists approach the study of crystals from at least as many different directions.

As chemists, we find ourselves in the analysis of the elements involved, how they fit together and the characteristics and properties they impart to the crystal. Frequently we find a natural mineral and see if we can make it in a lab. We try to optimize their qualities and speed up their growth; none of us wants to wait a half million years to form a crystal as Nature so patiently does. We as scientists start to think of how we can tailor properties to our specific needs armed with the entire pallet of elements Nature has provided us with called the periodic table.

The long range order of a single crystal's rigid framework offers some very desirable physical properties. Compact, portable, dense, and robust, crystals are used in watches, computer chips, lasers, lenses, transparent screens and the list goes on. A pure solid, crystals are easily handled, physically stable, and can be easily manipulated. Because of the intense interest by a diverse array of industries an equally diverse array of crystal growth methods has emerged over many hundreds of years from crystallization of salt from the ancient seas to the crystals of high-power advanced lasers of today.

Methods of crystal growth

Crystalline material can be produced in a number of ways. Assuming the crystal is adequately soluble in some solvent, growth from solution can be an effective technique,

as in the mine in Mexico. Growth occurs in this type of a system when evaporation of the solvent causes solute to precipitate in a slow, ordered way resulting in what can be very large, good-quality crystals. The properties that cause this method to work so well for such a broad array of crystals is also, unfortunately, the same property that makes it impractical for other types of crystals. Clearly, the crystals grown from a solution will be soluble in that solution. If the crystal is to be grown from an aqueous solution, for example, the crystal will *dissolve* in water, including water in the air, which for most applications is not practical, or at least not desirable.

Conversely, many of the robust, hard, damage-resistant, dense crystals needed for a variety of applications are not readily dissolvable in *any* solution which, while good for durability and resistibility, makes this type of growth from solution not a viable option. One widely used alternative is a broad class of methods based on growth from a melt. Direct melting of components or the material itself to form larger, good-quality single crystals is commonly used to form crystals of all types. Frequently metal oxide components, when melted under the appropriate conditions, will form a desired single crystal when cooled. Simply melting the correct components, however, does not always lead to the desired, stoichiometric crystal, as is the case when the components are not congruently melting. In cases such as this other phases are favored at melt temperatures and even though components may be present in the correct ratios, the desired product does not form. In other cases components evaporate before they can be incorporated into the crystal lattice. Even if the components *do* melt to form the intended crystal, the melt temperatures can be very high.

The crystals that are the focus of this work are generally targeted for use in laser applications, and particularly include garnets and sesquioxides (M_2O_3), which are refractory oxides that have melting points of about 1730°C – 2800°C.[2] Such temperatures can be challenging to attain and require the use of special crucibles, like platinum, rhenium, and iridium that are usually quite expensive. Here again, the property that makes this type of growth possible and desirable can also make it difficult to achieve. The high heat needed for melt-grown crystals can often cause other detrimental effects. This harsh environment can cause unwanted impurities from the crucible which, over repeated use, is actually consumed in the process. Air bubbles, inclusions and other light scattering imperfections like stress fracturing, thermally induced stress birefringence and cracks in the crystal decrease its desirability especially in light manipulating applications such as optics.

While there are a great many (and growing) melt-based methods, probably the most widely used technique is called the Czochralski method (Cz), named after Jan Czochralski who, in 1916, stumbled upon the method while writing.[3] Accidentally dipping his pen into a nearby crucible of melted tin instead of ink he pulled out a thin strand of single-crystalline tin. Thus the basis of the method that bears his name was conceived. From this accidental beginning, as with so much of science, Czochralski's method and its modifications have become probably the most widely used, melt-based crystal growing technique today and is versatile enough to produce single crystals of silicon for use in microchips to optical-quality crystals of yttrium aluminum garnet (YAG) for use in lasers. While it may seem a simple matter to produce very large boules

of good-quality single crystals using this melt method there are actually great number of factors that go into pulling a crystal and can affect its quality.

The modern Cz method is adapted from this initial discovery and employs both a rotation and a drawing out of a seed crystal (Figure 1).[4] Once the components are melted

Figure 1. Feedstock is melted in a crucible. A seed introduced to the surface induces crystallization. As the seed is rotated, it is slowly drawn upward resulting in a boule.

in a crucible, in order to induce crystallization a seed crystal of the same (or crystallographically similar) material is introduced to the molten surface as it is slowly pulled from the liquid while slowly rotating. The rotation necessary to keep the melted feedstock at the correct and constant temperature throughout the process can result in the formation of a twisted core down the entire length of the resultant boule rendering it unusable for optical applications. Along with this core can come other optically undesirable regions in which crystallographic orientation changes relative to other portions of the boule and as a result, the final crystal can contain relatively little usable crystal. All of this, in addition to the air bubbles, impurities and other high temperature

effects mentioned can limit the use of this method in certain circumstances. As mentioned, it is important in a melt-based method such as this that the components melt congruently or in a smooth way that reliably gives the intended product. If all of the components do not behave in this predictable way it can become challenging or impossible to use this method. For example, certain volatile components like gallium can evaporate from a melt, constantly changing the composition, which can make careful control of it difficult.

There are many other techniques based on melting components,[5] such as the Kyropoulos Method which, like Cz, uses a seed crystal and a molten feedstock. Crystals grow as the temperature of the crucible is slowly lowered. The growth rates are lower than those for Cz, but this method is nonetheless used for growth of halide crystals. Another related method also involves a crucible going through temperature zones in the Bridgeman Method. The Heat Exchanger Method (HEM)[5] is another melt-based method used for growing sapphire crystals making use of both a heated, molten feedstock and a cooled seed crystal. All of these high-temperature methods, unfortunately, require a crucible of some sort and crystals grown by them are subject to crucible impurities. One interesting melt-based method that does not require a crucible is called Skull Melting. In it a "skull" is formed from sintered powder which serves as a crucible in which the feedstock is held and heated using radio frequency. This method, while ingenious, is also hard to control and often produces imperfect crystals which are not ideal for optical applications.

Another common type of crystal growth called flux growth is a kind of hybrid method between melt and solution methods and takes place at much lower temperatures. For example, a lead-based flux of a PbO/PF_2 mixture can be used to grow YAG at around 1300°C, which represents a reduction in temperature by almost half compared to a melt. A flux can be thought of as a solid solvent that usually has much lower melting point than the components that it will dissolve. The flux is added together with the components and heated. The melted flux then dissolves the components and crystal growth then resembles growth from solution occurring over many hours to days during cool-down. The flux subsequently needs to be removed which can leave impure crystals as flux impurities are sometimes trapped within the crystal structure.

Although both of these crystal growth methods are regularly used in industry, the high-temperature effects and impurity inclusions that are commonly experienced make them less than ideal candidates in a wide range of applications in optics and alternative growth methods that take these concerns into consideration warrant further investigation.

While a staggering array of crystals has been grown with these two broad methods and their various modifications, there are relatively fewer methods that can produce an individual crystal of multiple compositions, such as a layering of a functionally different crystal on a structurally similar substrate. In optics applications it is often necessary to have not just one crystal in a system but multiple different crystals. One way to achieve this is, quite simply, to stack the desired crystals in line, and is in fact frequently how it is accomplished. The loss of light at each surface and interface through

scattering, reflection, and refraction as well as the physical space needed for such a design, however, belies its practicality in our world of constant miniaturization. Shrinking optical components of greater and greater complexity necessitates a better method. Binding crystal layers together as a single crystal in a process called heat diffusion bonding is one a way to avoid some of the obstacles of miniaturizing optics.

Heat diffusion bonding is not a method of crystal growth, *per se*, as it is assumed that two or more crystals of optical quality, appropriately sized and doped already exist. Two crystals of different composition are effectively combined into a single crystal in this process, presuming a good bond was achieved. The two crystals need to first be polished to extremely high tolerances. Flattening the surfaces to atomic precision helps assure the bond will be good (non-light-scattering) and strong (resistant to damage, both mechanical and from heat generated during operation). Once prepared, the surfaces are pressed together under high pressure and temperature, usually about 2/3 of melt temperature which can be around 1400°C or more. Under these conditions, ions migrate across the interface, knitting the two crystals together at the atomic level. The resulting bond can be very strong and clear. The process is expensive, time consuming and limited to flat surfaces however, and very thin crystals run the risk of being broken.

Other types of coating methods include those based on deposition from vapor, liquid, and solid phase. Chemical vapor deposition (CVD), molecular beam epitaxy (MBE), pulsed laser deposition (PLD), and liquid phase epitaxy (LPE)[6,7] are some of the more common methods used today. While the specifics of each method vary, the basic

principle on which these methods are based is a condensation of the desired layer onto a seed crystal or other surface. This deposition builds up layer by atomic layer of single–crystalline material very slowly and can take some time to grow big enough for the intended application. For example, layers grown by MBE grow less than about 1μm per hour and for this reason these methods are typically used for very thin layers. While this list is growing every day and is certainly not exhaustive by any means, the survey of the more common methods was intended to give an idea of some the challenges facing today's crystal growers and should make clear that none of the methods discussed is applicable to a very wide variety of situations. New applications are being conceived all the time requiring continued study of crystals, their growth methods, and properties by people in all segments of science and industry.

Hydrothermal Crystal Growth

The crystal growth method that will be discussed throughout this writing requires much lower temperatures and is versatile enough to both grow and coat crystals. Hydrothermal growth (HT) normally takes place at high pressures below about 700°C above the critical point of water (374°C and 22.064 MPa) and is also based on dissolution. In a hydrothermal growth system, typically the same types of components are used as in melt-based methods, metal oxides, halides, etc. They are enclosed in a sealed, inert environment, in our case, small, sealed silver ampoules with some kind of aqueous solution that will aid dissolution called a mineralizer. Acids are not typically used in our research due to their corrosive nature towards the silver reaction tubes in which growth takes place. Salt mineralizers have also proven very effective especially in lower

concentrations despite their reactive nature toward the silver liners sometimes. The most common mineralizers in our lab are basic solutions such as alkali carbonates, hydroxides, or fluorides, and even combinations of these have given good results. Concentrations can range from plain water to 10 or even 20M.

Growth by spontaneously nucleation

In this program typically a completely sealed silver reaction tube containing the desired ratio of components and a small amount of aqueous mineralizer is loaded into a heat-resistant apparatus called an autoclave that is capable of controlled zone heating and transmitting counter pressure to the enclosed ampoules to prevent them from bursting when heated. Our autoclaves are equipped with a high pressure gauge with release valve and are made of high-temperature Inconel, a nickel alloy, structurally sound when heated to at least 700°C and able to withstand these conditions during a growth cycle that may last several weeks.

It is important to note here that, while we may think of this as "high-temperature" growth, it is actually very low in comparison to the other crystal growth environments discussed earlier, up to about a quarter or less. Specific growth temperatures are based on the particular system and are typically between about 400 and 700°C. At these temperatures pressure of up to 35000 psi (ca. 240 MPa) develop inside the autoclave causing a supercritical hydrothermal fluid to form in which the components dissolve. Growth of what can be moderate-sized crystals ~1-2 mm or more is possible after runs of typically three to four days.

The closed nature and relatively mild reaction environment addresses some of the problems encountered with the other methods because we have control over exactly which elements are present. In the closed tubes evaporation of components is not usually an issue, though we should be aware of any gases that could form possibly causing the small reaction tube to be breached or burst during growth. Next, components that are not melting clearly do not need to melt congruently. Some crystals that are problematic to produce by Cz for this reason *can* be produced hydrothermally, as we shall see later. The low temperatures used do not require rhenium, platinum, or iridium crucibles, so inclusions and contaminants from them are eliminated. Air inclusions are also not usually seen in this mild an environment.

Thermal stress is introduced when a crystal grows at high temperatures which tend to expand a crystal lattice. After growth, as the solid crystal begins to cool down, its lattice tries to contract again, causing internal strain and sometimes even fracturing. This strain is lessened at lower growth temperatures. And, no less important, the silver ampoules used as reaction tubes are not consumed in the growth process and can be recycled and re-extruded indefinitely.

This closed environment of HT growth, while providing some distinct benefits, also gives rise to some difficulties, as it is not easily possible to monitor the process during growth and indeed is often not even well-understood. In the case of epitaxial growth discussed below, many wasted days and weeks have been endured as a result of the hanging seed crystal falling into the feedstock early into the growth cycle only to be

discovered weeks later as a solid mass of feedstock components with a destroyed seed crystal at its center. Thus it is important to double- and triple-check the tying and placement of seeds, integrity of weld-seals, and to keep a close eye on temperature and pressure readings of one's autoclaves.

This simple method described above is used to grow spontaneously nucleated crystals (SN) and is one of two broad categories of hydrothermal crystal growth. As the name suggests, nucleation, or the development of small crystals, occurs spontaneously and in general leads to many small crystallites. This type of crystal growth is particularly useful for descriptive chemistry projects because typically only very small crystals are required for these types of characterization such as powder pattern matching to a database entry (or possibly a new addition to the crystal database!) and crystal structure elucidation through single crystal diffraction data. It is usually a quick way to survey what crystals might form in a particular environment because many experiments can be done at once and the reaction duration is on the order of only a couple of days.

For example, we could explore phase-space with a series of alkaline earths to see what types of fluorides they may form, or with a fluoride we know will form but with a series of different mineralizers to see which works best. Predicting which crystals may grow based on phase diagrams and solubility charts is a good place to start but gets us only so far and sometimes ultimately the best method is to just see what we can pull out of a tube. Contrary to how we think as scientists, sometimes when a crystal that we initially think should *not* form in a certain environment leaves us with the task of

explaining what happened when it *does* form, often leading to some very interesting crystals.

Hydrothermal epitaxial growth

The other broad category of HT growth, though, leads to much more macroscopic

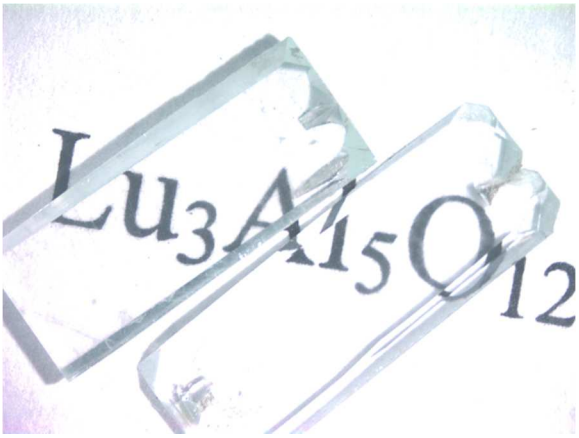

Figure 2. Two polished slabs of LuAG grown by epitaxy. Harvested from a YAG seed.

crystals and it is the method used to create most of the crystals presented throughout. Crystal growth due to mass transport of feedstock to an existing seed crystal is called epitaxial growth. Epitaxy, as it applies in the current context, is an ordered coating on an existing crystalline surface. Because the result is a single crystal the surrogate and its coating need to be crystallographically similar in terms of their space group and lattice parameters to allow this growth to take place,[8] although we have some flexibility to engineer the properties of a crystal, which will be expanded a bit in the next chapter.

Epitaxy is often greatly preferred because it leads to much larger crystals in general. Instead of growth taking place on many smaller crystallite seeds, growth is

maximized because it is directed instead onto a single seed. While this coating method may initially seem limited in scope, it can be quite versatile allowing novel layering of functional components for optical systems such as micro-lasers, for example. If the layer produced is thick enough, it can even be harvested from the surrogate by wire-saw to produce a new seed which can then itself be coated using epitaxy. Figure 2 shows the optical clarity of harvested slabs of LuAG grown by epitaxy on a YAG substrate of 5 x 14 mm polished to about 1 mm thick. It takes just a little imagination to see the almost endless possibilities this method of growth affords. Our group has demonstrated a wide range of novel layering architectures based on this process, some of which will be presented in later chapters. The quality and versatility granted to us by the hydrothermal method lends itself nicely to the growth and design of crystals for optical applications and laser crystals in particular.

Optimizing conditions for a particular system is not a straightforward undertaking, though, and along with a good knowledge of the phase diagram for the components, a lot of results-guided trial and error is necessary and still may or may not lead to a satisfactory growth protocol.

Interaction of light with matter

In his 1917 paper entitled The Quantum Theory of Radiation,[9] Einstein theorized about the interaction of radiation with matter by means of absorption and emission of photons and predicted the phenomenon of stimulated emission, which is the basis of a laser.

One of the many ideas presented in Einstein's work was the quantized nature of the interaction of light with matter. There is a probability that an electron will be promoted to an excited state if it can absorb a photon of wavelength equal to the energy difference between ground state and excited state, ΔE. This gives us a definite population in the excited state versus the ground state. For a laser to emit by stimulated emission the population in the excited state must be greater than the population in the ground state, or there must be a population inversion. Once in this excited state, the electron has several

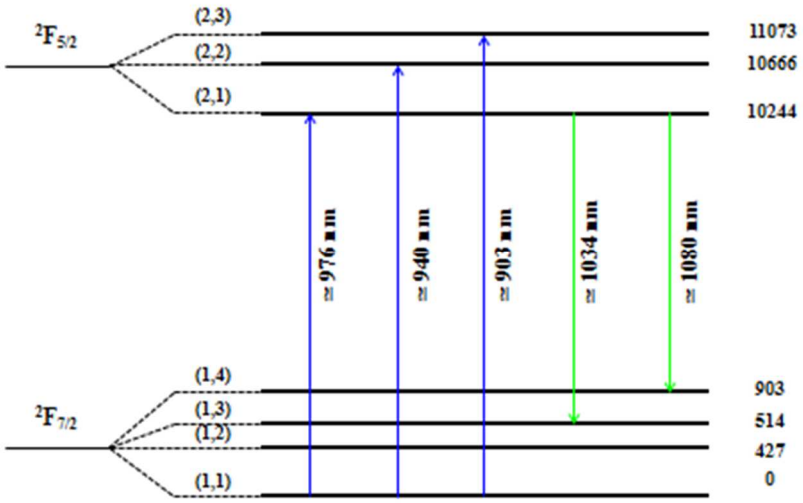

Figure 3. The simple energy level diagram for Yb:YAG showing its ground and excited state manifolds.

routes to relaxation back to the ground state, either radiative, by giving off another photon, or non-radiative, by some other route that releases energy in another form, like heat for example. If it does relax by way of photon release it can be either stimulated emission or spontaneous emission.

The energy level structure of the laser-active ions determines their behavior towards radiant energy, such as absorption and emission spectra and is the basis of all spectroscopic analysis. Because of the shielded nature of the unfilled f-orbitals of these ions, the absorption spectra for a specific ion tend to be largely unaffected by the bonding environment and host, although we do see differences in relative intensity and shifting towards longer or shorter wavelengths. An ion like Yb^{3+} has a very simple energy level structure and will be discussed at length in Chapter 6 but can serve as a good example in the present discussion. In Figure 3 we can see two manifolds which each contain several Stark levels. Enough ambient energy is present at room temperature to allow for a thermal population of the sublevels of the ground state, the Boltzmann factor. Upward pointing lines represent the energy transition an electron goes through when absorbing a photon of the energy corresponding to this wavelength. In the Figure we can see that the available levels in the upper state would require absorption of a photon of 914 nm, 941 nm, and 968 nm for this Yb:YAG laser crystal. The downward pointing arrow represents one available route to radiative relaxation by emission of a photon of 1029 nm, or that of a Yb:YAG laser.

It is also possible for an electron to absorb a photon ending up in some vibrationally-excited level of the upper manifold, relax to some other state of the upper level by a discharge of heat, and then radiatively relax to the ground state, which is most often the case. This type of vibrational relaxation can be a source of a lot of waste heat during laser operation, so much so, that a crystal can even be destroyed at high pump power. Difficulty in thermal management of laser systems is a huge hindrance in the

development of ultra-high powered lasers. Because of this limitation, the thermal conductivity of a crystal, specifically the ability of a crystal to be able to dissipate heat efficiently is a very important property. This is discussed in greater detail in Chapter 6 on Yb-doped crystals.

Cryogenic cooling of the crystal reduces the amount of thermal energy available thus decreasing the population of the higher energy sub-levels of this ground state. This has the effect of both sharpening an absorption peak and increasing its intensity. Cooling of a crystal also increases its thermal conductivity, further improving its ability to dissipate heat. For the first time, to our knowledge, the cryogenic absorption spectra of several laser crystals have been collected and are presented in the appropriate chapters.

Lasers and Laser Crystals

Building on Einstein's theory, in 1954, Charles H. Townes, born in Greenville, SC, and co-workers, at the direction of the Office of Naval Research succeeded in the construction of a working Maser (**M**icrowave **A**mplification by **S**timulated **E**mission of **R**adiation) and was issued a patent for it in 1959.[10] Townes as a consultant with Arthur Schawlow of Bell Laboratories later extended this idea to much shorter wavelengths, thus the conception of the laser (**L**ight **A**mplification by **S**timulated **E**mission of **R**adiation), while Theodore Maiman succeeded in constructing the first working laser in 1960 based on a ruby.[11] Since their initial inception lasers have since been built based on all three states of matter: gas (He-Ne in 1960, by Ali Javan), liquid (organic dyes) and solids.[12] Lasers have found a wide variety of uses such as in range finders, laser surgery, optical

data storage devices, weapons defense, remote sensing, and many more spanning all areas of industry and beyond.

Solid-state lasers include those based on polymers, glasses, transparent ceramics, and even semiconductors (laser diodes), and of course, crystals like Maiman's ruby laser, which is $Cr:Al_2O_3$ or chromium-doped corundum. In it the chromium ion is doped or substituted into the corundum crystal structure, known as the host, in a very small percentage. In addition to alumina, crystalline lasers can be based on a number of other hosts such as the garnet structure.

Garnets as hosts

Natural garnets are a diverse group of silicate minerals that can be found across the globe.[13] Some of the major minerals of the garnet family are Pyrope ($Mg_3Al_2Si_3O_{12}$) Almandine ($Fe_3Al_2Si_3O_{12}$), Spessartine ($Mn_3Al_2Si_3O_{12}$), Andradite ($Ca_3Fe_2Si_3O_{12}$), Grossular ($Ca_3Al_2Si_3O_{12}$), and Uvarovite ($Ca_3Cr_2Si_3O_{12}$) and have the general chemical formula $A_3B_2B'_3O_{12}$. YAG is an example of a synthetic garnet that has found wide application as a laser host as well as a grinding powder and even in jewelry.

Garnets have a cubic structure with *Ia-3d* symmetry and are of the highest symmetry possible. The tight-packing of this structure can be seen in Figure 3 with a lattice parameter, a, of between 11.94 – 12.89Å[14], with Z=8 units per cell, leads to robust, dense crystals, hard (~8.5 on the Mohs scale) and resistant to damage.

Some of the most ubiquitous solid state lasers today are based on YAG,[15] or yttrium aluminum garnet, $Y_3Al_5O_{12}$, and its analogs such as the Lu and Gd versions, LuAG and GGG (gadolinium gallium garnet), respectively. We can see the local bonding environment in LuAG in greater detail in the figure below. Figure 4 (left) shows the local bonding environment of Lu^{3+} with their complement of oxygen anions. The 8-coordinate,

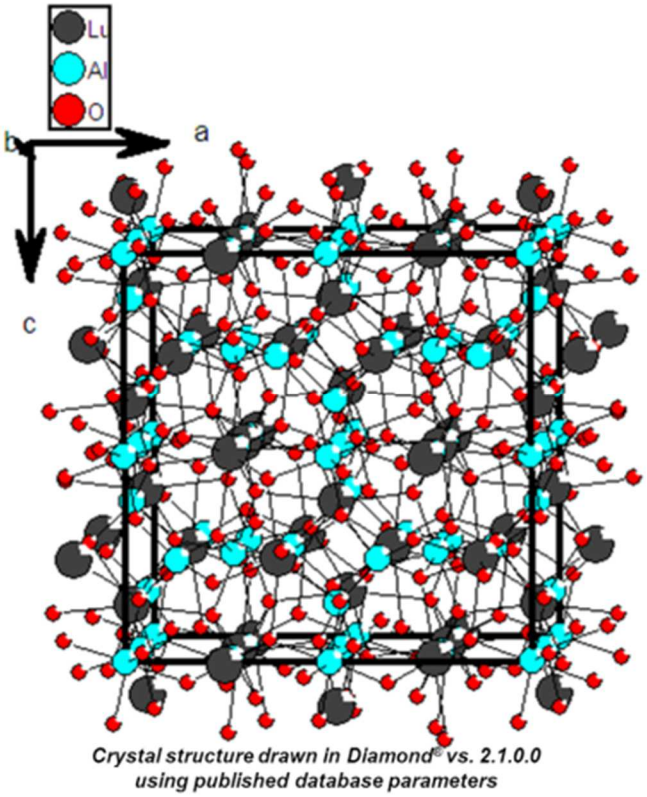

Figure 4. LuAG unit cell looking down the b-axis.

dodecahedral Lu^{3+} ion is represented by A in the above general formula and has a local site-symmetry of D_2. In this depiction the two different bond lengths of Lu-O are represented by green (2.27Å) and red (2.38Å), summarized and compared to YAG and GGG in Table 1.

B and B' represent the two different bonding environments of the Al^{3+}, 6-coordinate and 4-coordinate, respectively, (Figure 4, right) while oxygen anions take up

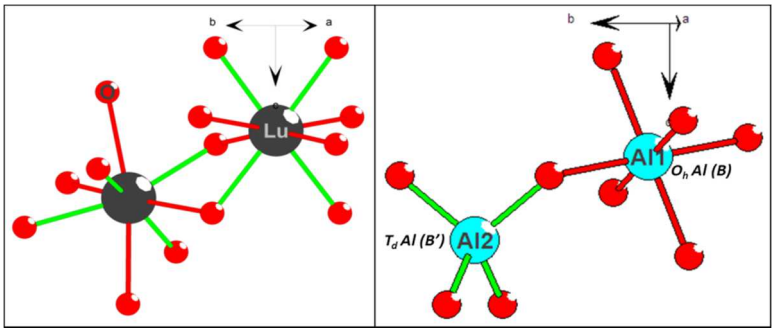

Figure 5. Local bonding environments of Lu (left) and Al (right).

the rest of the general positions of the structure. The 4-coordinated Al^{3+} has Al-O bonds of 1.78Å (green, above right) and 1.93Å (red, above right) for the six-coordinate, also summarized in Table 1. The percentages in the right column are relative bond lengths compared to YAG.

It is interesting to note how these distances are affected when ions of different crystal radii are substituted into the lattice, for example, while the substitution of smaller Lu^{3+} in for Y results in a contraction of both Lu-O bonds, it comes with a corresponding lengthening in both of the bonds to Al^{3+}. For GGG the substitution of larger ions in both positions results in a lengthening of all four bonds.

LuAG			
O	**Al1**	**1.93**	**0.47%**
	Al2	**1.78**	**0.34%**
	Lu	**2.27**	**-1.65%**
	Lu	**2.38**	**-2.46%**
YAG			
O	**Al1**	**1.92**	

	Al2	1.77	
	Y	2.31	
	Y	2.44	
GGG			
O	Ga1	2.01	4.48%
	Ga2	1.85	4.35%
	Gd	2.36	2.25%
	Gd	2.47	1.48%

Table 1. Oxygen bond lengths to Al and RE for LuAG, YAG and GGG. Percentage differences in the right column are compared to YAG.

Sesquioxides as hosts

Closely related to the garnets are the sesquioxides (sesqui- one and a half, as in the ratio of oxygen atoms to REs), and in particular Re_2O_3 (Re= Y, Lu). They are also cubic laser hosts with a space group of *Ia3*, bixbyite type, with a general formula of $(A_{0.75}A'_{0.25})_2O_3$ where A-site is of C_2 symmetry and A' C_{3i} of which only the C_2 site is radiative owing to its lack of inversion center (Figure 6). Hosts of this type can have even more

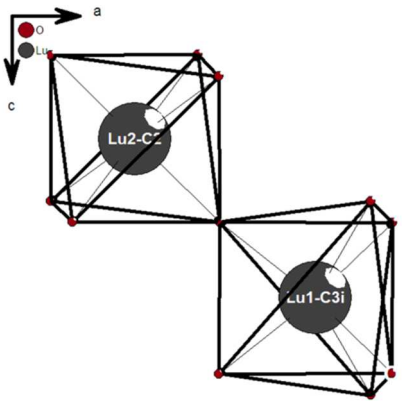

Figure 6. Local bonding environment of Lu_2O_3 sesquioxide showing both radiative and non-radiative sites.

favorable properties, such as a greater density and higher heat conductivity than the garnets and have attracted a lot of attention recently and are discussed is greater detail in

Chapters 6 and 7.[16-28] Table 2 summarizes some of the properties of YAG, LuAG, Y_2O_3 and Lu_2O_3.

Host	Space Group	Lattice Parameter, a (Å)	Calculated Density (g/cm^3)	Hardness (Mohs scale)	Calculated total possible dopant sites (x 10^{22} cm^{-3})	Thermal conductivity (undoped) W/m*K
YAG	Ia3-d	12.01	4.552	8.25 – 8.5	1.386	10
Y_2O_3	Ia3	10.60	5.033	6.8	2.687	13.6
LuAG	Ia3-d	11.91	6.71	8.5	1.421	8.3 - 9.6
Lu_2O_3	Ia3	10.39	9.426	7	2.846	12.6

Table 2. A comparison of some important properties of laser hosts.[18,21,29-31]

Laser active ions

These garnets and sesquioxides are just hosts, though, and do not lase as such. In order for a host to become a laser, a laser active ion needs to be introduced into the crystal lattice during growth in a process called doping, a controlled intentional addition of an impurity into the pristine host. Y^{3+} is not a laser active ion, due in part to its lack of unfilled orbitals, but because of the size and the charge density around it, its site is easily replaceable by most if not all of the lanthanides whose most common oxidation state is also 3+ and whose crystal radii are similar and range from 1.117Å – 1.288Å[32], (Figure 7). During growth, a statistical distribution of these dopant ions can replace Y^{3+} ions in the structure.

Many of the oft-forgotten lanthanides are capable of lasing when substituted into some suitable host, such as YAG. In fact, this top row of the f-block offers a very rich array of laser active ions with low-lying, well-protected, unfilled f-orbitals.[33] It is the protected-nature of these unfilled orbitals that leads to the characteristic sharp and intense

absorption and emission lines of these lanthanide elements because the f-orbitals do not overlap well with common ligand orbitals, such as oxides.

In general, the dodecahedral site is the substitution site for garnets and both of the A-sites in the sesquioxides although, as mentioned, only the C_2 site is a radiative site. In addition to making a host into a laser, doping at the A-site in either of these hosts with these laser active ions completely or partially can affect the properties of the bulk crystal. Properties such as density, index of refraction, frequency of light absorbed and emitted, resistance to damaging radiation, thermal conductivity and lattice parameter are attributes that can be adjusted based on a variety of specific needs. One could see how good control of doping can become a very important tool and our hydrothermal method is shown to

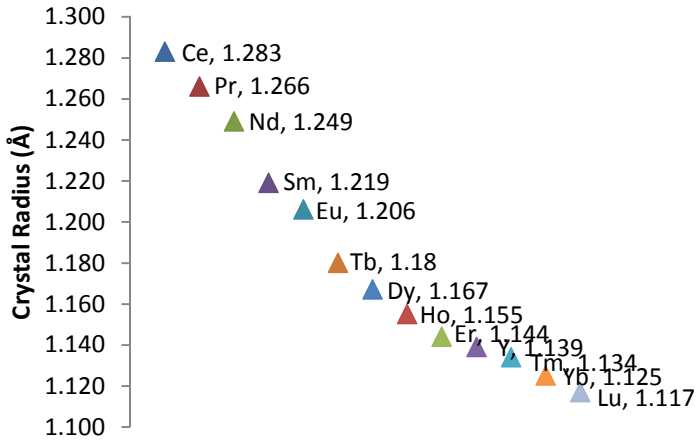

Figure 7. The Ln^{3+} ions arranged by crystal radius. Notice where Y fits into this arrangement.

give us good results. Lanthanides are not the only possible ions that can be doped into a host and when first row d-block ions, such as Cr or Co, are doped into the lattice they typically occupy either of the B-sites.

The lutetium-based analogs, LuAG which is the focus of Chapter 3, and Lu_2O_3 are attractive alternatives to Y-based hosts for a number of reasons. Not only is Lu more massive than Y leading to a denser crystal with less of a mass-mismatch to the laser-active ions, its smaller crystal radius also helps to increase its density as well as leading to a greater energy level splitting. These have important ramifications in the area of thermal management which will be discussed in greater depth in later sections.

Although yttria and lutetia have better properties in some respects than the related garnets, having greater density and thermal conductivity in general, their growth has proven to be somewhat problematic with their melt temperature approaching 2500°C. At such high temperatures conventional melt techniques tend to yield crystals fraught with impurities from the crucible. Our group has demonstrated hydrothermal growth of Lu_2O_3 at temperatures less than 700°C and will be discussed in more depth in the next chapter.

The continued study of solid-state lasers has possibly never been more important with the growing importance of crystals and laser technology coupled with consumers' demand for constant miniaturization. Crystals that are difficult to grow by traditional methods sometimes do not get appropriate attention simply because there is no suitable growth method. Indeed, new laser crystals never before considered can be studied if a convenient route to their growth can be established.

Nature has a particular flair for finding the most elegant way of accomplishing something. She has already perfected hydrothermal crystal growth evidenced by spectacular displays around the world. We have shown that by borrowing this knowledge

we can improve upon traditional growth methods while adding versatility to the process. The closed environment of hydrothermal growth gives us greater control of the components including the impurities that we do want (the dopants), while temperature requirements well below melt temperatures alleviate high temperature effects like stress fracturing and inclusion and oxidation of the crucible. In an effort to gain even greater control of dopant concentrations, a metathesis reaction was used that leads to pre-doped components whose use gave a higher homogeneity throughout the growth process. This is discussed in greater detail in the next chapter.

Garnets are an exceptionally interesting area of study not only because of their favorable properties, as discussed earlier, but their flexibility in being doping by rare earths in the 8-coordinate A-site and both of the B-sites with d-block elements and metalloids. All of these options give us many opportunities to engineer the properties of a crystal.

In our attempt to learn more about the garnet system, the study of natural garnet resulted in the growth of several interesting silicate crystals presented in Chapter 4. The same metathesis reactions used in pre-doping components was modified in an attempt to target new precursors for recrystallization and also lead to some interesting mixed-phase and phase-pure powders.

The hydrothermal growth of doped LuAG crystals allowed us to examine these relatively under-studied laser crystals with a wide variety of dopants including their growth parameters and absorption spectroscopic properties. The growth and cryogenic

absorption spectroscopy of variously-doped lutetia crystals is in its infancy and the ability to grow them hydrothermally gives us the opportunity to vastly add to the literature as these crystals are even less common than LuAG. The spectroscopy results are presented in Chapters 6 and 7.

CHAPTER TWO

EXPERIMENTAL METHODS AND TECHNIQUES OF ANALYSIS

Hydrothermal crystal growth

One of the unique benefits afforded us by the closed-nature of this hydrothermal growth environment is strict control of purity of the grown material. Unlike many of the other methods discussed earlier, potential impurities are limited by the purity of the starting material only. While growing garnets we have seen no evidence of incorporation of either silver from the reaction tube or any of the mineralizers used during crystal growth. In general, the feedstock used to grow all of the crystals used in analysis by hydrothermal technique have been grown using metal oxides with a purity of 3N7 or higher.

Spontaneous Nucleation (SN)

Growth of spontaneously nucleated crystals was performed in both ¼ and 3/8" o.d. tubes. In this type of growth, as the name would imply, small crystallites nucleate spontaneously and grow as they become preferential nucleation sites. Use of the smaller tubes was particularly suited for exploration of systems that are not well known, such as the calcium aluminosilicates presented in Chapter 4. The smaller tubes allows for an array of experiments to occur at once. Tubes are typically cut to around 3" in length which allows five or six to be stacked within an autoclave. Use of longer, larger diameter tubes has some distinct benefits, however, that often offset the fact that only a single experiment can be performed at once.

Figure 8 shows a series of SEM images of SN grown YAG with clearly defined facets. The rhombic dodecahedral morphology typical of most garnets is most commonly observed. These spontaneously nucleated crystals display both {110} and {211} crystal

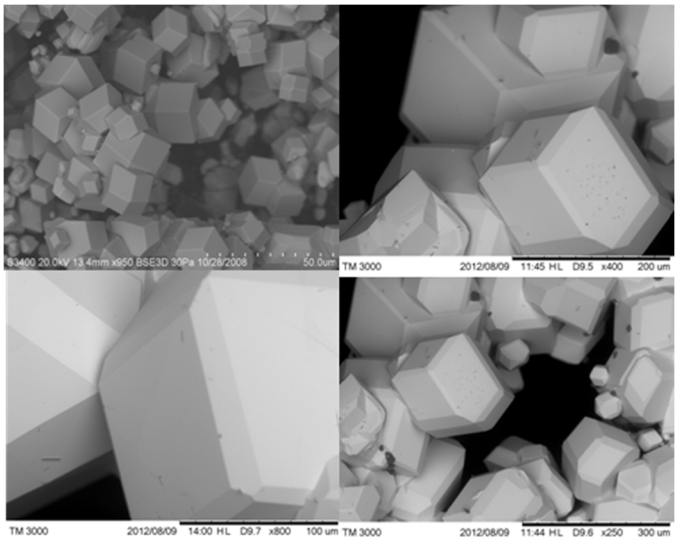

Figure 8. SEM of SN YAG shows surface morphology with secondary facets becoming more prevalent in the larger crystals.

habits, with {110} being the more prevalent forms. We do, however, note that the {211} habit becomes more apparent in the larger crystals, and in some cases (Figure 7, bottom right) can be almost as large as the {110} forms.

Aside from allowing more starting material (about ten times the amount in the smaller tubes) to react which generally leads to larger crystal formation, the larger tubes can be cut to about 8" in length, which allows for a larger thermal gradient to be established. Dual ceramic band-heaters can be set over a wide gradient, which can encourage transport and crystal growth at any temperature along its gradient. The top

band can even be turned off to maximize the gradient. Because we have no way of cooling a section of the autoclave, even when the top band is off, the heat from the lower band will still keep the top section hot and we are limited in the total gradient we can choose to less than about 100°C. However this is generally far more than is normally required and typically only 20-30˚ gradients are suitable. This method is often useful if

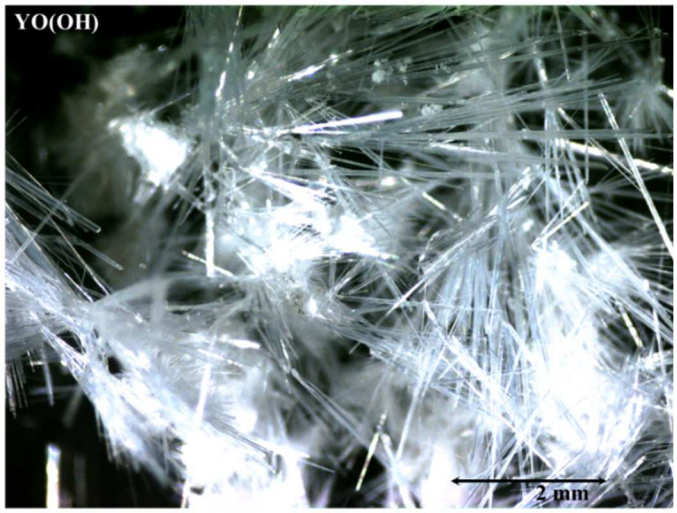

Figure 9. Micrograph of crystals of YO(OH) grown by SN.

there is a number of phases that the components can go through over a particular temperature range. Larger autoclaves can even accommodate three bands or more which allows for a more tightly controlled gradient. The clusters of colorless needles in Figure 9 are YO(OH) and were grown with this method.

SN of Doped Lutetia Crystals

Growth by SN is the method by which all of the doped lutetia crystals discussed in this work have been grown. Although great progress has been, and is continuing to be

made by Colin McMillen[18] and more recently Duminda Sanjeewa[34] on the growth of doped lutetia crystals hydrothermally by both increasing the molarity of hydroxide mineralizer used and increasing the temperature, it is still the only method we use to reliably produce good quality crystals as we continue to grow larger crystals and perfect their crystallization by transport growth. In the SN technique, simple Lu_2O_3 powder feedstock is placed in a silver tube and concentrated KOH (ca. 15M) solution is added. After welding and placing in an autoclave the reactions are performed over a thermal gradient of 640-670˚ for 7-10 days. The simple internal gradient allows for transport of feedstock spontaneously to the top of the tube where the crystals, generally 3-8 mm in size, can be manually harvested. For Lu_2O_3 optimal growth conditions are significantly harsher than for the garnets and require molarities of base solutions of 10 to 20M. Because this far exceeds the solubility of KOH and NaOH at room temperature, in these cases solid hydroxide was added to the tubes with the appropriate amount of water.

Transport Growth and Epitaxy

It was mentioned that epitaxial transport growth is preferred over SN because of the size of the crystal produced. It is not a straightforward matter, though, as shown by our continuing study of the epitaxial Lu_2O_3 system. How and why crystal growth by epitaxy occurs can better be understood by considering the dependence on temperature of the solubility of the feedstock components. In our garnet system for example the components have prograde solubility, or they become more soluble at higher temperatures and their solubility decreases at cooler temperatures.

Although this is not always the case, it is much more common than the reverse case, or retrograde solubility. The temperature of the lower zone is such that the components will slightly dissolve upon heating in the supercritical fluid that forms and hence is called the dissolution zone. This nutrient-rich fluid rises by thermal convection to the upper, cooler zone. At this cooler temperature the solubility of solute is decreased

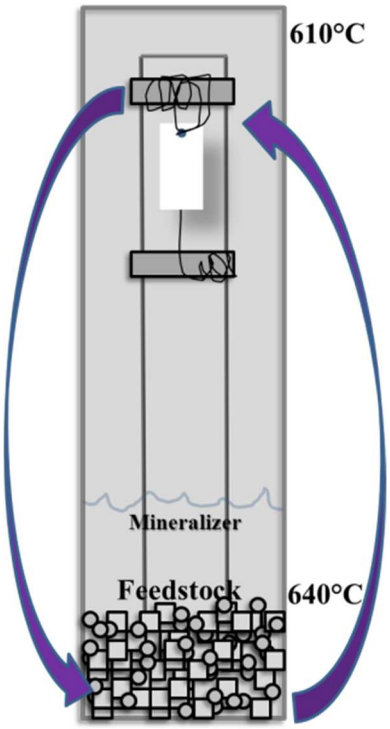

Figure 10. A schematic of the inside of an autoclave showing how crystals grow by mass transport.

enough that it crystallizes out of the solution. The position of the seed within this gradient and the temperatures of both zones are adjusted to encourage this crystallization from solution, ideally onto the seed. The depleted, cooler, denser fluid sinks again to the dissolution zone to pick up more feedstock and the process continues throughout the duration of the growth as depicted in Figure 10.

When optimizing an epitaxial growth on a relatively new system such as lutetia, the transport parameters are not well understood so it is, unfortunately, common to either dissolve the seed crystal or simply have no growth at all. In addition, it obviously requires the presence of an initial seed of suitable size and quality. Since these are not readily available we must gradually increase the size of SN crystals to serve as seeds. With epitaxial systems that have already been optimized, such as for growth of YAG,[35-37] crystal growth is much easier, as in the following example.

In the case of this well-known YAG system, a 5 - 6" ladder was constructed out of pure silver wire (Alfa Aesar, 99.99%, 1.0 mm) that serves to physically stabilize the seed during growth, it holds the seed in the cooler growth zone and is just long enough to easily fit into an outer silver reaction tube of 7 - 8". Two rungs on the ladder one near the top and another farther down allow further stabilization of the seed by enabling anchoring of the seed hang-wire Figure 11, left).

Commercially available YAG seeds were prepared by cutting pieces from a larger 2 mm thick disk with top and bottom faces along the (100) direction, rectangular pieces cut along the (100) or (110) directions to dimensions of about 5 x 10 mm (Figure 11, center). The cutting of hard crystals like YAG is easily done with a water-cooled diamond-encrusted wire saw with a diameter of 0.3 mm. These seeds were then drilled with a diamond-coated drill bit (Starlite Industries, Bryn Mawr, PA, 0.75 mm dia.) near one or both ends and tied with thin silver wire (California Fine Wire Co., Grover Beach, CA, 99.99%, 0.1 mm).

Because the precise concentration (within reason) of mineralizer solutions does not greatly affect crystal growth, stock solutions are typically made up in advance except in the case of the sesquioxides, as mentioned. In any case, extreme care was given to the purity of starting materials added in an attempt to limit additional impurities. This prepared ladder (5 – 6") was then inserted into an extruded pure silver reaction tube 6-7" x 3/8" o.d. along with a stoichiometric ratio of components, usually metal oxides, in this case Y_2O_3, and any other dopant. Along with the metal oxide solid sapphire chunks were

Figure 11. A silver ladder (left) holds a 1 – 2 cm YAG seed (center, magnified) in the growth zone, and a fully grown crystal still on ladder (right).

added as the source of Al, in the case of garnet growth. This was prepared by pulverizing solid sapphire windows into small pieces and granules about the size of table salt able to fit inside the tubes. About 5 mL of a 2M aqueous K_2CO_3 solution is appropriate and affords a 60-70% fill of the tube. The loaded reaction tube was then carefully cleaned inside the top edge and dried to help ensure a good seal and then crimped and arc-welded

closed. After careful inspection under a microscope for integrity, it was then itself inserted into the autoclave with enough water for counter-pressure to prevent bursting of the tube when heated generally leaving a centimeter or two of head-space. The fully loaded autoclave was then finally sealed by tightly screwing on the pressure head assembly.

A temperature gradient was created using two digitally-controlled, ceramic band heaters, each equipped with a dual-metal thermocouple, that were securely wrapped around the body of the autoclave, one for the cooler, growth-zone near the top (610°C) and another for the hotter, dissolution zone near the bottom (640°C). The fully-assembled apparatus was then lowered into an insulated concrete pit and completely covered with vermiculite where it remained undisturbed for the duration of the growth.

A typical growth cycle for an epitaxial coating usually lasts two to four weeks depending on the desired thickness. After this time, the heaters were turned off and the autoclave allowed to cool naturally to room temperature or to be quick quenched with an air stream. The reaction tube was then extracted and carefully cut open (Figure 11, right).

It is necessary to harvest the new growth from the seed when analyzing just the epitaxial layer and this can also be accomplished by wire-saw by affixing the as-grown crystal in a hard wax on a cutting stage. Sawing is then done by cutting edge-wise through the length of the seed crystal. The resulting two slabs can then be polished from the seed side until all seed material is removed. This is also the method to remove the thin

silver hang-wire is usually embedded into the new growth and for any analysis or heat-treatment must be sawed off of the ends of the crystal.

Usually only about a quarter to half of added feedstock actually gets transported to the seed. Analysis by SEM of the leftover feedstock from a 10% Yb:YAG to YAG growth shows well formed YAG SN (Figure 12, right) both primary and secondary facets. The micrographs (left and center) show the exceptional clarity and well-defined facets.

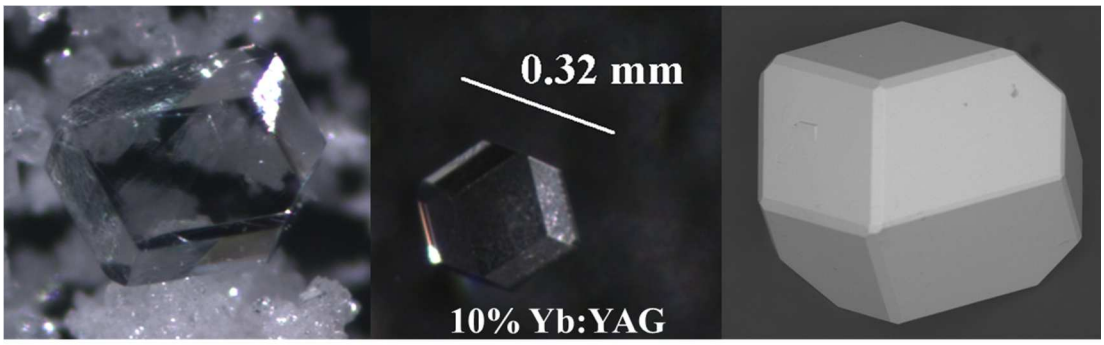

Figure 12. Micrographs (left and center) of Yb:YAG crystals grown by SN show the clarity and quality. The secondary facets emerging can be seen in the SEM image (right).

Polishing of crystals was done in one of two ways. For the larger epitaxially-grown harvested slabs a GemMaster gem polishing system was used with progressive metal lapidary discs and, depending on the amount of material that needs to be removed, starting with a 1200 grit followed by 3000 and ending with a ceramic disk coated with 100,000 mesh diamond spray to give an inspection polish suitable for spectroscopic analysis. This method was especially appropriate for larger crystals grown by epitaxy but proved to be much more difficult with the small crystals obtained by SN. The other

method, discussed in detail in Chapter 5, is a manual method customized for these types of crystals where polishing with and electric lap risks causing damage.

A portion of a YAG seed that has been coated with LuAG was cut from a grown crystal and polished for analysis and can be seen in the SEM element map in Figure 13. It shows a clear segregation of Y in the lower left portion of the left picture corresponding to the YAG seed and concentration of Lu in the upper right portion corresponding to the new LuAG growth. A rough corner was specifically chosen to show smooth coating

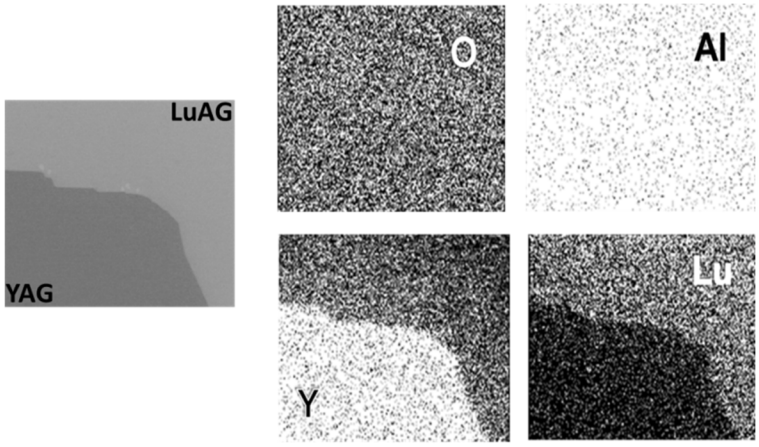

Figure 13. Element mapping shows smooth growth of LuAG around a rough corner of a YAG seed.

around the edge of the seed and demonstrate that all surfaces of the seed crystal are coated with this method. The ramifications of this result are important and highlighted in Chapter 8. Any dopant was also added into the original feedstock in the desired stoichiometric ratio, usually as an oxide or chloride, such as Nd_2O_3 or $NdCl_3$ for example.

Because doping concentrations are typically very low, usually around one atomic percent or less, the logistics of adding precise amounts of dopants to reaction tubes

provided a particular technical challenge. An important point is whether the dopant would grow in a consistent concentration throughout the whole growth cycle. It seemed unlikely that within the tube there would be exactly the same ratio of dissolved starting materials at any given point during growth. Ensuring consistent availability of components throughout the growth run, especially that of the dopant, should increase the likelihood of uniform dopant concentration throughout the crystal. Because good control of doping is very important, a number of techniques were investigated to address this concern.

Pre-doping feedstock for greater control of dopant

A technique common in the preparation of ceramics called coprecipitation is a way of pre-combining starting materials into a single feedstock. In this method all components are first dissolved in either acid or water, combined in the desired ratios, and then dripped slowly into a solution of precipitating agent. This wet powder is washed and dried and then calcined in a furnace for a period of time to densify and partially crystallize the solid powder.

For example, to make 1% Nd:Lu_2O_3 for feedstock, 5 g of Lu_2O_3 was dissolved in hot, concentrated nitric acid with stirring until perfectly clear. In our experience, if the metal oxide is not completely dissolved a mixed phase including the metal oxide will result. In a separate Erlenmeyer 0.0427 g of Nd_2O_3 was dissolved resulting in a ratio that would provide 1 at.% substitution of Lu ions. Although a variety of water-soluble sources

including nitrates and chlorides have been used with good results and do not require the use of acid for dissolution, oxides were chosen simply on the basis of cost.

After cooling each solution they were combined and thoroughly mixed. This new solution was then dripped slowly into a vigorously stirring basic solution consisting of a 1:1 ratio of NH_4OH (~29 wt%) and water to about 400 mL total volume. Periodic testing of the pH was done to ensure that the solution remained sufficiently basic, at least pH 13, to cause precipitation of all of the metals as they were introduced. Ammonium hydroxide is not the only possible precipitating agent, but it was used not only because it is inexpensive and relatively harmless, but also because it tends to give a precipitate that is large and settles out of solution easily making filtering and washing easier which suits our purposes well.

The solids were then washed with DI water by repeatedly settling the precipitant, decanting and adding more water until the wash-water was pH neutral. Final isolation of this solid can be done by centrifuge, filtering, or simply decanting. The clean, wet powder was put into a beaker or crucible and then into an oven at about 200°C for several hours until completely dry. Drying this wet powder completely before calcining helps to prevent spattering of the material during calcining. The temperature was then increased to 1000°C as calcination took place over the course of several hours while crystallites began to form and grow larger. Identification of the crystalline powder was done by powder pattern matching and elemental analysis by energy dispersive X-ray.

Powder pattern matching

In order to help confirm the composition of the material prepared as described above, PDXL or powder pattern matching was used. The powder pattern match to a database pattern of Lu_2O_3 gives not only a good indication of its identity as an oxide, but also an idea of its crystallinity or crystallite size. Powder pattern matching is often used in crystallography to give supporting evidence of the identity of a crystalline powder. It is a non-destructive method that only requires a small amount of material.

Samples used for identification were well-ground and placed on an aluminum disk target. A Rigaku Ultima IV powder diffractometer equipped with Cu K_α radiation (λ = 1.54056 Å) was used to generate powder patterns (2θ = 5-65°, scan speed of 1.0°/min). Phase identification was made by comparison patterns indexed by the International Centre for Diffraction.

In the example of 6% Nd:Lu_2O_3 the powder pattern progression in Figure 14 shows the comparison of patterns of the same coprecipitated feedstock after drying, and after at least 2 hours at each temperature listed: 300°C, 400°C, 500°C and normal calcination temperature of 1000°C. Compared to the major lines (black) from the database entry for Lu_2O_3 it is reasonable to conclude that the material is at least structurally very similar to Lu_2O_3 even if we cannot unequivocally determine the presence of dopant by this method alone.

Just after drying and even up to heat treatment at 300°C, it can be seen that the material is still amorphous due to the only feature being a broad, low-intensity band around 2θ = 30°. Above that, however, peaks start to become apparent as the crystallites

begin to form. After treatment at 1000°C we see a pattern with an exact match to database Lu_2O_3 and with fairly sharp peaks. The other thing that can be observed is the shifting of the peaks in relation to the database.

The exact position of the peaks in a powder pattern is a function of the d-spacing in the crystal structure or the spacing between crystallographic planes. As the lattice is expanded, the d-spacing is also increased and this effect becomes greater with increasing θ and is inversely proportionate tending to shift peaks towards smaller θ. In the powder

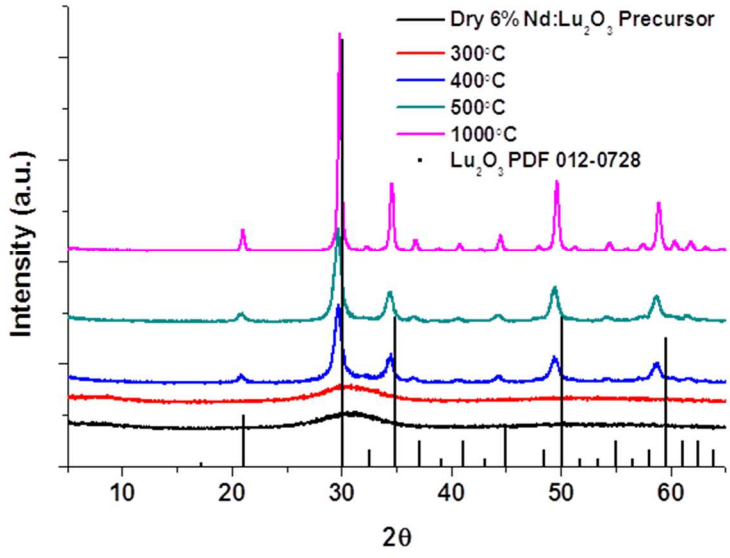

Figure 14. The powder patterns of a 6% Nd:Lu_2O_3 precursor calcined at a series of temperatures show peaks first emerging after 300°C and sharp and intense at 1000°C. Peak shifting in relation to undoped Lu_2O_3 can also be seen.

pattern for 6%Nd:Lu_2O_3 above, we have substituted Nd with a crystal radius of about 1.12Å in for Lu which has a radius of about 1.0Å. In order to accommodate this larger ion the lattice expands slightly in agreement with Vegard's law that predicts that a

crystal's lattice parameter varies approximately linearly with the concentration of an impurity.[38] Evidence of this is seen in a powder pattern by a shifting of peaks towards smaller θ with greater shifting at higher values of θ as observed in the calcined material. Depending on the degree of adherence to Vegard's law, the dopant concentration should be able to be estimated by the amount of expansion of the lattice and, by extension, the amount of shifting of the peaks in the powder pattern.

Lattice parameter matching

This expansion or contraction of the lattice by substitution of a larger or smaller ion has important implications, especially concerning lattice parameter matching of a crystal with its epitaxial layer. To show control of a lattice size, we doped a series of LuAG coprecipitates with Ga.

The three microcrystalline powders of LuAG feedstocks were prepared using virtually the same protocol as for doped oxides with the addition of Al in the form of $Al(NO_3)_3$ which is inexpensive, easy to work with and quite water-soluble, and Ga^{3+} from $Ga(NO_3)_3$. Gallium was chosen for lattice expansion because of the greater crystal radius

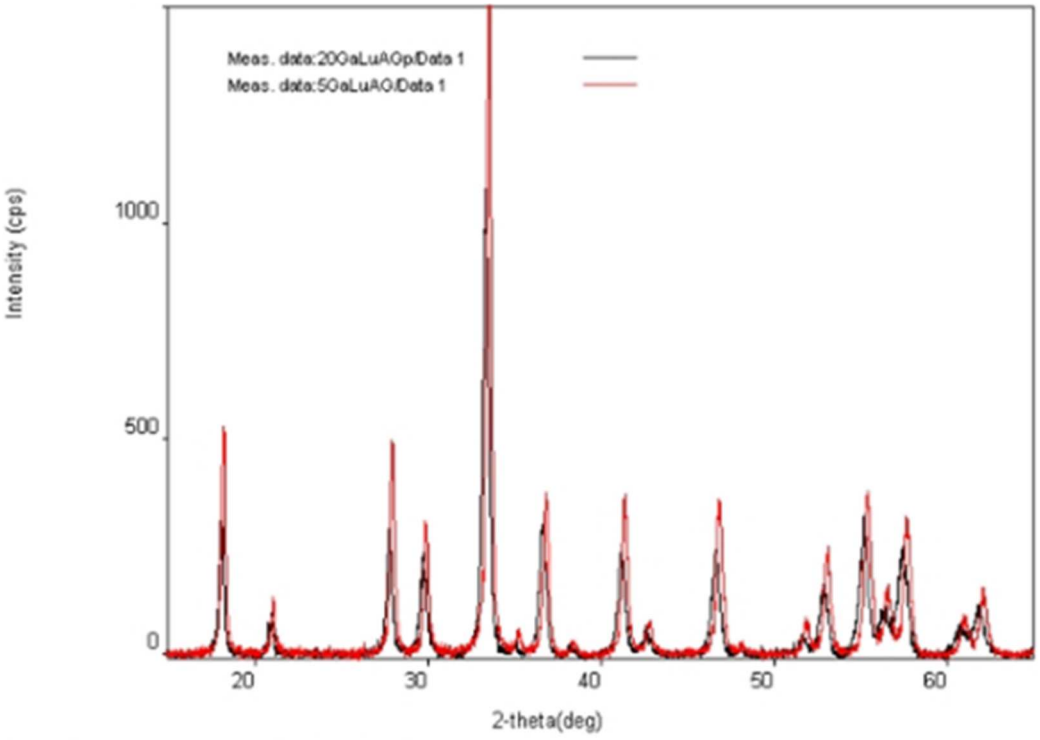

Figure 15. A whole powder pattern comparison of 5% Ga: LuAG to 20% Ga:LuAG. Greater doping in the 20% pattern shows significant shifting at higher values of θ compared to 5%.

(0.61Å and 0.76Å for tetrahedral and octahedral respectively)[32] compared to Al for which it substitutes (0.53Å and 0.675Å) and because it is spectroscopically silent. In Figure 15 we can see the whole pattern comparison of Ga:LuAG from 5% to 20% doping, with the increased shifting towards lower θ on the right side.

The powder pattern in Figure 16 shows the patterns for 20 at.% Ga:LuAG (black line), 5 at.% Ga:LuAG (blue line), and "0 at.% Ga:LuAG" or undoped LuAG (red line). As expected, we see evidence of peaks shifting towards lower values of θ with greater

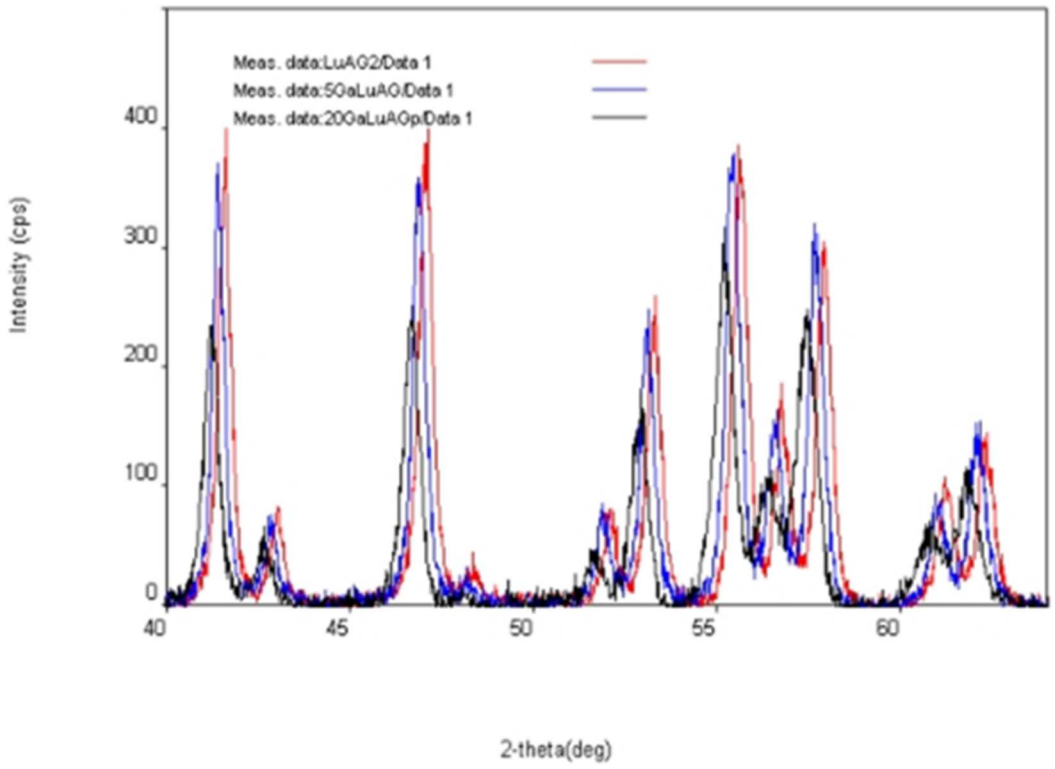

Figure 16. The 2θ region between 40 and 65 shows the clear peak shifting of undoped LuAG, 5% Ga:LuAG and 20% Ga:LuAG.

doping indicating that there has been a lattice expansion.

Epitaxial growth requires good lattice match between the layer and the seed crystal and this method of controlled lattice expansion or contraction has important ramifications. The epitaxy has to be of the same space group and the same lattice parameters within 15%.[8]

When there is a lattice mismatch between seed and epitaxy layer defects at the interface can propagate throughout the entire new growth (see Chapter 3, Figure 23) and, indeed, where the mismatch is too great there will be no growth at all. Having some control over the lattice parameter could tune it to a better fit with a surrogate seed or an additional epitaxial layer. For example, Nd:YAG ($a > 12.01$Å) has a lattice parameter greater than undoped YAG ($a = 12.01$Å) due to the larger Nd^{3+} (1.249Å) in place of Y^{3+} (1.139Å) in the lattice. The greater the Nd-doping the greater the lattice parameter and the more of a lattice mismatch would exist between the Nd:YAG and the LuAG ($a = 11.91$Å) layer. If, however, the lattice of the LuAG layer could be expanded closer to that of the Nd:YAG, less of a mismatch would exist, in principle giving better growth. The peak shifting evidence of Figure 16 indicates that the parameter of Ga:LuAG *is* larger compared to undoped LuAG, and, consequentially closer to that of the YAG seed.

Evidence that Ga is incorporated into the Ga:LuAG layer is offered in the SEM element map in Figure 17. The Al is concentrated in the seed portion, but in the Ga-doped layer there is a uniform, but reduced, concentration. This supports a partial doping of Ga for Al and not a complete substitution, while the Ga is found only in the epitaxial layer as would be expected.

In relation to the scale bar, we also see that there appears to be good growth even at the interface. We see that Y is concentrated in the region on the left corresponding to the YAG seed, but we also see the presence of small concentrations of Y into the epitaxial layer, decreasing farther from the interface. This is presumably due to a small

but definite back-dissolve at the beginning of the growth cycle, which is common in our experience. This is supported by the absence of Lu in the seed area, but its increased presence farther from the seed.

While this phenomenon is often seen, it appears to be small and concentrated very near the interface, up to about a hundred microns. Too much of an initial back-dissolve can dissolve a seed completely or enough to cause it to drop off of the ladder into the feedstock, but a slight back-dissolve can be desirable because it can prepare a better surface for growth to begin.

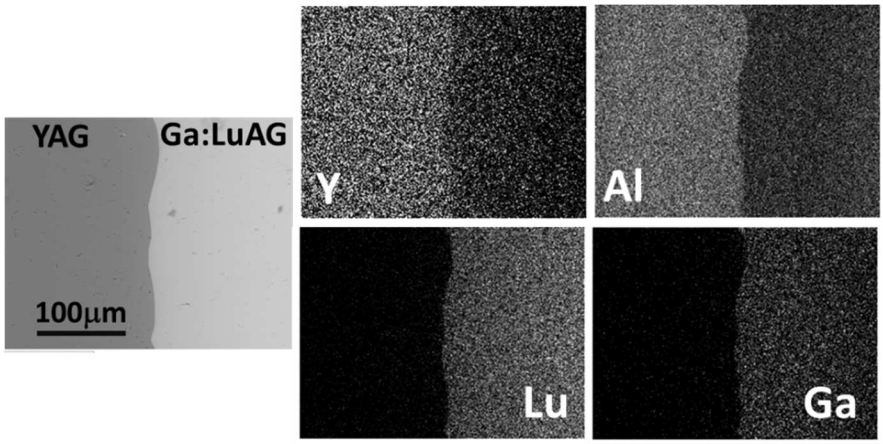

Figure 17. Element mapping of an epitaxial layer of Ga:LuAG on a YAG seed. Ga is concentrated in the region of new growth while there is a concomitant, uniform decrease in the concentration of Al between the seed and new growth.

The SEM image of a polished cross-sectional piece of 6 at.% Yb:YAG grown on a YAG seed shows significant back-dissolve (Figure 18). The original seed is the darker portion in the center of the image and is estimated to be only about a quarter of its original thickness with a much rougher surface.

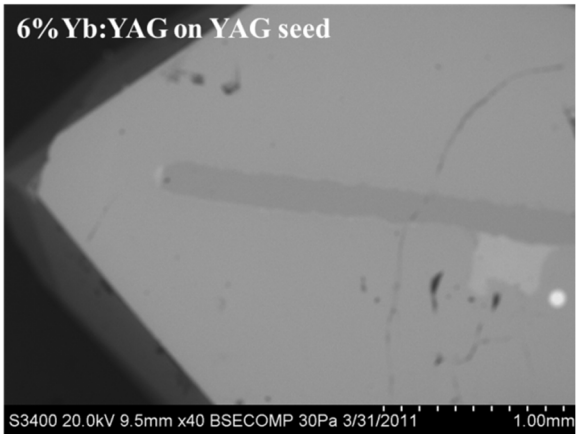

Figure 18. An SEM image looking end-on through a cross-section of Yb:YAG on a YAG seed.

Elemental analysis by Energy Dispersive X-ray

Powder pattern matching alone does not suffice for analysis of pre-doped feedstocks in that, especially for lightly-doped components, the powder patterns of Lu_2O_3, 1%Yb:Lu_2O_3 and Yb_2O_3, for example, look very similar due to their similar lattice sizes and crystal structures. For this reason, elemental analysis by SEM was also used to verify the presence of a dopant as well as its concentration. Energy Dispersive X-ray (EDX) and element mapping were done on both powder and crystal samples using a Hitachi 4800 High Resolution SEM (Tungsten filament source, Resolution: 4 nm at 30 kV (BSE) equipped with Inca software package, SU6600 Variable Pressure SEM

(Resolution: 1.2 nm at 30 kV, Schottky diode source) or TM3000 Tabletop SEM (15kV) against a Cu standard.

EDX is an X-ray scattering technique that bombards samples with high-energy X-rays causing ejection of core electrons. The energy given off as outer electrons drop into

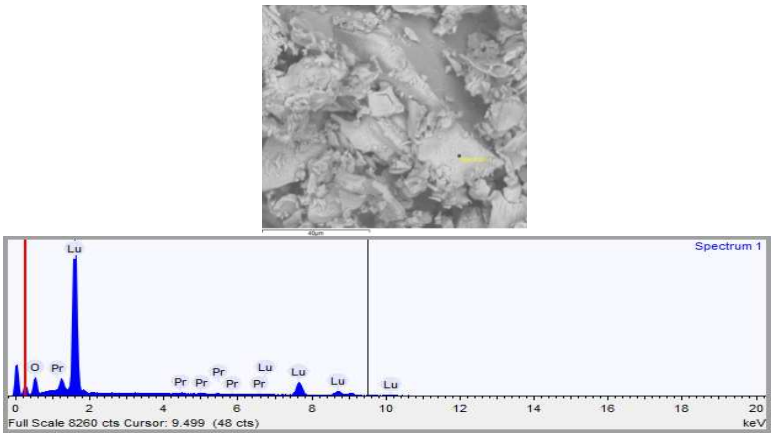

Figure 19. EDX of the powder sample (top) gives a quantifiable spectrum match to each element detected (bottom).

those vacancies creates a pattern unique to each element that is then quantified. Figure 19 shows both an SEM image of powdered sample of coprecipitated Pr:Lu_2O_3 as an example feedstock with its EDX spectrum. The data in Table 3 shows the atomic percentage of Pr to total RE-sites (Pr + Lu) at about a 2.6 atomic doping percent. Although doping can be reported as the number of ions per cubic centimeter doping percentages are usually reported as a percentage of replacement of a native ion.

Element	Weight %	Weight % σ	Atomic %
Oxygen	18.089	0.364	70.612
Praseodymium	1.743	0.317	0.773
Lutetium	80.168	0.439	28.615

Table 3. Elemental analysis by EDX of a powder sample of Pr:Lu_2O_3 feedstock gives a 2.6 % doping of Pr with respect to Lu-sites.

When this pre-doped material is used as the sole source of both native ion and doped ion, we can be sure that only the precise amount of dopant is available with respect to the native ion during the entire growth process. An electron microscopy technique using a series of spot analyses supports this hypothesis as shown in Figure 20 for a sample of 30 at.% Er:LuAG grown on a YAG seed.

This sample was grown using a 30% Er:Lu_2O_3 feedstock prepared as described previously. After growth a cross-sectional slice was cut and polished to a parallel flat

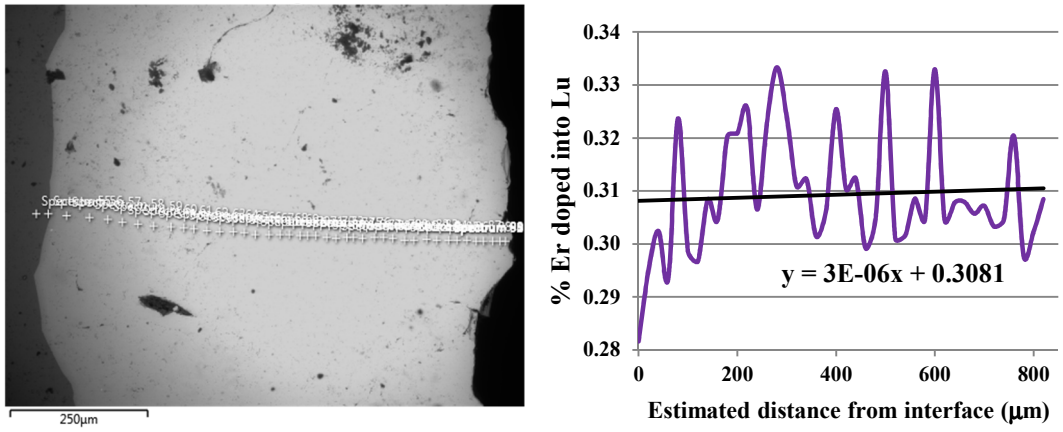

Figure 20. Elemental analysis at closely-spaced points from seed – epitaxy interface to crystal surface shows homogeneity of doping concentration throughout the growth. Doping level is also close to the intended 30%.

slab. Samples for analysis by SEM were securely affixed to an aluminum sample target with carbon tape and no coating was necessary. This is a significant result because it demonstrates the highly consistent concentration of dopant across the entire layer.

Analysis spots indicated by crosses in the SEM image were spaced at as regular distances as possible (~15 – 20 µm) across the YAG / Er:LuAG interface on the left throughout the new Er:LuAG growth on the right to the crystal edge at the right edge.

The two things that are apparent from the data above is that the doping level is fairly constant from the seed interface to the outer edge as attested by the slope of the trend line being very nearly zero and that the doping percentage is centered very close to the intended 30% doping. This gives us evidence that the pre-doped feedstock does offer some control and consistency in cases where the amount and homogeneity of dopant are important. It is for this reason that most of the garnets discussed herein were grown using a doped metal-oxide precursor in the feedstock.

Index matching by single-crystal diffractometry (XRD)

Single crystal samples used for crystal structure analysis by XRD for were mounted to a small glass fiber using two-part, five-minute epoxy. In general, crystals of the best quality were chosen with no visible intergrowth and the smallest size of particular morphology in order to increase the chance of getting a solvable dataset.

Identification was then done by unit cell index matching to a database using diffraction data from a set of 12 preliminary scans through a range of incident angles or by complete solution of a full set of 480 scans using a Crystal Clear data analysis software package. Data sets were obtained on a Rigaku diffractometer using 3 second scans.

CHAPTER THREE

LuAG

Lutetium aluminum garnet (LuAG), the lutetium analog to YAG, is much less well-known than YAG in part because of its lack of availability and suitable methods to grow large optical quality crystals. This is partly due to its high melt temperature, which is close to 2500°C and can sometimes result in thermally induced defects and large regions of optically unusable crystal. Because of the substantially higher cost of lutetium compared to yttrium a method less wasteful of an expensive feedstock is worth pursuing. This makes its growth by the hydrothermal method an attractive alternative requiring much lower temperatures. Although it has many of the same desirable properties as YAG such as an isotropic, cubic structure and good physical stability, the promise of even better properties such as greater density which leads to a more durable crystal, a smaller lattice parameter which leads to a greater effective doping per path length is intriguing. The greater density of LuAG compared to YAG also leads to greater radiation hardness for scintillation applications when doped with such ions as Pr^{3+} and Ce^{3+} for high-energy particle detection and quantification.[39]

This lattice contraction also increases the splitting of the Stark energy levels and shifting absorption peaks slightly towards shorter or sometimes longer wavelengths with respect to a YAG host which could further improve its properties such a shifts towards pump source wavelengths or, in the case of Tm-doping, further into the NIR, out of the

range of absorption of atmospheric water and carbon dioxide, making its use more attractive for range-finding using light (lidar), applications.[40]

The fact that the mass of the Lu ion is much closer to that of the laser-active lanthanides (e.g. Yb, Er, Tm) leads to less of a decrease in thermal conductivity at higher doping levels.[41] Also the similarity of crystal radii offers the possibility of greater doping and there does not appear to be a doping limit based on size of ion. The effect of mass-mismatch of the Lu host ion and dopant ion on the thermal conductivity is discussed in greater detail in Chapter 6 on Yb-doping.

LuAG is also one of the few materials transparent under about 200 nm retaining a high refractive index and fairly low intrinsic birefringence (30.1 nm/cm) making it attractive for use in 193 nm immersion lithography.[42] These potential benefits of a LuAG host over YAG enticed us to study its hydrothermal growth and properties in depth. In this chapter we describe the development of a hydrothermal growth method of LuAG single crystals, as well as a protocol for the systematic growth of doped LuAG containing any other rare earth ion of interest.

Hydrothermal crystal growth

The hydrothermal growth of various garnets was reported in the 1960s but there has been no significant addition to the literature essentially since the mid-1970s when Laudise, Ferrand, Puttbach and Kolb each reported briefly on some aspect of the hydrothermal growth of YAG.[37,43-47] We recently demonstrated the growth of high-quality refractory oxides[35] and other garnets[36] by the hydrothermal method including by

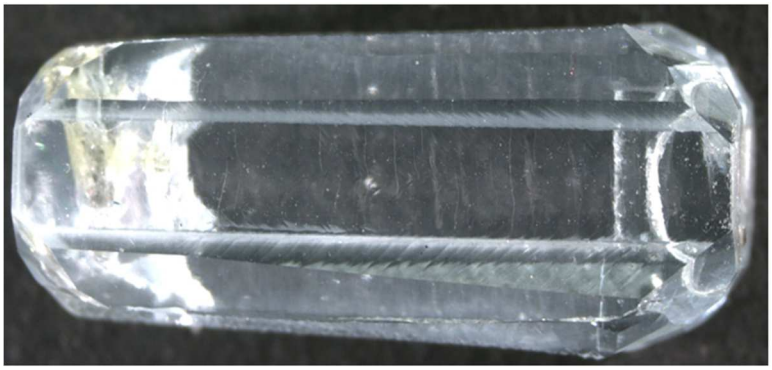

Figure 21. Undoped LuAG grown on a YAG seed. A slight tapering of the LuAG growth can be seen from right to left due to a thermal gradient across the seed during growth. The final length of the crystal is 14.41 mm.

hydrothermal epitaxy. Given our success with the growth of YAG, this method was extended to include LuAG in the exploration of its growth in our hydrothermal system.

Although ideally, growth of doped LuAG would be done onto a LuAG seed, the lack of availability of LuAG seed crystals makes their use as seeds difficult and expensive. YAG seeds were a suitable alternative with a lattice mismatch of only about 0.6%. Growth of undoped LuAG on YAG was done using powdered Lu_2O_3 and crushed sapphire feedstock with 2 M K_2CO_3 mineralizer with a 610°C – 640°C thermal gradient, in a procedure analogous to that of YAG which was discussed in Chapter 2.

Undoped LuAG has been grown on a YAG seed in Figure 21 showing the quality and clarity that is possible with hydrothermal epitaxy. Due to a thermal gradient along the seed, growth of the LuAG layer can be seen tapered slightly from right to left.

In Figure 22, though good clarity, there is evidence of slight cracking of the epitaxial 1% Nd:LuAG coating on YAG (left) which is a view looking through the edge of the seed and less so in the harvested slab on the right. This cross-hatch pattern implies a possible defect from lattice mismatching that has propagated out from the interface. It is possible that this cracking could be mitigated by using a more-controlled cooling profile after growth. The extent of defect propagation can be easily seen in the harvested polished slab of undoped LuAG that was grown on YAG (Figure 23) after the YAG seed was polished away leaving only the hydrothermally grown LuAG. The quality of the crystal improves from the bottom (where the seed was) towards the outer surface (top).

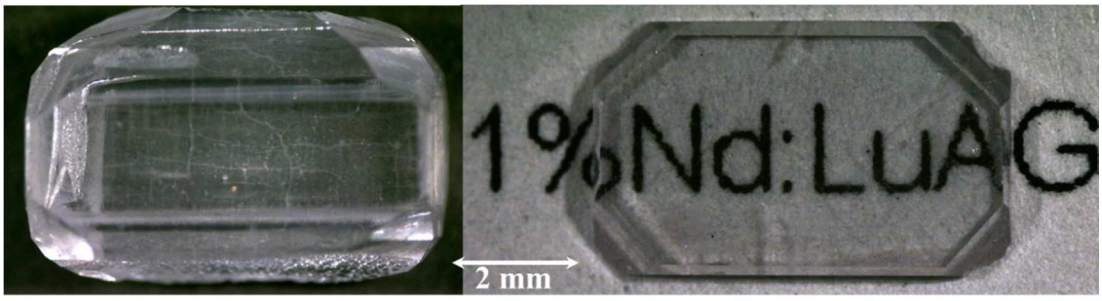

Figure 22. Slight cracking can be seen in the LuAG on YAG seed (left). Harvesting and polishing (right) shows the clarity of the pure LuAG slab.

Cooling for all epitaxial crystals was done either quickly by an air stream, which can take less than an hour to go from a growth temperature of 640°C to room temperature, or more slowly by turning off the bands while still under insulation and allowing it to cool naturally which can take twelve hours or longer. Quick cooling by air stream is done to minimize the time that the system is in the cooler temperatures that lead

to competing phases, such as REO(OH) and $RE(OH)_3$ but could potentially add to the cracking by thermal shock as the crystal lattice is forced to shrink as it cools quickly.

Slower cooling at higher temperatures followed by a faster cooling at lower temperatures could slow the lattice contraction enough to lessen cracking while still minimizing overall cooldown times.

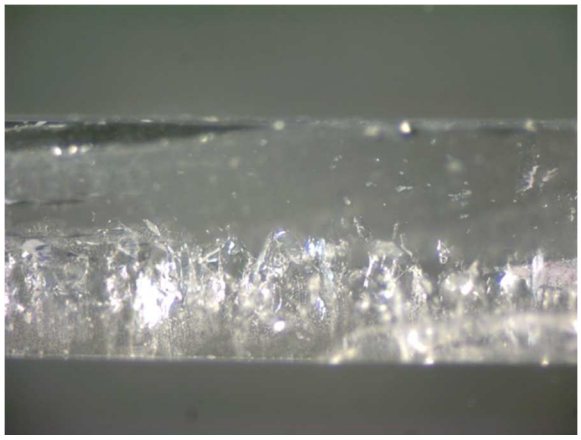

Figure 23. Harvested and polished slab of Nd:LuAG grown on YAG seed shows how interfacial defects can propagate out from the seed through the new growth.

Growth of Ga:LuAG

To address the lattice mismatch issue, 30% Ga:LuAG was grown onto a YAG seed from components using the same protocol as for YAG, 5 mL of 2M K_2CO_3 mineralizer and a temperature gradient of 610°C on top and 640°C on bottom. A duration of seven days was chosen to show proof of this concept and after this time the crystal had almost doubled in weight from 0.2396 g to 0.4526 g in uncontrolled growth as shown in Figure 24.

The slab in the center was cut near the hanging wire, which caused the waist-like indentation. The SEM image on the right gives a better look at the internal quality of the growth and its elemental analysis shows a Ga-doping of 28% in the area near the crystal surface (green box.) When growth is very fast, as in this case, it is typically of poor quality, but there are methods to slow down growth such as narrowing the thermal gradient or using a reduced mineralizer concentration, that are likely to improve the quality. In this case we were not particularly concerned with overall crystal quality but only in proof of concept of growth of Ga doped LuAG.

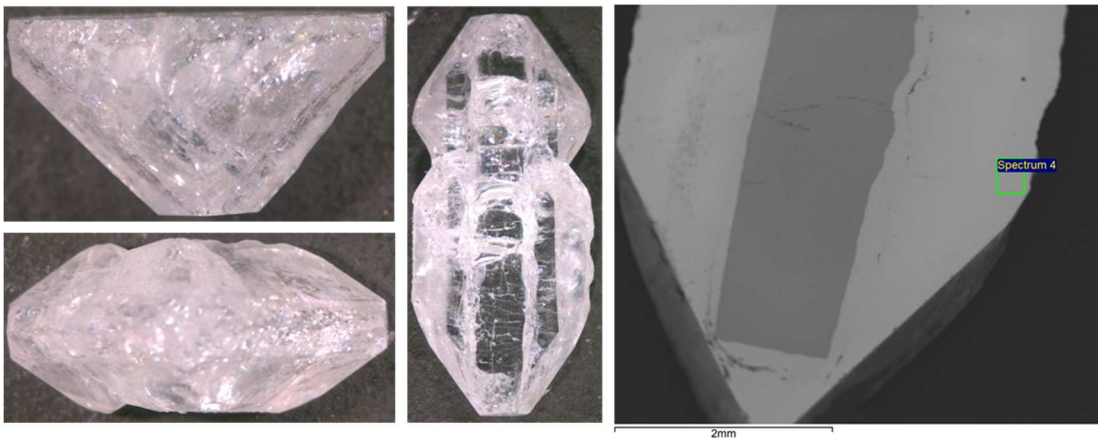

Figure 24. Ga:LuAG grown on YAG seed using same parameters as for YAG growth. Growth was too fast and could likely benefit from a milder growth environment. SEM image on right shows the relatively poor quality.

Another technique that has been shown to improve the quality especially at the interface is based on a gradual widening of the thermal gradient during growth. While we have gotten very good quality growth of garnets by immediately setting both bands to their final gradient (610°C – 640°C) we got consistently better results by initially setting a very narrow gradient of 3°C (637°C – 640°C) for three days followed by a gradual

widening to the final gradient.[48] This protects the seed from extensive back-dissolve by keeping a positive solubility gradient while allowing time for equilibration of the system. Gradual widening of the gradient by lowering the temperature of the top band encourages slow, controlled growth rate at the beginning of the cycle which is then increased as the gradient is widened.

Early in the course of this work, growth of gadolinium gallium garnet (GGG) was also performed. GGG is a garnet used for magnetic bubble devices and to a much lesser extent as a laser host. Its growth was attempted according to growth parameters published by Kolb and co-workers[43] from components, 12 M NaOH mineralizer with a thermal gradient of 440°C - 500°C. Seven days at these conditions gave a 10% weight gain of moderate quality with prominent faceting. It is interesting to note that, although a garnet, its growth parameters differ markedly from those of YAG and although we regularly get good quality growth of LuAG using the same parameters that we use for YAG, it is possible that further optimization is possible.

Nd:LuAG

One of the goals of this investigation was to grow a series of LuAG crystals doped with an array of lanthanides. Aside from Nd-doped lasers being one of the most common, Nd has one of the largest crystal radii of the lanthanides, and hence has a relatively large difference between dopant and host Lu ion, which has one of the smallest. In our exploration of the LuAG system it was our thinking that if it was possible to grow

crystals of Nd:LuAG with this size difference, the other, smaller, lasing ions would present no additional challenge. It was for these reasons that we began with Nd:LuAG.

Initial growth of a Nd:LuAG crystal used a pre-doped Nd:Lu_2O_3 component with a targeted doping of 4% as the metal oxide component (Figure 25). Subsequent spectroscopic analysis of the slab suggested that actual doping levels were closer to 2.6%, however,[49] and was corroborated by neutron activation analysis (2.7 ± 0.3%). This result is surprising and significant because, even though the lattice is smaller in LuAG, this is still a very high level of Nd doping. In fact it is a much higher level than is attainable in Nd:YAG crystals grown by the Czochralski method, which is around 1%. The ability to

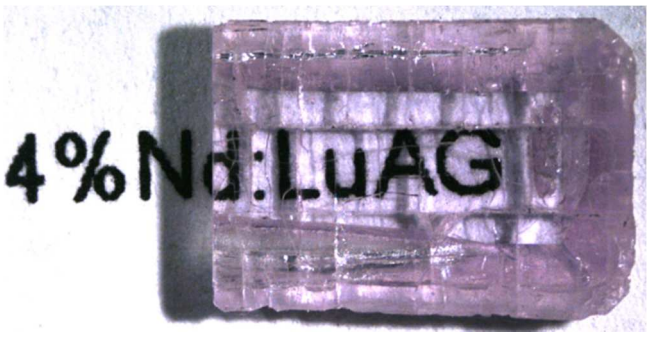

Figure 25. Nd:LuAG grown on a YAG substrate. Extensive cracking implies that growth conditions are probably not optimized.

dope higher concentrations of active ions into a laser host could necessitate smaller laser cavities, possibly lowering cost and mitigating thermal management issues. The upper limit of Nd-doping into a hydrothermally grown LuAG crystal is unknown, but warrants further investigation.

The normalized, room temperature high-resolution absorption coefficient spectrum of Nd:LuAG is presented in Figure 26 and is compared with Nd:YAG. While they are very similar, a subtle difference can be seen. There is a reversal of intensities between the peaks at 590 and 808 nm but there appears to be no other significant

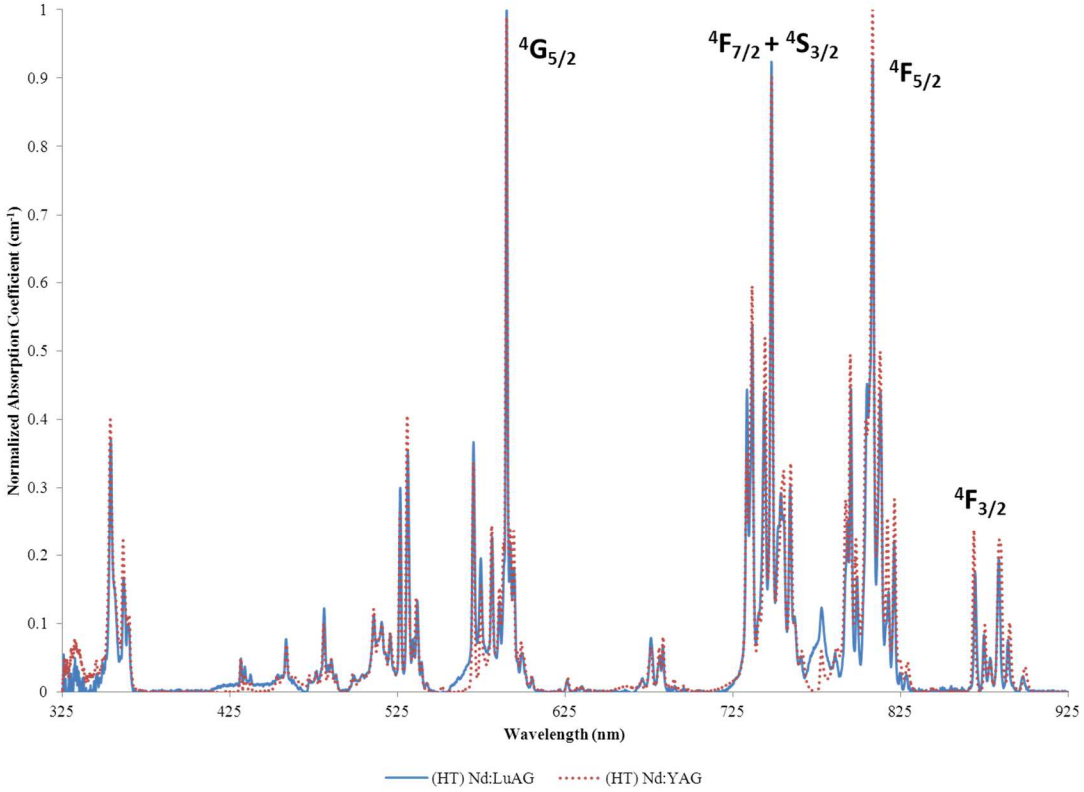

Figure 26. The normalized room temperature absorption coefficient comparison of Nd:LuAG to Nd:YAG shows no appreciable difference except a reversal of intensity of the peaks at 590 nm and 808 nm.

differences between the two spectra including the position of their pump band at ~ 808 nm. This compares well with spectra from crystals grown by other methods.[50-53] A more detailed analysis of the room-temperature comparison of Nd-doped LuAG, YAG, Lu_2O_3

and Y_2O_3 as well as a series of cryogenic absorption spectra of Nd:Lu_2O_3 is presented in Chapter 7.

The absorbance spectrum from 750 nm to 1000 nm is over-layed with its emission spectrum excited at 808 nm in Figure 27. Typically laser pumping is done into the band at 808 nm indicated by the blue line. Along with the strong 1064 emission typical of Nd-

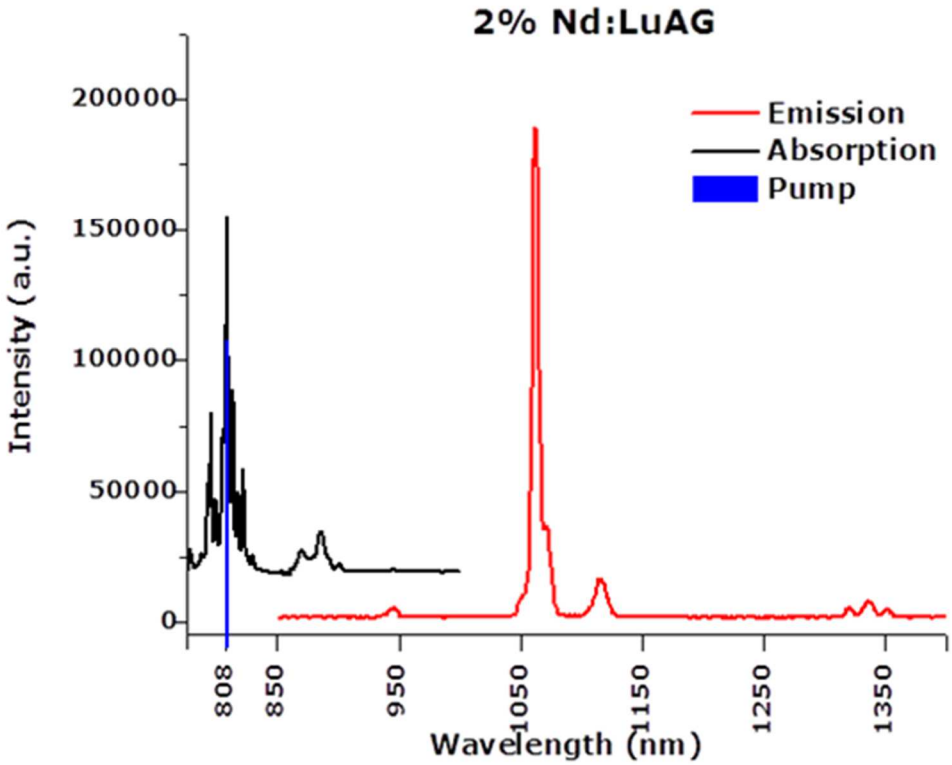

Figure 27. The absorption spectrum of Nd:LuAG along with its emission spectrum excited at 808 nm. the pump line is shown in blue.

doped lasers, we can see much less intense emissions at around 946 nm and 1130 nm, as well as a small cluster around 1340 nm.

Yb:LuAG

Ytterbium is the heaviest of laser active ions and has a very simple two-manifold energy level structure. The ramifications of this are important and warrant further discussion. This is presented in Chapter 6 along with a detailed comparison of the cryogenic absorption coefficient spectra of different Yb-doped hosts. Several preliminary aspects of the doping chemistry are presented here.

Closer inspection of the electron configuration of ytterbium in the 3+ state (Yb^{3+}:[Xe] $4F^{13}$) suggests that its 2+ state might also be stable owing to its isoelectronic configuration to that of the inert gas Xe and, indeed, this has been shown experimentally to be the case.[54]

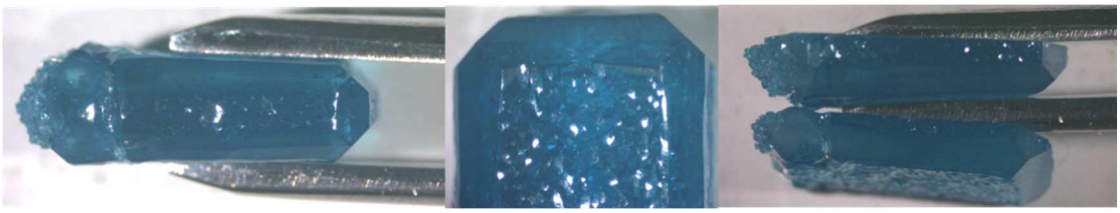

Figure 28. An as-grown Yb:LuAG on YAG crystal shows attached SN (left) on one end of the blue crystal and normal hillock growth (center). Two slabs result from cutting through the YAG seed lengthwise which will then be polished away.

We have demonstrated growth of Yb:LuAG from metal oxide components, Lu_2O_3 and both Yb_2O_3 and $YbCl_3$ and from pre-doped Yb:Lu_2O_3. In our experience, when Yb is doped into a LuAG host it can enter into the lattice in a partially reduced state, where a small number of the Yb ions are in the 2+ state, which is a dark- to light-blue color (Figure 28). It does not appear to be the result of the type of components used during growth.

Annealing the blue Yb:LuAG crystal in an open-air furnace at 1000°C for at least 2 hours has proven to be sufficient to oxidize any Yb in the 2+ state to the colorless 3+ state (Figure 29). Spectroscopic evidence given in the large, broad absorption bands

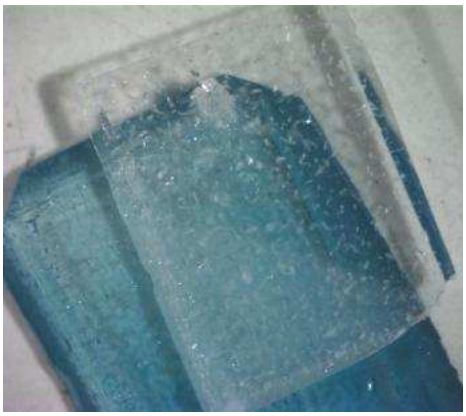

Figure 29. The blue color of as-grown Yb:LuAG is removed by annealing at 1000°C.

around 600 nm and 385 nm can be attributed to this Yb^{2+} impurity (Figure 30, top spectrum) and in the lower spectrum, with its lack of absorption bands in the visible region, the colorless Yb^{3+} appears to be the only valence state present. It is likely that only a small number of Yb ions are in the 2+ state owing to the similarity in intensity of

absorption peaks in the 930 nm – 970 nm spectral region before and after annealing. The inset shows the pump area in greater detail.

While this heat treatment does effectively oxidize any Yb^{2+} present it would be

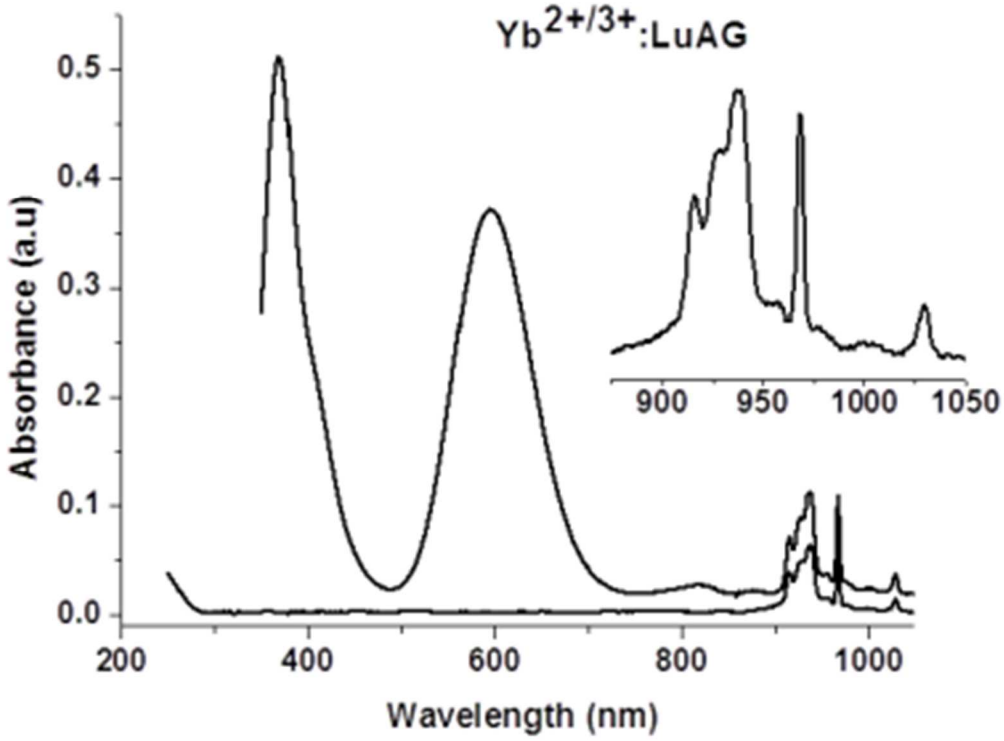

Figure 30. Absorption spectrum before annealing shows a broad absorption feature in the visible region (top) which is absent after annealing (bottom).

preferable to grow these layers in a purely 3+ state and to be able to forego heat treatment which, in addition to requiring a furnace capable of maintaining 1000°C also tends to degrade crystal quality. Although for reasons that are unclear, this mixed-valence growth does not occur every time and other groups have seen the same phenomenon using other growth methods[55,56] and its exact cause is not known.

The room-temperature spectrum of hydrothermally grown Yb:LuAG is compared to Czochralski-grown Yb:YAG and presented in Figure 31 showing the $^2F_{7/2} \rightarrow {}^2F_{5/2}$ absorption transitions. There is a more pronounced reversal the intensity of peaks at 943 nm and 970 nm than in Nd garnets from the previous section. There is also a slight contraction of the peaks spread between 900 nm and 1000 nm in LuAG relative to YAG. A much better resolution of the doublet peaks at 927 nm and 938 nm can be seen in the

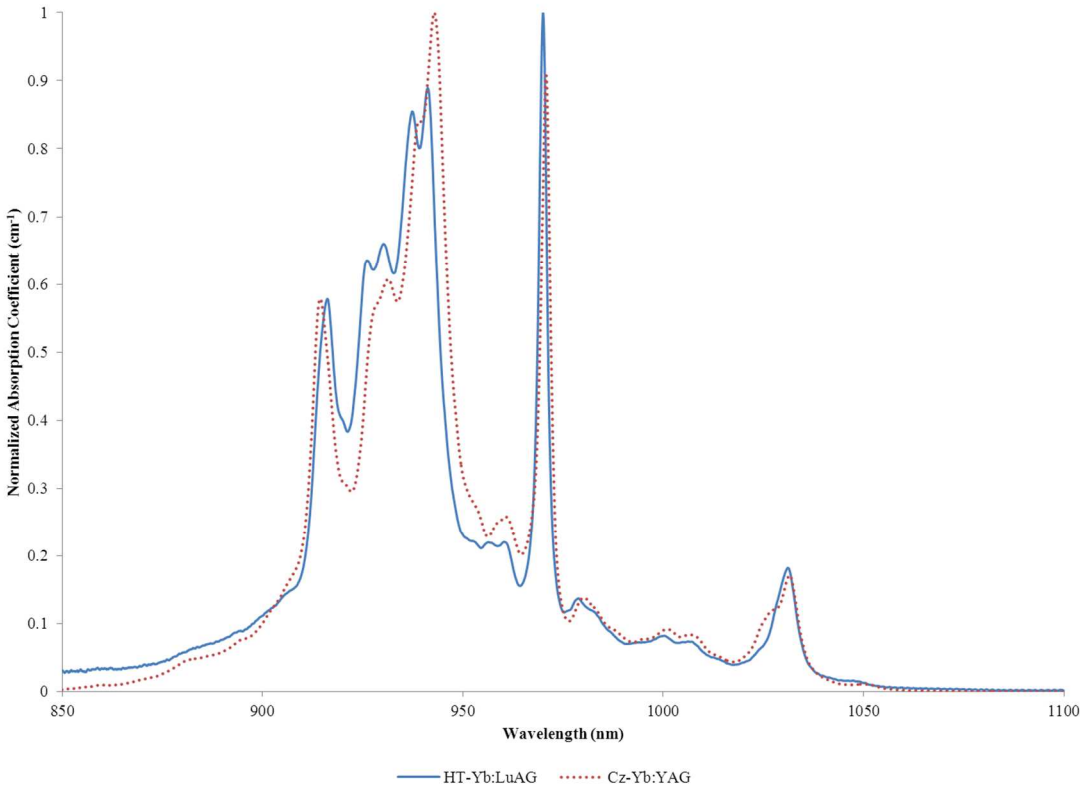

Figure 31. A room-temperature absorption coefficient spectrum comparison of Yb-doped LuAG and YAG shows are reversal of peak intensity at 943 nm and 970 nm.

LuAG host compared to YAG. Because both spectra were produced using the same parameters, this appears to be an actual phenomenon and not instrument-related. A full

treatment of the cryogenic absorption spectra series for Yb:LuAG is presented in Chapter 6.

Ho:LuAG

Lasers emitting in the eye-safe, 2-μm regions, such as Ho-doped garnets[57-60] are of interest in applications such as lidar and the long-range detection of atmospheric contaminants. One of the differences of LuAG versus YAG is a result of the smaller lattice of LuAG. The energy levels are split more by the closer proximity of neighboring ions separating levels with respect to the ground state more in LuAG, raising the terminal laser level (upper ground state) with respect to its lower ground state in the $^5I_8$ manifold.

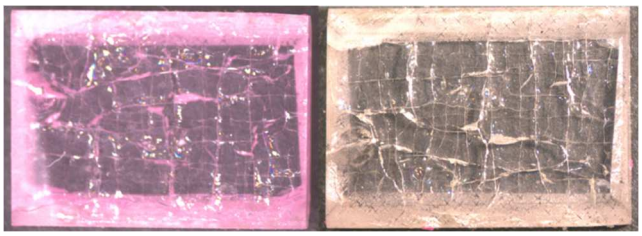

Figure 32. A Ho:LuAG slab seen under fluorescent light appears pink (left) and yellow in sunlight (right).

This greater separation of energy means that there will be less of a thermal population in the lower laser level compared to YAG, reducing the pump threshold for lasing, making Ho:LuAG a particularly attractive candidate for eye safe lasing.[61]

The harvested Ho:LuAG crystal in Figure 32 was grown hydrothermally using pre-doped 5% Ho:Lu_2O_3 feedstock. In addition to some moderate cross-hatch cracking, it appears pink under artificial lights and yellow in natural light as common with Ho-containing crystals. Ho^{3+} has a complex energy level structure,[62] and the room-

temperature absorption spectrum of Ho:LuAG between 200 nm and 700 nm is presented in Figure 33 with insets of the regions further into the NIR.

To access their ~2.1 μm laser line, the $^5I_7 \rightarrow {}^5I_8$ transition, Ho-doped lasers are

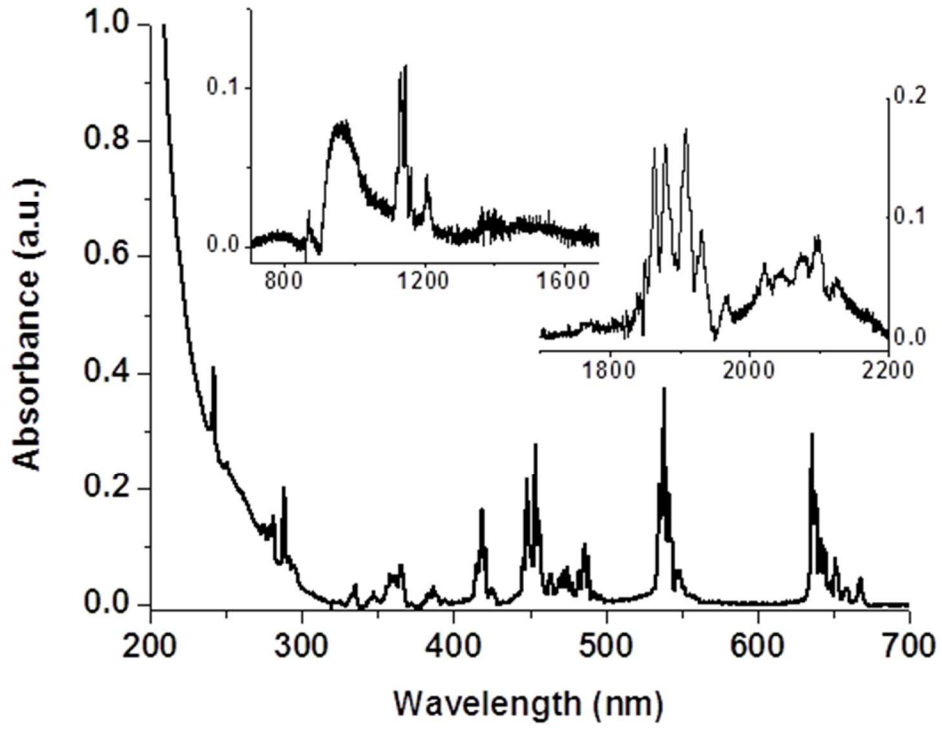

Figure 33. The room-temperature absorption spectrum of Ho:LuAG.

normally pumped in the region between 1700 nm and 1950 nm, including the moderately intense 3-peak cluster around 1900 nm. Other major absorption bands occur at regularly spaced intervals centered at roughly 450 nm ($^5I_8 \rightarrow {}^5G_6$), 540 nm ($^5I_8 \rightarrow {}^5F_4$), and 640 nm ($^5I_8 \rightarrow {}^5F_5$) which illustrate the sharp absorption transitions common between f-electron states.

Tm:LuAG

Tm-doped lasers are used as pump sources for Ho:YAG lasers and are also of interest for lasing in the 2 μm regime. The Tm:LuAG crystal in Figure 34 was grown from 5% Tm:Lu_2O_3 feedstock and gave the absorption spectrum in Figure 35. It is consistent with those found in the literature[40,63-65] with its characteristic sharp line at 682 nm that is four times greater than any other transition line due to absorptions from the ground state, $^3H_6$, to both $^3F_2$ and $^3F_3$ states. The group of peaks around 790 nm, due to $^3H_6 \rightarrow {}^3H_4$ transition, is the pumping region for lidar applications, and is less than a

Figure 34. Tm:LuAG grown from 5% Tm:Lu_2O_3 feedstock is still on a YAG seed. The crystal is about 1 cm in length.

quarter as intense as the absorption at 682 nm. Other groups of absorption peaks at around 1140 nm and 1740 nm are similar in intensity and are due to ground state to $^3H_5$ and $^3F_4$ state transitions respectively.

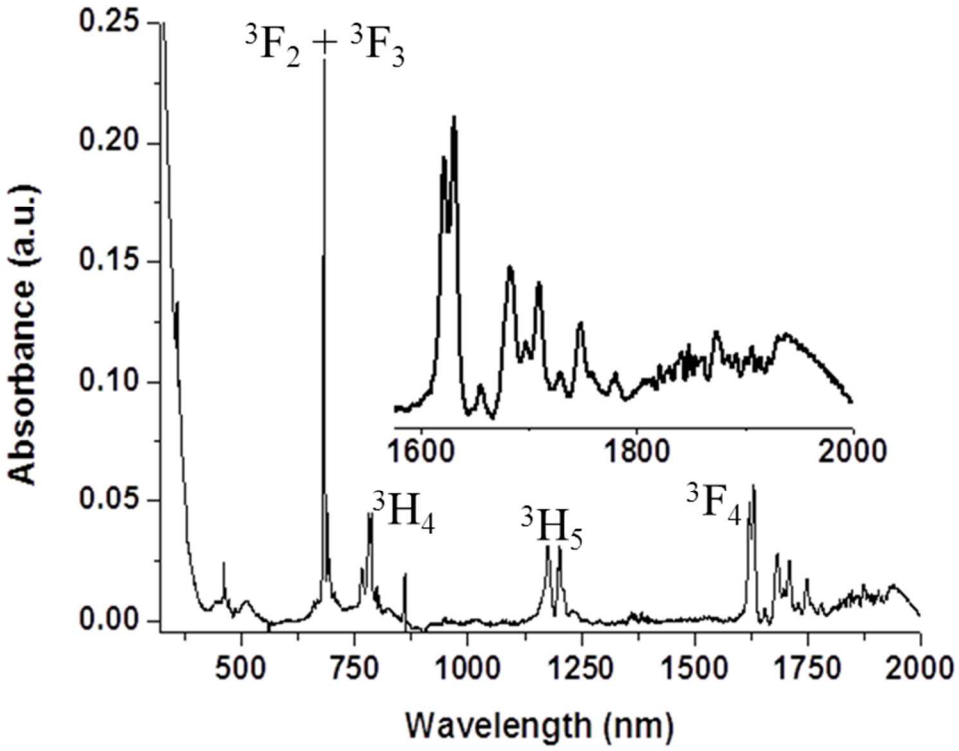

Figure 35. The room-temperature absorption spectrum of Tm:LuAG shows its characteristic sharp peak at 682 nm.

Er:LuAG

When lightly doped at less than half a percent, erbium-doped lasers are used for their $^4I_{13/2} \rightarrow {}^4I_{15/2}$ emission around 1.5 μm but when highly doped at around 30% the 3-μm emission from $^4I_{11/2} \rightarrow {}^4I_{13/2}$ is of interest.[66-68] We have demonstrated hydrothermal growth of 1%, 5%, and 30% Er:LuAG using pre-doped Er:Lu_2O_3 feedstock at the appropriate doping levels. In this case the close match of the ionic radii between the dopant and host Lu allows for a close match between the dopant ion concentration in the feedstock and grown crystal. The consistency of dopant levels throughout the entire growth process was presented in Chapter 2, Figure 20, using 30% Er:LuAG as an

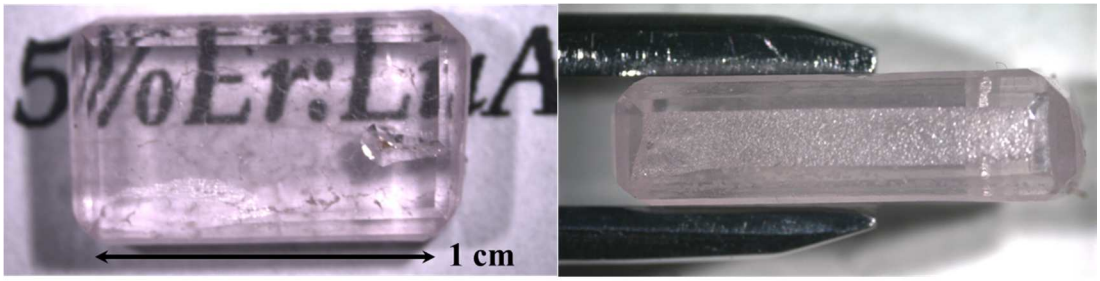

Figure 36. Hydrothermally grown Er:LuAG still on its YAG seed.

example. The elemental analyses of points spaced across the growth cross-section attests to the homogeneity this pre-doping methods affords. The distinctive pink color of erbium can be seen in the as-grown crystal in Figure 36 with 5% Er-doping.

Er:LuAG has a complex absorption and emission behavior. Its absorption spectrum is shown in Figure 37 and is characterized by five clusters of sharp peaks

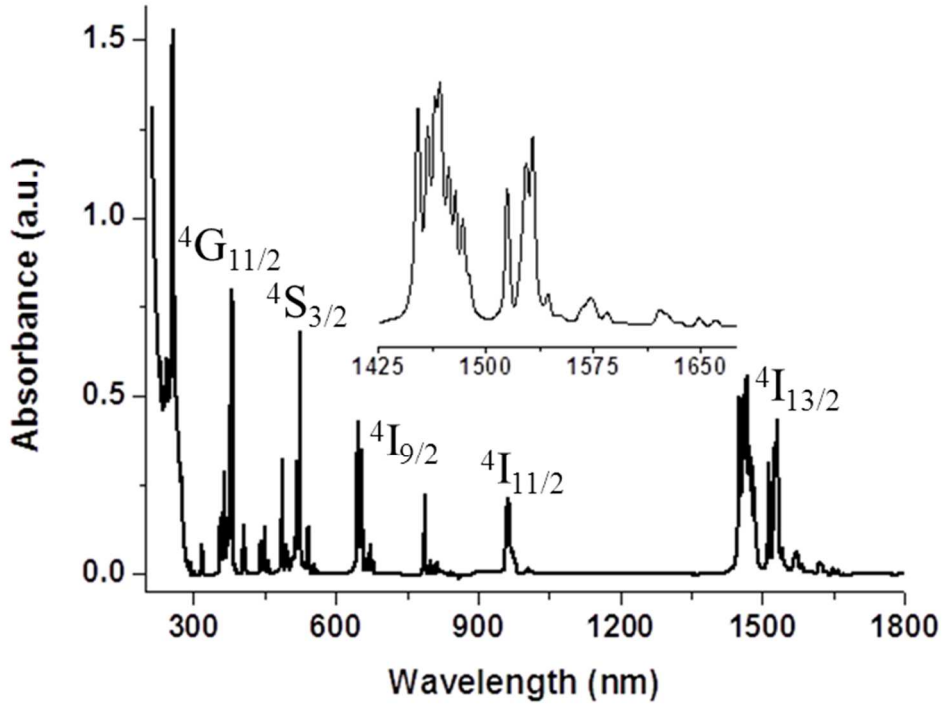

Figure 37. The room-temperature absorption spectrum of 30% Er:LuAG.

between 300 nm and 1000 nm spaced at regular intervals with decreasing intensity, and a set of two fairly intense, well-resolved peaks centered at 1500 nm, that are due to the transitions assigned in the figure. This absorption spectrum is consistent with other Er:LuAG spectra in literature.[67]

Pr:LuAG

There is interest in both Pr- and Ce-doped crystals for use in scintillator applications. Doped LuAG is of particular interest because the added mass from Lu compared to Y in YAG serves to increase its stopping power to high energy particles and increases its density and radiation hardness. For use in high energy particle detectors Pr:LuAG absorbs γ- or X-rays and converts it into a quantifiable emission in the visible region between 310 nm and 380 nm, that is proportionate to the energy absorbed.

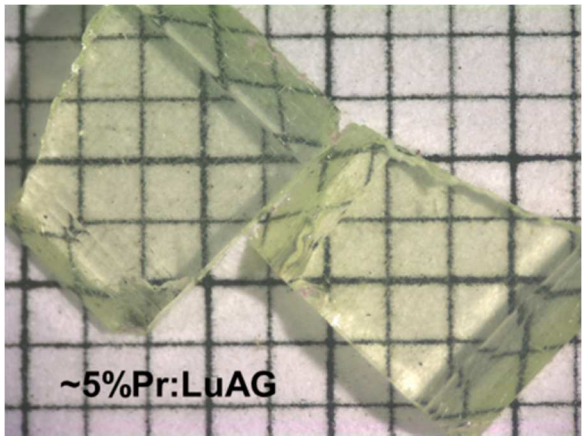

Figure 38. Polished slabs of 5%Pr:LuAG.

We have demonstrated high quality hydrothermal growth of Pr:LuAG using a coprecipitated 5% Pr:Lu_2O_3 feedstock. The source of Pr was mixed-valence Pr_6O_{11} which starts out black and turns a bright lime-green when dissolved in HNO_3. Following the procedure detailed in Chapter 2 results in a light green powdered feedstock, which has a perfect powder pattern match to Lu_2O_3. Growth of Pr:LuAG for a duration of 25 days with a thermal gradient of 610°C – 640°C gave a weight gain of 140%.

The resulting epitaxial layer was harvested from the YAG seed and unfortunately cracked in half during polishing, but the product has good clarity (Figure 38). The room temperature absorption spectrum is presented in Figure 39 and is characterized in the visible region by groups of four moderately intense peaks between 430 nm and 500 nm,

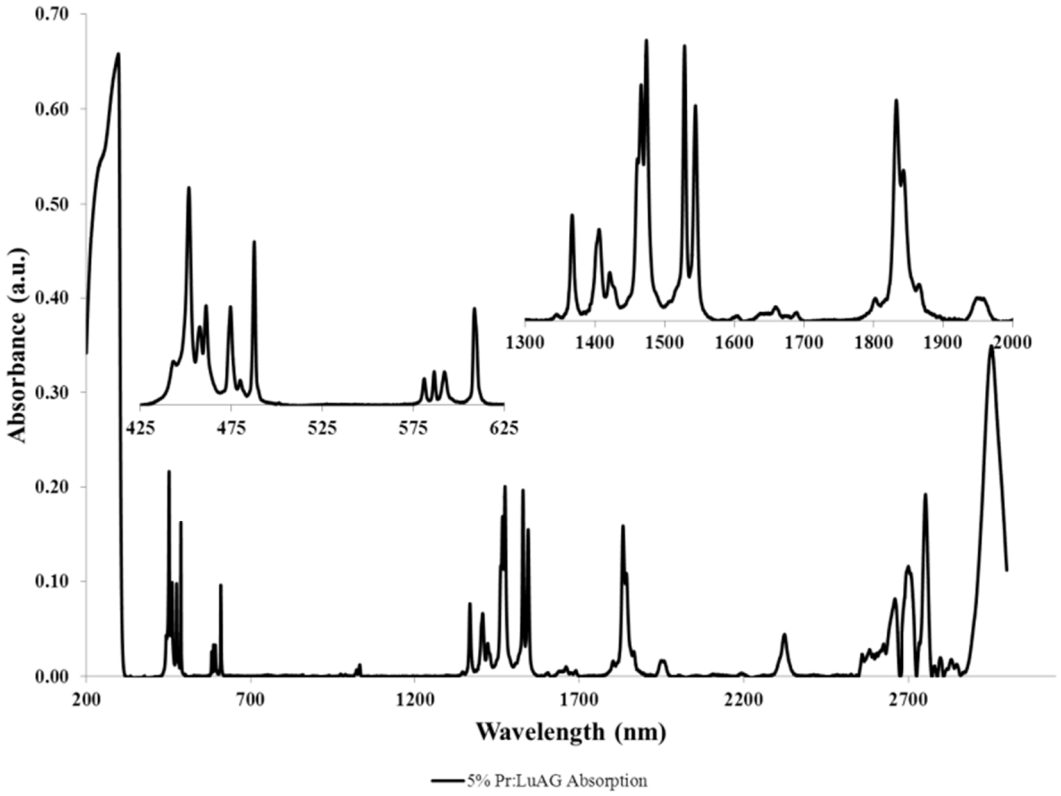

Figure 39. The room-temperature absorption spectrum of Pr:LuAG.

four peaks about half the intensity centered between 580 nm and 620 nm (inset, left). Further into the NIR between 1350 and 1550 nm are peaks at 1367 nm and 1405 nm and two sets of well-resolved doublets centered at 1470 nm and 1536 nm (inset, right). In addition the broad 4f-5d transition is clearly visible at 250 nm.

Ce:LuAG

LuAG doped with Ce is another attractive material for γ-ray detection in scintillator applications.[69] Because Ce has 2 stable oxidation states, Ce^{4+} and Ce^{3+}, it was unknown whether it was necessary to begin with Ce^{3+} as the starting material or if a source of Ce^{4+} could be used. To investigate this, coprecipitation of a pre-doped 1% $Ce:Lu_2O_3$ was attempted with both $Ce(OH)_4$ and CeF_3 using the method described in Chapter 2. After calcining, both materials were a very light yellow color and showed

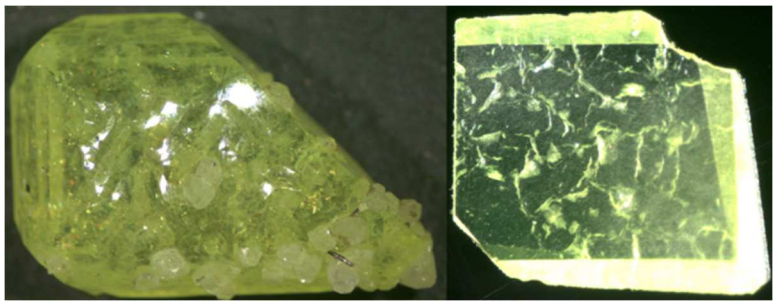

Figure 40. As-grown Ce:LuAG crystal on YAG seed (left) and a harvested, polished slab (right) ready for spectroscopy.

perfect powder pattern matches to database Lu_2O_3 and there was no reason to suspect that they were different materials. EDX analysis of the doped powder made from $Ce(OH)_4$ over 4 areas of powder sample showed an average Ce-doping of 1.33%. The powder resulting from CeF_3 gave an average of 1.51% Ce-doping over 6 different areas, both were close within the range of targeted doping. Interestingly, coprecipitation using starting materials containing Ce in both oxidation states resulted in pure Ce^{3+} powders of $Ce:Lu_2O_3$ after calcining.

The Ce:LuAG crystal in Figure 40 was grown with the pre-doped Ce:Lu_2O_3 feedstock prepared using $Ce(OH)_4$ and its room-temperature absorption spectrum is presented in Figure 41. Two well-separated, fairly intense peaks in the visible region at 345 nm and 449 nm give it its distinct bright yellow color. The only other feature is a moderately intense doublet centered at 2993 nm in the NIR.

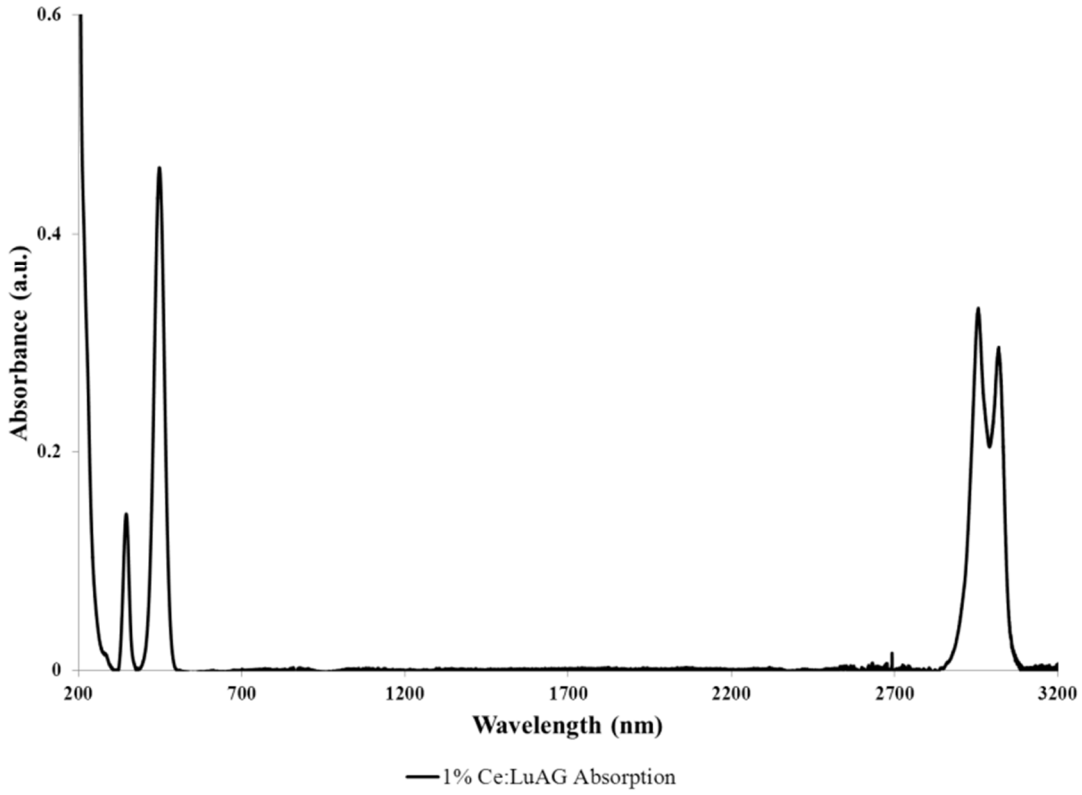

Figure 41. Room-temperature absorption spectrum for Ce:LuAG between 200 nm and 3200 nm.

Sm:LuAG

Because of the absorption behavior of Sm^{3+} in the region of Nd-emission, around 1064 nm, it has been proposed to use Sm-doped garnet in ASE suppression. Sm:LuAG is spectroscopically silent in the 808 nm pumping region of Nd:YAG and therefore would

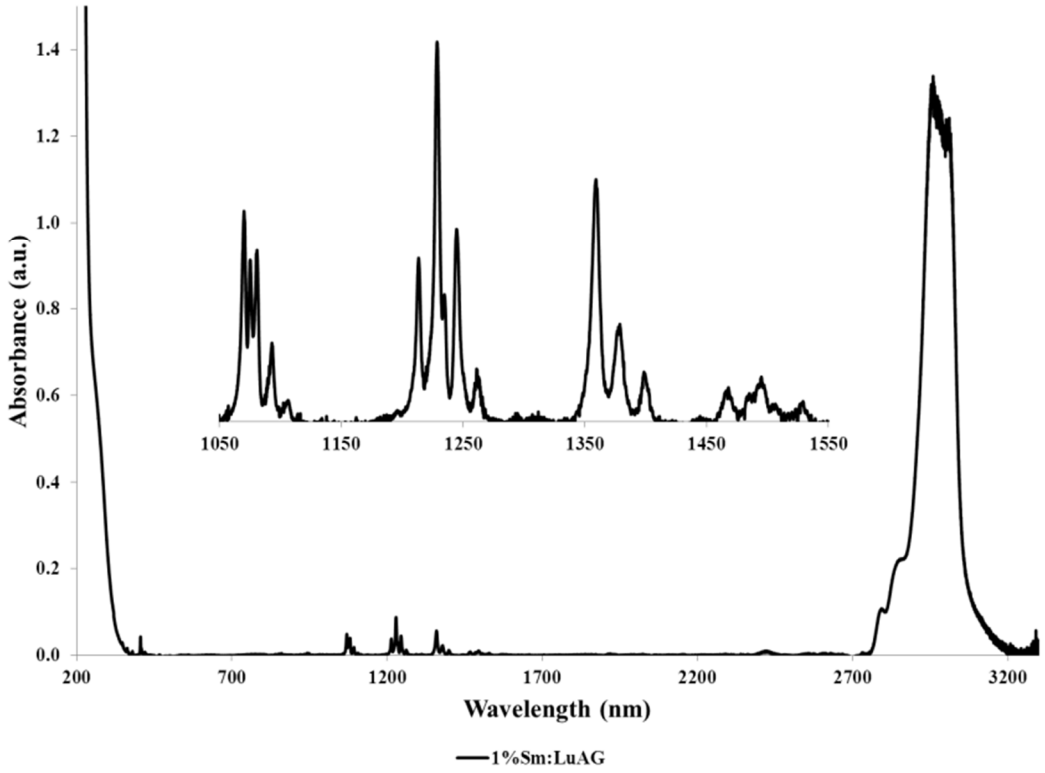

Figure 42. Room-temperature absorption spectrum of Sm:LuAG. The non-zero absorption at 1064 nm and transparency around 808 nm makes this a possible candidate for ASE suppression of Nd-doped lasers.

not interfere with longitudinal pumping of a Nd:YAG laser rod (Figure 42). Because the emission of Nd:LuAG is slightly blue-shifted compared to Nd:YAG, there is less of an absorption at this wavelength as can be seen in Figure 43 that shows how the emission

lines of Nd:YAG and Nd:LuAG align with the absorption behavior of Sm:LuAG. Nevertheless, Sm:LuAG has a non-zero absorption at around 1064 nm.

In addition to the significant absorption band in the NIR between 2.7 and 3.2 μm, the absorption of Sm:LuAG is characterized by several regularly spaced groups of peaks

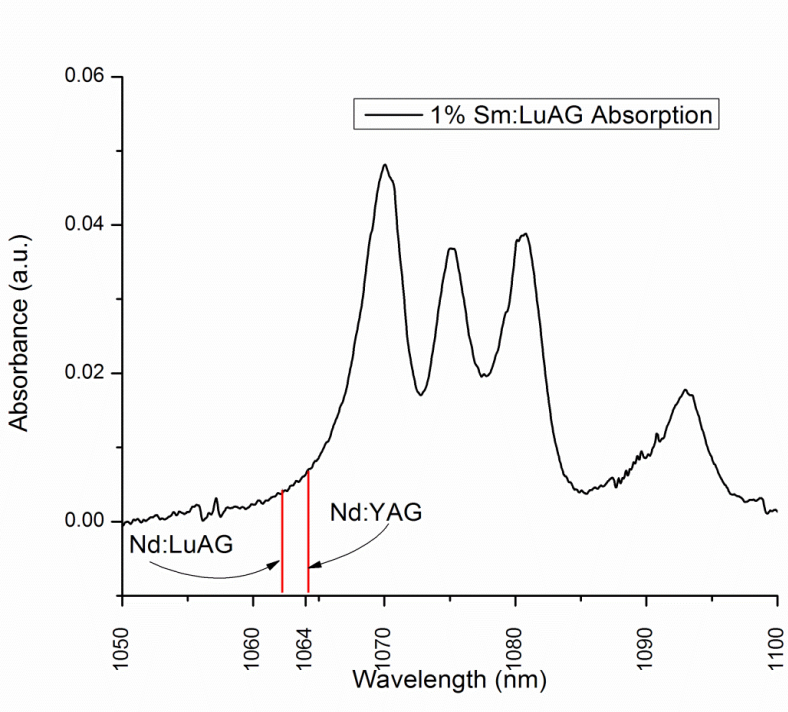

Figure 43. Sm:LuAG has a non-zero absorption of the 1064 nm laser emission of Nd:YAG but less of an absorption of the 1063 nm emission of Nd:LuAG.

between 1050 and 1550 nm with a set of five centered at 1075 nm, a set of four at 1228 nm and three at 1378 nm.

It was our goal in this chapter to highlight the hydrothermal growth of LuAG, a relatively uncommon laser host, using very similar conditions to YAG, to demonstrate

the variety of dopants that are possible, and to present spectroscopic characterization. While LuAG has the potential of having better physical and spectroscopic properties than YAG, it is much less-common than YAG due in part to its melt temperature that is even higher than YAG. The ability to easily grow high-quality crystals of LuAG is enticing as it allows for study of this material and its properties in depth.

We have shown the versatility of the hydrothermal method in not only growing crystals by SN, but also in transporting feedstock to a seed crystal for use in a layered, multi-functional crystal or as a surrogate that allows for the eventual harvesting of the single-composition layer. Additionally, we have shown the ability to grow high-quality LuAG doped with a wide array of rare-earth dopants in a wide range of percentages. The development of a coprecipitation technique for the preparation of a pre-doped feedstock can considerably aid in the control of homogeneity of these dopants.

The hydrothermal method is used in the next chapter to study the growth of the parent garnet, grossular garnet, in an effort to gain a better understanding of the garnet system. In addition, the coprecipitation method described in Chapter 2 and again in this chapter was adapted for use in creating novel powdered precursors for grossular and other interesting related materials.

CHAPTER FOUR

EXPLORATION OF NATURAL GARNET

"You learn nothing from an experiment you never do." *Colin McMillen*

Grossular Garnet

The mineral grossular garnet, $Ca_3Al_2(SiO_4)_3$, is one of a very large group of aluminosilicates. Being a garnet it is cubic in structure with the same $A_3B_2B_3'O_{12}$ general formula used to describe YAG, with slightly more complexity owing to the cation valence states of 2+, 3+ and 4+ for Ca, Al, and Si respectively, with atomic percentages of 15%, 10%, 15% and 60%, which is, of course, analogous to those in LuAG. This similarity coupled with the fact that almost all aluminosilicates are grown in natural hydrothermal environments seemed to make this a logical launch site in our initial exploration of garnets.

What might be even more intriguing than the similarities, however, are the differences between natural garnet and synthetic YAG. In addition to doping in the A-site with triply-ionized lanthanides, it might additionally be possible to dope the B-sites with many of the d-block and metalloid elements. This added complexity gives us many more opportunities to tailor the properties of a crystal. The converse of this is also true, because natural minerals are almost exclusively contaminated with sometimes complicated mixtures of elements, for example magnesium- and iron- containing grossular, preparing

pure forms of minerals like $Ca_3Al_2(SiO_4)_3$ can sometimes give insight into inherent properties of the mineral itself that are not related to dopants, such as thermal conductivity measurements, a precise unit cell parameter, and crystal structure.

The intriguing possibilities of this synthetic garnet provided the motivation. Our knowledge about the growth of YAG and other garnets provided the guidance in our preliminary investigation of this complex calcium aluminosilicate system and its phase space using the hydrothermal method. The synthetic garnets YAG and its analogs have been shown by our group to grow very well in hydrothermal systems using oxide components with both OH^- and CO_3^{2-} mineralizers in moderately low concentrations for YAG and LuAG with CO_3^{2-}. Higher concentrations to about 12 M using OH^- was used in the growth of GGG but with much lower temperatures closer to 550°C, although no attempts were made to further optimize the GGG system (See Chapter 3). Higher temperatures above about 640°C are used for growth of YAG and LuAG because, below this temperature, we sometimes see the formation of REO(OH) and $RE(OH)_3$.

Inspiration in designing experiments in a new system can come from a number of different directions. Individual components, such as Al_2O_3, SiO_2 and CaO and more complex components, such as $CaSiO_3$ and Al_2O_3 are both valid approaches. Simply changing the source of different elements and the use of varied mineralizers can result in some interesting products. There are even novel approaches in the preparation of these components themselves that can lead to interesting materials in their own right. Often the best way to start is simple, but it is not guaranteed to result in the intended material, and,

indeed, synthesis of the targeted compound is not always the best judge of success. A reaction that does not lead to what was intended can sometimes be even more intriguing often nudging experimentation in a different direction. Something can be learned from every experiment.

Crystal Growth

As mentioned, it is possible to do a survey of experiments in a single growth run by using multiple small silver reaction tubes in an autoclave and stacking five or six individual tubes at a time. This method of crystal growth typically results in small sample sizes and small crystals. This does not usually present a problem, however, because analytical techniques usually require only very small samples. For single crystal analysis by XRD, small crystals are desirable for characterization and crystals that are too big must be broken in order to help ensure a more perfect sample of the crystal. Use of a large array of reaction conditions is an effective way of allowing determination of, say, what effect different mineralizers will have on the growth of a target crystal or the effect of different mineralizer concentrations.

Using a series of congener elements, for example, substitution of Mg, Sr, and even Ba in for Ca, can give us an idea of what effect, if any, the substitution might have on the crystal structure. We can even try Ga to see if it might substitute for Al in the structure, and if so, what that substitution might do to the structure. We can explore a wide variety of conditions relatively quickly; reaction durations are only on the order of a few days and not weeks as for epitaxy. Subsequent reactions can then be designed based

on that information with the goal of ultimately synthesizing the intended product. Of course sometimes NOT succeeding in the original goal can be even *more* interesting and frequently results in some very interesting products, if somewhat unexpected.

Attempted synthesis of grossular from components

In our first attempt of the synthesis of grossular, a series of 3/8" o.d. x 3" long silver reaction tubes were prepared by welding the bottoms of cleaned, cut lengths of pure silver tubing. Components in the correct 3:2:3 ratio of Ca, Al, and Si using $Ca(OH)_2$, powdered Al_2O_3, and SiO_2 (powdered silica) totaling about 2.8 g of solid feedstock were carefully added followed by about 0.4 mL of each mineralizer. In this case a series of concentrations of CsOH was used: 0.72 M, 0.86M, 3.19 M, 5.03 M, and 5.75 M. These solutions were prepared *in situ* by adding the appropriate amount of a premade 50/50 (w/w) solution of CsOH and water. The tubes were thoroughly cleaned inside at the top to help ensure a good weld seal.

After sealing, the tubes were vigorously shaken to help distribute components and mineralizer to better help with percolation during growth as we have occasionally experienced a solid mass of components stuck at the bottom of a sealed tube after a growth run if mixing is not sufficient. Individual tubes were stacked in the autoclave and an amount of water was added to the volume around the tubes in the autoclave to prevent bursting when heated, usually about a cm. Two band heaters were used both set to 620°C and allowed to ramp directly to growth temperatures which typically takes about two

hours. This temperature was chosen as the first of three reaction temperatures: 620°C, 650°C and then 670°C to encompass an entire range of temperatures.

After three days the heaters were turned off and the autoclaves were allowed to return to room temperature naturally overnight. Each tube was then opened with side-cutters and the product was rinsed onto a filter paper using vacuum filtration which served to both collect any powdered or crystalline product while allowing the product first to be thoroughly washed with a water stream and then to be dried using acetone. The dried powdered or crystalline product was then ready for immediate analysis.

The products from the tubes that used lower molarity mineralizer was a mix of powders that was a good database match to pollucite, a cesium aluminosilicate ($CsAlSi_2O_6$, PDF 29-407, *Ia-3d*), and another cesium aluminosilicate phase, $CsAlSiO_4$, (ICSD #160822, *Pna2₁*) along with peaks from at least one other phase that could not be identified. Single crystals of $CsAlSiO_4$ have also been grown hydrothermally by Diego Gatto[70] from Al_2O_3, SiO_2 and Cs_2O in water at 695°C. Single crystals of pollucite were also formed in this study from the treatment of components with carbonate mineralizers (see experimental summary at the end).

Single crystals of pollucite were formed in the reaction targeting spurrite and its alkaline earth analogs, with the intentional addition of CO_3^{2-} using a Cs_2CO_3 mineralizer from components, detailed in the experimental summary. Al_2O_3 and SiO_2 components with $Sr(OH)_2$, $Ca(OH)_2$, or $MgCl_2$ and 5M Cs_2CO_3 mineralizer all resulted in the growth of pollucite single crystals. Several of the crystals resulting from the components with

$MgCl_2$ were chosen from the product and thoroughly ground giving the pattern in Figure 44. The match to aluminum metal in the figure is from the aluminum sample holder that can sometimes occur if there is not a sufficient amount of powder to completely cover the area in the X-ray beam. The other match in the figure is to phase-pure pollucite. A suitable crystal (a = 13.74Å) was chosen for PXRD and was index-matched to pollucite

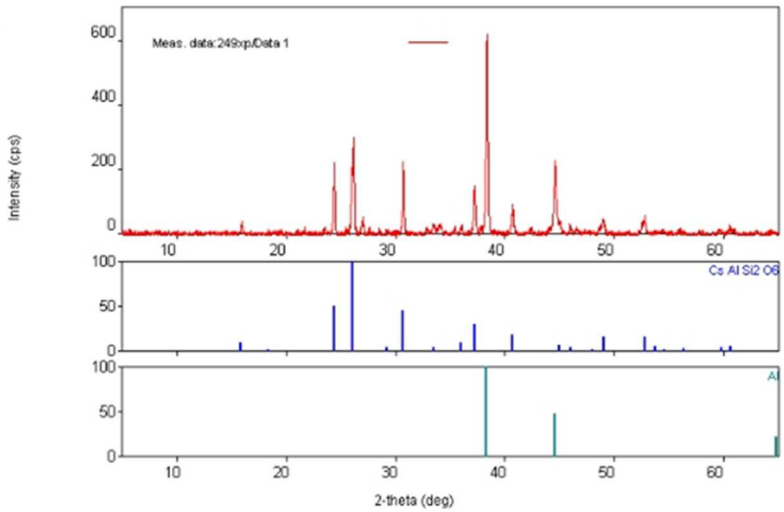

Figure 44. Ground crystals from the reaction of Al_2O_3 and SiO_2 with $MgCl_2$ and 5M Cs_2CO_3 mineralizer gave a phase-pure match to pollucite.

(ICSD #84321, a = 13.6645(3)Å).

While naturally-occurring pollucite is mined as the major source of Cs metal, synthetic pollucite has been proposed in the sequestration of radioactive Cs-containing nuclear waste.[71,72] In light of the power plant disaster in March of 2011 in Fukushima, Japan, because of its high density, insolubility in water, and the requirement of completely breaking the pollucite framework in order to liberate the cesium from the

crystal, it has been suggested that sinking these hydrothermally-grown, ^{137}Cs-rich crystals to the bottom of the ocean might actually be the *safest* place this nuclear waste.[73]

Synthesis of dellaite single-crystals

As the concentration of CsOH was increased to the upper end of the range (above about 5 M), however, clear, colorless elongated polyhedra of 1-2 mm were produced as shown in Figure 45 along with powders of both pollucite and $CsAlSiO_4$. Several of the larger columns were individually chosen from the reaction and thoroughly ground for analysis by PDXL. The crushed powder of these crystals was a clean match to the (PDF 29-376) entry for dellaite (Figure 46), a naturally occuring, hydroxylated calcium silicate ($Ca_6Si_3O_{11}(OH)_2$, *P-1*) with a Ca to Si ratio of 2:1 containing no Al.

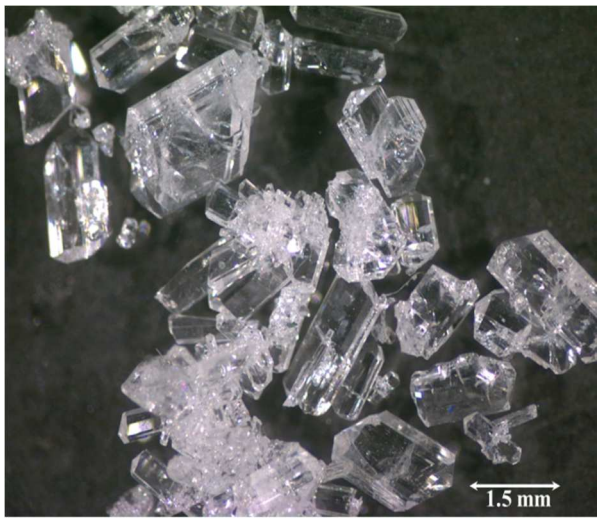

Figure 45. Hydrothermal treatment of components with hydroxides leads to large well-formed crystals of dellaite $Ca_6Si_3O_{11}(OH)_2$.

Since it was first synthesized by its namesake, Della Martin Roy at Penn State, not much has been written about this synthetic crystal.[74] Due to the fairly large crystal size and good quality and the ease of which it forms in a hydrothermal system, further

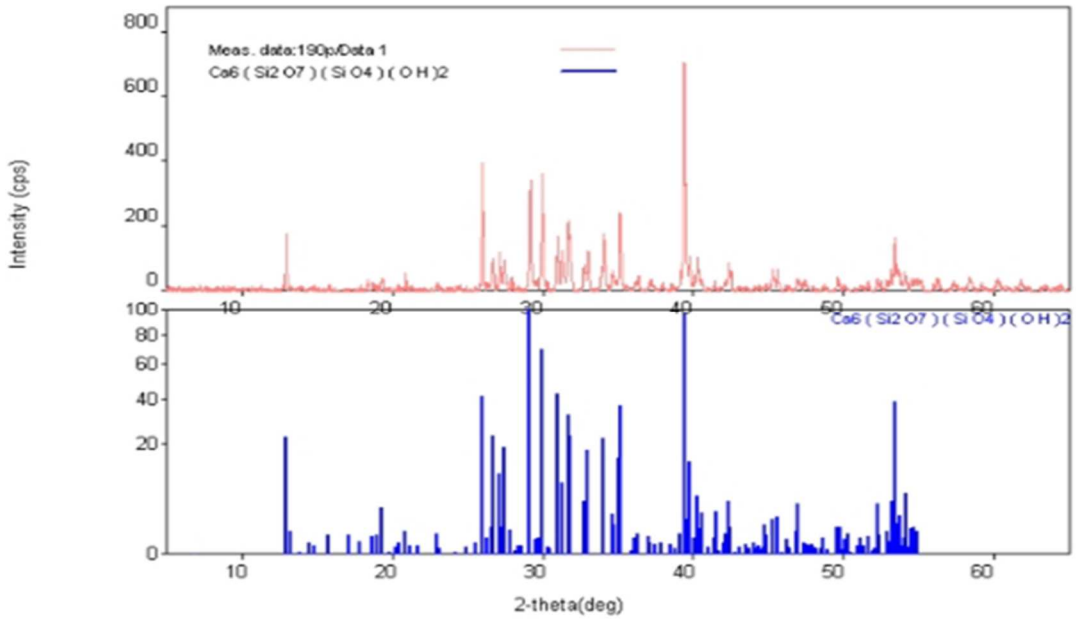

Figure 46. Powder pattern match to dellaite (PDF 29-376).

exploration of this crystal could significantly add to the literature. Both dellaite powders and crystals have been grown with a variety of starting materials and conditions, *vide infra*.

Synthesis of spurrite single crystals

Hydrothermal treatment with highest concentration of CsOH (5.75 M) also gave a polycrystalline powder with colorless columns. The powder pattern of the composite sample was a match to both $CsAlSiO_4$ and spurrite, $Ca_5(SiO_4)_2CO_3$, (PDF 13-496, $P2_1/a$)

a rare, but naturally-occuring calcium silicate carbonate also containing no Al, which has a Ca to Si ratio of 5:2, (Figure 47).

A suitable column was chosen and also gave an index match by single-crystal diffractometry (a=6.7224(42)Å, b=10.4755(73)Å, c=14.1582(98)Å, α=90.0781(203)° β=101.3966(233)°, γ= 89.9232(214)°) to database spurrite, (ICSD #156625, a=10.484(1)Å, b=6.712(1)Å, c=14.156(2)Å, a= 90°, b=101.27(1)°, c=90°). But how could this be when there was no carbonate added to the original feedstock? Inspection of and some research into the starting materials themselves revealed that an aqueous solution of CsOH is prone to the absorption of carbon dioxide from the air and was likely

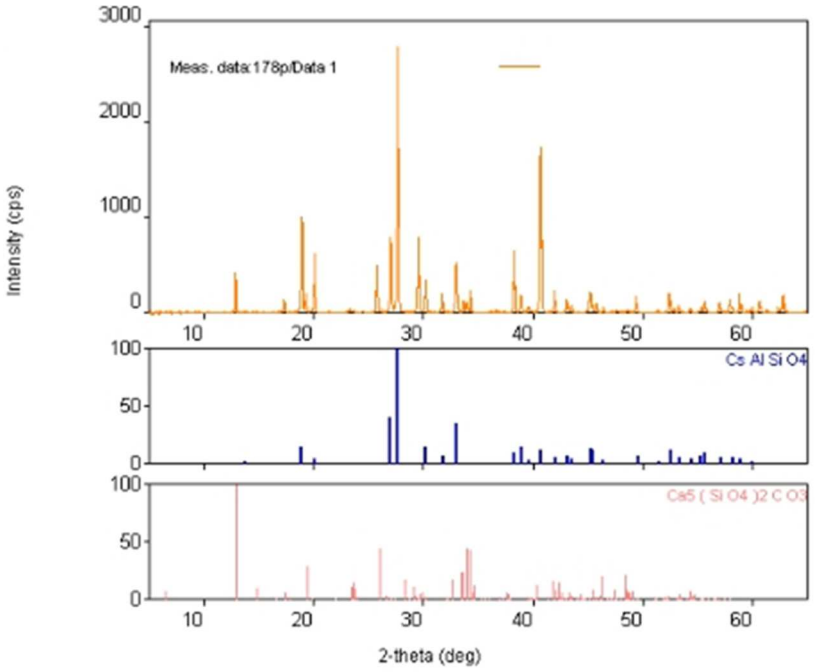

Figure 47. The material from hydrothermal treatment of components with 5.75M CsOH gave a powder match to $CsAlSiO_4$ and spurrite.

the source of the carbonate product. This hypothesis is also substantiated by the increase

of carbonate-containing product with increasing molarity and the lack of those products at lower concentrations.

Coprecipitation of anorthite precursor for growth of grossular

Because the products that were being formed contained little to no Al, an aluminum-containing precursor was targeted as a way to ensure that the product would contain Al. The coprecipitation method described in Chapter 2 and detailed in the

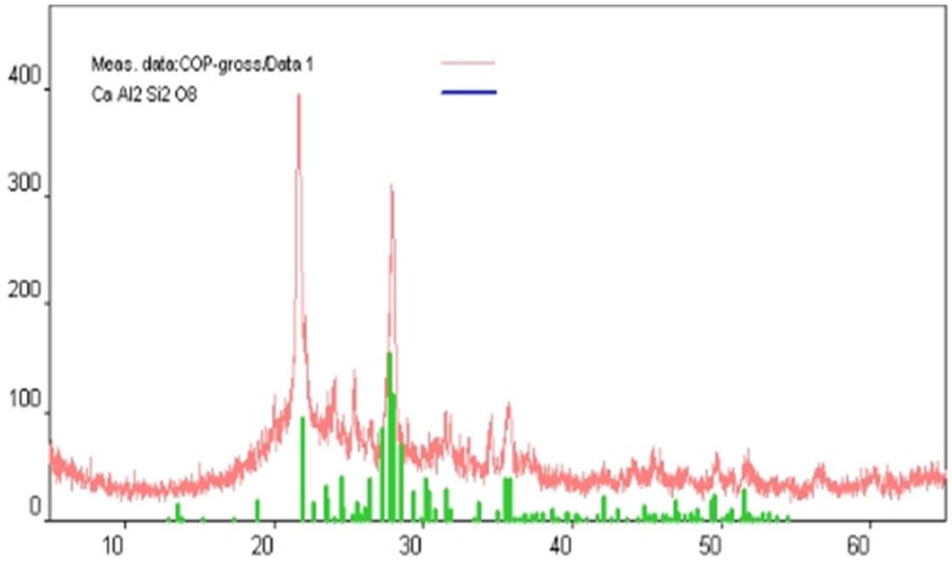

Figure 48. First attempt to coprecipitate a grossular precursor resulted in anorthite powder.

experimental summary at the end of this chapter was used to produce the material with the powder pattern in Figure 48, a slightly amorphous, but convincing match to anorthite, another calcium aluminosilicate, $CaAl_2Si_2O_8$ (PDF 70-287, *P-1*) with atomic percentages of 7.7%, 15.4%, 15.4%, and 61.5%.

This precursor was used as a starting material and enriched to the correct ratios for grossular using additional components of $Ca(OH)_2$ and SiO_2. Hydrothermal

crystallization was attempted using various 2M hydroxide mineralizers with a thermal gradient of 530°C on top and 618°C on bottom for three days. Separate treatment with NaOH, RbOH, CsOH, all produced white powders with tiny colorless needles that proved too difficult to mount for analysis by single-crystal diffractometry. Their powder patterns

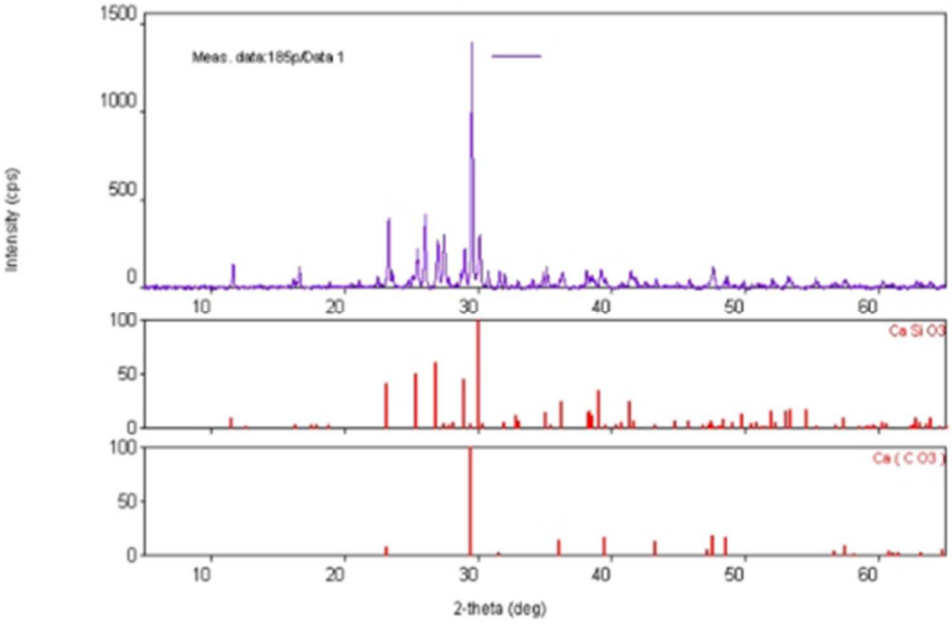

Figure 49. Anorthite precursor treated with hydroxide mineralizers gave a product that matched $CaSiO_3$ and $CaCO_3$.

were complex but all included a match to wallastonite, $CaSiO_3$ (PDF 42-547, sg *P-1*).

Treatment of the same enriched precursor with 2M K_2CO_3, however produced a white powder, colorless needles, and clusters of small colorless polyhedra. The finely ground composite sample gave the powder pattern in Figure 49 which is a clean match to both wallastonite and calcite, $CaCO_3$, (PDF 5-586, *R-3CH*).

Synthesis and identification of a gehlenite precursor

An alternate coprecipitation method detailed in the experimental summary was used to synthesize a precursor with atomic ratios that were closer to that of grossular. $CaCl_2$ and $AlCl_3$ were used as sources of Ca and Al respectively because they are water soluble and needed no additional treatment. Because $AlCl_3$ is vigorously reactive in air / water, extreme caution was used with its handling.

All solutions were made very slowly and in a well-ventilated hood. Silica was dissolved, with some difficulty, in a boiling solution of concentrated KOH or NaOH under constant stirring. The atomic ratio of elements for grossular was used based on about 2g of $CaCl_2$, which was dissolved in a small amount of water. $AlCl_3$ was also dissolved separately following the noted precautions. Following precipitation and drying as summarized in the experimental summary, the wet powder was placed in an alumina crucible and lightly covered.

During calcination the furnace was raised to 600°C and allowed to remain at temperature for at least two hours. At that time a small sample was taken and the temperature was raised to 800°C. After two hours at this temperature another sample was taken and the temperature was raised again to 900°C. After two hours another sample was taken and the furnace was raised to its final calcination temperature of 1000°C. A powder pattern was collected for each of the samples and the result is shown in Figure 50. Peaks are not pronounced until a calcination temperature of 800°C was reached and we begin to see a database match to both grossular as a minor phase and gehlenite, $Ca_2Al_2SiO_7$, (PDF 35-755, *P-42₁m*, atomic percentages 16.7%, 16.7%, 8.3%, 58.3%).

This precursor is interesting first because it contains all of the elements needed for

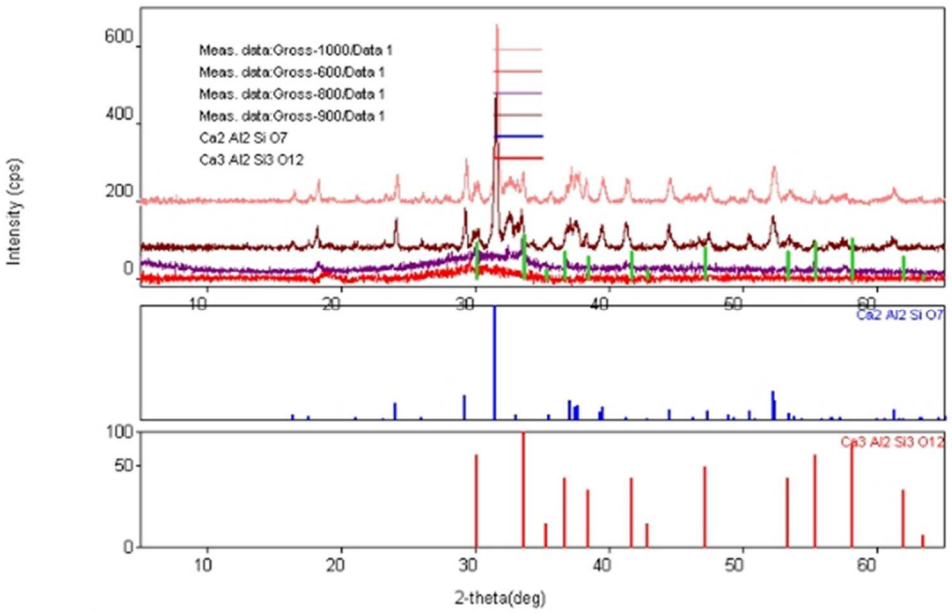

Figure 50. An alternate method of coprecipitation for a grossular precursor resulted in a mix of gehlenite with a minor grossular product.

grossular and, second, that gehlenite is acentric and is itself used as a laser host.[75-79]

Subsequent attempts to create gehlenite precursor directly were done using the same starting materials in the atomic ratios of gehlenite, paying special attention to the complete dissolution of SiO_2 and to a thorough washing of the precipitate and is detailed in the experimental summary.

After 36 hours in the furnace at 1000°C, the resulting powder gave the pattern in Figure 51 which shows a much cleaner match to database gehlenite. In the figure we can see that while all of the peaks are present at 875°C (lower pattern), they become much sharper and more intense after complete calcination at 1000°C (upper pattern). We also see a near-perfect database match (green lines) with the lack of impurities from grossular.

Attempted recrystallization of gehlenite using carbonates

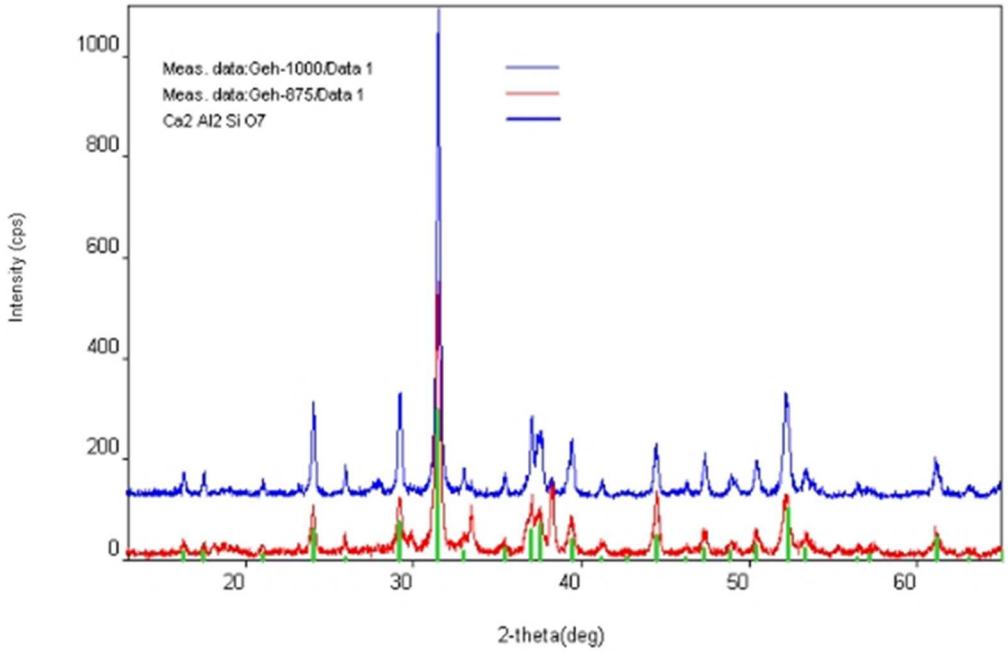

Figure 51. Coprecipitated precursor is a clean powder match to gehlenite.

Recrystallization attempts using coprecipitated gehlenite as the sole starting material at a temperature of 575°C on both top and bottom bands with 2 M K_2CO_3, Rb_2CO_3 and Cs_2CO_3 mineralizers all resulted in white powders with colorless polyhedra, which were likely calcite, (see below). Powder patterns of the composites all included a match to calcite as well as both pollucite and $CsAlSiO_4$.

Raising the mineralizer concentration of Rb_2CO_3 to 2.5 M and using higher temperature (640°C with no gradient) the hydrothermal treatment of gehlenite powder for 3 days gave a mostly crystalline product whose crystals (a=4.9940(17)Å, b=4.9934(46)Å, c=6.3826(61)Å, α=90.0052(1016)°, β=66.9900(746)°, γ=59.9613(569)°) were an index match to calcite (ICSD #40114, a=4.978(3)Å, b= 4.978(3)Å, c= 17.3540(90)Å, a=90°, β=120°), (Figure 52). All attempts to recrystallize gehlenite and grossular with carbonate mineralizers resulted in the formation of calcite or an incorporation of the carbonate ion into the structure (spurrite).

Attempted Recrystallization of gehlenite using hydroxides

Hydrothermal treatment of gehlenite powder with 0.5M and 1M RbOH at 550°C for five days gave white polycrystalline powders that gave a complex pattern matching bicchulite, $Ca_2Al_2SiO_6(OH)_2$, (PDF 27-66, *I-43m*), with atomic ratios of 13.3%, 13.3%, 6.7%, 46.7%, which is compositionally very similar to a hydroxylated form of gehlenite,[80] gehlenite and another minor phase that was not identified.

Because at lower growth temperatures the incorporation of OH^- tends to be more pronounced, the temperature was raised to 640°C with no gradient and mineralizer concentrations were raised to ca. 8M for subsequent growth experiments. Treatment of the gehlenite precursor under these new conditions gave large, well-formed, colorless polyhedra that were index-matched by XRD to dellaite when mineralized with each of

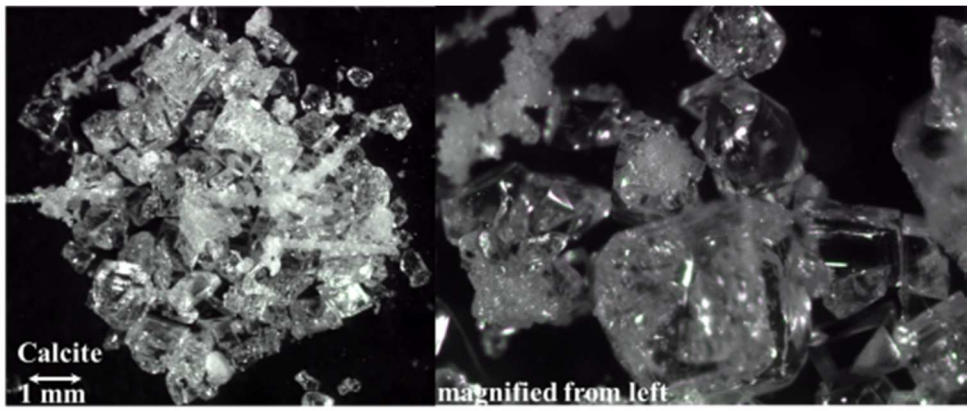

Figure 52. Calcite crystals from treatment of gehlenite precursor with carbonate mineralizers.

10M NaOH, 8.5M RbOH, and 5.75M CsOH, detailed in the reaction summary.

Gehlenite precursor treated with hydroxides of Rb and Na between 1 and 10 M at temperatures between 575°C and 650°C resulted in powders and crystals of dellaite, with the largest crystals and purest phases occurring at the highest temperatures.

Recrystallization of gehlenite using chlorides

In order to help prevent incorporation of both CO_3^{2-} and OH^-, a series of Cl^- mineralizers was used at 575°C with no gradient. Powdered gehlenite treated with 2M NaCl for four days gave a white polycrystalline powder with a clean powder match to

synthetic bicchulite, (Figure 53). A powder pattern match does not rule out the presence of Cl- necessarily, though, and a thorough analysis would include both EDX to help verify the lack of Cl- as well as an IR spectrum showing the broad OH- absorption peak between 3200 and 3400 cm^{-1}.

Although chloride mineralizers in higher concentrations tend to be reactive towards the silver tubing, lower molarities can effectively be used with short growth

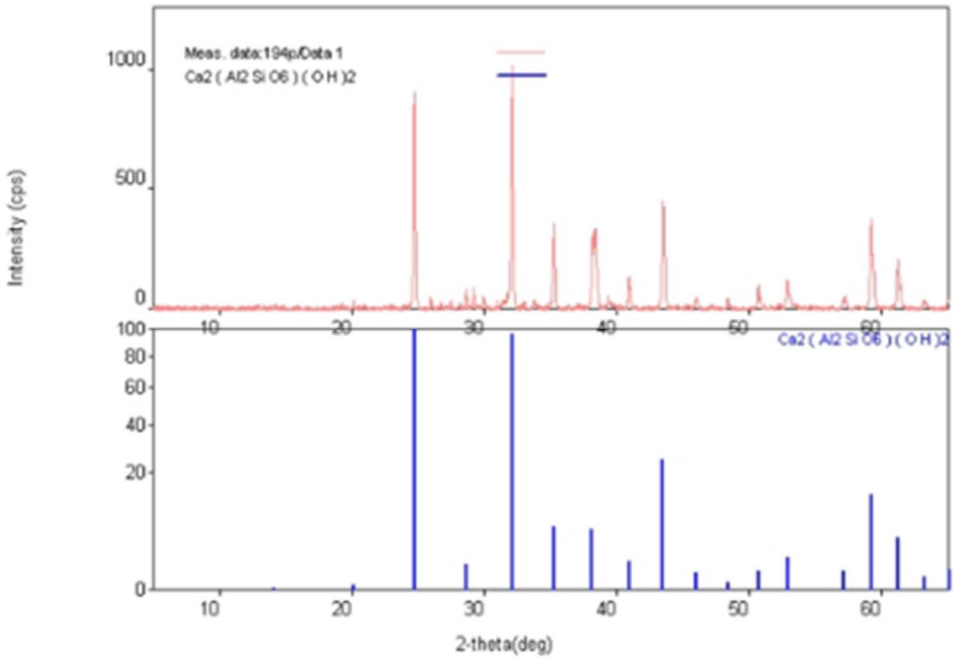

Figure 53. Gehlenite treated with 2 M NaCl gives a clean match to bicchulite.

duration. A series of 0.1, 1, and 3 M NaCl mineralizer with gehlenite feedstock was hydrothermally treated for six days at 650°C. While each of the products contained silver flakes from the tubing in addition to powder (Figure 54), a significant part of the product was larger colorless crystals, both polyhedra and columns mostly clustered with the silver

flakes for the highest molarity Cl^-. The columnar, single crystal (a=8.199Å, b=12.9154Å, c=12.8797Å, α=85.7918°, β=88.7149°, γ=81.1565°) was an index match to database anorthite, (ICSD #86317, a=8.175(1)Å, b= 12.873(1)Å, c= 14.170(1)Å, α= 93.11(1)°, β= 115.89(1)°, γ= 91.28(1)°). Another colorless polyhedron (a=7.0920(28)Å, b=7.5529(35)Å, c=7.7032(31)Å, α=115.1413(62)°, β=100.6940(34)°, γ=106.4099(74)°) gave an index match to the sodium-containing albite ($NaAlSiO_8$, *P-1*), (ICSD #9830, a=7.1190Å, b= 7.6256Å, c=7.6463Å, α=115.202°, β=101.115°, γ=106.440°). These reactions are also detailed in the experimental summary.

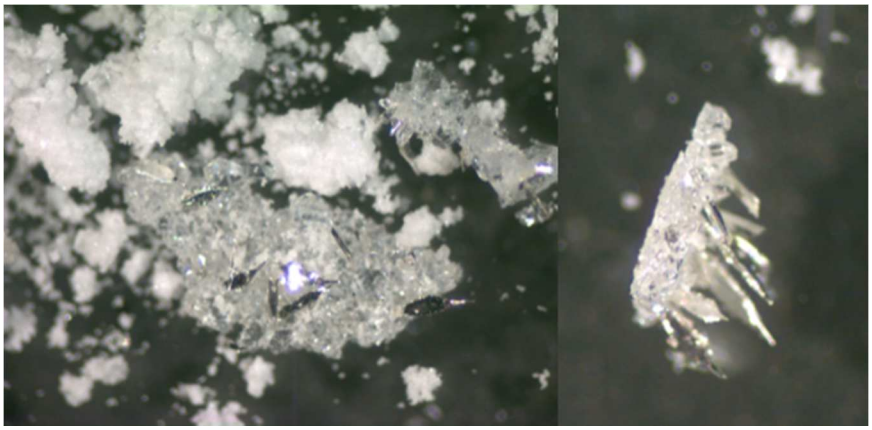

Figure 54. Crystals of anorthite and albite clustered with silver flakes from the reaction tube.

Powder pattern matching of this composite product indicated, along with albite and anorthite, the presence of grossular. Because of the extensive clustering behavior of these crystals choosing a good quality sample for single crystal analysis proved very difficult and it is possible that grossular was among the single crystals produced and not

strictly in the polycrystalline powder. It also seems reasonable to conclude that the silver flakes are helping to nucleate crystal growth because crystals were only found clustered in the flakes.

Interestingly, while crystals of anorthite were not formed using an anorthite powder precursor, it was one of the major products when this coprecipitated gehlenite powder was treated with 3 M NaCl at 650°C.

Attempted formation of grossular from $CaSiO_3$ and sapphire

Many different phases came out of these reactions with coprecipitated precursors, and indeed, the precursors themselves were very interesting. While many of them are worth pursuing, likely many, many more were also possible owing to the rich diversity of silicates occurring naturally. It is for this reason that we shifted gears slightly to a different route that proved successful in getting us much closer to single crystalline grossular.

Powdered alumina as the aluminum source in YAG transport reactions, curiously, gives no appreciable growth, in contrast to the use of solid sapphire chunks, which gives consistently good growth. We tried an analogous approach for the crystallization of grossular using solid sapphire chunks plus calcium silicate as the feedstock with a number of different mineralizers.

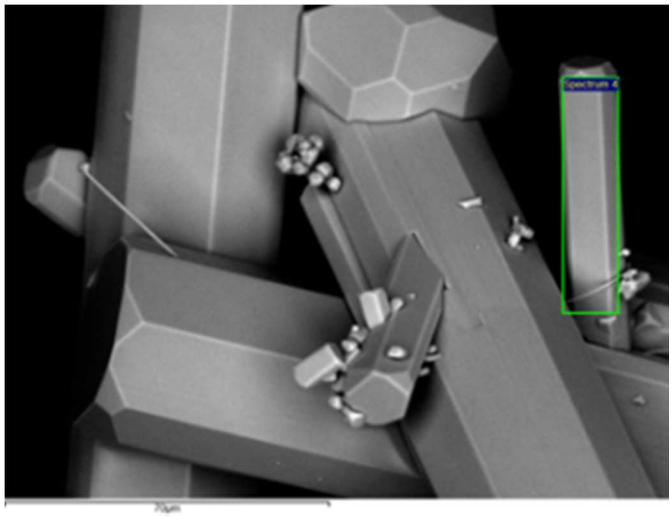

Figure 55. SEM image of product from vesuvianite reaction.

Synthesis of vesuvianite

At 670°C for five days with no gradient, powdered $CaSiO_3$ and crushed sapphire treated with a 0.5 M NaOH mineralizer gave a complex mix of clusters of colorless polyhedra, cubes and rods which were very difficult to distinguish by morphology alone with no discernible powder present. The SEM image in Figure 55 gives a good idea of the intergrowth of the columns that predominate throughout the sample. A complete rod was chosen for single crystal analysis.

A single crystal data set was indexed to vesuvianite, $NaCa_{18}Al_{13}Si_{18}O_{70}(OH)_8$,

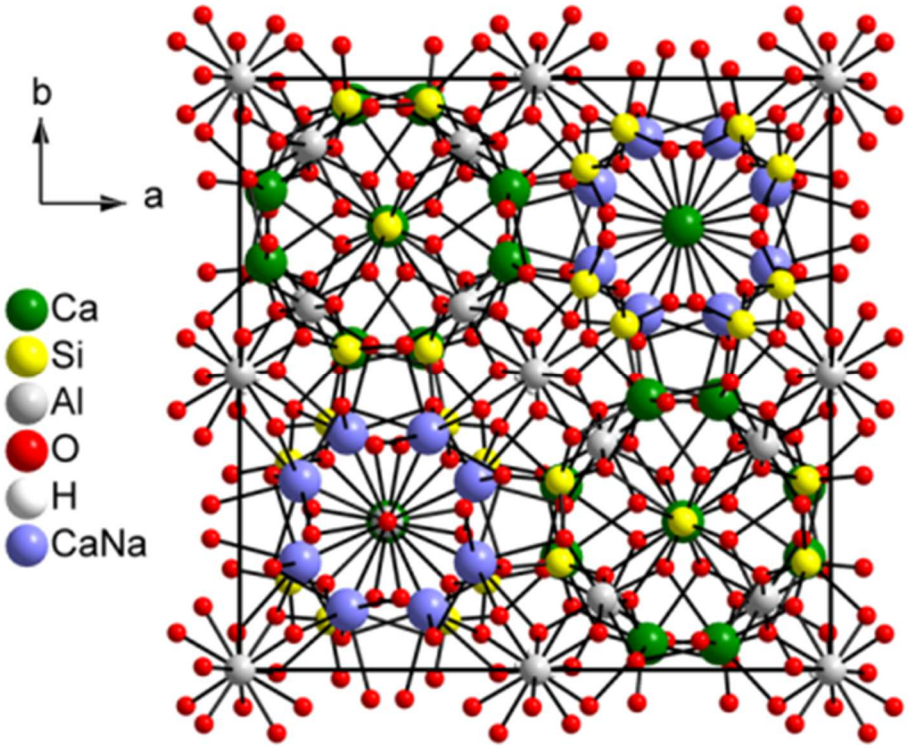

Figure 56. A new vesuvianite, $NaCa_{18}Al_{13}Si_{18}O_{70}(OH)_8$, in which charge balance for Ca^{2+} is due solely to Na^+.

(*P4/nnc*). A complete solution revealed the structure in Figure 56 looking down its c-axis (McMillen, in preparation). This is interesting because it is the first vesuvianite ($Ca_{19}MgFe_2Al_{10}Si_{18}O_{70}(OH)_8$) in which charge balance is due solely to Na^+ for Ca^{2+}. The unit cell contains three distinct channels, one containing alternating AlO_5 and CaO_8 groups, the second containing alternating SiO_4 and CaO_8 groups, and a third containing $AlO_4(OH)_2$ octahedra (Figures 56 and 57).

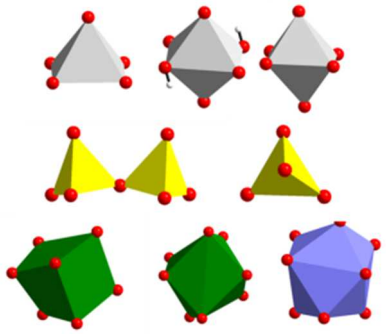

Figure 57. The local bonding environments in vesuvianite.

Figure 57 shows the bonding environments of both the ordered Ca (green, bottom left and center) and disordered Ca/Na (bottom right), the typical tetrahedral Si sites (center row) and the octahedral Al sites, with and without hydroxide groups (top, center and right) and an uncommon, 5-coordinate Al site (top, left).

The elemental analysis of the rod in Figure 55 (green box) gave a Ca:Al:Si:O ratio of 3:2.17:3:13, which, allowing for the Na-disordering with the Ca, is also consistent with vesuvianite and very close to that of grossular (3:2:3:12). The powder pattern match from the composite was a match to a mixture of vesuvianite and grossular (Figure 58) with no other phases present and grossular as the predominant phase. The green lines are those of

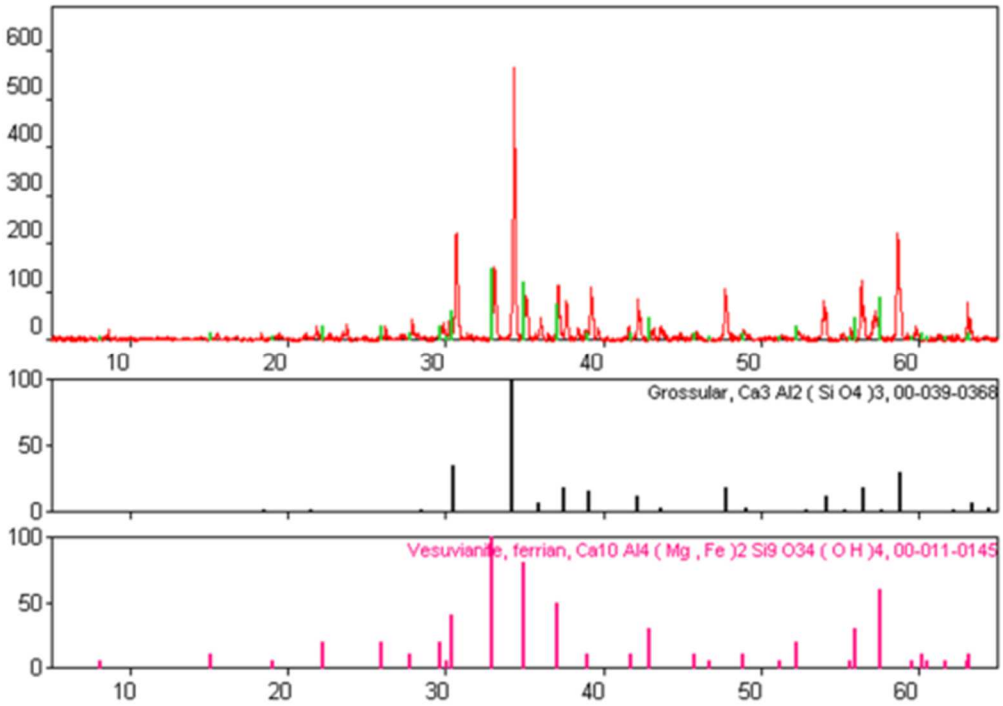

Figure 58. A powder pattern match to grossular and an iron- and magnesium-containing vesuvianite.

a database overlay for an iron- and magnesium-containing vesuvianite mineral (PDF 00-011-0145).

The remaining peaks in the sample pattern on top completely match grossular (PDF 00-039-0368) with no additional phases present. Because of the lack of powder this

time, it is logical to assume that crystals of grossular *had* been produced and it was left to choose a good quality sample from the product.

Also interesting was that the same starting materials treated hydrothermally with 0.5 M RbOH mineralizer produced a product of mostly tiny rods with the powder pattern

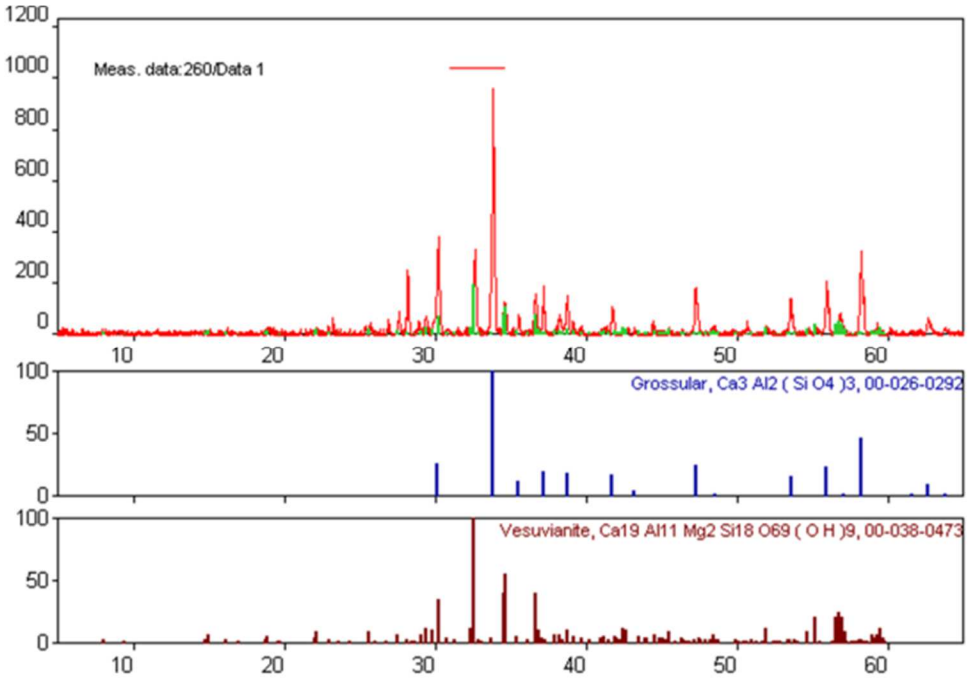

Figure 59. Because no Na was used in the reaction that produced the powder in this pattern, it is reasonable to assume that this may be a new Rb-containing vesuvianite phase.

in Figure 59. This pattern is a match to both grossular and another vesuvianite (PDF 00-038-0473) containing Mg but no Fe, but in the absence of any Na source it is unlikely that it is the same Na-containing vesuvianite that we previously synthesized. Unfortunately these rods were so tiny and clumped together with severe intergrowth that a sample of sufficient quality for complete structural analysis could not be obtained, although it is possible that it might be a new rubidium containing vesuvianite phase.

EDX of the small polyhedra (area in green) in Figure 60 from the above RbOH reaction gave an elemental composition that is consistent with grossular, but is not statistically different from that of vesuvianite and cannot be identified unequivocally based strictly on elemental analysis. The presence of Rb was not detected by EDX, but if

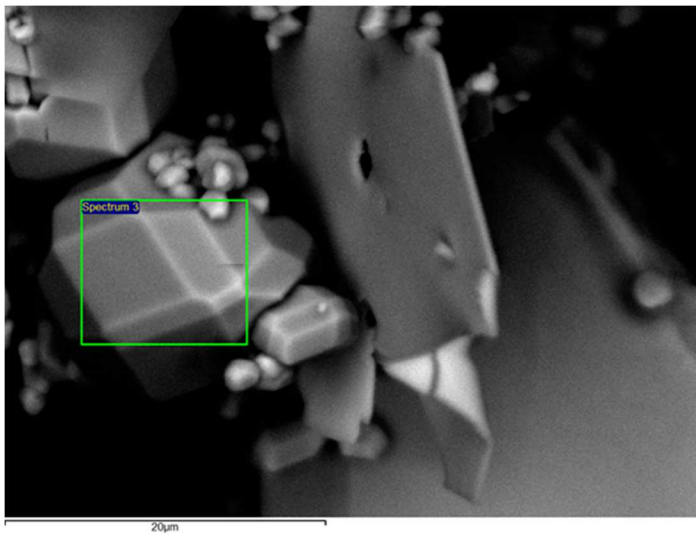

Figure 60. Elemental analysis is consistent with grossular or vesuvianite.

it is the same type of disordered structure as in Figure 56, with an atomic percentage of Na of < 0.8%, we might not be surprised at its absence.

Treatment of the same components with 0.5 M RbCl for 5 days at 670°C gave polycrystalline material. PDXL of the finely ground composite sample gave the powder pattern in Figure 61 which is a match to phase-pure grossular. The use of pure DI water also resulted in a similar looking product with the same phase-pure match to grossular.

	% Ca	% Al	% Si	% O
Experimental	10.473	7.652	12.158	69.717
std (n=3)	0.157	0.084	0.207	0.152

Idealized	15	10	15	60

Table 4. EDX of the product from components treated with 0.5 M RbCl mineralizer.

The SEM image in Figure 62 shows the different morphologies present in the composite sample. Elemental analysis of the region in the green box encompassing all morphologies present gave percentages summarized in Table 4. Even though EDX samples are under vacuum during measurement, we have consistently seen elevated atomic percentages of oxygen, possibly due to the oxidation of surfaces. The exaggerated atomic percentage of oxygen has skewed the other percentages, which are closer to the idealized ratios of Ca:Al:Si, 3:2.2:3.5. While these atomic percentages are not identical to

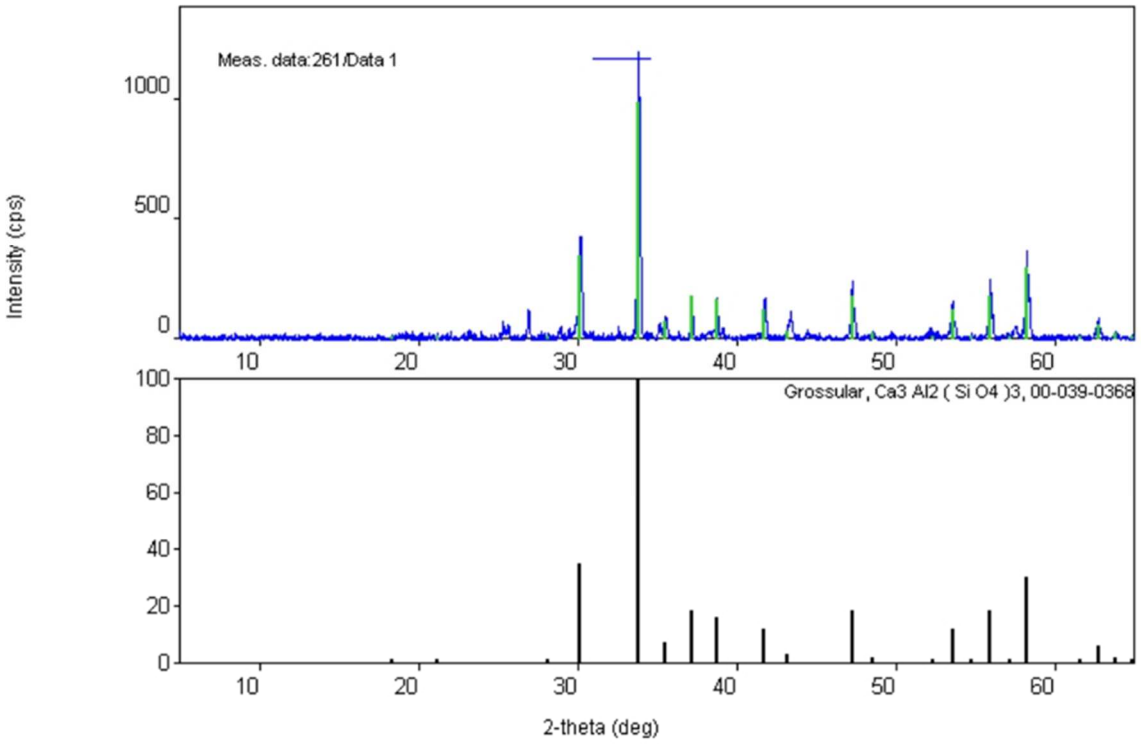

Figure 61. $CaSiO_3$ with crushed sapphire treated with 0.5 M RbCl at 670°C gave a polycrystalline powder consistent with phase-pure grossular.

that of idealized grossular, this data taken together with the powder pattern match in Figure 61 give convincing evidence of phase-pure grossular.

The most phase-pure crystals of grossular resulted from a stoichiometric ratio of $CaSiO_3$ plus crushed sapphire using low molarity Cl- solutions (~ 0.5 M) or plain water with the highest temperature that was tested, 670°C, and is summarized in the experimental section at the end. The powder pattern from this product showed a phase-

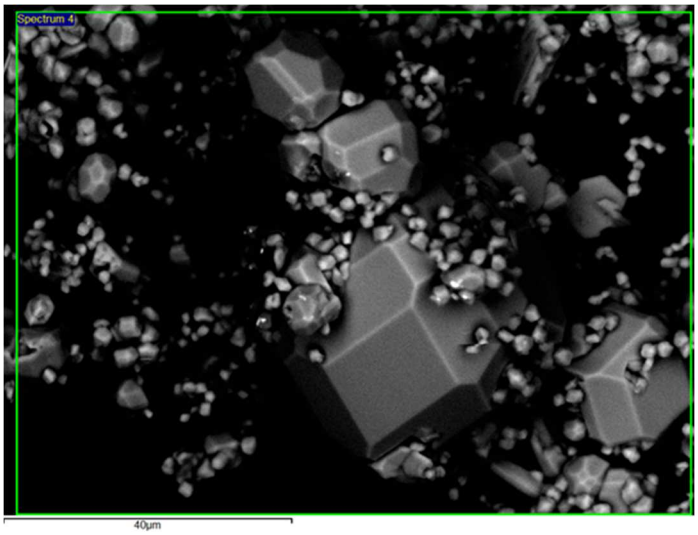

Figure 62. Elemental analysis and powder pattern are consistent with grossular.

pure match to grossular and the elemental analysis was also in agreement with expected ratios.

While the formation of natural garnet $Ca_3Al_2Si_3O_{12}$ proved to be more challenging than initially expected, major progress toward its synthesis has been made and many other interesting phases were encountered. A single longer, larger-diameter

tube at higher temperatures ~700°C might give even larger crystals of grossular while discouraging the formation of the hydroxylated species, vesuvianite, due to the propensity of the hydroxide ion to incorporate at lower growth temperatures. The addition of a small amount of SiO_2 to the gehlenite starting material might also support the production of grossular plus corundum, as Henmi and co-workers have suggested.[81] A summary of experimental methods for selected reactions is provided below.

Summary of silicates

Silicates are a diverse category of crystals and a wide variety of interesting phases were created in our exploration of natural garnet. Our tangential formation of spurrite, a silicate carbonate, opens the door for additional exploration of other carbonates which is likely another rich area of crystal chemistry, including bastnasites, another class of Y- and other rare earth-containing carbonate fluorides.

Only a small sampling of a large assortment of starting materials was utilized in this work and, based on the number of phases that were garnered by the few components that were tried, likely many more phases could be formed using other components, such as Na_2SiO_3, CaO, and even sand, SiO_2.

Another route to the preparation of different starting materials that is likely to produce useful precursors is coprecipitation. In targeting a coprecipitated powder of grossular, phase-pure powders of anorthite and gehlenite were produced and many more precursors are possible by precipitating dissolved components in novel ways.

A number of calcium aluminosilicates and related crystals including grossular, dellaite, albite, anorthite, and pollucite were synthesized. Attempted growth of analogs of these would certainly result in an expansion of our knowledge of these crystals as well as an expansion of the literature regarding them. While there is much in the literature about minerals, there is usually much less about the study of their synthetic versions. Only small slice of the rich array of these silicates was explored and analyzed throughout the course of this work leaving a great many unexplored that could, in itself, be the center of another complete Ph.D. dissertation. Focus was shifted for this reason back to laser crystals and their spectroscopic properties at the expense of further calcium aluminosilicate study.

Summary of experimental methods

Preparation of powdered anorthite

A powdered anorthite ($CaAl_2(SiO_4)_2$, *P-1*) feedstock was prepared by the coprecipitation reaction detailed in Chapter 2. About 2 mL of 70% (about 16 M) HNO_3 was carefully added to 2g of powdered $CaCO_3$ with about 5 mL of water with stirring and mild heat until completely dissolved. After cooling, this solution was added to a separate solution of 5g $Al(NO_3)_3 \cdot 9H_2O$ dissolved in about 10 mL of water. This was then dripped slowly into a NH_4OH solution with vigorous stirring, resulting in a dense precipitate. This was allowed to settle, decanted, and rinsed with fresh DI water until the pH was neutral. The isolated powder was slowly dried over several hours and then calcined at 1000°C overnight. The powder pattern showed a slightly amorphous, but

definite match to anorthite. It is possible that further calcining would have sharpened the peaks.

Preparation of powdered gehlenite

Powdered gehlenite ($Ca_2Al_2SiO_7$, *P-42₁m*, was prepared in a similar manner. A solution of hot concentrated NaOH was made by dissolving as many NaOH pellets as would dissolve into about 20 mL of boiling DI water with stirring on a hot plate. To this 1g of powdered SiO_2 was added and dissolved with some difficulty. While this was slowly dissolving, a solution of 3.685g of $CaCl_2$ in a small amount of water was prepared. Because $AlCl_3$ is very reactive in water, it was opened in a well-ventilated hood and placed on a balance only long enough to weigh 4.426g and then placed back in the hood. While still under ventilation enough water was *slowly* added to dissolve the $AlCl_3$ into a light yellow, clear solution and allowed to cool and then combined with the $CaCl_2$ solution. The warm SiO_2 solution was added drop-wise with a 5 mL syringe to the combined Ca/Al solution with vigorous stirring resulting in a thick gel-like precipitate. It is likely that the addition order is not important and the Ca/Al solution can be dripped into the SiO_2 solution with the same results. This gel was vacuum-filtered and washed several times with DI water until a neutral pH. Depending on thickness of gel, a repeated process of spinning in a centrifuge at 4°C until a well isolated pellet resulted, decanting, replacing the water, sonication and re-centrifuging until pH neutral also worked well.

The wet precipitate was then dried in an oven at about 150°C overnight. After complete drying, it was transferred to an alumina crucible, lightly covered, and calcined

for 36 hours. The prepared powder gave a sharp and complete match to database gehlenite. Careful attention to complete dissolution of SiO_2 as well as longer dwell-time at 1000°C during calcination resulted in a cleaner, sharper powder pattern match.

Preparation of dellaite crystals

Single crystals of dellaite ($Ca_6Si_3O_{11}(OH)_2$, *P-1*) were synthesized hydrothermally using components. Stoichiometric ratios of $Ca(OH)_2$ (0.1233g), powdered SiO_2 (0.1g), powdered Al_2O_3 (0.0565g) were used to target a total powder weight of 0.3 g. This feedstock was treated with 0.4 mL of a premade 3M CsOH solution for 3 days at 620°C resulting in small colorless polyhedra. Because this stock solution was likely contaminated by CO_2 from the air, (see above sections) dellaite crystals were competing with crystals of spurrite. Yield could possibly be increased by this route with the use of freshly-prepared CsOH mineralizer.

Single crystals of dellaite were also prepared from powdered gehlenite feedstock. 0.2g of the powdered feedstock described above was treated with 8.5 M freshly-prepared RbOH mineralizer for 3 days at 650°C resulting in larger colorless polyhedra. It appears that higher mineralizer concentrations and temperatures result in larger crystals of better quality.

Preparation of crystals of calcite

Large, good-quality crystals of calcite, ($CaCO_3$, *R-3CH*), were prepared hydrothermally by treating 0.1 g of coprecipitated gehlenite precursor with 0.4 mL of a 2.5 M Rb_2CO_3 mineralizer for 3 days at 640°C with no gradient (see Figure 8).

Preparation of powdered bicchulite

A polycrystalline powder with a clean match to bicchulite was prepared by the hydrothermal treatment of 0.1g of gehlenite powder with 0.4 mL of 2M NaCl mineralizer at 575°C with no gradient for 4 days.

Preparation of crystals of anorthite and albite

Crystals of both albite (sg *P-1*, $NaAlSiO_8$), and anorthite were formed in the hydrothermal reaction of 0.2g of powdered gehlenite precursor with 1 mL of 3M NaCl mineralizer at 650C with no gradient for 6 days. Larger diameter tubes were used and starting materials were scaled up appropriately likely contributing to the large number and quality of crystals formed.

Large crystals of anorthite were also formed from the hydrothermal treatment of 1 g of gehlenite powder with 5 mL of 2M CsCl mineralizer in a 3/8" silver tube cut to 6" in length. This reaction was set to a 600°C – 650°C thermal gradient for 8 days. The resulting crystals, clustered together with silver flakes, were an index match to anorthite. The powder was a clean match to grossular.

Preparation of crystals of vesuvianite

Vesuvianite crystals were grown by the hydrothermal treatment of 0.1g $CaSiO_3$ and 0.03g of crushed sapphire with 0.04 mL of 0.5 M NaOH mineralizer at 670°C with no gradient for 5 days resulting in a purely crystalline material with no powder present. The crystals were a complex mix of morphologies including colorless square columns, polyhedra, and inter-grown rods.

Preparation of crystals of grossular

The reaction of 0.1g powdered $CaSiO_3$ and 0.03g of crushed sapphire with both 0.4 mL 0.5M RbCl mineralizer and pure DI water treated at 670°C with no gradient for 5 days resulted in a fully crystalline product with no powder. Although a suitable single crystal could not be found, both powder patterns were a perfect database match to grossular with no additional phases present.

Preparation of crystals of $CsAlSiO_4$

Crystals of $CsAlSiO_4$ were formed in the reaction of 0.1g gehlenite powder with 0.4 mL 10M CsF mineralizer. A reaction duration of 5 days at 660°C with no gradient resulted in mostly colorless polyhedra and square columns with white powder.

Preparation of crystals of pollucite

Single crystals of pollucite were formed from a variety of reactions targeting spurrite, with the intentional addition of CO_3^{2-} using a Cs_2CO_3 mineralizer from components. The best quality crystals were grown hydrothermally at 650°C with no gradient for 6 days from 0.1g of powdered SiO_2 with 0.0565g of powdered Al_2O_3 and 0.158g $MgCl_2$ and 0.4mL of 5M Cs_2CO_3 which resulted in a mostly crystalline product consisting of small to moderate-sized colorless polyhedra up to about 3 mm with very little powder.

CHAPTER FIVE

CRYSTAL PREPARATION

To maximize the light going through a crystal, analysis by spectroscopic methods first requires both sides of the sample to be flat and parallel. The method of polishing by an electrically rotating lapidary disc mentioned in Chapter 2 is an effective way to polish larger crystals that, more or less, have parallel flat faces to begin with, such as for epitaxial layers that have been harvested from the seed. In such cases, though, cutting a small, hard crystal lengthwise through its edge can be more art than science.

Harvesting from a seed

Because the dimensions of these crystals in even the best circumstances are only on the order of 1 x 1 x 1 cm clamping a crystal in place for cutting is not practical and so beeswax is used to hold the crystal onto a soft graphite cutting stage. While this works well for crystals that are sufficiently wide, it becomes much more challenging to accurately line up a crystal perpendicularly on its edge if it is tall with a base that is much narrower. Because the wire saw is designed to cut perpendicularly straight down to the cutting surface, it is very important that the crystal be waxed in as close to a perfect arrangement as possible as correcting a wedge-cut crystal by polishing alone is exponentially more difficult in addition to requiring more of the crystal to be polished away.

While it is possible to coat enough wax on each side of the crystal to build up the base, the perpendicularity issue is still not addressed. If enough material has been

transported, however, epitaxially grown crystals usually develop pronounced facets which are a product of their crystallographic orientation. We used these natural facets in two ways to make cutting easier and more precise.

Along with the properly oriented crystal sample, two small blocks of graphite similar to bookends were affixed to the carbon cutting stage with beeswax. This both increased the size of the crystal base to be glued and, because the squared sides of the small graphite blocks were pressed up against the crystal while the wax was hardening the orientation was forced into orthogonality. Thus oriented, slow and even cutting by a water-cooled wire-saw is greatly facilitated.

Polishing with electric lapidary discs

Both sides of these two resulting harvested slabs must then be polished to remove the remaining seed and to eliminate any surface imperfections that can reduce the amount of light going through the crystal. Because it is important that the crystal be held very securely onto a metal post with a large flat end (a dop), two-part fast drying epoxy was used instead of wax. The epoxy has a dry time of five minutes, but a complete cure takes several hours. As with alignment of the crystal prior to harvesting, it is very important that the crystal be glued parallel to the dop end.

The fully-cured dop with the crystal sample is then held normal to the rotating lap as it is polished. A water stream cools and lubricates the crystal and lapidary surface while removing the material that has been polished away. Discs with higher grit are used as the polish improves ending with a fine diamond spray on a smooth ceramic disc for a

final, inspection polish. The crystal can then be removed from the dop by soaking in acetone for several hours after which, the complete process is repeated on the reverse side.

While time-consuming, this method of crystal polishing works well for larger, flat slabs. As the crystals get smaller, however, handling gets much more difficult and sometimes the force of the crystal onto the rotating disc can be too much for the epoxy to maintain a good bond and crystals can fall off the dop sometimes travelling quite a distance. Even if the epoxy is able to hold the crystal tight, the polishing force is sometimes enough to crack or even shatter a small crystal. Small spontaneously nucleated crystals with no obvious orientation present a special challenge in polishing because of their size and the difficulty of gaining a pair of parallel sides.

Manual polishing of crystals

A method of manually polishing these smaller crystals was adapted and works well for both large and small crystals, takes less time, and eliminates the risk of losing or destroying samples from the electric lapidary disc. Because there is much more control of the crystal with this manual method, epoxy was not necessary, decreasing polishing time dramatically.

A 7" diameter glass telescope blank was used for the polishing lap (United Lens, Southbridge, MA), Figure 63, left. Because flatness is important, the glass lap itself was flattened by polishing with coarse grit 40 μm particle size alumina slurry (Universal Photonics, Inc., Hicksville, NY) on a granite slab.

A permanent black marker (or similar marking) was used on the top surface of the lap to reveal any surface imperfections. While polishing, the removal of all black markings indicated that the lap was flat. Because the crystal to be polished should never in theory come into contact with the glass of the lap, progressive polishing was not necessary and only the coarsest grit was used. Similar flattening of the polishing lap was redone after about 10 polishing cycles.

A smaller 2.5" diameter glass telescope blank was used to hold crystal while it was being polished. It was flattened initially in the same way for the lap on a granite slab.

Figure 63. Flattened glass lap, left. Spacers, right top, and bottom, right, guard against rounding of the crystal.

It was further prepared by wrapping masking tape around the entire disc and covering its surface with a shaved wax bond (Unibond 6.5 Adhesive, Universal Photonics, Inc., Hicksville, NY) to a depth of ~1 mm. Heating of the prepared disc using a hot plate melted the wax enough so glass "feet" could be inserted (Figure 63, bottom center and right).

Several spacer feet were placed in the melted wax flat against the glass disc covering most of the surface leaving space in the center for the crystal(s) to be polished (Figure 63, bottom, right). These are necessary to protect the crystal from accidentally getting caught on the edge of the lap and to ensure a flat surface of the crystal by preventing rounding. Because the feet have to be both taller and softer than the crystal a series of small squares were cut from ~1 mm thick glass microscope slides. Thicker feet were made by gluing stacked pieces together to make 2- and 3- mm thick feet.

While crystals grown by spontaneously nucleation often have no obvious faceting, there are usually flat portions that can serve as a starting point for polishing. The largest flat face that could be found was oriented towards the lap and pressed firmly into the melted wax making sure the crystal was as flat as possible up against the glass disc.

Depending on the degree of flattening necessary polishing 5 – 10 minutes per grit was usually sufficient starting with 20 μm particle size alumina slurry with inspection every two minutes or so of the surface. When no visible improvement was noted, the lap was rinsed and the next finer grit slurry was applied. Successive grits of 20 and 12 were used followed by 3 mm on an adhesive felt polishing pad. A couple of minutes on the hot plate was sufficient to soften the crystal enough to turn it over to expose the other side for polishing and the same treatment was given to the other side. After both sides were polished, the crystal(s) were removed and put into acetone for several minutes with sonication to help remove any wax. The method described was adequate for all of the sesquioxides and garnets polished.

Figure 64. A small clear window was polished open for spectroscopy in this 0.45%Ho, 1.57% Yb:Lu_2O_3 crystal with a final path length of 2.10 mm.

The before / after picture in Figure 64 shows an as-grown Ho,Yb:Lu_2O_3 crystal of ~5.6 x 6.3 mm. Polishing is a compromise between opening a large enough window for spectroscopy while leaving as much material as possible to maximize the path length. After polishing a clear window, the path length was 2.10 mm (Figure 64, right).

Figure 65 shows an as-grown 10%Yb:Lu_2O_3 (left) coated with LuO(OH) needles which occurs sometimes as the temperature in the autoclave drops through the phase stability boundary between the higher temperature (above 650°C) Lu_2O_3 and lower temperature (600°C) LuO(OH) phases.

Polishing this crystal by hand as described above, revealed a relatively large inclusion in the center of the crystal but also two clear portions to either side which were

large enough for absorption measurements. Properly prepared crystals were then ready for analysis by absorption spectroscopy.

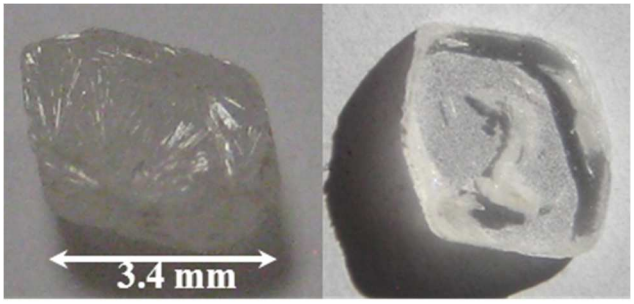

Figure 65. Polishing away a layer of LuO(OH) revealed windows of sufficient size for spectroscopy on either side of an inclusion in the center of this Yb:Lu_2O_3 crystal.

UV-Vis-NIR Absorption Spectrometry

Absorption spectra were collected in transmittance mode with a Shimadzu SolidSpec-3700DUV spectrophotometer. Polished samples were mounted in a custom-made aluminum alloy cryogenic cell with two fused silica windows capable of maintaining crystal temperatures between 298K and 80K to within +/- 5°.

The crystal in the cryogenic cell was kept under vacuum at less than 5 x 10^{-4} torr to help prevent condensation during cooling and subsequent warm-up of the apparatus (Figure 66). User-controlled flowing liquid nitrogen provided the cooling via a feed-through mounted underneath a copper sample holder equipped with a digital RTD sensor with a LakeShore Model 218 temperature probe affixed near the sample. To ensure good thermal conductivity, samples were securely held to the heat sink using indium foil and a

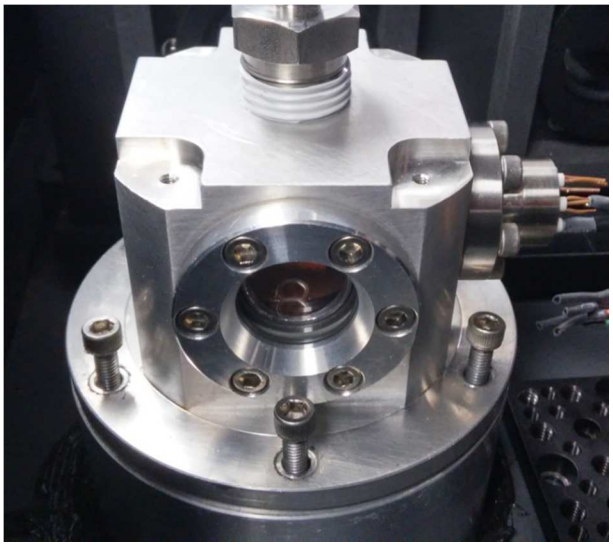

Figure 66. The aluminum alloy cap is equipped with 2 fused silica windows and is bolted down to hold a pressure of 5 x 10^{-4} torr during measurement.

spring loaded copper plate with 2 mm aperture.

The copper sample holder has two interchangeable face plates with apertures of 2 mm and 4 mm diameter depending on sample size (Figure 67). Crystal temperature was controlled manually by adjusting the flow of LN and kept within +/- 5°C. Cryogenic data sets were performed at 298K, 250K, 200K, 150K, and 80K. Resolution was 0.1 nm with

a scan speed of 1.67 nm /sec over the appropriate wavelength range between 300 - 2200 nm using a sampling interval of 0.05 nm unless otherwise specified. Detectors used were PMT (165-850nm), InGaAs (850-1700nm), and PbS (1700-).

Additional data sets were originally collected at 100K, as well. Getting consistently good quality data sets at this temperature, however, proved to be very

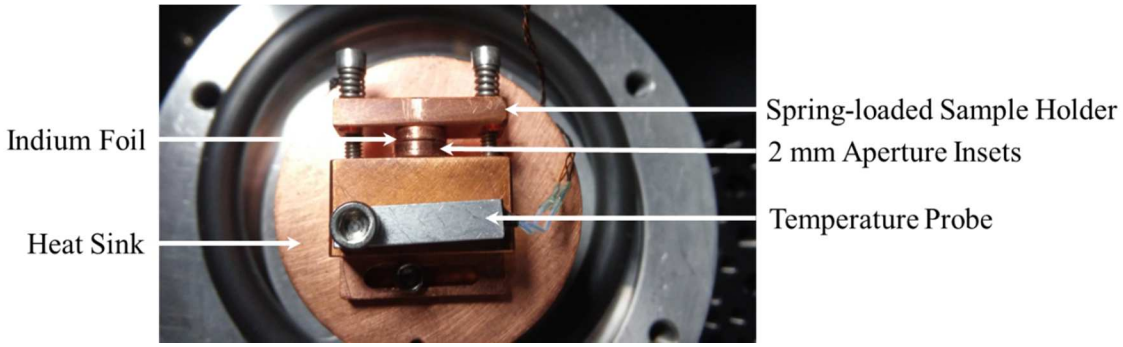

Figure 67. The copper sample holder with temperature probe inside the cryogenic cell. The crystal is held between spring-loaded copper plates coated with indium foil for good thermal contact.

challenging. Manually controlling the flow of LN boil-off gas at a temperature so close to the liquid – gas phase boundary was very difficult. The mixture of gas and liquid dramatically affected the temperature of the system and immediate drops of 20°C were frequently seen leading to data that was not consistently reliable. While data sets performed at 150K required careful attention to gas flow, it was possible, with practice, to get good quality data.

This first-generation cryogenic cell was offered as a proof-of-concept and was and can be improved upon in a number of ways. Reducing the distance from LN tank to inlet of the feed-through by shortening the copper tubing used and by adding insulation to

this tubing, helped by not only reducing the amount of heat lost to the surroundings on the way to the heat-sink in the cell, but also by allowing more of an immediate and direct control of the gas flow.

Another challenge was the condensation sometimes seen on the outer surfaces of the cell windows. Even under vacuum, after long periods at low temperatures caused the cell cap to get cold enough to condense water in the air onto the windows. This problem was addressed by stopping the collection, heating the cell cap and windows slightly with a heat gun until they were at room temperature. The collection could then be continued with a slight overlap of spectral region. Keeping the cap warm can be done much more elegantly by equipping the cap with a self-heating device in the form of a band heater or other source of heat. The presence of water in the first place can be prevented with a nitrogen or argon purge.

The raw transmittance data was corrected for Fresnel loss from dispersion at both crystal surfaces first by using published Sellmeier equations,[31] empirical formulas that that fit index of refraction to wavelength and is of the form

$$n^2 = 1 + \frac{B_1\lambda^2}{\lambda^2 - C_1} + \frac{B_2\lambda^2}{\lambda^2 - C_2} + \frac{B_3\lambda^2}{\lambda^2 - C_3}$$

where B1, B2, B3, C1, C2, and C3 are experimentally determined fitting constants. The reflection coefficient (R) was determined from the index of refraction at each wavelength using the equation

$$R = \left(\frac{n_2 - n_1}{n_2 + n_1}\right)^2$$

which, in air, simplifies to

$$R = \left(\frac{n-1}{n+1}\right)^2$$

the loss term can then be calculated by

$$= (1-R)^2$$

This can then be converted to absorption coefficient by the relation

$$\alpha = -\ln\left(\frac{\frac{T}{loss\ x100}}{path\ length\ (cm)}\right)$$

In addition to correcting for these dispersive losses, the spectra were also corrected for baseline flatness and zeroing. Because reliable doping analysis was not always available, most spectra are presented as absorption coefficient as a function of wavelength. If the concentration of dopant is known with high certainty, the absorption cross-section can then be determined by dividing the absorption coefficient by doping the ion density in ions cm^{-3}.

Summary of preparation techniques

It was important to develop gentler methods of harvesting and polishing to help insure less crystal waste from excessive polishing and imperfect cutting techniques. The method of hand-polishing described earlier was efficient and very effective in preserving crystal material. Properly prepared crystal samples invariably lead to better spectra.

Several improvements were suggested to enhance the design of the cryogenic cell for future iterations, including a self-heating cap and a method allowing better control of the flowing LN. As a first-generation cryogenic absorption spectroscopic instrument,

however, the spectra obtained were of high quality and showed good resolution overall, especially at lower temperatures. The cryogenic absorption spectra of doped-lutetia are presented in the next two chapters and were obtained using the first-generation cryogenic cell described in this chapter and corrected using the equations in the previous section.

CHAPTER SIX

CRYOGENIC ABSORPTION SPECTROSCOPY OF Yb-DOPED LASER HOSTS

There has been much interest lately in Yb-based lasers[16,17,19-21,23,28,49,56,82-85] due in large part to their favorable properties in regard to heat management (see below). This is especially important in high power applications where considerable waste heat builds up during operation. As a result of the single electron vacancy in its f-shell Yb^{3+} has a relatively simple energy level diagram Figure 68 and all absorptions are due to transitions between various Stark levels of the $^2F_{7/2}$ ground state to $^2F_{5/2}$ excited-state manifold. [34] Because there is no readily accessible manifold above its upper level, competing processes such as upconversion and excited state absorption are not observed.

Of particular interest is the proximity of the Yb^{3+} pump band (ca. 970 nm), which is easily accessible by newer diode sources (InGaAs ~980 nm), to its emission wavelength at around 1030 nm. Pumping into a band that is closer in energy to its

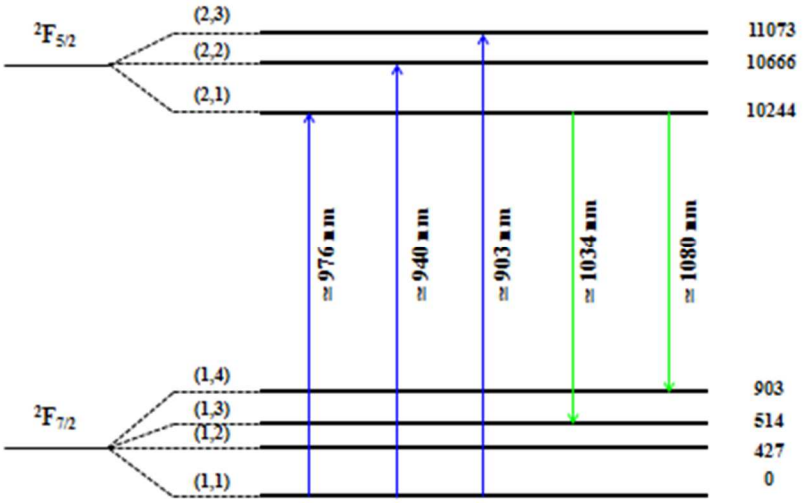

Figure 68. The simple energy level diagram of Yb^{3+} shows some possible absorptions and emissions.

emission band minimizes the quantum defect that leads to the generation of waste heat, one of the biggest limiting factors to the continued development of high-power lasers, and can cause a whole host of problems from thermal lensing and thermal expansion to even destruction of the crystal itself.

Obviously the most well studied host system for Yb is YAG, typically with 2-10% doping in Yb:YAG. Also of particular interest is the unique host system of Lu_2O_3

doped with Yb to form Yb:Lu_2O_3. The focus on this material is due to its thermal conductivity and thermal stability. The thermal conductivity (κ) of a laser crystal is important because of its ability to remove heat that is generated during laser operation. While garnets and sesquioxides have relatively good thermal conductivities when undoped, the differences start to become apparent when they are doped.

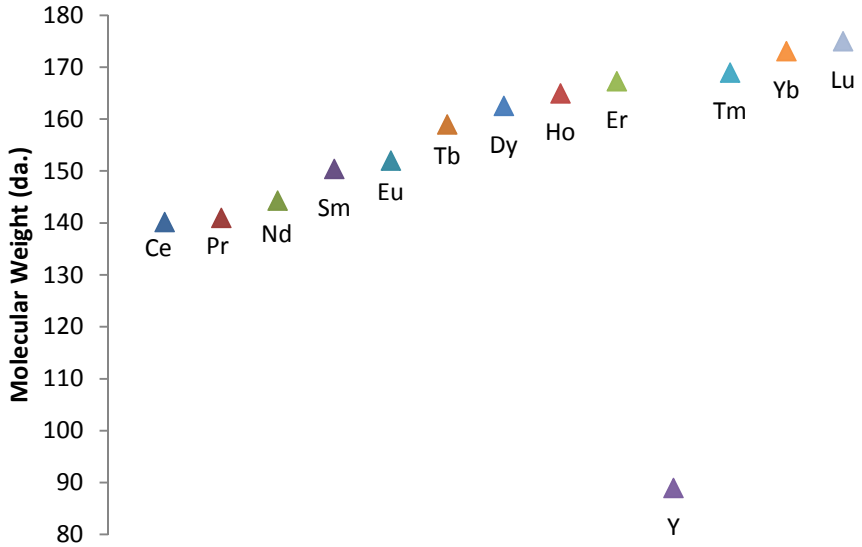

Figure 69. The similarity of mass between the laser active ions and Lu is apparent. Y is placed in this series based on its crystal radius. Its mass is about half of any of the other ions.

Consider the Y-based hosts YAG and Y_2O_3 when doped with Yb. The mass mismatch between the native Y (average atomic mass 89.905 g/mol) and dopant Yb (173.04 g/mol) and, indeed, any of the other f-block elements, is almost double when compared to the mass difference of Lu to Yb which is only 1.1%.

One of the ways that the heat is dissipated is through phonon conductivity. However phonons conduct poorly when there is a large mass difference between the host

ion and dopant ion because the phonons are scattered by the dopant ion. The greater the phonon scattering, the less efficient they are at carrying heat out of the crystal and this effect is exacerbated with increased doping.

Figure 69 shows the mass comparison of the common laser ions plus yttrium and lutetium. Yttrium is placed in the figure based on its crystal radius, between Er and Tm. While the difference between Y and the rest of the ions is dramatic, lutetium has only a very small mass difference between itself and typical laser ions like Tb, Ho and Yb. In fact the difference between Lu and Yb is almost non-existent. It is this similarity of mass that allows the phonons to move unimpeded. As a result, the thermal conductivity of these lutetium-based hosts almost independent of doping levels of Yb.

	Undoped	3%	5%	20%
YAG[22]	11	6.8		
YAG[86]	9.5			7
YAG[18]	10			
Y_2O_3[22]	13.6	7.7		
Y_2O_3[87]	15.94		8.34	
LuAG[86]	7.5			7.4
Lu_2O_3[18]	12			
Lu_2O_3[88]	14.32		12.42	
Lu_2O_3[22]	12.5	11		

Table 5. A comparison of thermal conductivities (κ) of Yb-doped hosts at varying percentages. Y-based hosts have more of a decrease in κ with greater doping.

Thermal conductivity (κ) measurements by K. Beil show[86] the effect of increased doping percentages of Yb in YAG versus LuAG hosts (Table 5). While κ decreases from 9.5 to 7 for undoped YAG to 20% Yb doping it is nearly constant on going from 7.5 to about 7.4 in undoped to 20% doped LuAG. Mun and co-workers found that in undoped Lu_2O_3 grown by the by μ-PD method, κ goes from 14.32 to 12.42 in 5%Yb:Lu_2O_3. The

relation appears to flatten out after about 4% and additional doping does not result in a further decrease in κ.

Because κ increases with decreasing temperature, cryogenic cooling of the crystal is used both to help remove this heat and to increase κ. While both lutetia and YAG exhibit this behavior, it is even more pronounced in Lu_2O_3 with respect to YAG as we have previously reported.[18] While both undoped hosts have similar room temperature thermal conductivities, around 10 W/mK for YAG and 12 W/mK for lutetia, κ at cryogenic temperatures is 30 W for YAG, or about three times greater. The difference for lutetia, however, is more than four times as great, going from 12 W/mK to about 50 W/mK. The fact that the lutetia host has an even higher thermal conductivity than YAG at low temperatures, doping with Yb, even at relatively high levels and the small quantum defect of Yb^{3+} taken together make this crystal particularly attractive for use in cryogenic lasers.

The thermal conductivity of Yb-doped Lu containing hosts is potentially promising but the actual spectroscopy is not as well explored as it is for more traditional hosts such as Yb:YAG. For high power laser applications the detailed understanding of the lasing ion is vital since maximum efficiency and output is required. Thus it is essential to obtain as complete an understanding as possible of the spectral behavior of the Yb^{3+} ion in the specific host environment. This data can be later used as a model for the design of lasing behavior in eventual high power laser applications.

One very promising approach to high power Yb lasers is to perform the lasing at cryogenic temperatures. Aside from the increased thermal conductivity at low temperatures, as we have just seen, several other changes occur. At room temperature there is a non-zero population of the vibrationally excited Stark levels of the ground state due to thermal population by ambient energy. A transition from this mix of states, therefore, would give an absorption that is broadened and decreased in intensity. At low temperatures, however, there is not enough energy to allow this thermal population of any state except the lowest vibrational level of each Stark level. This also dramatically decreases the pump energy required. As with all transitions originating from a common same state, the result is a sharpened peak of greater intensity.

This is not the only difference that is seen between room-temperature and low-temperature absorption behavior. Cooling a crystal to cryogenic temperatures also causes a contraction of the crystal lattice which increases the splitting between Stark levels. This increased splitting is responsible for shifting of peaks in either direction towards shorter or longer wavelengths. It is not always clear the effect all of these phenomena will have on the final absorption behavior of the crystal and thorough testing at cryogenic temperatures is very important. This type of analysis of the comparison of room-temperature and cryogenic spectra of several crystals is presented below.

Spectroscopic analysis of hydrothermal Yb:Lu_2O_3

The polished 2% Yb:Lu_2O_3 crystal in Figure 70 has a path length of 1.42 mm and was grown hydrothermally by SN, as described in Chapter 2. A stoichiometric ratio of powdered Lu_2O_3, Yb_2O_3 (HEFA Rare Earth, CA, 99.997%), and crushed sapphire to total 1.5 g of solid feedstock were used with 3 mL of a 20M KOH (MV laboratories, 99.99%)

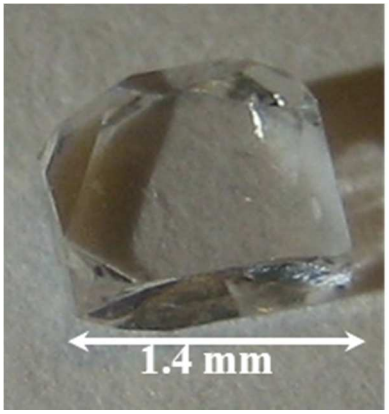

Figure 70. Polished 2% Yb:Lu_2O_3 crystal grown hydrothermally by SN. The facets can clearly be seen on its face.

mineralizer and a thermal gradient of 670°C -700°C for 12 – 14 days. We have previously reported the hydrothermal growth of doped-lutetia[18] and its cryogenic absorption spectroscopy of Yb:Lu_2O_3 is presented, to our knowledge, for the first time here in Figure 71 between 850 nm and 1100 nm for the temperatures of 298K, 250K, 200K, 150K, and 80K. In addition to 2% Yb:Lu_2O_3, high-quality crystals of various Yb-containing Lu_2O_3 have also been grown by SN using the hydrothermal method and will be discussed later in the chapter.

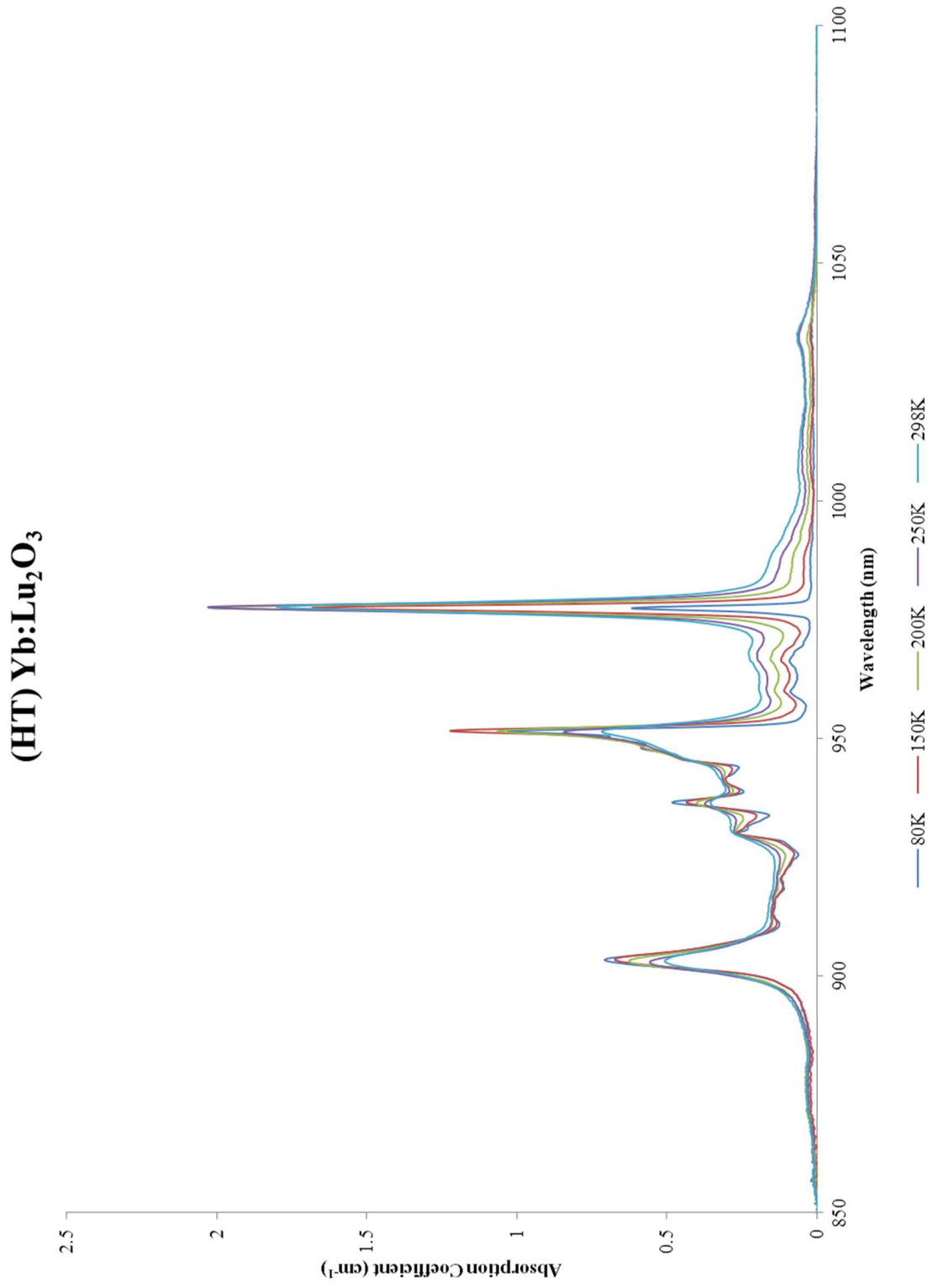

Figure 71. The cryogenic absorption coefficient of Yb:Lu_2O_3 between 850 nm and 1100 nm for 298K, 250K, 200K, 150K, and 80K.

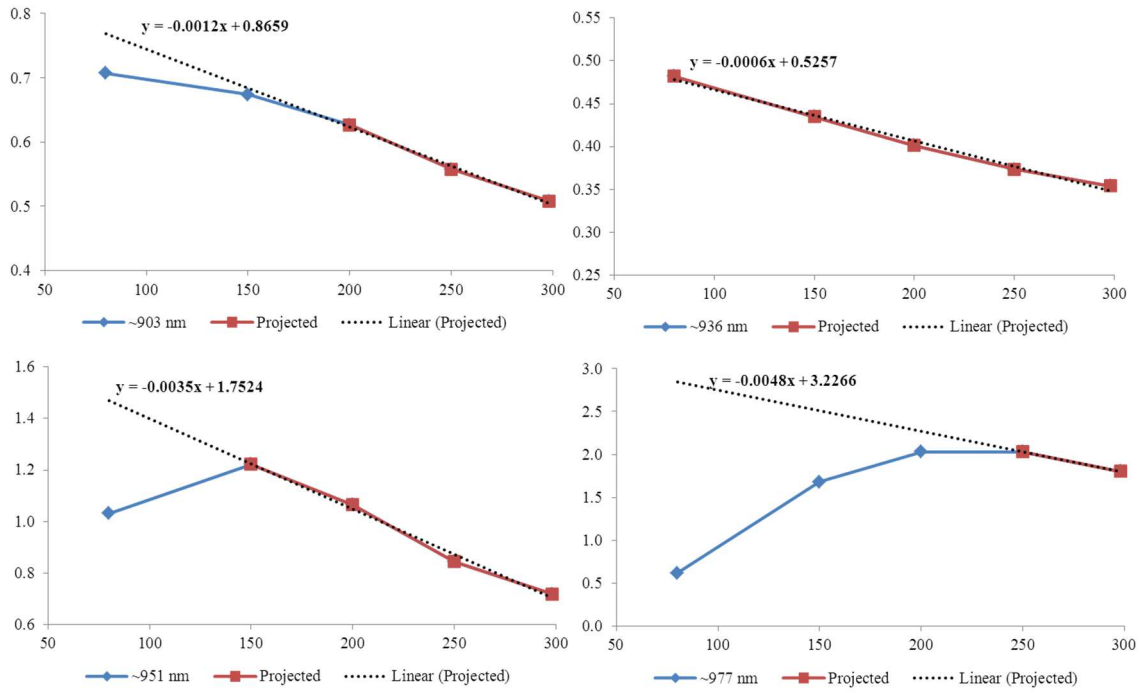

Figure 72. Yb:Lu_2O_3 Absorption coefficient intensities for a cryogenic series. Projected intensities are calculated based on trend lines of the warmest temperatures that appear to follow the trend.

	(HT) Yb:Lu_2O_3 Absorption Coefficient (cm^{-1})			
Temperature (K)	**~903 nm**	**~936 nm**	**~951 nm**	**~977 nm**
80	**0.707 (0.770)**	**0.482**	**1.031 (1.472)**	**0.618 (2.843)**
150	**0.674 (0.686)**	**0.435**	**1.223**	**1.682 (2.507)**
200	**0.626**	**0.401**	**1.065**	**2.028 (2.267)**
250	**0.557**	**0.373**	**0.844**	**2.030**
298	**0.508**	**0.354**	**0.717**	**1.801**

Table 6. A summary of the absorption coefficient of Yb:Lu_2O_3 for the chosen transitions as a function of temperature.

Analysis of peak intensities for Yb:Lu_2O_3

The peak intensities for selected transitions of Yb:Lu_2O_3 are plotted in Figure 72 as a function of temperature. We would expect to see a narrowing of the band width and an increase in intensity as we go from higher temperatures to lower. For the peaks listed we generally see an intensity increase except in the case of the 977 peak (the zero-phonon

peak) where we see anomalies in the intensity at 150K and even greater at 80K. This is likely explained by the inability of our spectrophotometer to record this peak that is likely very sharp and intense. We postulate that the line is too narrow (<0.1nm) at these cryogenic temperatures for our monochromator. Projecting the peak intensity of the two highest temperatures that appear to follow the expected trend backwards to 80K we get values of about 2.267 cm^{-1} at 200K, 2.507 cm^{-1} at 150K, and 2.843 cm^{-1} for 80K. These values including actual measured intensities and those predicted based on trend lines are summarized in Table 6.

Analysis of peak positions for Yb:Lu_2O_3

As mentioned earlier Yb has a simple energy level structure and the absorptions can be seen to be due to transitions from the $^2F_{7/2}$ ground state (1,1) to different Stark levels of the $^2F_{5/2}$ excited state manifold, (2,3), (2,2), and (2,1) corresponding to the wavelengths of 903.10, 951.45, and 977.70 nm. For the (1,1) - (2,3) transition at 903 nm. Going from higher to lower temperatures we also see a shifting of maximum peak positions. The position of maximum intensities for each temperature for Yb:Lu_2O_3 is also plotted in Figure 73 and summarized in Table 7. At lower temperatures we would expect to see a regular shifting of maximum peak wavelength due to the increased splitting of the energy levels with the lattice contraction. We see a slight blue shifting of the zero phonon peak position from 977.65 nm to 977.35 nm or only a 0.3 nm shift between room temperature and 80K.

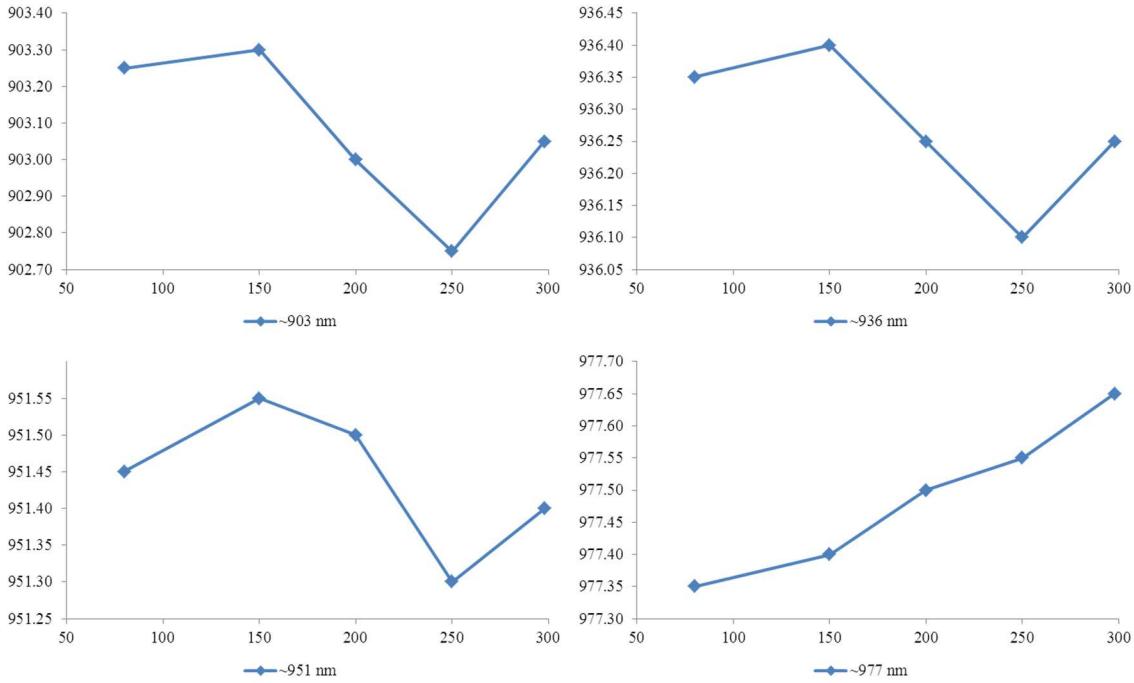

Figure 73. The shift in peak position of Yb:Lu_2O_3 for the chosen transitions as a function of temperature.

The trends for the other transitions appear to follow one another but do not follow the same trend as for the 977 nm transtion. We see a slight blue shift for the other chosen transitions on going from room temperature to 250K but then a red shifting at 200K and then again at 150K and a final blue shift again at 80K. These positions should not be affected by the resolving power of the spectrophotometer and are likely a real trend. The greatest shifting seen in any of the specific peaks, however, is only 0.5 nm between 250K and 80K for the peak around 903 nm.

	(HT) Yb:Lu_2O_3 Peak Center			
Temperature (K)	**~903 nm**	**~936 nm**	**~951 nm**	**~977 nm**
80	**903.25**	**936.35**	**951.45**	**977.35**
150	**903.30**	**936.40**	**951.55**	**977.40**
200	**903.00**	**936.25**	**951.50**	**977.50**
250	**902.75**	**936.10**	**951.30**	**977.55**

298	**903.05**	**936.25**	**951.40**	**977.65**

Table 7. Peak center shifting for Yb:Lu_2O_3 for a cryogenic set. The zero-phonon transition at ~977 nm follows a regular blue-shifting trend while the others do not.

Spectroscopic analysis of hydrothermal Yb:LuAG

Yb:LuAG has the distinct advantages over Yb:YAG discussed previously, and although Yb:LuAG does not appear to have as high a thermal conductivity overall as Yb:Lu_2O_3, our group has demonstrated the hydrothermal epitaxial growth of high-quality single crystal (see Chapter 3) while, at least as of this writing, the same epitaxial growth has not been established for the hydrothermal growth of Yb:Lu_2O_3. To our knowledge the first cryogenic absorption spectroscopy of hydrothermal Yb:LuAG is described in this thesis, including 298K, 250K, 200K, 150K, and 80K absorption coefficients between 850 nm and 1100 nm is presented in Figure 74.

The spectroscopic analysis of Yb:LuAG is presented in this chapter rather than in Chapter 3, specifically concerning doped LuAG, because given the in-depth discussion of cryogenic spectroscopy of Yb-doped hosts in this chapter, its inclusion here was more appropriate. The sample of Yb:LuAG used for the cryogenic absorption spectra was grown by the hydrothermal epitaxy method discussed in Chapter 2, harvested and polished for testing using the electric polishing system also described in that chapter.

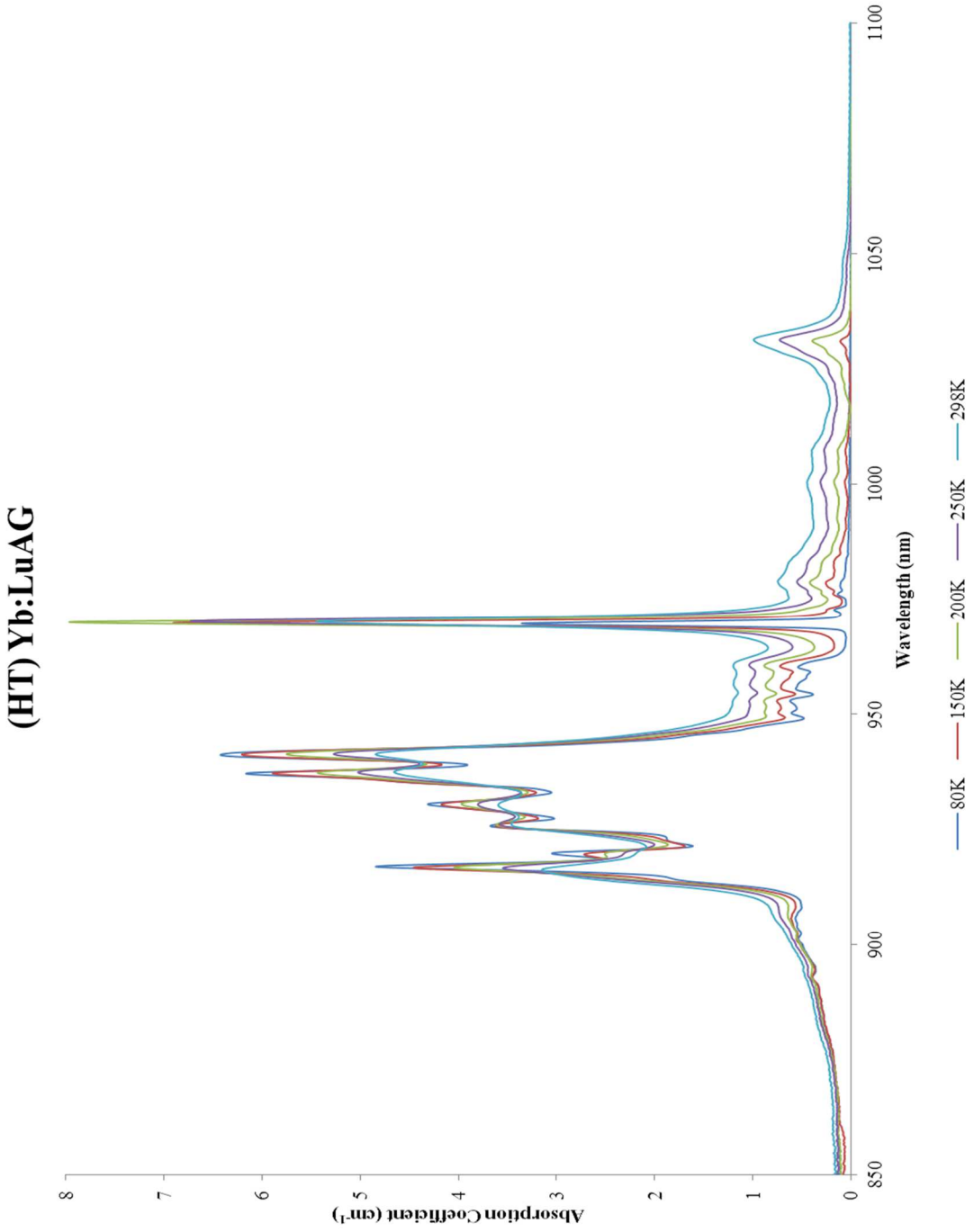

Figure 74. The cryogenic absorption coefficient of Yb:LuAG between 850 nm and 1100 nm for 298K, 250K, 200K, 150K, and 80K.

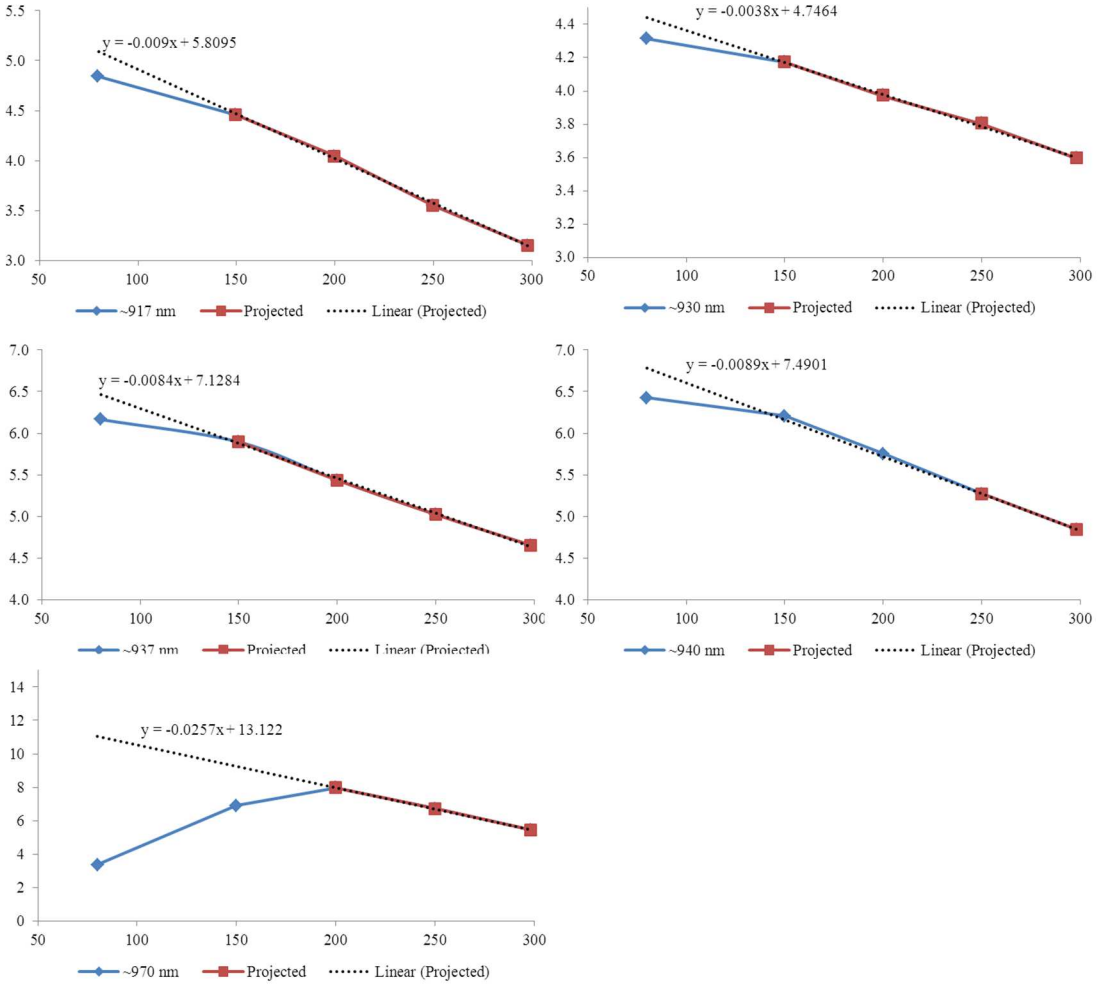

Figure 75. The absorption coefficient of Yb:LuAG for the chosen transitions as a function of temperature.

	(HT) Yb:LuAG Absorption Coefficient (cm^{-1})				
Temperature (K)	**~917 nm**	**~930 nm**	**~937 nm**	**~941 nm**	**~970 nm**
80	**4.84185 (5.0895)**	**4.31148 (4.4424)**	**6.16374 (6.4564)**	**6.42509 (6.7781)**	**3.35624 (11.066)**
150	**4.46**	**4.17**	**5.89**	**6.21**	**6.90708 (9.267)**
200	**4.04**	**3.97**	**5.44**	**5.75**	**7.97**
250	**3.55**	**3.80**	**5.02**	**5.27**	**6.73**
298	**3.15**	**3.60**	**4.66**	**4.84**	**5.45**

Table 8. A summary of the absorption coefficient of Yb:LuAG for the chosen transitions as a function of temperature.

Analysis of peak intensities for Yb:LuAG

The same type of analysis for Yb:Lu_2O_3 in the previous section is presented below for Yb:LuAG. The absorption peaks in the garnets compared to the sesquioxides are not as narrow. This agrees with the plots of intensity in Figure 75 summarized in Table 8 which appear to follow the expected trend much better than for Yb:Lu_2O_3 and only the intensities of the 80K plot are anomalous. We see this stray from predicted intensity much more pronounced in the zero-phonon line around 970 nm.

In light of the discussion in the last section regarding the possible inability of the spectrophotometer to capture the true intensity of the zero-phonon line for Yb:Lu_2O_3, it makes sense for this anomaly to be seen here also for the zero-phonon line in Yb:LuAG, which is also likely the most intense and narrowest. Even in this case, however, only the peaks at the two lowest temperatures seem to be affected, while those at the higher temperatures appear to follow the trend closely.

Analysis of peak positions for Yb:LuAG

Similar to Yb:Lu_2O_3, there appears to be no overall trend seen for peak shifting with temperature. The peaks at 937 nm, 940 nm, and 970 nm do follow a general blue shifting from 298K to 80K, while the 917 nm and 930 nm peaks follow a rough red shifting over the same temperatures. One important difference between Yb:Lu_2O_3 and Yb:LuAG can be seen between their zero-phonon (pumping) bands. While the peak intensity of this line for LuAG is only at 970.65 nm at room temperature compared to its emission at 1028 nm (Figures 76 and 77, Table 9), lutetia is 977.5 nm at room

temperature compared to its emission at 1032 nm.[21] This represents a shift of pump wavelength by almost 3 nm closer to its emission wavelength for Yb:Lu_2O_3 compared to Yb:LuAG, which further aids in reducing waste heat production in lutetia. While the

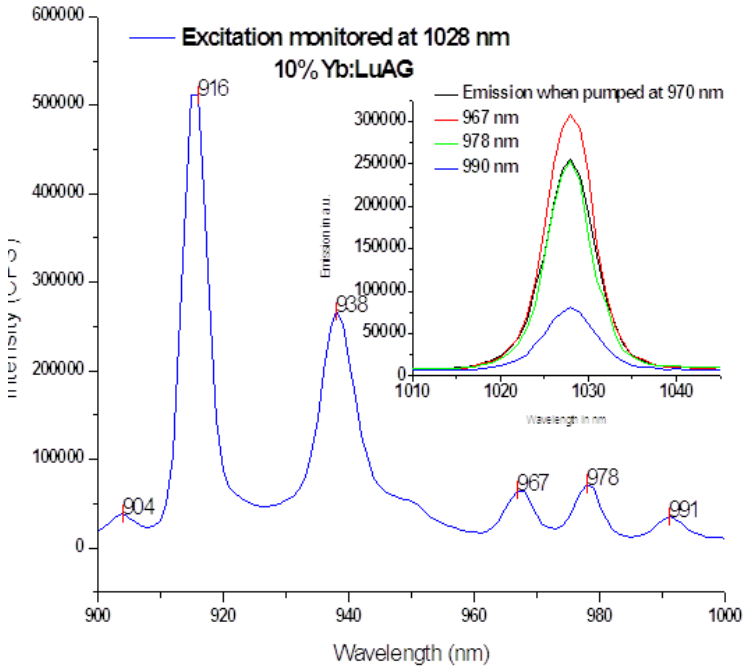

Figure 76. Excitation monitored at 1028 nm for 10%Yb:LuAG. Although emission is greatest when pumped at 967 nm (inset), the quantum defect is also greater.

emission intensity at 1028 nm is greatest when pumped at 967 nm, the quantum defect is much greater. It is also interesting to note that there is also a non-zero absorption around 990 nm that contributes to the 1028 nm emission in Yb:LuAG which could further reduce the quantum defect.

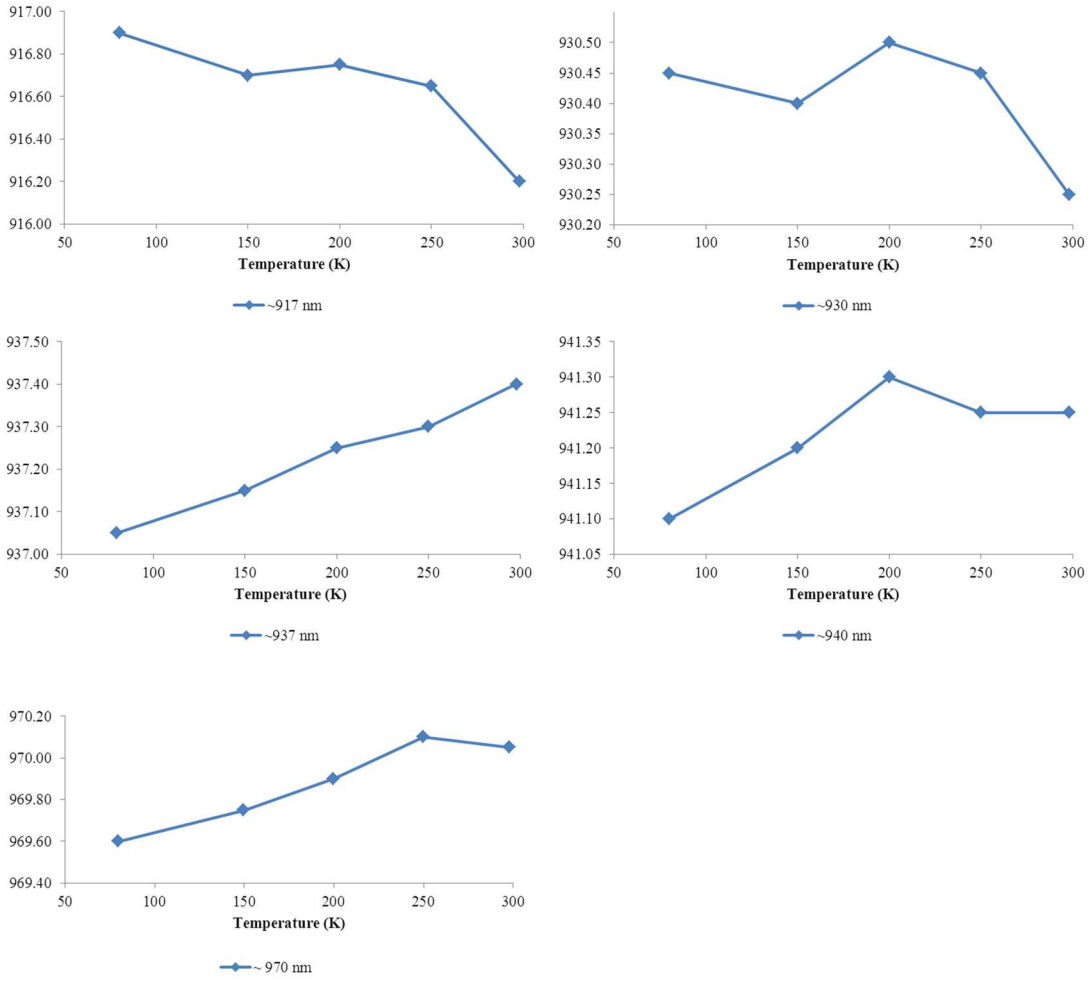

Figure 77. The shift in peak position of Yb:LuAG for the chosen transitions as a function of temperature.

	(HT) Yb:LuAG Peak Center				
Temperature (K)	**~917 nm**	**~930 nm**	**~937 nm**	**~941 nm**	**~970 nm**
80	**916.90**	**930.45**	**937.05**	**941.10**	**969.60**
150	**916.70**	**930.40**	**937.15**	**941.20**	**969.75**
200	**916.75**	**930.50**	**937.25**	**941.30**	**969.90**
250	**916.65**	**930.45**	**937.30**	**941.25**	**970.10**
298	**916.20**	**930.25**	**937.40**	**941.25**	**970.05**

Table 9. A summary of the shift in peak position of Yb:LuAG for the chosen transitions as a function of temperature.

Spectroscopic analysis of CZ Grown Yb:YAG

While Czochralski-grown Yb:YAG is a reasonably well known material, its absorption coefficients were collected on the same spectrophotometer at cryogenic temperatures with cryogenic cell described earlier and is presented here in Figure 78 for completeness and direct comparison with our data for Yb:Lu_2O_3 and Yb:LuAG. Figure

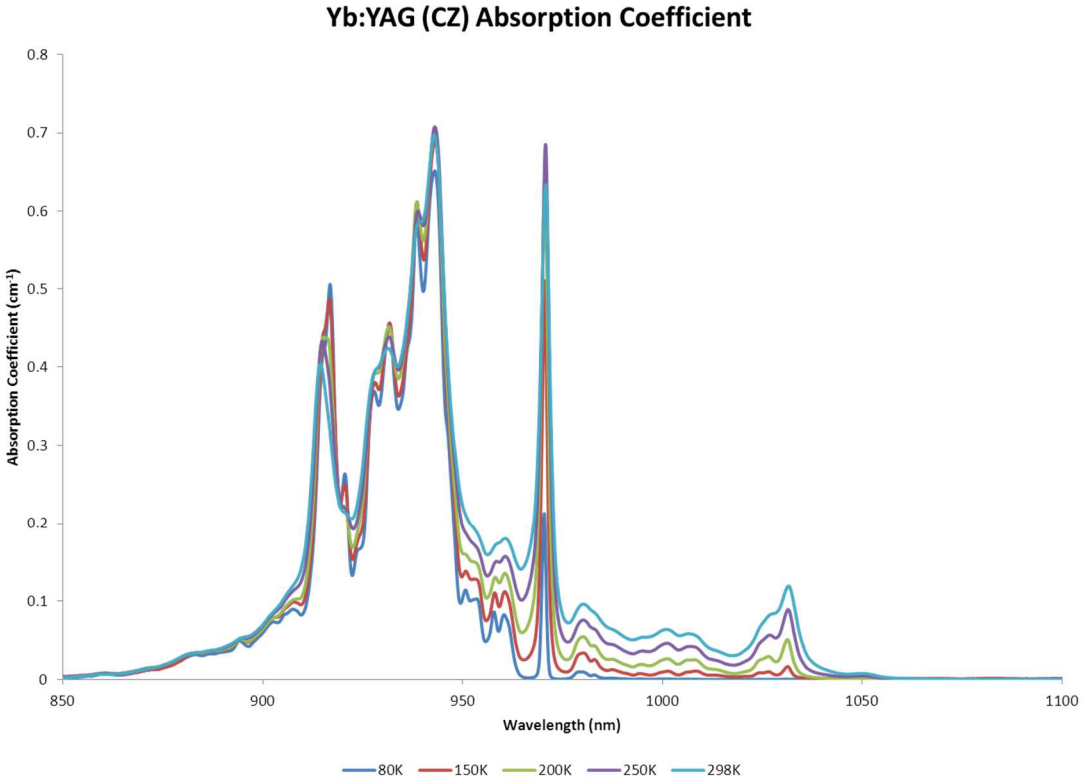

Figure 78. The cryogenic absorption coefficient of Yb:YAG between 850 nm and 1100 nm for 298K, 250K, 200K. 150K. and 80K.

79 shows the absorption coefficient intensities as a function of temperature for the chosen peaks that is summarized in Table 10.

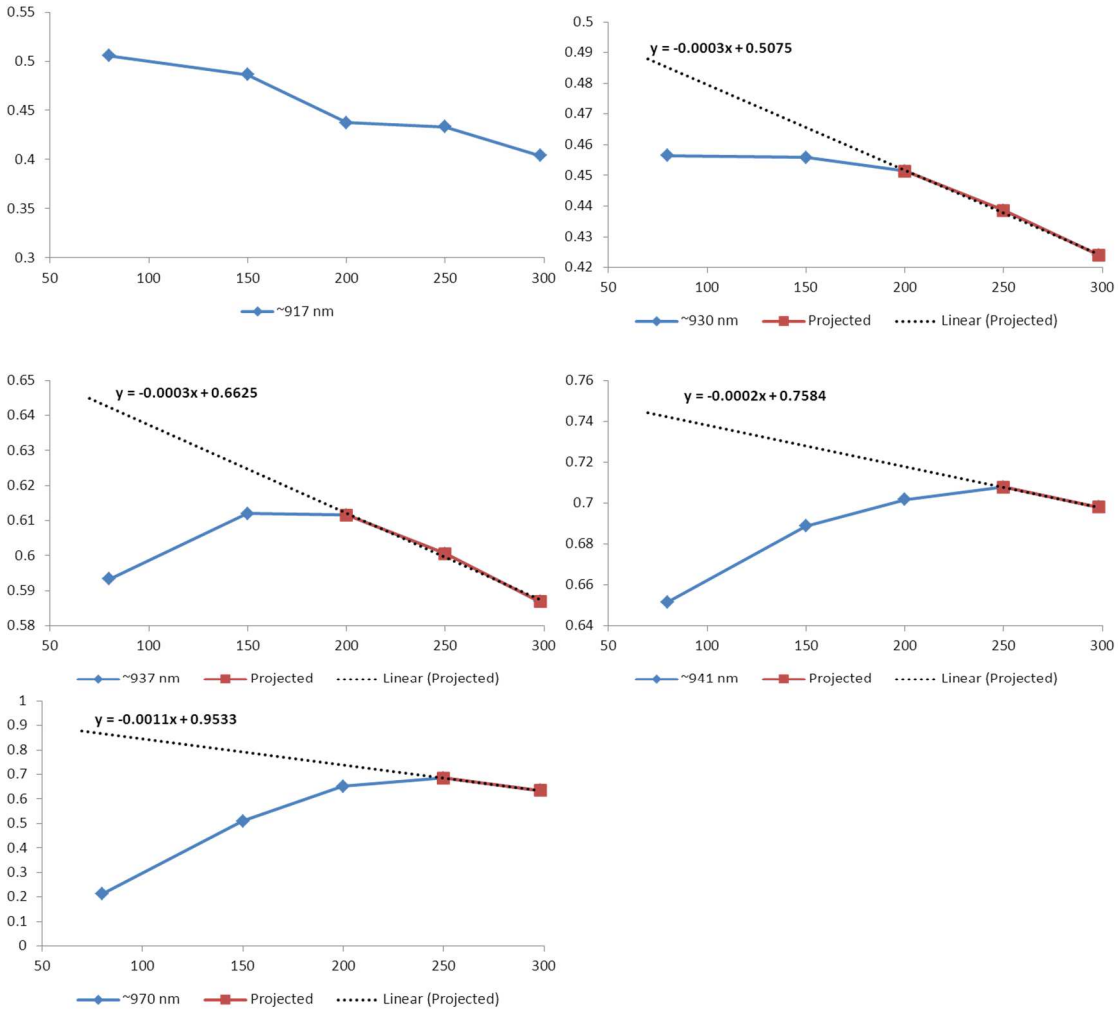

Figure 79. The absorption coefficient of Yb:YAG for the chosen transitions as a function of temperature.

	(CZ) Yb:YAG Absorption Coefficient (cm^{-1})				
Temperature (K)	**~917 nm**	**~930 nm**	**~937 nm**	**~941 nm**	**~970 nm**
80	**0.506**	**0.456 (0.482)**	**0.593 (0.628)**	**0.652 (0.742)**	**0.213 (0.865)**
150	**0.486**	**0.456 (0.462)**	**0.612 (0.618)**	**0.689 (0.728)**	**0.510 (0.788)**
200	**0.438**	**0.451**	**0.612**	**0.702**	**0.651**
250	**0.433**	**0.439**	**0.601**	**0.708**	**0.685**
298	**0.404**	**0.424**	**0.587**	**0.698**	**0.634**

Table 10. A summary of the absorption coefficient of Yb:YAG for the chosen transitions as a function of temperature.

Analysis of peak intensities for Yb:YAG

The trend in absorption coefficients seen in Yb:YAG is very similar to that seen in Yb:LuAG only with exaggerated anomalies at lower temperatures. The peak at 917 nm follows the general expected trend of increasing intensity with decreasing temperature, but the others exhibit the same type of behavior seen in Yb:Lu_2O_3, where the absorption intensities at higher temperatures follow the expected trend and begin to deviate more and more with lowering temperatures in a smooth trend that appears opposite to what would be expected. Again, it is not known with certainty if this is the reason for the apparent anomaly, but if it is instrument-related, it is possible that lower temperature absorption coefficients can be predicted (Table 10, in parentheses) by using the trend line equations.

Analysis of peak positions for Yb:YAG

Interestingly, the zero-phonon peaks for each of the Yb-doped hosts in this chapter so far have followed the expected trend, and the peak near 970 nm for Yb:YAG is no exception (Figure 80 and summarized in Table 11). This peak smoothly blue-shifts about 0.35 nm from room-temperature to 80K. Also generally following this trend is the peak near 937 nm that also blue-shifts by about 0.75 nm. The other peaks do not follow a clear trend.

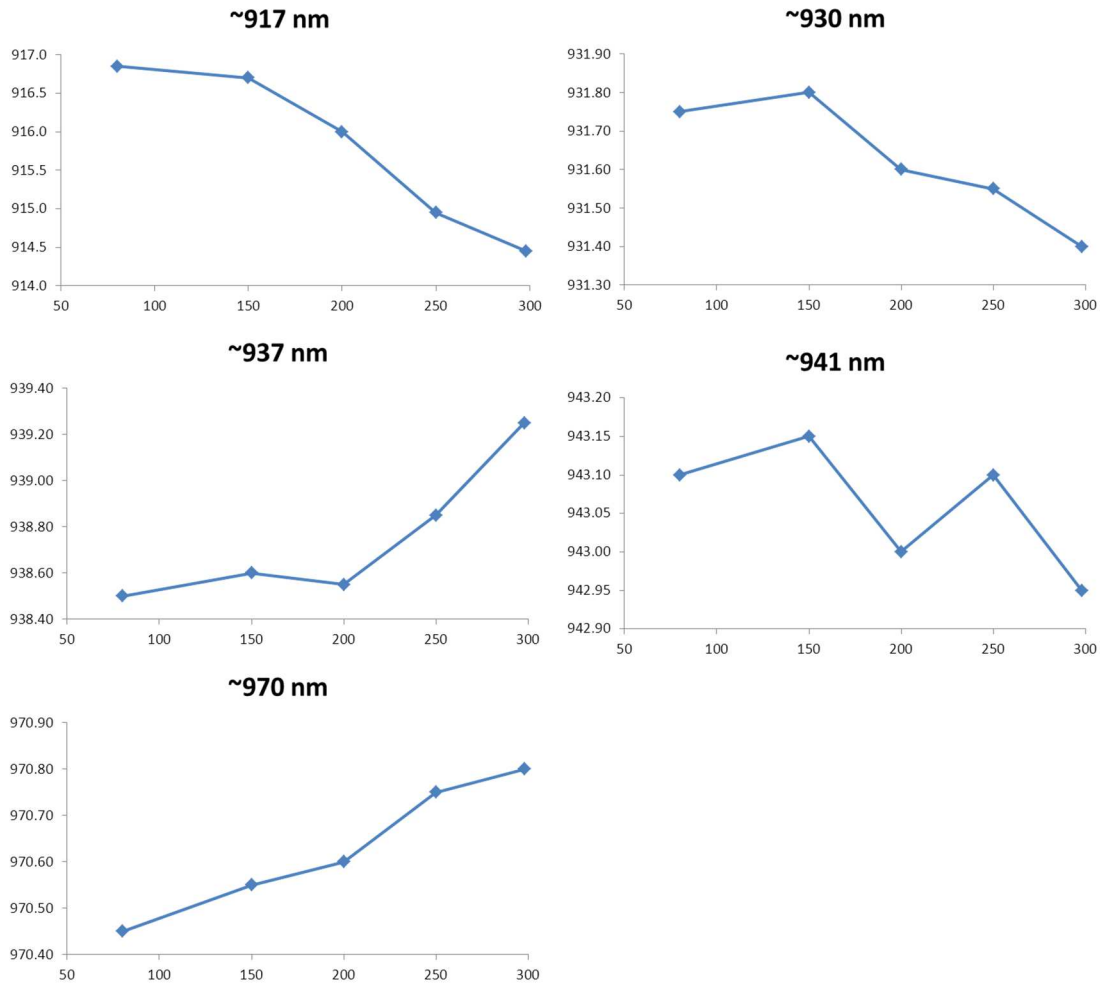

Figure 80. The shift in peak position of Yb:YAG for the chosen transitions as a function of temperature.

	(CZ) Yb:YAG Peak Center				
Temperature (K)	**~917 nm**	**~930 nm**	**~937 nm**	**~941 nm**	**~970 nm**
80	**916.85**	**931.75**	**938.50**	**943.10**	**970.45**
150	**916.70**	**931.80**	**938.60**	**943.15**	**970.55**
200	**916.00**	**931.60**	**938.55**	**943.00**	**970.60**
250	**914.95**	**931.55**	**938.85**	**943.10**	**970.75**
298	**914.45**	**931.40**	**939.25**	**942.95**	**970.80**

Table 11. A summary of the shift in peak position of Yb:YAG for the chosen transitions as a function of temperature.

A room temperature comparison of Yb-doped hosts

A normalized room temperature comparison of Yb:Lu_2O_3, Yb:LuAG and Yb:YAG is presented in Figure 81. It is interesting to note that the while the intensities of the cluster of absorption bands from 930 nm - 950 nm are similar for Yb:LuAG and Yb:YAG, they reverse intensity with respect to the zero-phonon band centered at 970 nm. They are very different for Yb:Lu_2O_3 as the zero-phonon band is about three times greater in intensity. It is also interesting that this cluster is spread over almost 49 nm for Yb:Lu_2O_3 and only about 29 nm for both Yb:YAG and Yb:LuAG. This agrees with results seen by Breiner, et al.[56], in their analysis of Yb:LuAG crystals grown by the vertical Bridgeman method. The pump band in Yb:Lu_2O_3 is shifted to longer wavelengths at about 978 nm and is not only closer to the 1030 emission but it also more closely coincides with the diode output at 980 nm.

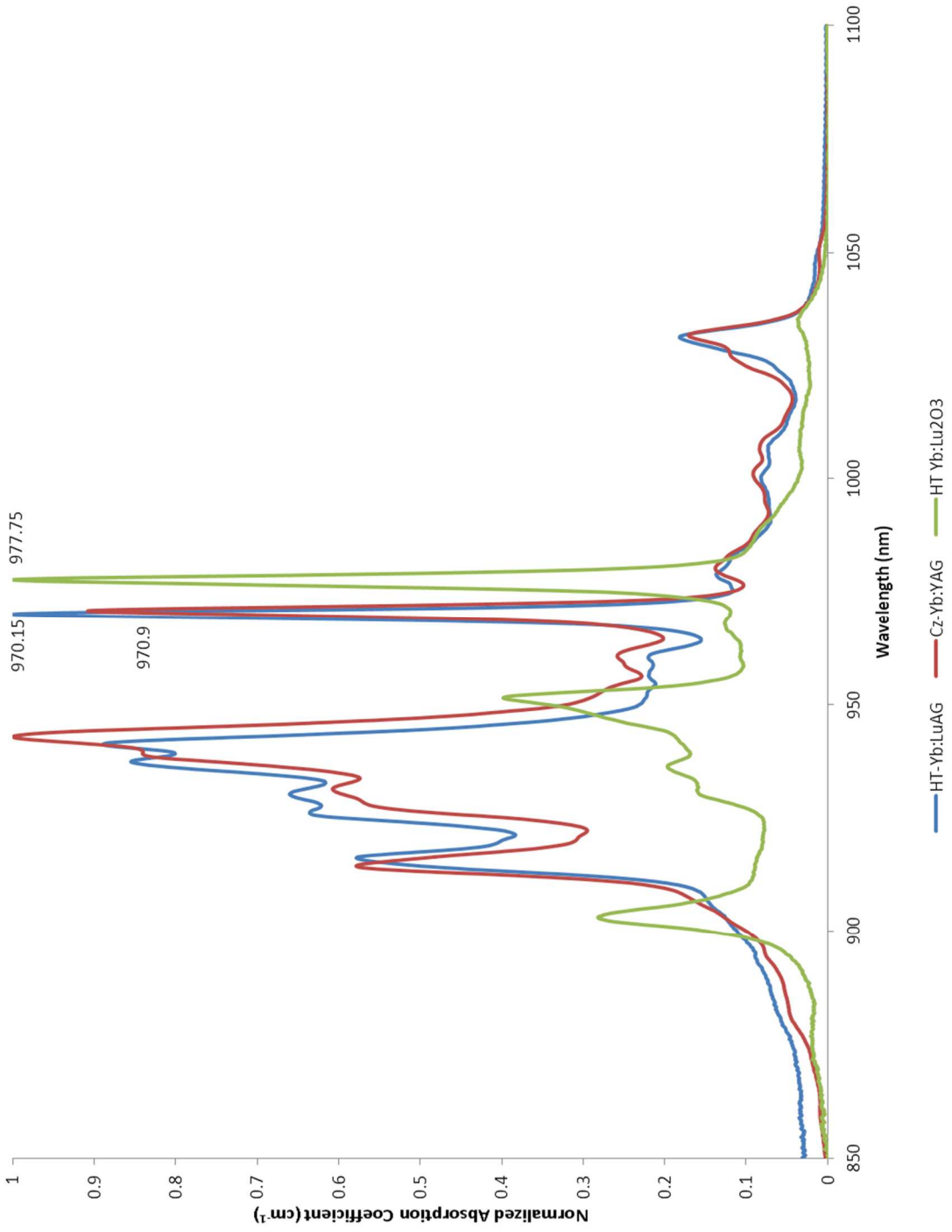

Figure 81. Normalized room temperature absorption coefficients comparing hydrothermal Yb:Lu_2O_3, Yb:LuAG, and Yb:YAG.

Other co-doped Yb- lutetia single crystals

With the many potential benefits and applications for Yb:Lu_2O_3 lasers, an entire chapter devoted to its study was warranted. The cryogenic spectra of an estimated 2% doped Yb:Lu_2O_3 was presented and compared to different hosts, including two garnets, YAG and LuAG, and to another sesquioxide, Y_2O_3. Other high-quality hydrothermal Yb- and Yb-codoped crystals have also been grown using the same techniques discussed here and in Chapter 2.

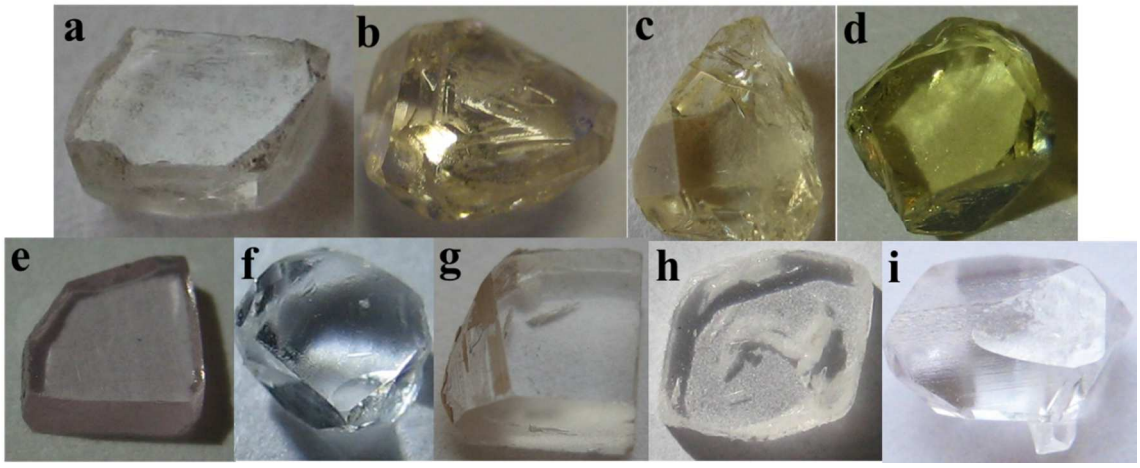

Figure 82. A sample collection of Yb-doped lutetia hydrothermally grown by SN, with or without co-dopants.

All of the crystals in Figure 82 are Yb-containing lutetia and some have a co-dopant. Sample **a** is a co-doped crystal that has an estimated doping of 1% Tm and 5% Yb and 2.45 mm in length. Samples **b**, **c**, and **d** are all co-doped lutetia that have estimated doping levels of 1% Ho and 5% Yb and are 5.29 mm, 6.28 mm 3.71 mm in length, respectively. In the second row, **e** is lutetia co-doped with both Yb and Er, estimated to be 4 % and 1.9 % respectively, and is 3.17 mm in length. Like the sample

scanned for the analyses in this chapter, **f** has an estimated doping of 2%. Crystals **g**, **h**, and **i** are all Yb:Lu_2O_3 with no co-dopant. Sample **g** is 5.29 mm in length with an estimated 3% Yb-doping. Sample **h** is 3.61 mm in length with an estimated doping of 10% and sample **i** is 6 mm in length with an estimated doping of 5%. The array of doped and co-doped crystals possible with the hydrothermal method, shown here, gives testament its power as a growth technique.

These crystals all appear to be of sufficient quality to give good spectroscopic data. The cryogenic absorption spectroscopy of these and other hydrothermal crystals is forthcoming and will be presented in future publications. While Yb-doped crystals are enticing, they are not, by any means, the only interesting doped-lutetia crystals worth studying. The cryogenic spectra of Nd:Lu_2O_3 and Dy:Lu_2O_3 and Dy:YAG are presented and analyzed in the next chapter.

CHAPTER SEVEN

GROWTH AND SPECTROSCOPY OF DOPED LUTETIA

In Chapters 1 and 6, the growth, improved properties, including heat management, higher density, favorable lattice parameter and cryogenic spectra of Yb-doped lutetia were presented and discussed. For these reasons, there is much interest in doped lutetia as an alternative to garnets. Presented in this chapter, for the first time to our knowledge, is the growth of hydrothermally grown lutetia crystals doped with other potential lasing ions, including Pr^{3+}, Ho^{3+}, and Eu^{3+}, along with the cryogenic absorption spectra of both Nd- and Dy-doped lutetia.

Nd-doped lutetia

The room-temperature absorption spectra of Nd:LuAG was presented and discussed in Chapter 3 and compared to Nd:YAG. Here we present the growth and cryogenic set of absorption spectra of Nd:Lu_2O_3 and compare its room temperature spectrum with Nd-doped LuAG, YAG and Y_2O_3.

Cryogenic absorption spectra of $Nd:Lu_2O_3$

The $Nd:Lu_2O_3$ crystals in Figure 83 are both about 3.5 mm in length and were grown by the SN method discussed in Chapter 1. Their doping percentages were estimated by EDX to be about 1.2%. The crystal on the left gave the cryogenic absorption spectra in Figure 84 from 300 nm to 1000 nm. The regions between 560 nm – 640 nm, 710 nm – 860 nm, and 850 nm – 950 nm are detailed in Figures 85, 86, and 87. The maximum absorption coefficients for the five chosen transitions from the $^4I_{9/2}$ ground state to $^4G_{5/2}$ (near 600 nm) , $^4F_{7/2} + {}^4S_{3/2}$ (near 745 nm), $^4F_{5/2}$ (near 808 nm), and $^4F_{3/2}$ (the peaks near 868 nm and 880 nm) are graphed as a function of temperature in Figure 88 for 80K, 150K, 200K, 250K, and 298K and are summarized in Table 12.

Analysis of peak intensities for $Nd:Lu_2O_3$

In the discussion in the last chapter regarding $Yb:Lu_2O_3$ it was noted that as the temperture is decreased, the absorption peaks are expected to increase in intensity and become narrower. It appears that the peaks for $Nd:Lu_2O_3$ do not follow this trend; indeed, even at higher tempertures the opposite appears to be true. The exception is the peak near

Figure 83. The Nd-doping percentage, estimated by EDX, is 1.2%. These crystals grown by SN are about 3.5 mm in length.

880 nm which seems to follow the increased intensity and narrowing trend as was seen with Yb:Lu_2O_3. Also similar to Yb:Lu_2O_3 is the apparent anomaly in the spectra for the two lowest temperatures, and following the same reasoning presented in Chapter 6 regarding these anomalies, the calculated actual intensities are given in parentheses where warranted in Figure 88 and summarized in Table 12.

Analysis of Peak positions for Nd:Lu_2O_3

Inspection of the graphs of peak position shifts (Figure 89) as a function of temperature and summary (Table 13) reveals no discernible pattern and very little shifting in the position of maximum intensity for the peaks chosen except for the peak near 868 nm which is blue-shifted by 2.5 nm on going from room-temperature to 80K. The next greatest shift is seen for the peak near 745 nm that is blue-shifted shifted by only 0.3 nm.

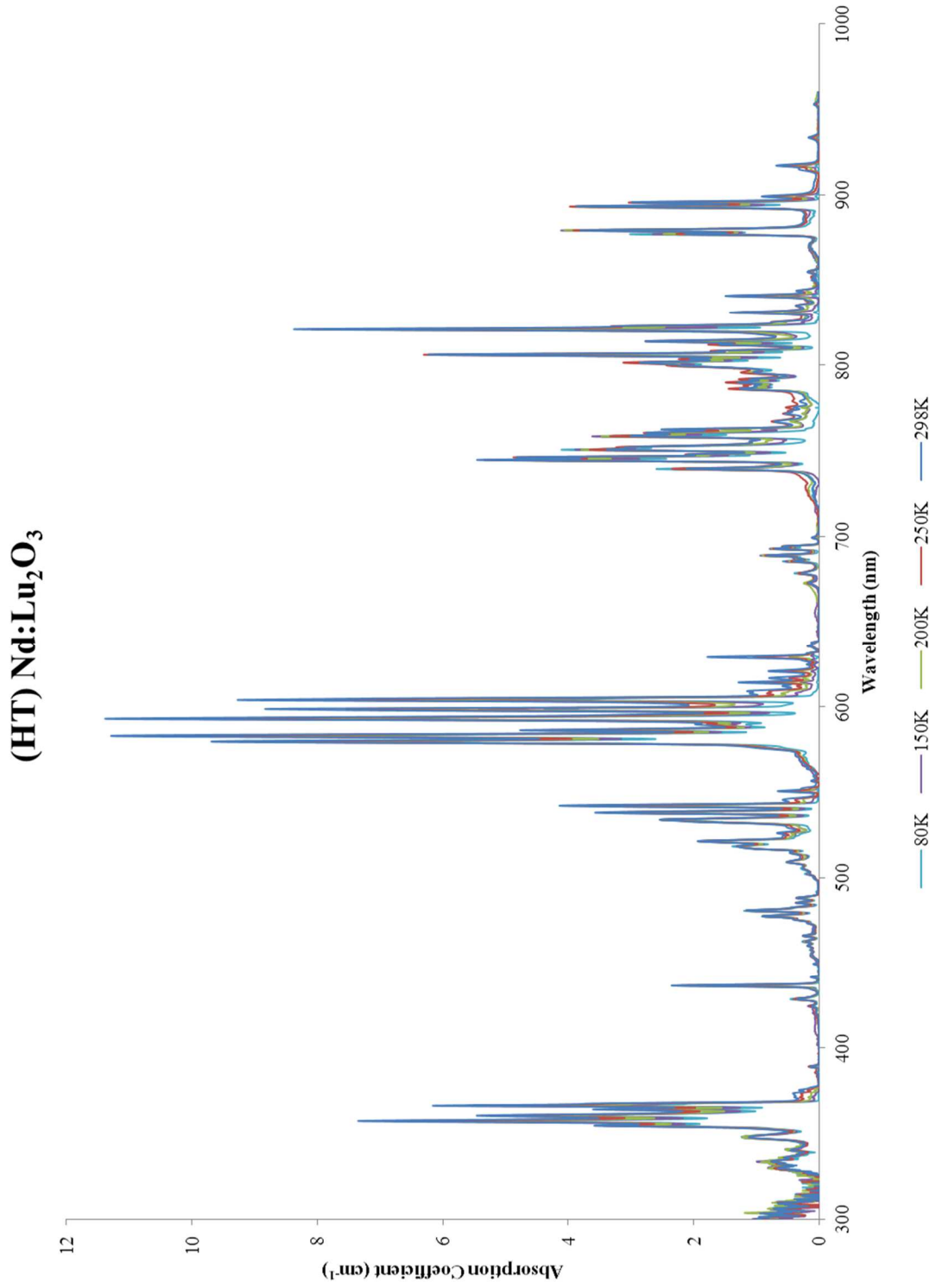

Figure 84. The cryogenic absorption coefficient of Nd:Lu_2O_3 between 300 nm and 1000 nm for 298K, 250K, 200K, 150K, and 80K.

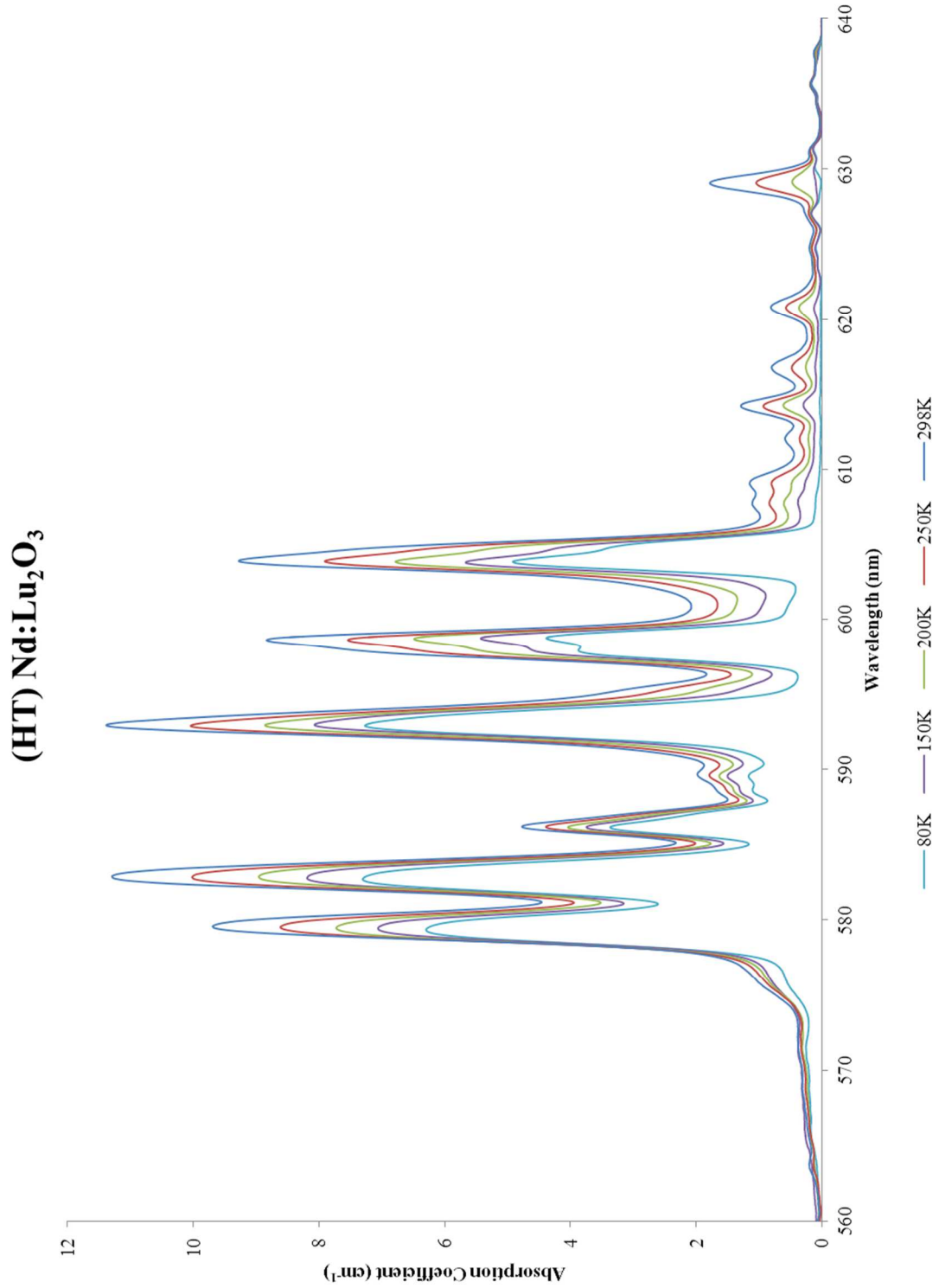

Figure 85. The detailed region of Nd:Lu_2O_3 between 560 nm and 640 nm.

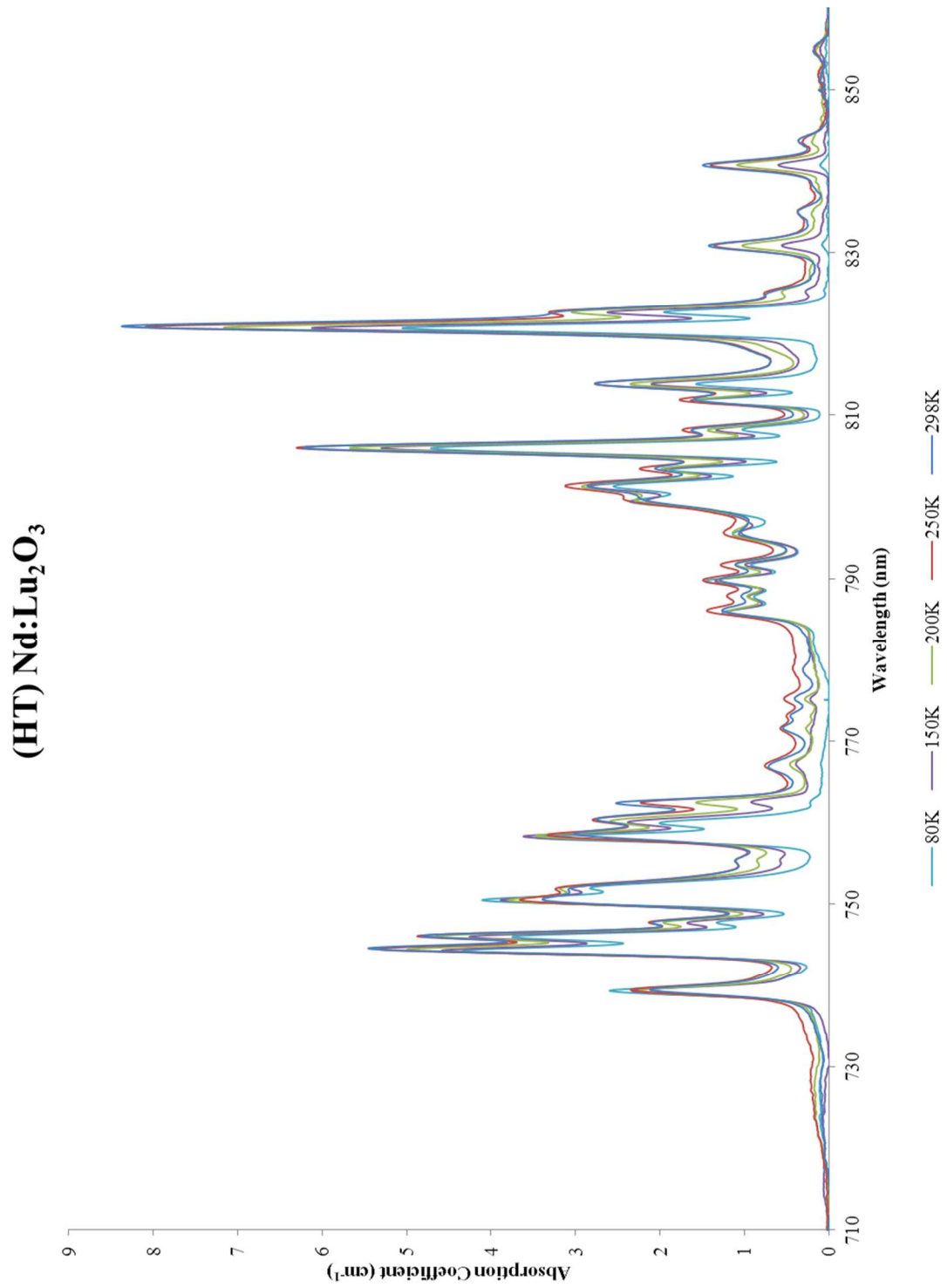

Figure 86. The detailed region of Nd:Lu_2O_3 between 710 nm and 860 nm.

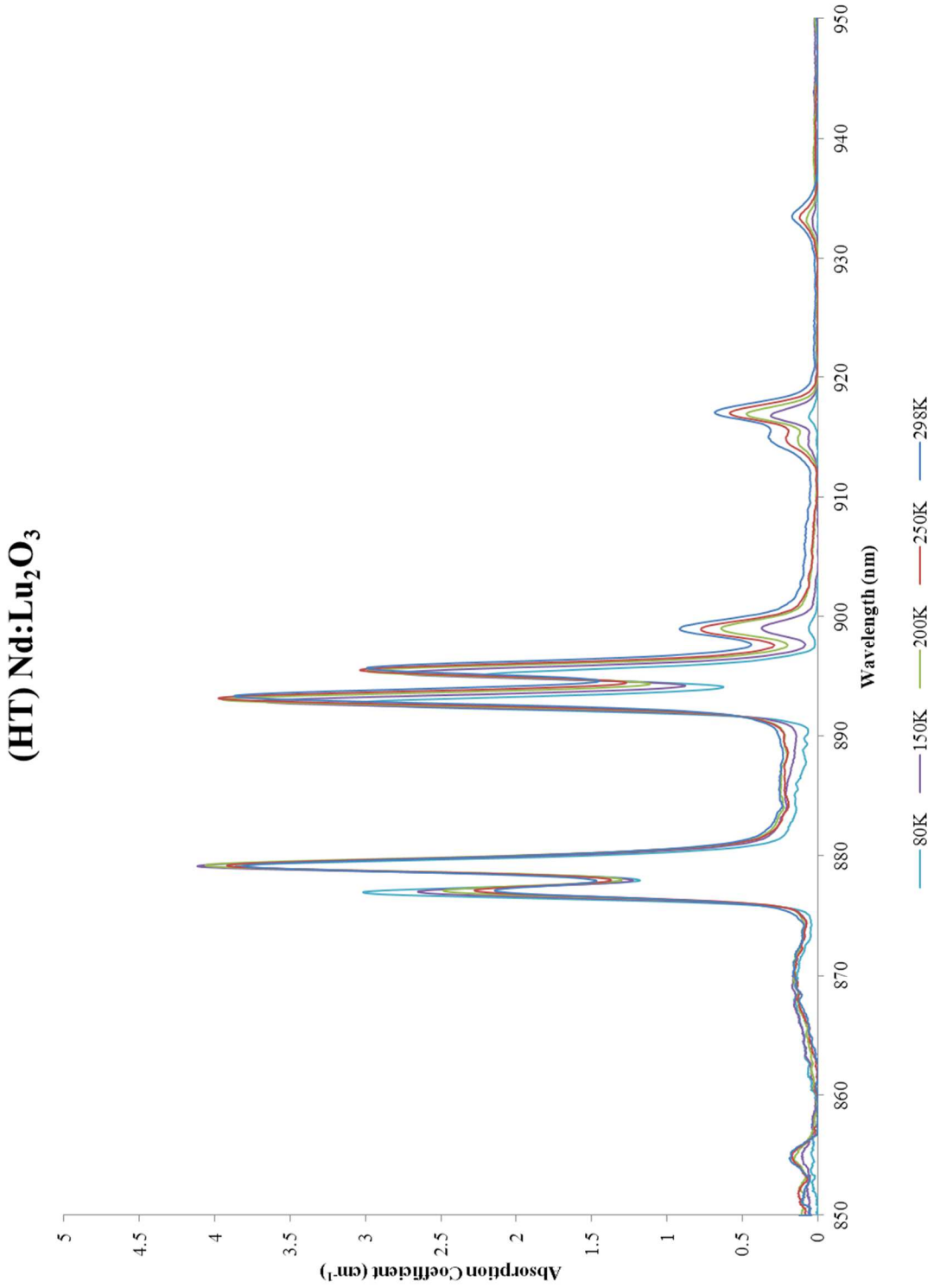

Figure 87. The detailed region of $Nd:Lu_2O_3$ between 850 nm and 950 nm.

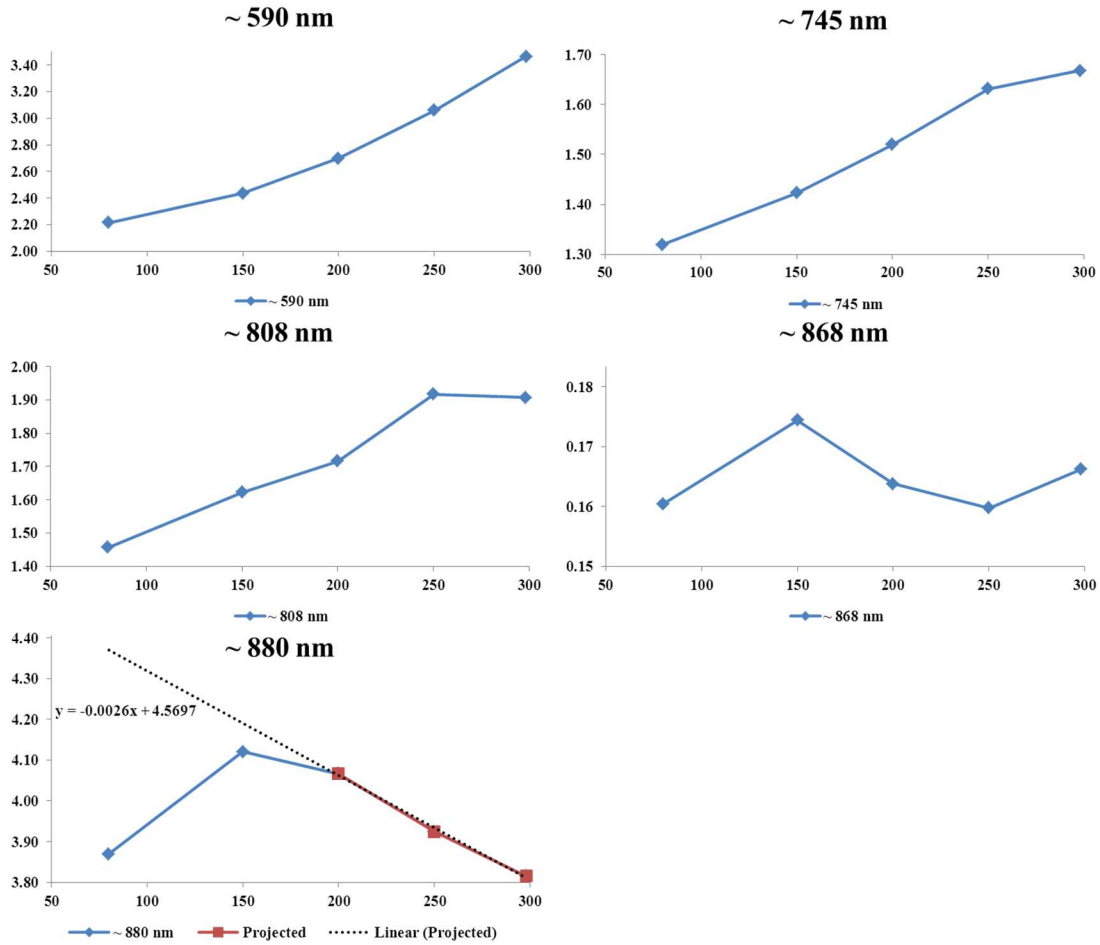

Figure 88. The absorption coefficient of Nd:Lu_2O_3 for the chosen transitions as a function of temperature.

	Nd:Lu_2O_3 Absorption Coefficient (cm^{-1})				
	$^4I_{9/2} \rightarrow {}^4G_{5/2}$	$^4I_{9/2} \rightarrow {}^4F_{7/2} + {}^4S_{3/2}$	$^4I_{9/2} \rightarrow {}^4F_{5/2}$	$^4I_{9/2} \rightarrow {}^4F_{3/2}$	$^4I_{9/2} \rightarrow {}^4F_{3/2}$
Temperature (K)	**~ 590 nm**	**~ 745 nm**	**~ 808 nm**	**~ 868 nm**	**~ 880 nm**
80	**2.215**	**1.319**	**1.457**	**0.159**	**3.864 (4.362)**
150	**2.435**	**1.423**	**1.623**	**0.172**	**4.115 (4.180)**
200	**2.698**	**1.519**	**1.716**	**0.162**	**4.062**
250	**3.060**	**1.632**	**1.917**	**0.159**	**3.919**
298	**3.464**	**1.668**	**1.907**	**0.165**	**3.810**

Table 12. A summary of the absorption coefficient of Nd:Lu_2O_3 for the chosen transitions as a function of temperature.

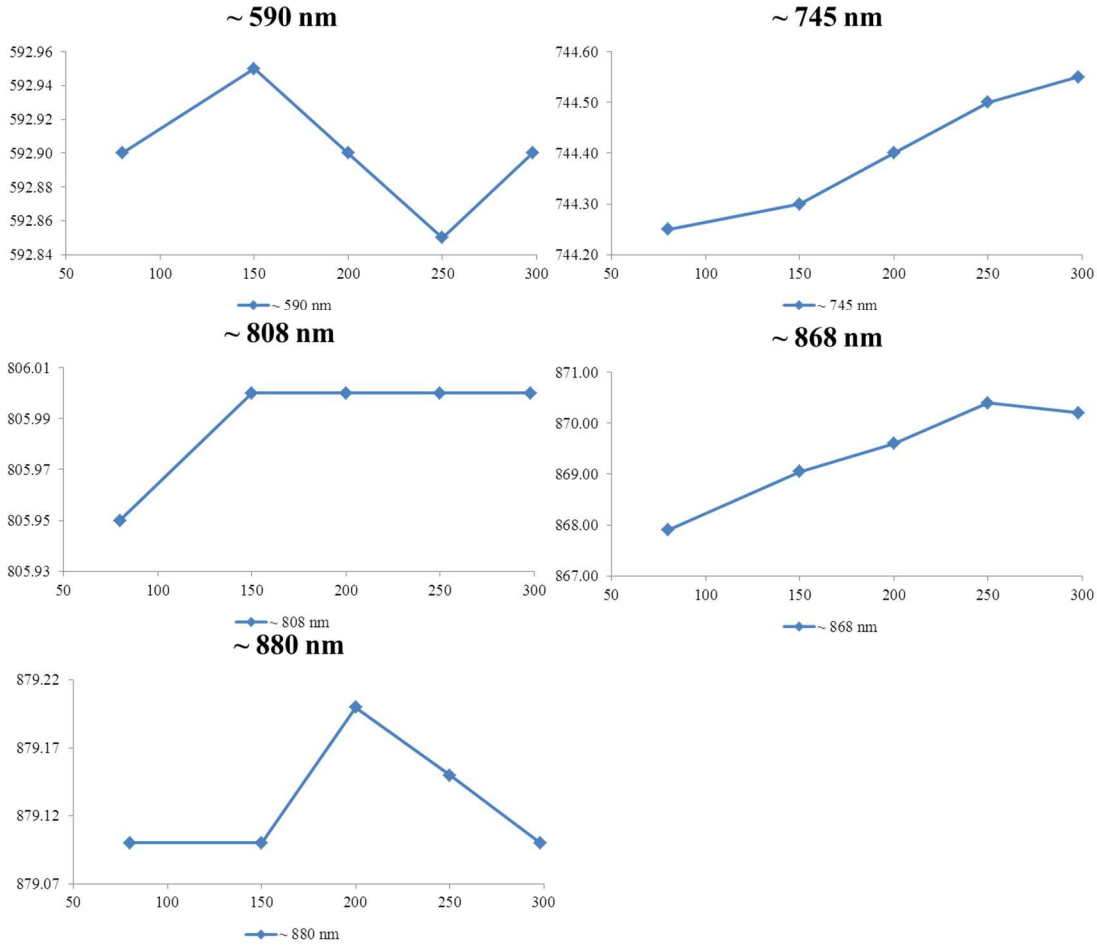

Figure 89. The shift in peak position of Nd:Lu_2O_3 for the chosen transitions as a function of temperature.

	Nd:Lu_2O_3 Peak Position (nm)				
Temperature (K)	**~ 590 nm**	**~ 745 nm**	**~ 808 nm**	**~ 868 nm**	**~ 880 nm**
80	**592.90**	**744.25**	**805.95**	**867.90**	**879.10**
150	**592.95**	**744.30**	**806.00**	**869.05**	**879.10**
200	**592.90**	**744.40**	**806.00**	**869.60**	**879.20**
250	**592.85**	**744.50**	**806.00**	**870.40**	**879.15**
298	**592.90**	**744.55**	**806.00**	**870.20**	**879.10**

Table 13. A summary of the shift in peak position of Nd:Lu_2O_3 for the chosen transitions as a function of temperature.

A room-temperature comparison of Nd-doped Lu_2O_3 and LuAG

In Chapter 3, a normalized, room-temperature comparison of the Nd-doped garnets Nd:LuAG and Nd:YAG (Figure 26) was presented and displayed, as expected, very little differences in the two spectra. In this chapter, the same type of comparison is given for the normalized, room-temperature spectra of the Nd-doped lutetium-containing hosts, Lu_2O_3 and LuAG (Figure 90). While the grouping of peaks around 593 nm for both Lu_2O_3 and LuAG contain the most intense line of the spectrum, the overall absorbance for all peaks in that group is greater for Lu_2O_3 compared to the peaks around 745 nm. This case is reversed for LuAG in that the total absorbance around 745 nm is greater than at 593 nm. The total absorbance around 808 nm, though, is about the same for both. It is interesting to note that while the pump band for Nd:LuAG is around 808.5 nm, it is shifted by almost 2.5 nm for Nd:Lu_2O_3 to 806 nm.

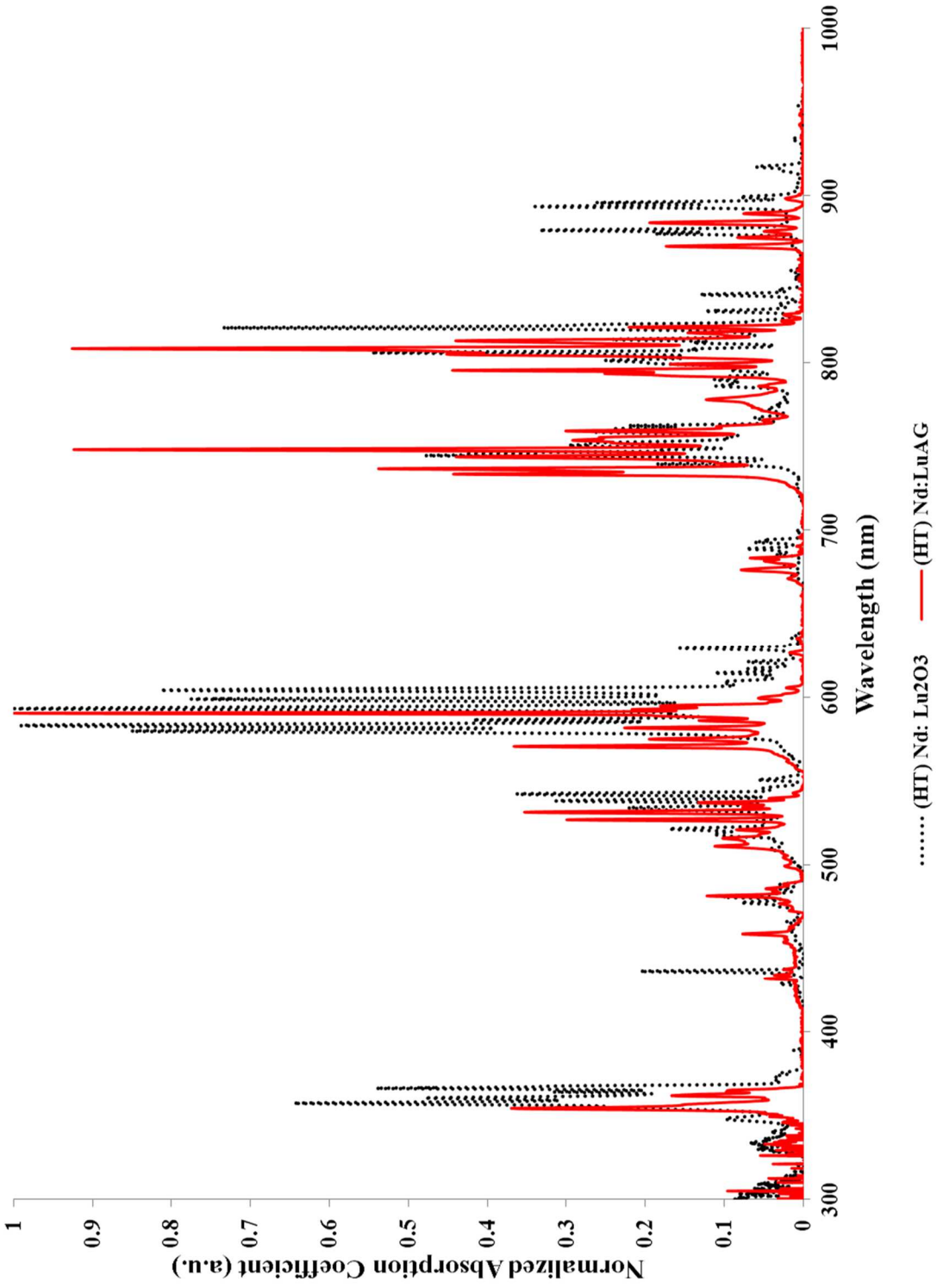

Figure 90. A room-temperature comparison of the normalized absorption coefficients of Nd-doped hosts, Lu_2O_3 and LuAG.

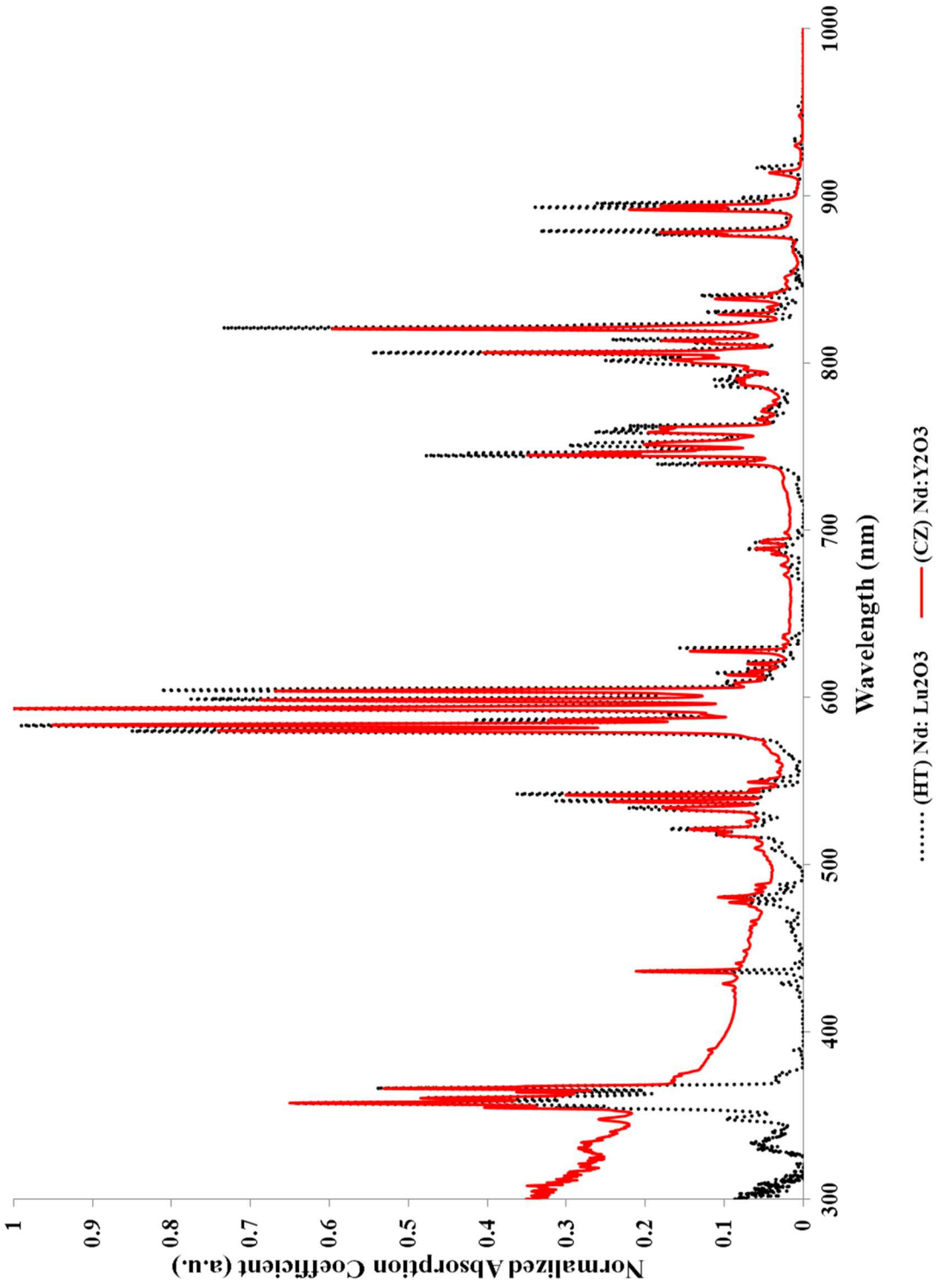

Figure 91. A room-temperature comparison of the normalized absorption coefficients of Nd-doped hosts, Lu_2O_3 and Y_2O_3.

A room-temperature comparison of Nd-doped Lu_2O_3 and Y_2O_3

The comparison of Nd-doped Lu_2O_3 and Y_2O_3 sesquioxides shows very similar room-temperature spectra (Figure 91 and Table 14) as the chosen peak positions are nearly identical (Table 15), Lu_2O_3 being blue-shifted by less than 0.3 nm for the peaks near 590 nm and 745 nm. The other peaks for Lu_2O_3 near 808 nm, 868 nm, and 880 nm are all red-shifted by 0.15 nm, 1.6 nm, and 0.75 nm respectively. Another difference can be seen in the absorptions above about 750 nm in which doped lutetia has greater intensities overall.

	Relative Intensities for Chosen Transitions				
	$^4I_{9/2} \rightarrow {}^4G_{5/2}$	$^4I_{9/2} \rightarrow {}^4F_{7/2} + {}^4S_{3/2}$	$^4I_{9/2} \rightarrow {}^4F_{5/2}$	$^4I_{9/2} \rightarrow {}^4F_{3/2}$	$^4I_{9/2} \rightarrow {}^4F_{3/2}$
Host	**~ 590 nm**	**~ 745 nm**	**~ 808 nm**	**~ 868 nm**	**~ 880 nm**
(HT) Nd:Lu_2O_3	1.000	0.479	0.547	0.014	0.335
(CZ) Nd:Y_2O_3	1.000	0.350	0.405	0.013	0.182
(HT) Nd:LuAG	1.000	0.924	0.926	0.174	0.195
(HT) Nd:YAG	0.989	0.902	1.000	0.238	0.223

Table 14. Assignments for chosen transitions for Nd-doped hosts. Absorption coefficient intensities have been normalized for comparison.

	Peak Position Comparison				
Host	**~ 590 nm**	**~ 745 nm**	**~ 808 nm**	**~ 868 nm**	**~ 880 nm**
(HT) Nd:Lu_2O_3	592.90	744.55	806.00	870.20	879.10
(CZ) Nd:Y_2O_3	593.00	744.85	806.15	868.60	878.35
(HT) Nd:LuAG	590.20	748.10	808.45	869.60	883.65
(HT) Nd:YAG	590.05	748.10	808.35	868.80	883.85

Table 15. A comparison of the peak positions for Nd-doped hosts, Lu_2O_3, Y_2O_3, LuAG, and YAG.

As discussed earlier, because the f-orbitals are protected, the particular environment of the ion typically has little effect on the absorption spectrum and as a result spectra from different hosts can be very similar. This is illustrated in Table 15, where the peak positions of the sesquioxides mirror one another and are fairly close in energy to those of the garnets which also mirror one another.

The absorption spectrum of Nd^{3+} in different hosts is quite a bit more complex than for the Yb^{3+}-doped crystals in the last chapter. Even more complex than Nd-doping is Dy-doping presented in the next section.

Dy-doping

Unlike Nd doping, crystals doped with dysprosium are much less common. The complex energy level structure gives Dy^{3+} a very detailed absorption spectrum.[89-93] Lasers doped with dysprosium are of interest for a few reasons. Their yellow emission near 583 nm, a result of the $^4F_{9/2} \rightarrow {}^6H_{13/2}$ transition, is an uncommon region of the spectrum for direct lasing emission.[94] Thanks in part to the recent development of newer pump sources, GaN for example, it has become easier to acces its pump band near 447 nm, boosting the interest in their development.

In Chapter 3, a possible use for a cladding of Sm:LuAG was suggested for the supression of ASE for the absorption of the strong emission of Nd-doped YAG or LuAG around 1064 nm. Another possible use for Dy-doped claddings is an analogous application for ASE supression of Yb-doped lasers between 976 nm and 1120 nm. Spontaneous emission occuring in a Yb-doped laser gain medium can significantly decrease the available pump power. A Dy-doped cladding might potentially reduce these competing processes by absorbing the photons that enter the cladding. Despite these potentially signficant properties the detailed spectroscopy of dysprosium has received very little study. Its cryogenic spectroscopy has been almost non-existent. Presented in

this section, for the first time to our knowledge, is cryogenic absorption spectroscopy of hydrothermally grown Dy-doped Lu_2O_3 (Figure 93) and -YAG (Figure 101).

Dy:Lu_2O_3

The crystal in Figure 92 was grown hydrothermally by the method discussed in Chapter 2 and is estimated by EDX to be approximately 5% Dy-doped. The region of interest for ASE supression discussed in the previous section is shown in red on the

Figure 92. This 5% Dy:Lu_2O_3 crystal was hydrothermally grown by SN and after manually polishing is 3.86 mm in length.

cryogenic set of absorption spectra including 298K, 250K, 200K, 150K, and 80K in Figure 93. The regions from 300 nm – 500 nm, 700 nm – 1000 nm, 1100 nm – 1450 nm, and 1550 nm – 1800 nm are detailed in Figures 94, 95, 96, and 97. The chosen peaks are a result of the transitions assigned in Table 16.

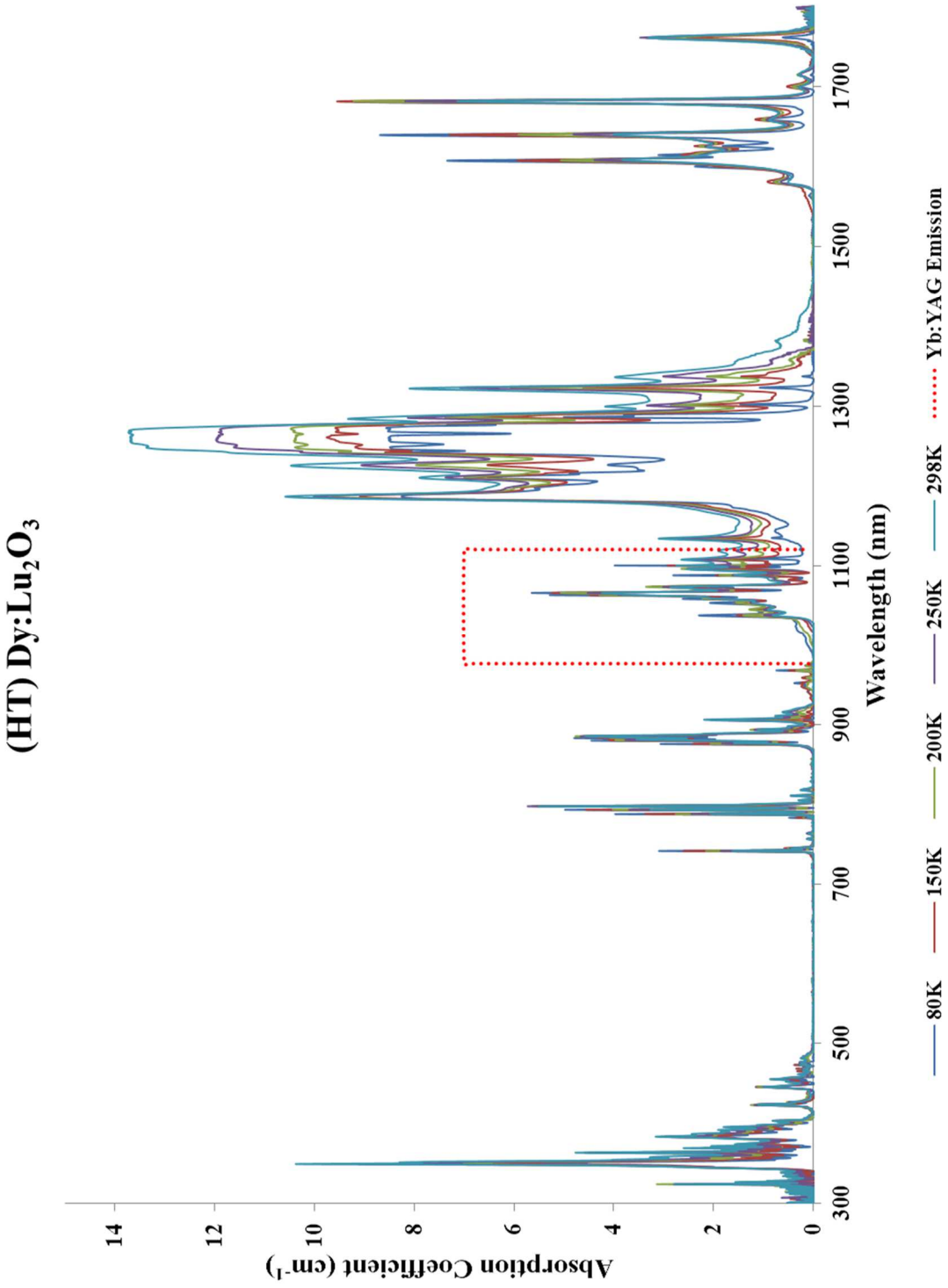

Figure 93. The cryogenic absorption coefficient of Dy:Lu_2O_3 between 300 nm and 1800 nm for 298K, 250K, 200K, 150K, and 80K.

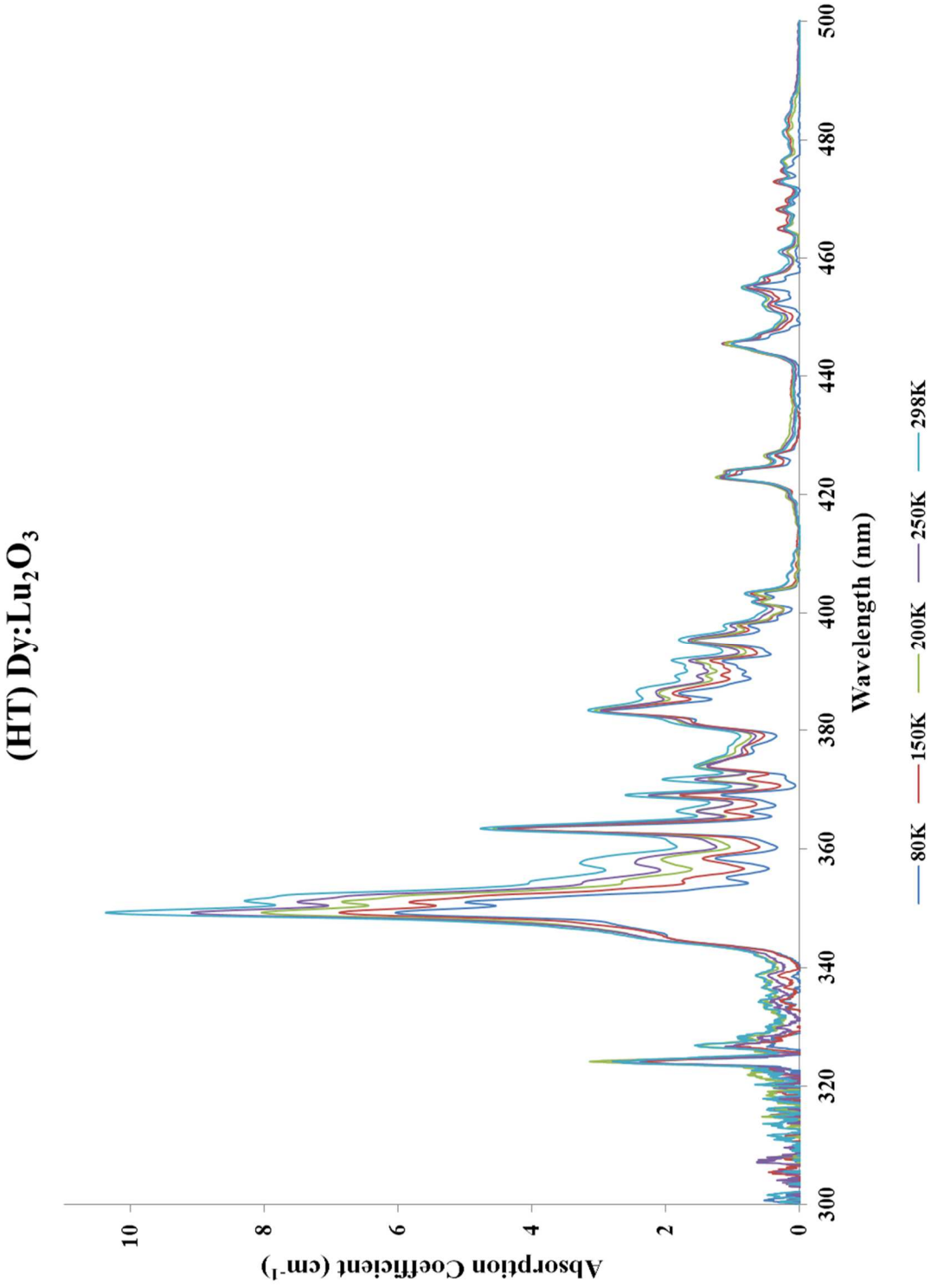

Figure 94. The detailed region of Dy:Lu_2O_3 between 300 nm and 500 nm.

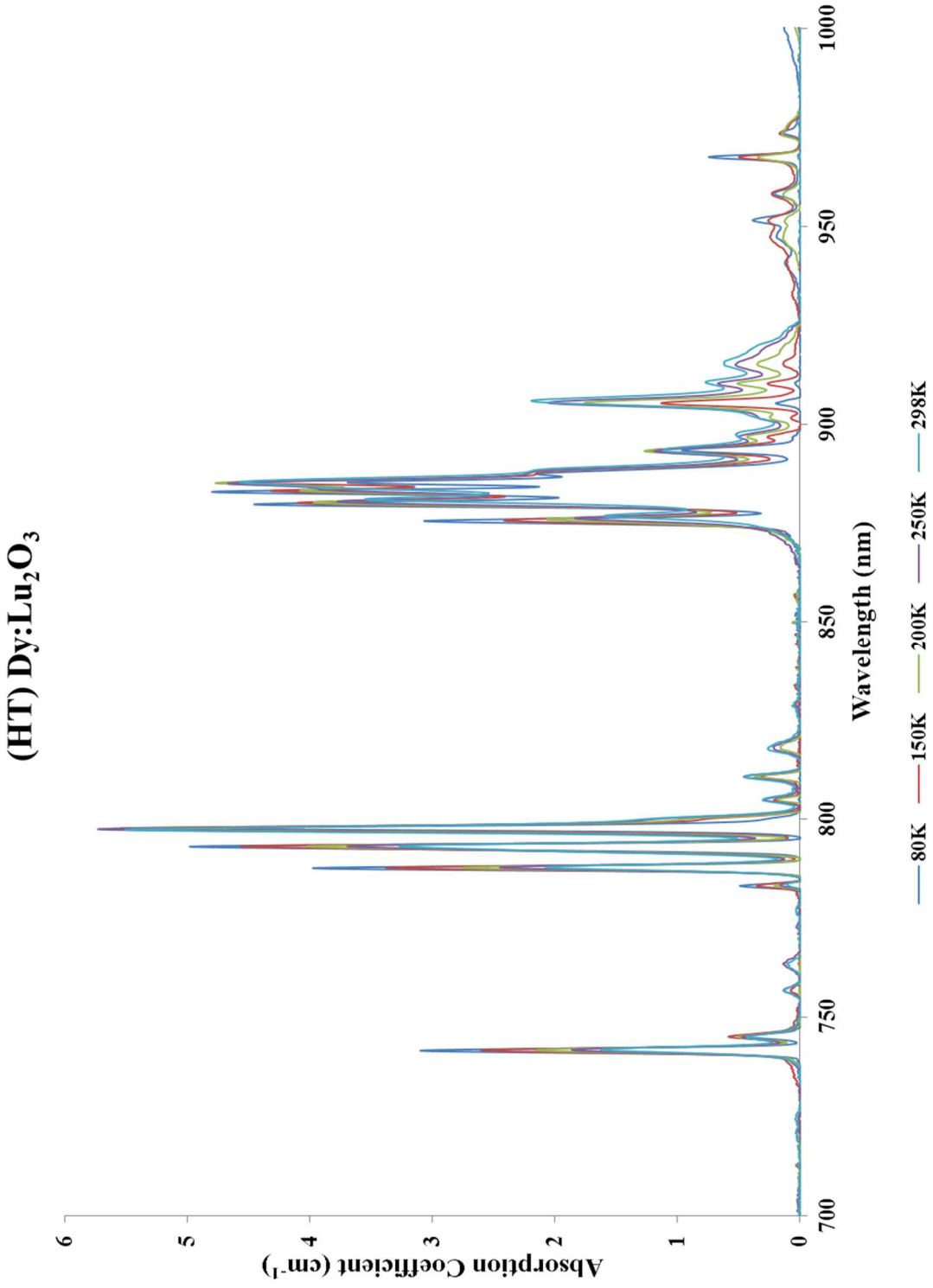

Figure 95. The detailed region of Dy:Lu_2O_3 between 700 nm and 1000 nm.

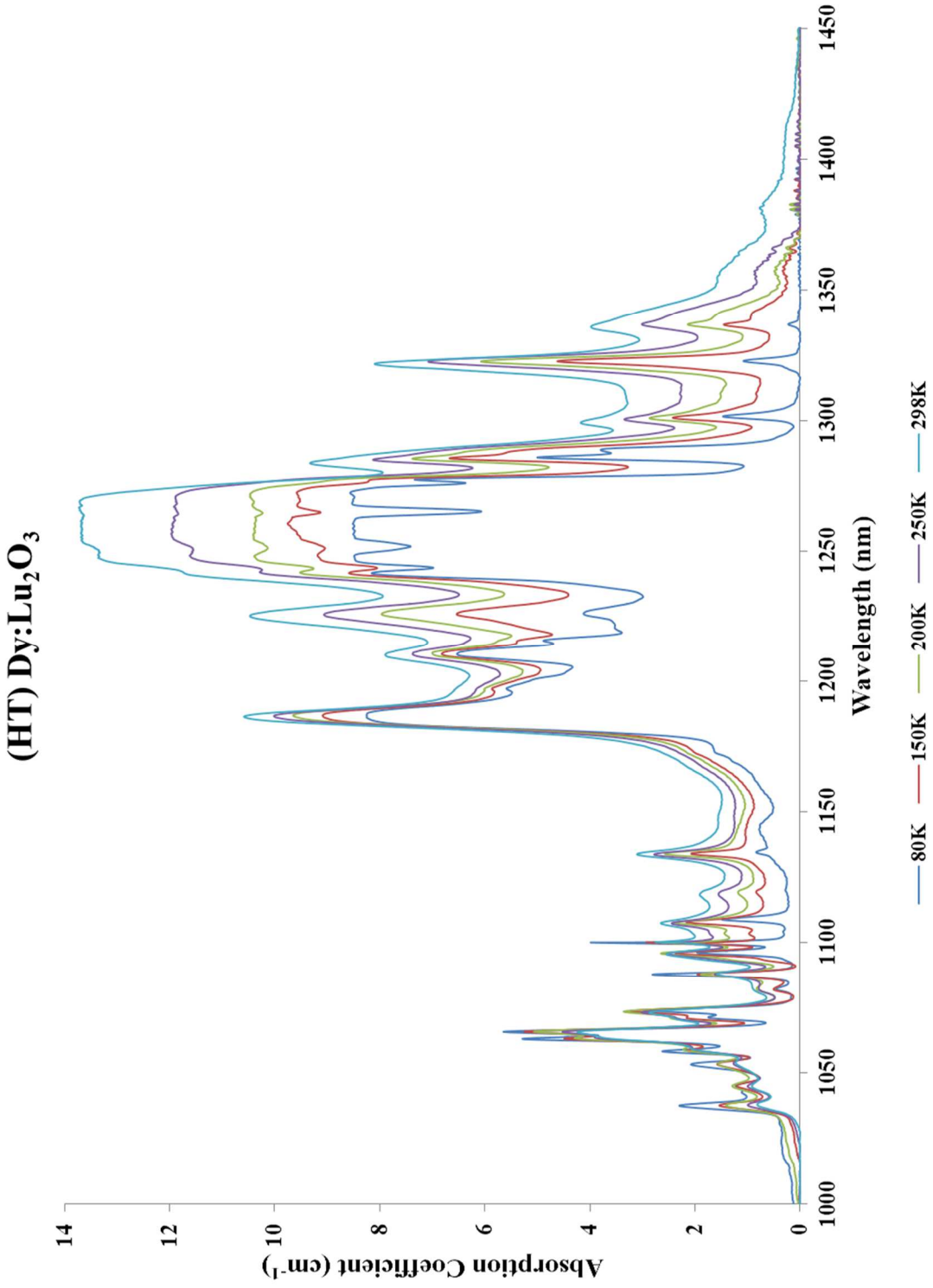

Figure 96. The detailed region of Dy:Lu_2O_3 between 1000 nm and 1450 nm.

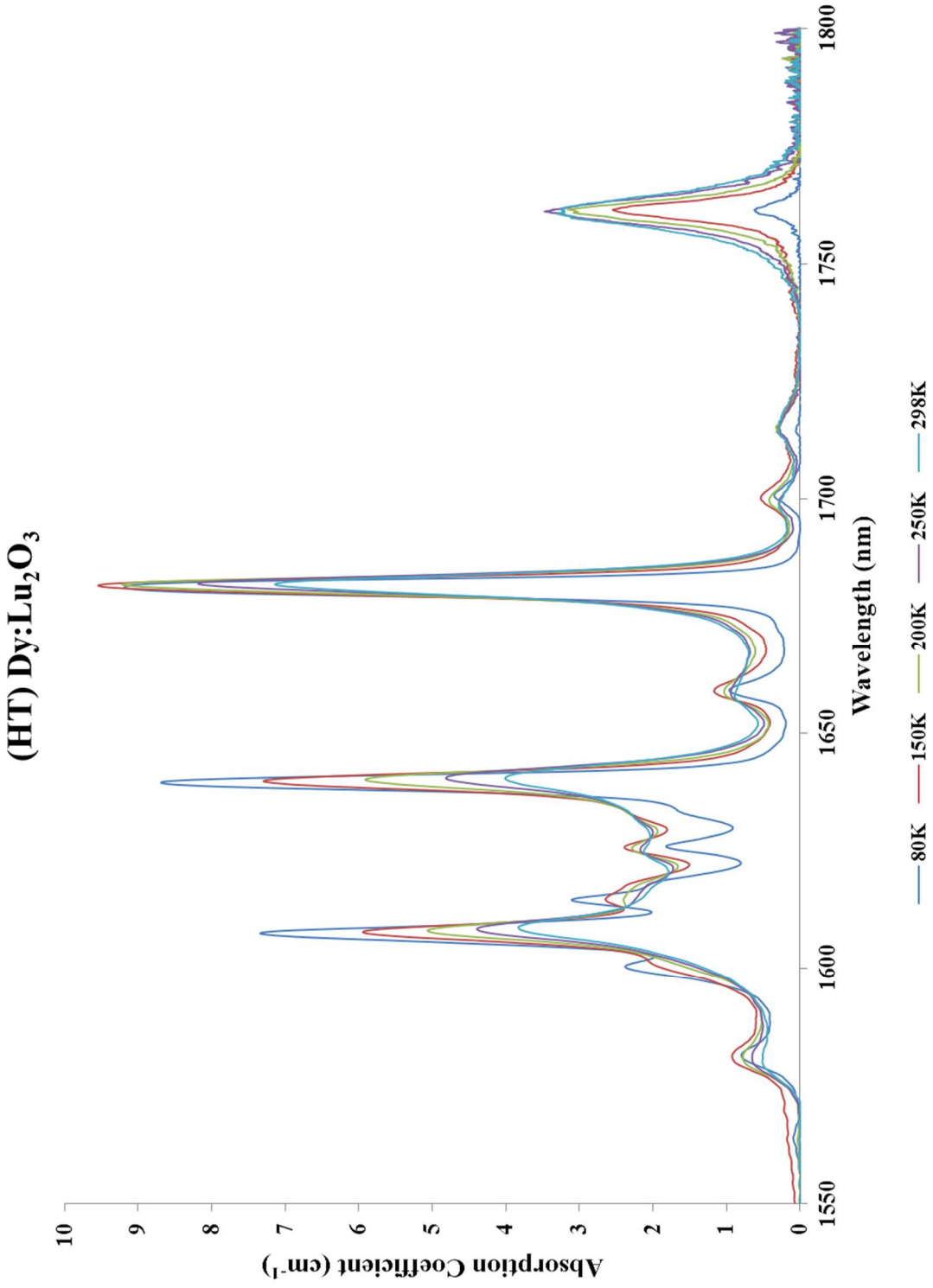

Figure 97. The detailed region of Dy:Lu_2O_3 between 1550 nm and 1800 nm.

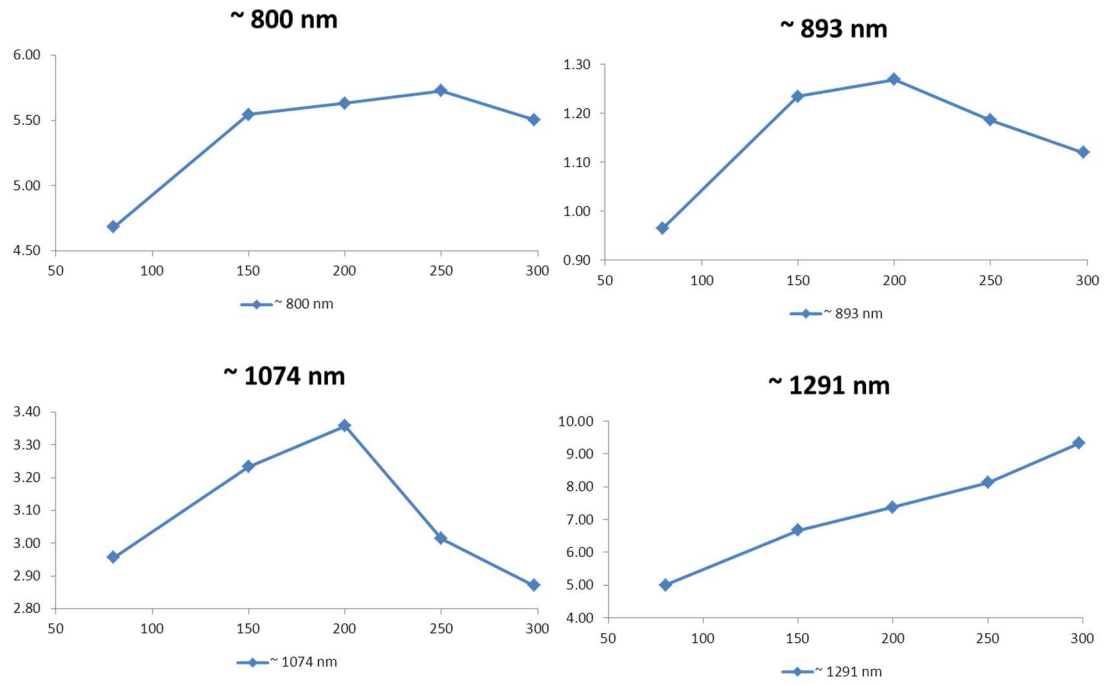

Figure 98. The absorption coefficient of Dy:Lu_2O_3 for the chosen transitions as a function of temperature.

	Dy:Lu_2O_3 Absorption Coefficient (cm^{-1})			
	$^6H_{15/2} \rightarrow {}^6F_{5/2}$	$^6H_{15/2} \rightarrow {}^6F_{7/2}$	$^6H_{15/2} \rightarrow {}^6F_{9/2} + {}^6H_{7/2}$	$^6H_{15/2} \rightarrow {}^6F_{11/2} + {}^6H_{9/2}$
Temperature (K)	**~ 800 nm**	**~ 893 nm**	**~ 1074 nm**	**~ 1291 nm**
80	**4.684**	**0.965**	**2.957**	**5.004**
150	**5.547**	**1.234**	**3.233**	**6.674**
200	**5.633**	**1.269**	**3.358**	**7.381**
250	**5.729**	**1.186**	**3.014**	**8.131**
298	**5.505**	**1.120**	**2.871**	**9.329**

Table 16. A summary of the absorption coefficient of Dy:Lu_2O_3 for the chosen transitions as a function of temperature.

Analysis of Peak Intensities for Dy:Lu_2O_3

In comparing the intensities of the absorption coefficients as a function of temperature (Figure 98 and summarized in Table 16), for the peaks listed due to transitions from the ground state, $^6H_{15/2,}$ to $^6F_{5/2}$ (near 800 nm), $^6F_{7/2}$ (near 893 nm), $^6F_{9/2}$ + $^6H_{7/2}$ (near 1074 nm), and $^6F_{11/2}$ + $^6H_{9/2}$ (near 1291 nm) we see the opposite trend to what would be expected, a general decrease in the intensity of each of the peaks chosen at lower temperatures. The exception to this may be for the peak near 893 nm which may follow the anomaly seen for the sharp intense peak for Yb:Lu_2O_3. If this is the case, we would expect the two lowest temperatures to have even greater intensities than the other, higher temperatures, but there is not enough evidence of this being the case, especially in light of the trending of the other peaks, which does not support this belief.

Analysis of Peak positions for Dy:Lu_2O_3

Lower temperatures would be expected to contract the lattice, increasing the energy level splitting, leading to a general blue-shifting of peaks between room-temperature and 80K, but interestingly, in keeping with the opposite trending seen in Dy-doping thus far, a smooth red-shifting can be seen in each of the chosen peaks, Figure 99 and summarized in Table 17. The peak at 893 nm for the 298K spectrum is the only point that does not fit with the smooth shifting mentioned above and the cause of this behavior is unclear, but may also be instrument-related. Nevertheless, the degree of shifting is very minimal at about 0.3 nm for the peaks near 800 nm and 893 nm. A shift of triple that can be seen for the 1074 nm peak, at 0.9 nm, and over 2 nm for the peak at 1291 nm.

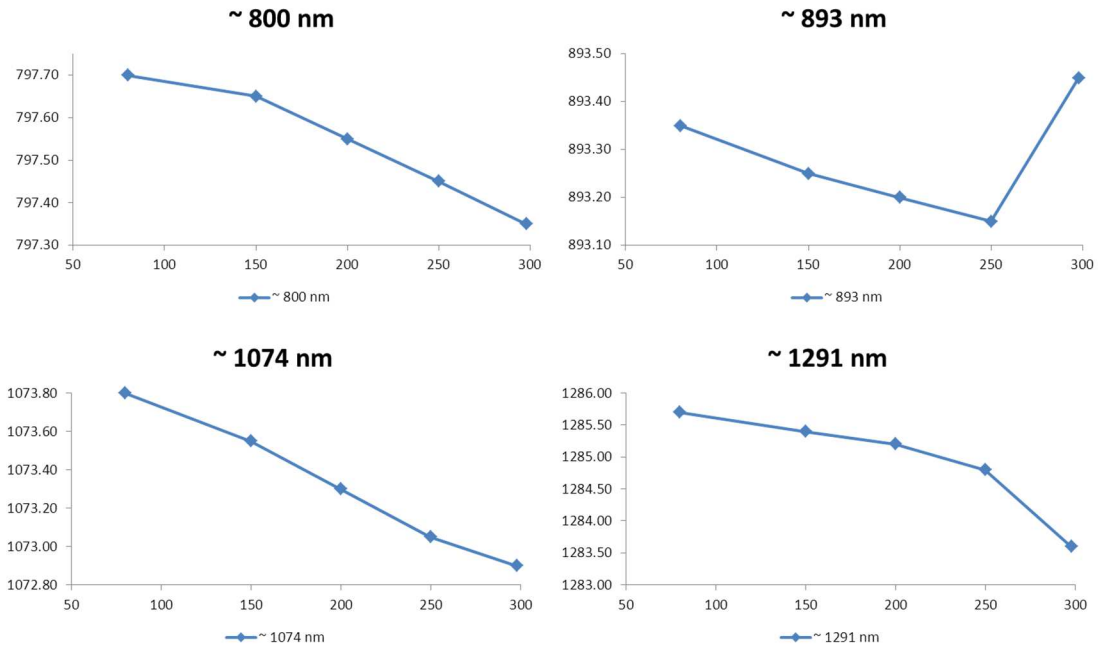

Figure 99. The shift in peak positions of Dy:Lu_2O_3 for the chosen transitions as a function of temperature.

	Dy:Lu_2O_3 Peak Position (nm)			
Temperature (K)	~ 800 nm	~ 893 nm	~ 1074 nm	~ 1291 nm
80	797.70	893.35	1073.80	1285.70
150	797.65	893.25	1073.55	1285.40
200	797.55	893.20	1073.30	1285.20
250	797.45	893.15	1073.05	1284.80
298	797.35	893.45	1072.90	1283.60

Table 17. A summary of the shift in peak positions of Dy:Lu_2O_3 for the chosen transitions as a function of temperature.

Dy:YAG

The crystal of Dy:YAG in Figure 100 was grown hydrothermally and is estimated by EDX to be 5% Dy-doping. Its cryogenic set of absorption spectra, including 298K, 250K, 200K, 150K, and 80K are presented for the first time to our knowledge in Figure 101 with the same region of interest for ASE supression for Yb-doped lasers highlighted around 1078 nm. The regions between 300 nm – 500 nm, 700 nm – 1000 nm, 1100 nm – 1450 nm, and 1550 nm – 1800 nm are detailed in Figures 102, 103, 104, and 105.

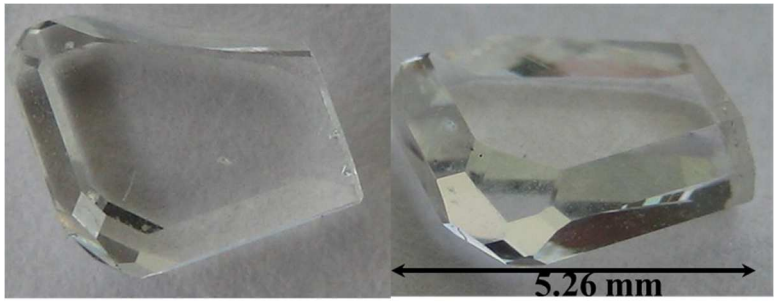

Figure 100. The doping percentage of this hydrothermal Dy:YAG crystal grown by SN is estimated to be 5%. It is as-grown and needed no additional preparation.

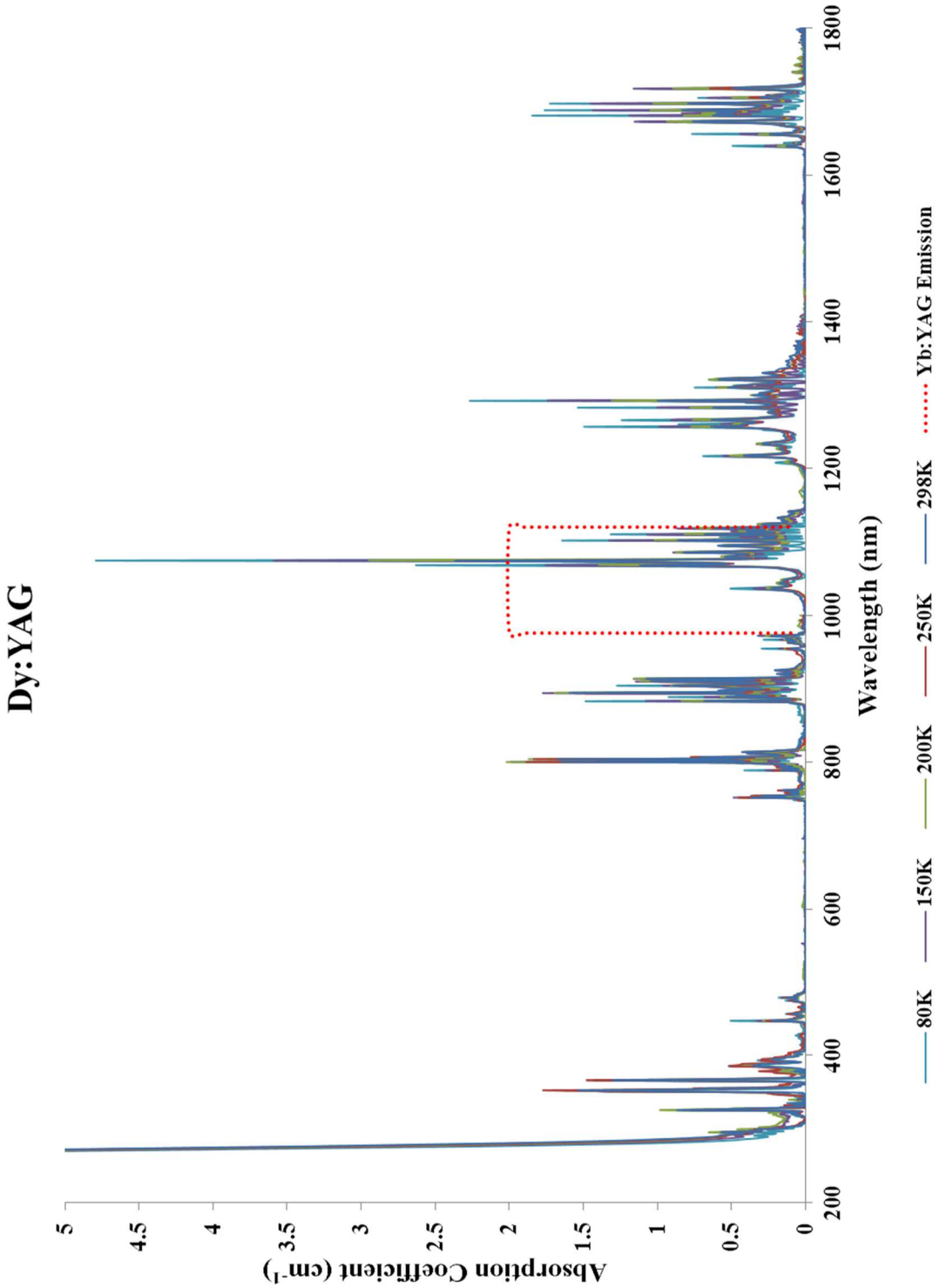

Figure 101. The cryogenic absorption coefficient of Dy:YAG between 200 nm and 1800 nm for 298K, 250K, 200K, 150K, and 80K.

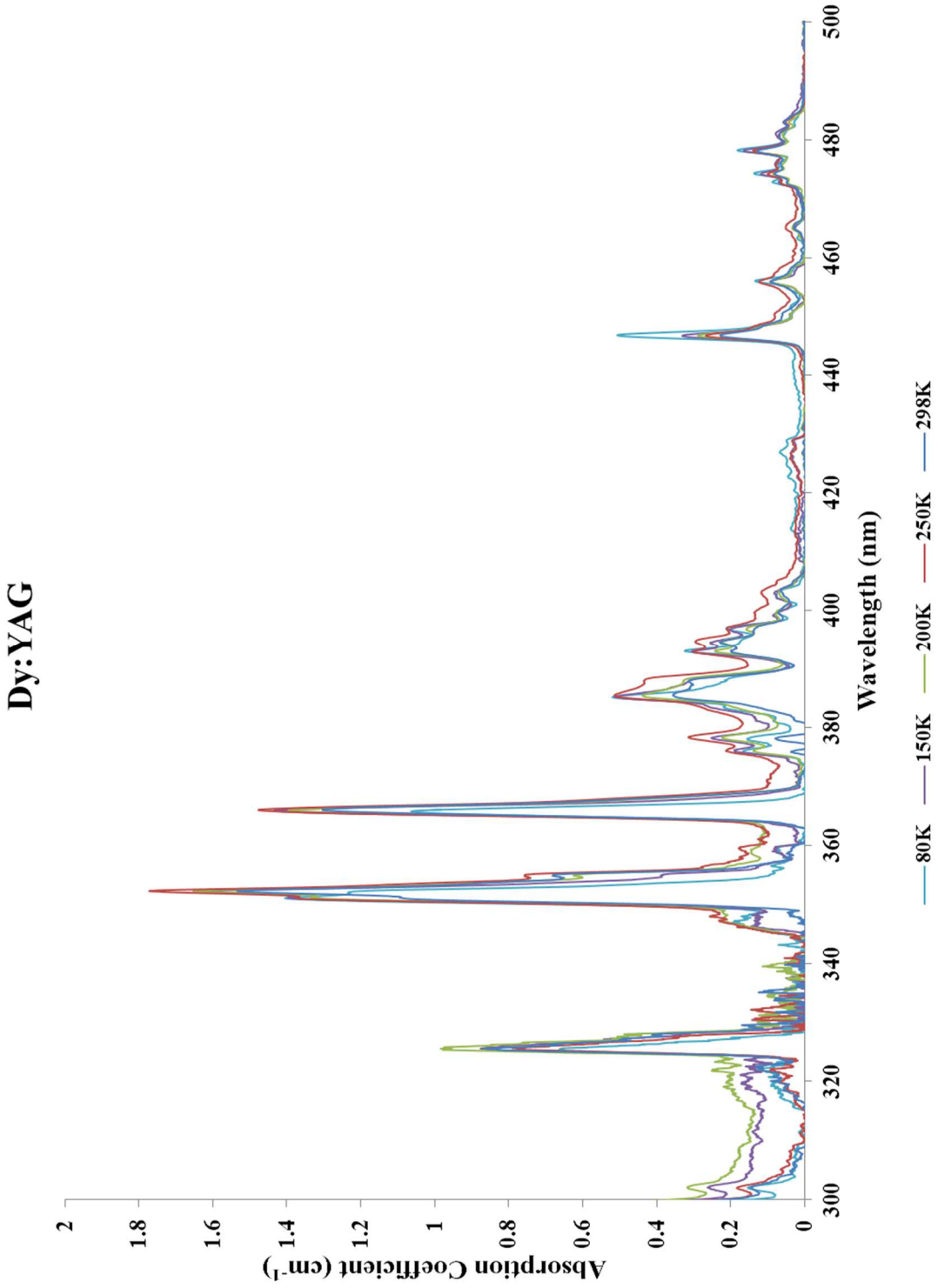

Figure 102. The detailed region of Dy:YAG between 300 nm and 500 nm.

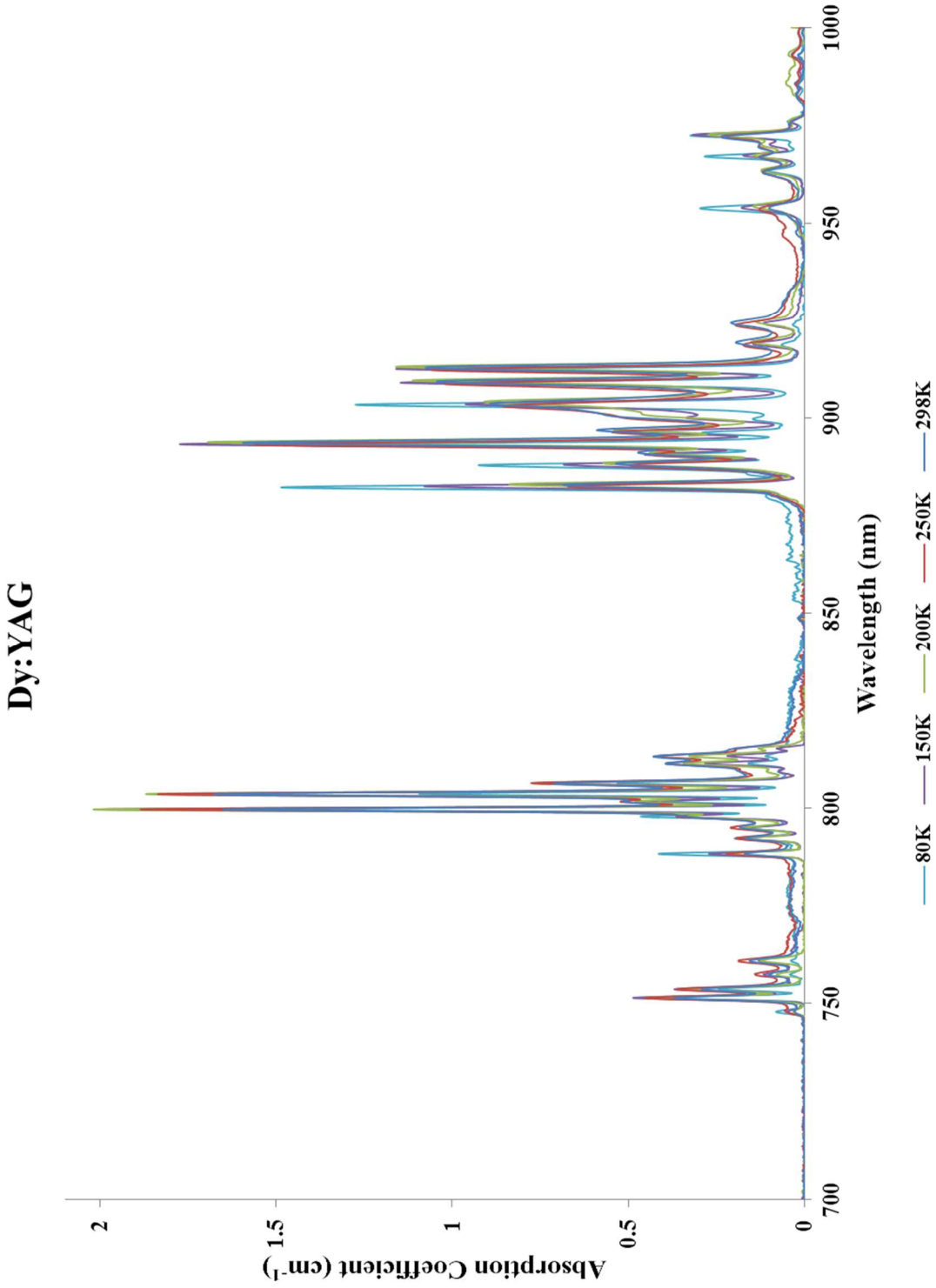

Figure 103. The detailed region of Dy:YAG between 700 nm and 1000 nm.

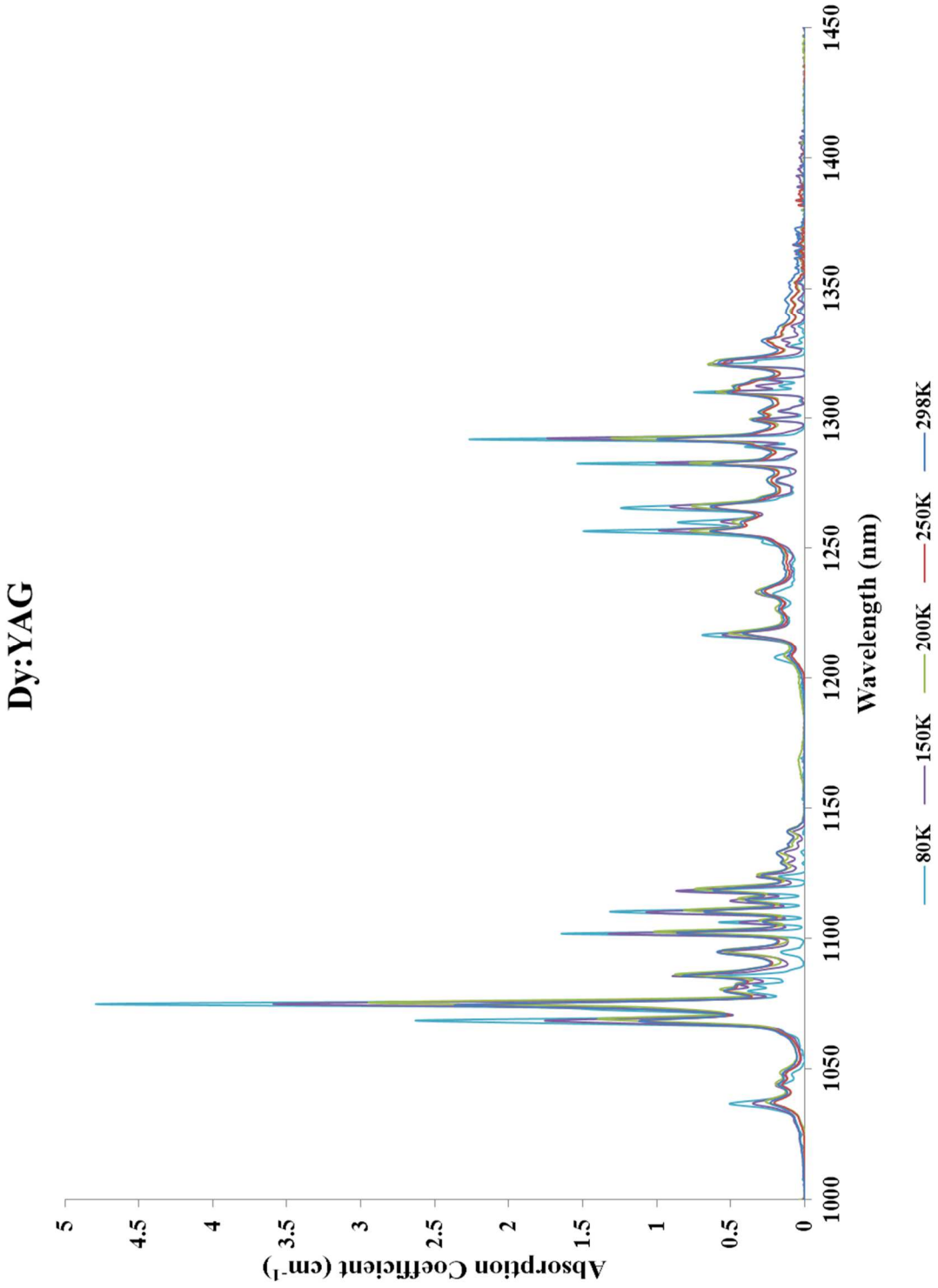

Figure 104. The detailed region of Dy:YAG between 1000 nm and 1450 nm.

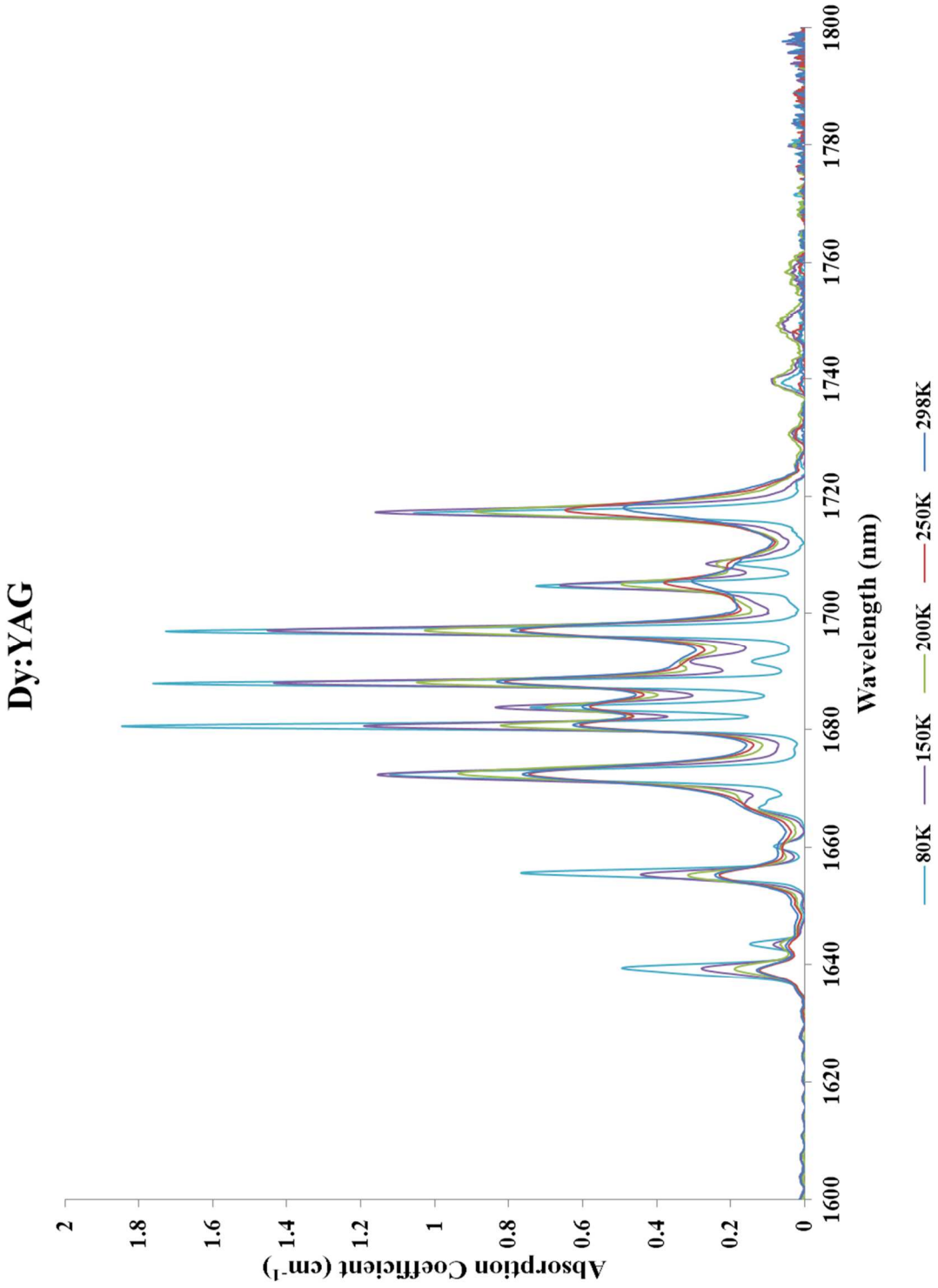

Figure 105. The detailed region of Dy:YAG between 1600 nm and 1800 nm.

Analysis of Peak Intensities for Dy:YAG

Contrary to what is observed for Dy:Lu_2O_3, we do generally see the expected trend of increasing intensity with lower temperatures for Dy:YAG. Again, the same type of anomaly that is seen in Yb:Lu_2O_3 is apparent for the zero-phonon peak around 800 nm, Figure 106 and summarized in Table 18, due to the likelyhood of the inability of the spectrophotometer to capture the sharpest, narrowest lines produced by the coldest temperatures. For this reason the same type of treatment is given in projecting the actual intensity for the two coldest temperatures. The estimated intensities, calculated by the trendline equation are given in parentheses, assuming that the error is instrumental, as we have done here.

Analysis of Peak positions for Dy:YAG

As can be seen in Figure 107 and summarized in Table 19, there is no clear shifting trend as a function of temperature in the chosen peaks, and move only very slightly towards higher and lower wavelengths. The zero-phonon peak around 800 nm is virtually identical at each temperature measured, varying by only 0.05 nm. Even the 1074 nm peak, which exhibits the greatest change in wavelength with temperature only varies by less than 1 nm.

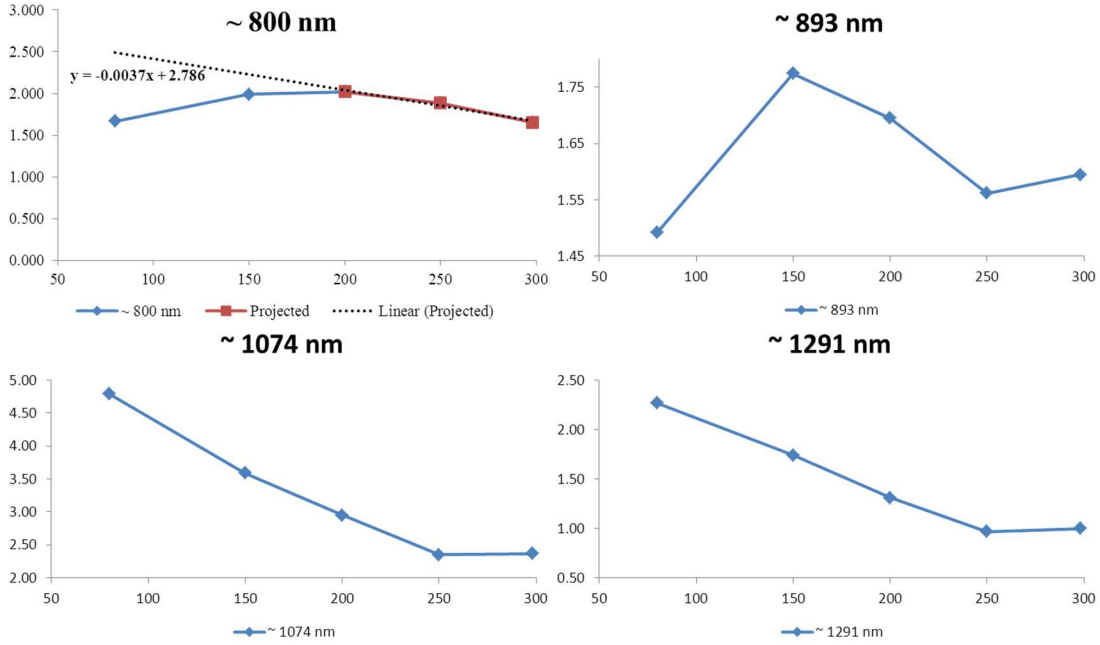

Figure 106. Dy:YAG intensities appear to follow the expected trend of increasing with lower temperatures except for the 800 nm peak. If this is due to instrument error, as suspected is the case for Yb:Lu_2O_3, the projected intensities at the two lowest temperatures can be calculated using the trend line equation.

	Dy:YAG Absorption Coefficient (cm^{-1})			
Temperature (K)	~ 800 nm	~ 893 nm	~ 1074 nm	~ 1291 nm
80	1.668 (2.490)	1.492	4.793	2.268
150	1.989 (2.231)	1.774	3.592	1.742
200	2.019	1.695	2.949	1.310
250	1.886	1.562	2.349	0.968
298	1.651	1.595	2.366	1.000

Table 18. Summary of cryogenic absorption coefficients for Dy:YAG as a function of temperature. The numbers in parentheses are expected actual intensities calculated from the trend line.

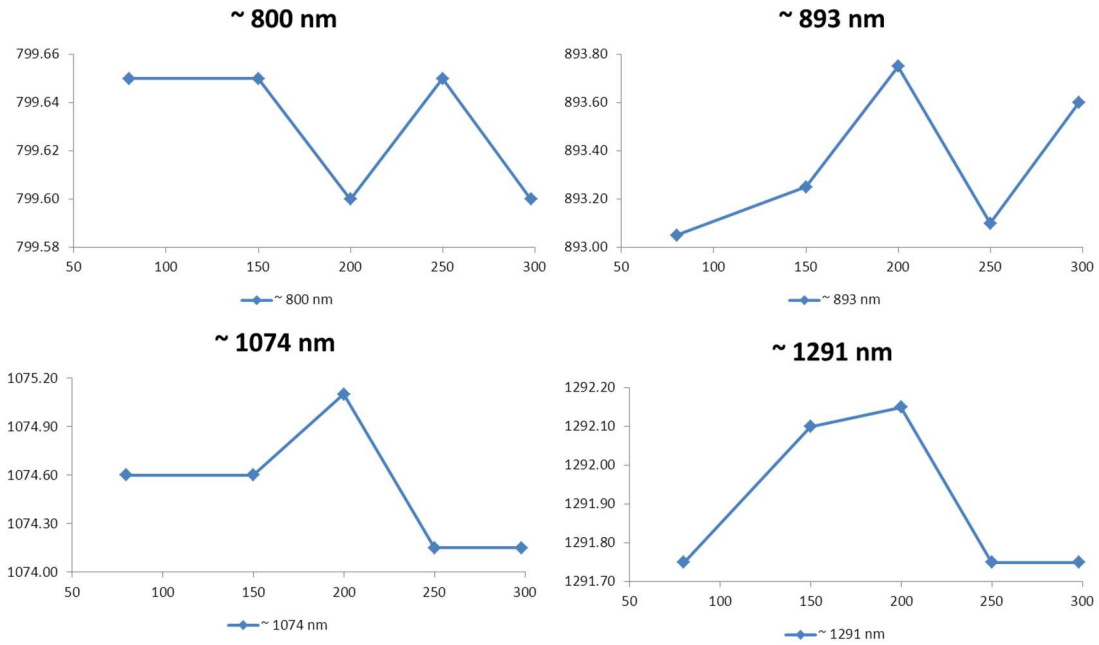

Figure 107. The shift in peak positions of Dy:YAG for the chosen transitions as a function of temperature.

	Dy:YAG Peak Position (nm)			
Temperature (K)	~ 800 nm	~ 893 nm	~ 1074 nm	~ 1291 nm
80	799.65	893.05	1074.60	1291.75
150	799.65	893.25	1074.60	1292.10
200	799.60	893.75	1075.10	1292.15
250	799.65	893.10	1074.15	1291.75
298	799.60	893.60	1074.15	1291.75

Table 19. A summary of the shift in peak positions of Dy:YAG for the chosen transitions as a function of temperature.

A room-temperature comparison of Dy-doped Lu_2O_3 and YAG

The complexity of the evergy level structure for both Dy-doped hosts is obvious from the spectra making it very difficult to assign transitions accurately. The sharp well-resolved peaks of both hosts, but Dy:YAG in particular are apparent in Figure 108. A comparison of the normalized room-temperture absorption coefficients of Dy-doped Lu_2O_3 and YAG reveals several general differences, however. Between 1100 nm and 1400 nm we see a much greater absorption in doped lutetia with respect to YAG. We also see a reversal in the peak cluster that contains the most intense absorption. For Dy:Lu_2O_3 the sharp peak near 1291 nm is the most intense, whereas for Dy:YAG it is near 1074 nm (Table 20).

Another major difference in the absorption spectra between Dy-doped lutetia and YAG is in the peak clusters between 1150 nm and 1450 nm, due to the $^6H_{15/2} \rightarrow {}^6F_{11/2} + {}^6H_{9/2}$ transition. The absorptions in lutetia occur between 1150 nm and 1450 nm, or over about 300 nm. In YAG they are much less intense overall and occur only over a 200 nm region, between about 1200 nm and 1400 nm. Additionally, the peak of greatest intensity in that region in lutetia is at 1266.6 nm. This represents a blue-shift for lutetia by 25.2 nm over the peak with greatest intensity in YAG, which occurs at 1291.8 nm (Table 21).

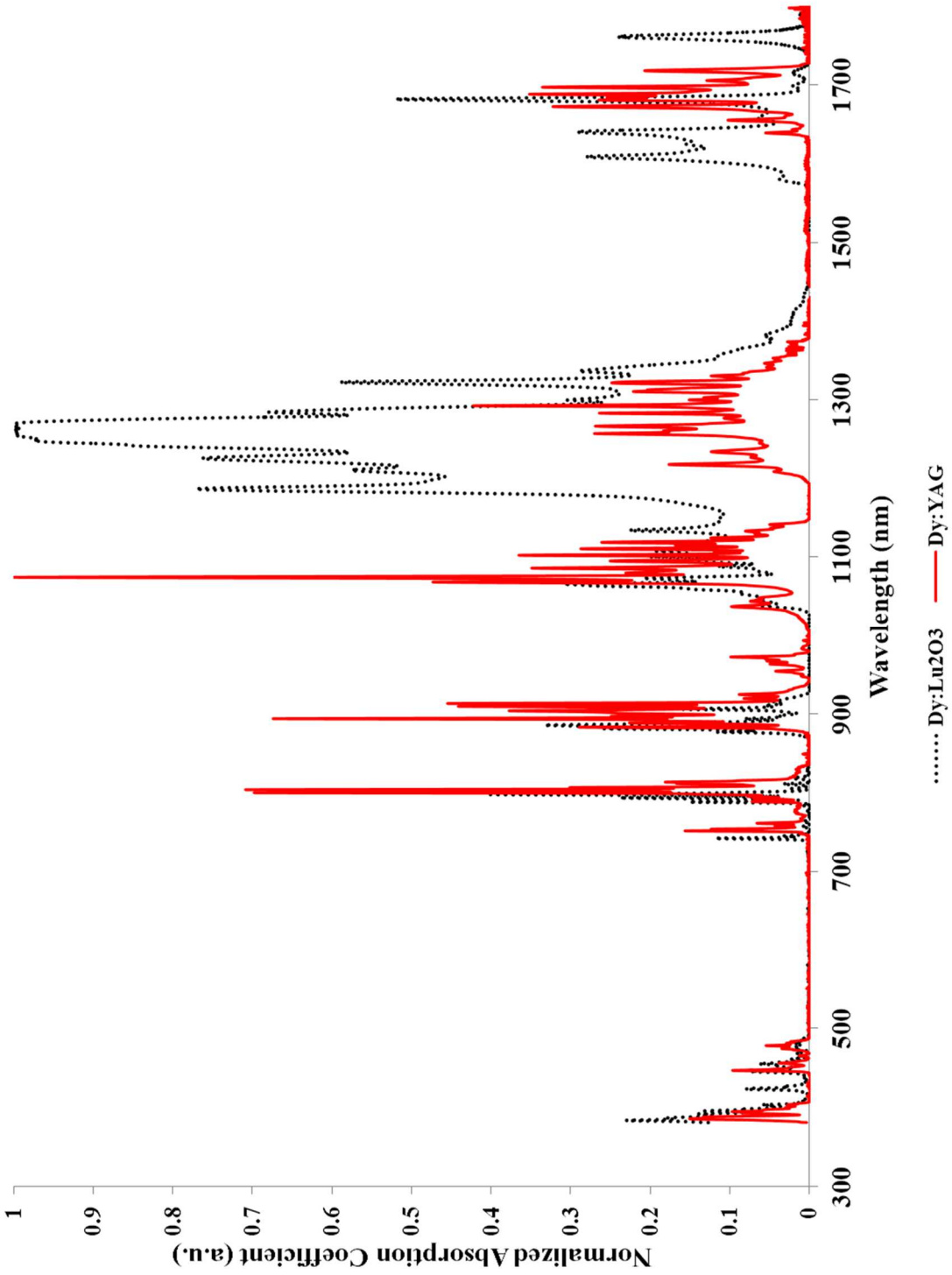

Figure 108. A room-temperature comparison of the normalized absorption coefficients of Dy-doped hosts, Lu_2O_3 and YAG.

	Relative Intensities for Chosen Transitions			
	$^6H_{15/2} \rightarrow {}^6F_{5/2}$	$^6H_{15/2} \rightarrow {}^6F_{7/2}$	$^6H_{15/2} \rightarrow {}^6F_{9/2} + {}^6H_{7/2}$	$^6H_{15/2} \rightarrow {}^6F_{11/2} + {}^6H_{9/2}$
	~ 800 nm	~ 893 nm	~ 1074 nm	~ 1291 nm
Dy:Lu_2O_3	0.401	0.082	0.209	1.000
Dy:YAG	0.698	0.674	1.000	0.423

Table 20. The relative intensities of normalized Dy-doped hosts Lu_2O_3 and YAG show a reversal of the strongest absorption line at 1291 nm for Lu_2O_3 and 1074 nm for YAG.

	Peak Positions for Chosen Transitions			
	~ 800 nm	~ 893 nm	~ 1074 nm	~ 1291 nm
Dy:Lu_2O_3	797.4	893.5	1072.9	1266.6
Dy:YAG	799.6	893.6	1074.2	1291.8

Table 21. Note the shift in position of the peak near 1291 nm. It has been shifted more than 25 nm for lutetia with respect to YAG.

Growth of Pr-, Ho-, and Eu- doped lutetia

Previously in this thesis the hydrothermal growth of LuAG and lutetia has been presented. Also presented was the ability to grow these high-quality crystals with a wide variety of dopants with well-controlled identities and concentrations using pre-doping of feedstocks. This ability coupled with the continuous development of new pump sources increases the feasibility of new lasers necessitating further exploration of doped crystals, especially lutetia.[22,23,25-27]

While we have reported the cryogenic absorption spectra of only a few dopants in lutetia crystals thus far (Yb, Dy, Nd), other doping schemes have been used very recently in the growth of Ho-, Eu-, and Pr-doped lutetia using the method described in Chapter 2. Hydrothermal growth by SN of high-quality doped lutetia is presented below.

The estimated doping by EDX of the Ho:Lu_2O_3 crystal in Figure 109, left, is 5% and it is 3.68 mm in length. After using the hand-polishing method described in Chapter 5, its path length is 1.21 mm. The quality appears to be excellent and is expected to give good cryogenic absorption data. The center picture shows three Eu:Lu_2O_3 from the same reaction that are each estimated to also be 5%-doped. Despite the relatively poor-quality, even after hand-polishing, the quality is expected to be sufficient to give acceptable cryogenic absorption spectra. The as-grown Pr:Lu_2O_3 crystal (Figure 109, right) also has

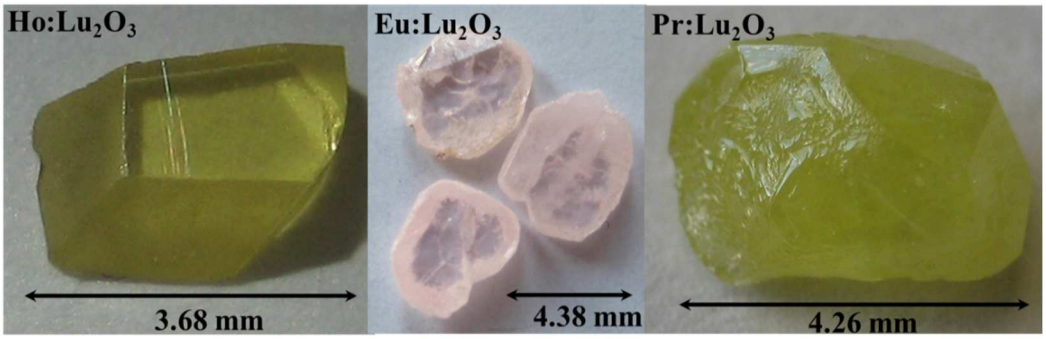

Figure 109. The growth of Ho-, Eu-, and Pr-doped lutetia is presented.

an estimated doping of 5% and is 4.26 mm in length. While it is impossible to judge its internal quality before polishing, it appears similar to most of the other high-quality crystals before polishing and is not expected to be of any less quality. The cryogenic absorption spectra of these and other crystals is expected to be reported shortly.

CHAPTER EIGHT

NOVEL GROWTH AND DOPING

Thus far, several methods have been introduced that offer potential benefits in designing and growing crystals. The advantages of the lower temperatures required by the hydrothermal method have been discussed and its unique closed-environment has been touched upon. Though the versatility that the hydrothermal method provides has been discussed several times thus far, it may not be clear to what end. In this chapter we attempt to bring together some of these advantages and suggest some practical ways they can be utilized.

Core growth using epitaxy

It was mentioned in Chapter 1 that the flexible nature of not only growing crystals but also being able to coat them epitaxially is a particular benefit of hydrothermal crystal

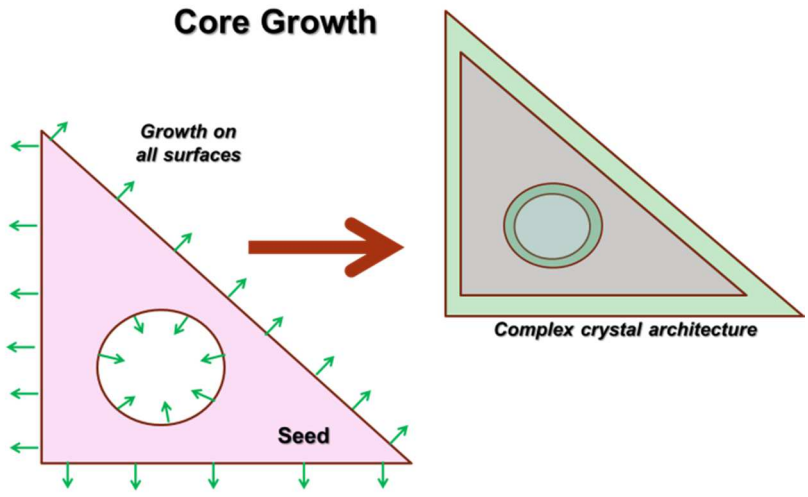

Figure 110. Hydrothermal epitaxy coats all surfaces of a crystal including inner surfaces.

growth. This concept can be expanded upon when one considers that not only is the outer surface coated during this process but inner surfaces as well, (Figure 110). This offers a distinct advantage over spray- or dip- coating methods for areas of industry such as micro lasers and other applications where a small, multifunctional crystal is desired. In crystal growth, each layer that needs to be grown requires time and money and it is always preferable to save both. The ability to grow several layers at once can accomplish just this.

Growing a layer onto a crystal in principle does not necessarily result in a larger crystal. It can in effect, grow a crystal smaller as the sketch in Figure 110 depicts, for

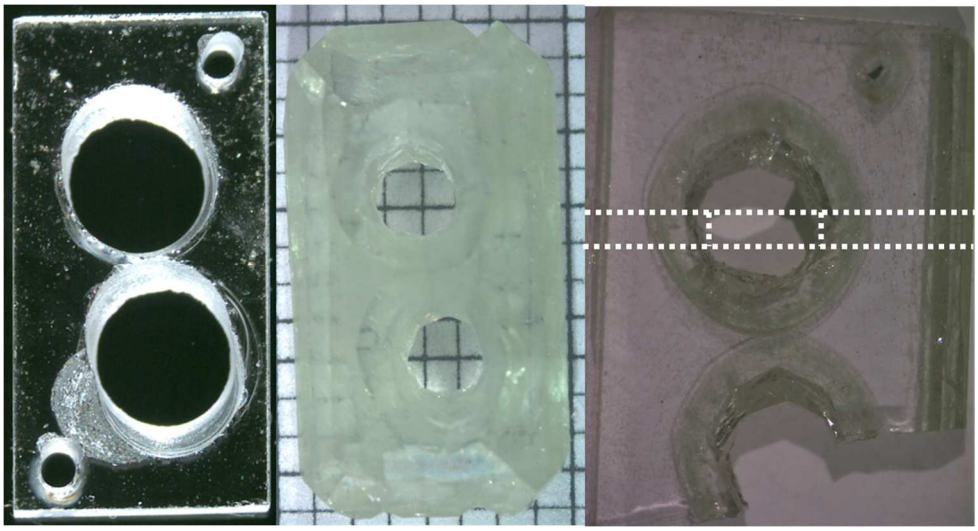

Figure 111. A complex crystal architecture (left) is completely coated by epitaxy (center). Polishing down to the seed reveals a smooth coating of the internal surfaces (right).

example. By thoughtfully designing a seed crystal, hydrothermal epitaxy can produce a complex crystal architecture without any added size by performing *internal* growth. Our group has demonstrated this coating of all existing surfaces presented first in Chapter 2

showing EDX analysis of smooth growth around the corner of a crystal. Proof of concept of coating an inner surface is offered in Figures 111 and 112. This architecture can then be further customized by cutting into bars, slabs or whatever shape is necessary. Figure 111 shows a YAG seed (left) about one centimeter long that has been prepared by core-drilling using a 2.25 mm dia. diamond coated drill bit along with two 0.75 diameter holes for the hang wire in the outer corners. Although the core-drilling of the seed crystal was done with a solid-core drill-bit, a hollow, diamond-coated bit designed specifically for core-drilling can be used. The center picture shows the result of growth using the reaction:

$$1\ g\ sapphire + 2.34\ g\ Lu_2O_3 + 0.0094\ g\ CrCl_3 \cdot 6H_2O + 5\ mL\ 2M\ K_2CO_3;\ \frac{610°C}{640°C}$$

for 22 days to target an epitaxial layer of 0.3% Cr:LuAG. The top and bottom surfaces were then polished down to the original YAG seed revealing only the coatings on the inside and outside edges. The cracking of the crystal was the result of the grinding step during polishing, and did not occur as a result of the growth process. The dotted lines suggest one possible cutting scheme resulting in two doubly end-capped laser bars. This system is also scalable and can produce crystals of unusual shapes as well as layers with different dopants.

Figure 112 shows a targeted layer of 1% Cr:YAG on a YAG seed (~ 1 cm a side) prepared with a single 2.25 bore-hole using the reaction:

$$1\ g\ sapphire + 1.33\ g\ Y_2O_3 + 0.052\ g\ CrCl_3 \cdot 6H_2O + 5\ mL\ 2M\ K_2CO_3;\ \frac{610°C}{640°C}$$

for 20 days using the slow warm-up procedure introduced in Chapter 2 to encourage better quality growth at the interface. We note that even with the thin silver hang-wire

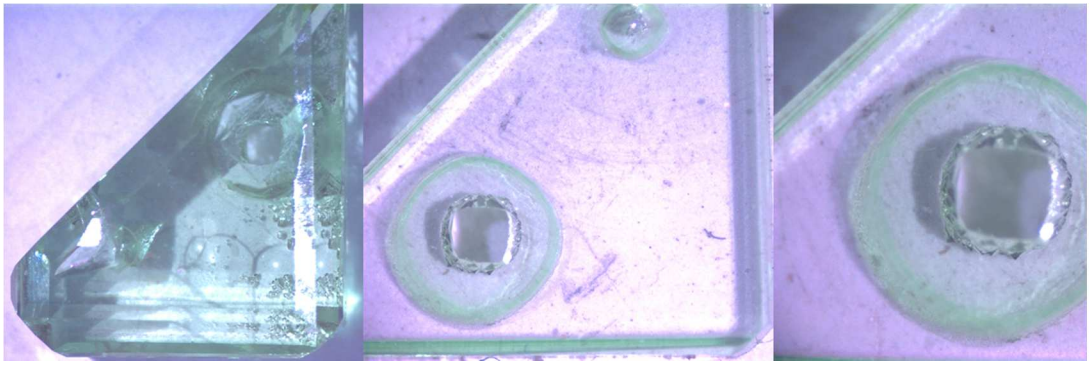

Figure 112. (Left) as-grown 1% Cr:YAG on a hole-drilled YAG seed.

inserted the hole was also filled (center picture, top center), indicating that both large and small holes tend to heal during epitaxial coating.

To further expand upon this idea, one could imagine a computer-guided diamond-coated bit being used to drill a complex design into a seed crystal. We were limited in this proof-of-concept example by what we could physically manage to drill and cut, but computer-guided machinery could allow for much more precise and intricate work to be done. This idea can be taken even further when one understands that customization of a seed crystal is possible not only by cutting and drilling holes. Consider the trough left by a drill that has gone half-way through a crystal. Now imagine this trough being drawn laterally through the crystal creating a line, square, or any design. Depending on the

depth or complexity of the trough necessary, laser etching could also be a useful tool to create customized seed crystals for this type of epitaxy.

Taking all of these ideas together with the ability we have shown of hydrothermally growing heterogeneous layer upon layer, it is left to the imagination to design almost any type of architecture. In summary, high-quality hydrothermal epitaxy has been shown to coat internal as well as external surfaces. Thoughtful engineering of multi-functional layers can result in tiny micro-laser crystals of almost endless complexity.

Hydrothermal growth of terbium aluminum garnet (TAG)

Also mentioned in Chapter 1 was the closed-nature of the hydrothermal system and the unique benefits this offers of reducing impurities and preventing evaporation of components. It also allows for control of the redox potential of the growth system. Not only does this tend to improve crystal quality, indeed, it sometimes allows the growth of a crystal that might otherwise be resistant to growth using other methods.

TAG, terbium aluminum garnet ($Tb_3Al_5O_{12}$), the terbium analog of YAG, for example, is a fascinating material that exhibits the Faraday Effect, which is the ability to rotate plane-polarized light under an applied magnetic field. Materials demonstrating this effect have found use as optical filters in laser applications. Laser light being reflected back to the source components can pose a significant risk of damaging those components. Rotating the plane of this light in conjunction with a polarizing filter creates a one-way valve for light passing through the filter. Light travelling in the opposite direction,

interestingly, is not rotated in the opposite way, but in the same way as the forward direction.[95,96] Because the plane of polarization of any reflected light is different on the return trip it is unable to pass again through the polarizer, effectively removing it from the system protecting the sensitive source components. The degree of rotation the material is capable of is measured by a temperature- and wavelength-dependent parameter, called the Verdet constant, which is the slope of the rotation angle as a function of applied magnetic field. Those materials with a greater Verdet constant would result in a greater rotation of the light with less doping, minimizing the associated cost.

Although TGG, or terbium gallium garnet ($Tb_3Ga_5O_{12}$), has a Verdet constant about 25% less than that of TAG,[97] it is a material that is widely used in industry for Faraday Rotators thanks to its good physical and chemical properties and comparative ease of growth;[98] large boules are easily grown by Czochralski and other melt-based methods. Because of its incongruent melting, however, single crystals of TAG are difficult to grow by conventional methods, as these systems tend to preferentially produce the perovskite phase, $TbAlO_3$ (TAP), which does not have as favorable properties as the garnet phases.[99,100] Although growth of optical quality single crystals of TAG on the order of 3 mm in diameter using a hybrid floating zone method has been reported by Geho recently,[97,101] in addition to preparation of the feedstock rods which requires sintering at 1600°C, a very complex system which employs four 30-W CO_2 lasers is also necessary. Stress fracturing is reportedly still possible using this method and extreme caution was used to help prevent it.

The incongruent melting behavior of this material is blamed for the difficulty of its growth and we see the usual high-temperature effects still present. For this reason, it seemed reasonable to attempt its growth using the hydrothermal method which is not affected by incongruous melting. Because TAG is a garnet, the initial attempt to grow this materially hydrothermally employed the same conditions as YAG: metal oxide components with a 2M K_2CO_3 mineralizer and temperature gradient of 610°C – 640°C. The binary oxides used were sapphire and the dark brown, mixed-valent Tb_4O_7 (HEFA Rare Earth, CA, 99.997%), using a 5.31 mm x 8.56 mm x 2 mm thick YAG seed weighing 0.3960 g. Under these conditions the back-dissolve during growth was so

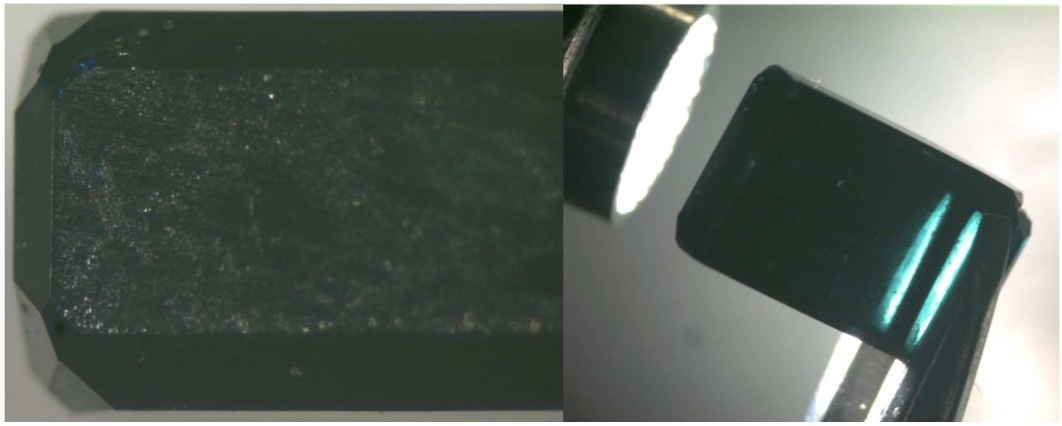

Figure 113. TAG growth on a YAG seed appears black (left) but is actually a very dark green-blue.

severe for this first attempt that the seed fell from the ladder into the feedstock and after 19 days resulted in a net loss in every dimension including a weight loss of 17%. The seed crystal, however, did show an epitaxial growth which was so dark it appeared black (Figure 113, left) implying that at least some of the terbium in the new growth was in the 4+ state, since Tb^{3+} does not have significant absorption bands in the visible region.[102]

Inspection through a bright light revealed that it was actually very dark greenish blue (Figure 113, right).

A cross-section was cut from this crystal through one of the ends and is a view looking through the thickness. It was then polished for the element map in Figure 114. By comparing the original 2 mm seed thickness (the darker portion in the center of the image) to the resulting seed thickness of about 500 μm, the scale bar in the SEM image

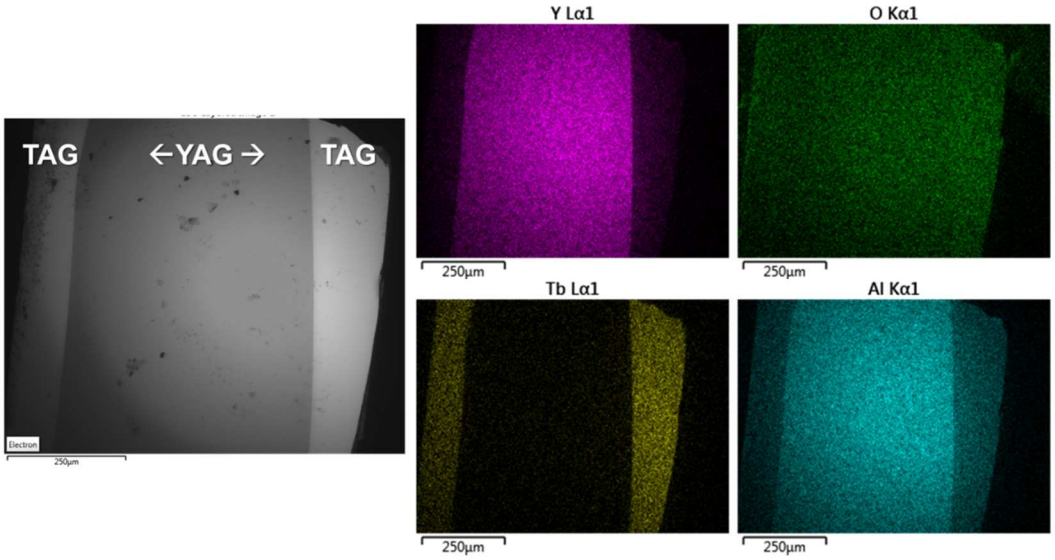

Figure 114. Elemental map of a cross-section of TAG grown on a YAG seed. Map of Tb shows it confined in the outer new-growth, while Y is concentrated in the YAG seed.

indicates that there was a net loss of the thickness by about 75%. Because there was no evidence of the hole for the hang-wire or the silver wire itself it was assumed that the seed had been sitting in the feedstock for at least some time. Even sitting in the feedstock, however, the growth was of remarkably good quality; the faceting was pronounced and the surface looked flawless, including a perfect healing of the drill-hole.

The element map for yttrium in the bottom left of Figure 114 shows a concentration in the center YAG seed, and also the presence of a trace amount of Y in the layer of new growth. With the significant back-dissolve that had occurred, it is likely that the new growth is not purely TAG, but closer to $(Y_xTb_{(1-x)})_3Al_5O_{12}$, where x is some small number <1. We also clearly see in the element map for terbium in the center of Figure 114 that terbium was incorporated into the new growth. Thus it is obvious that a layer of predominantly TAG can be grown hydrothermally on the YAG seed.

The element map for aluminum, however (Figure 114, bottom right), shows us something surprising. The aluminum content would be expected to be constant in both the seed and the new growth, but the map shows a definite reduction of Al ion concentration in the area of new growth. While the exact nature of the decrease of aluminum is unknown it is proposed that Tb^{4+} is occupying some of the Al-sites.[103,104] There is precedent for this type of behavior from the well-known doping of the aluminum sites in YAG with Cr^{4+} in making Cr:YAG for Q-switching.[105-107]

After these measurements, the crystal was heated in air. While post-growth annealing performed in an oxygen-containing environment usually serves to oxidize rather than reduce a species capable of oxidation, we witnessed a likely reduction from Tb^{4+} to Tb^{3+} as a result of annealing the crystal in Figure 115 at 1000°C for a few hours as it changed from dark blue Tb^{4+} to colorless as the Tb^{4+} was reduced to Tb^{3+}. Again, the exact nature of this reduction from 4+ to 3+ of terbium is unknown, but it is proposed that electrons trapped in the lattice in the as-grown, blue crystals are removed during

annealing results in the colorless Tb^{3+}. Post-growth annealing is a harsh process that allows oxygen from the environment to diffuse into the crystal removing oxygen vacancies in the crystal structure. Rather than seeing oxidation due to the presence of O_2 from air during heating, we see reduction. This is probably due to the thermal migration of oxide defects and stabilization of a lower metal oxidation state as is well known for

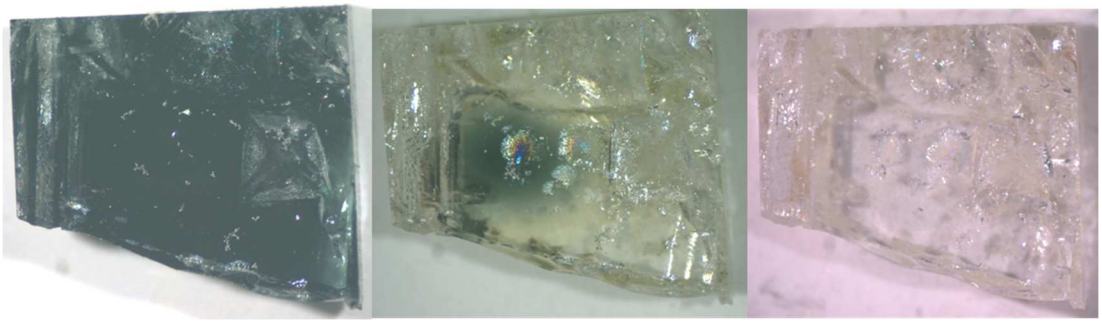

Figure 115. As-grown blue TAG crystal on YAG seed (left) after annealing at 800°C for at least 2 hours (center) and colorless after fully annealing at 1000°C for 2 hours (right).

metal oxides. The air is a just a spectator in this case. Annealing can cause anything from a slight reduction of the crystal quality to a complete destruction of the crystal and if the need to anneal can be circumvented, it is greatly preferred.

The crystal in Figure 115 is still on the YAG seed and shows the color before annealing (left). Because of the presence of internal SN we tried to find the most gentle annealing conditions possible. The crystal was placed in a crucible in the furnace and slowly ramped up to 300°C over about an hour and left at that temperature for at least 2 hours. After this time the crystal was removed, its color noted, and temperature raised 100°C. This process was continued to 1000°C. No change in color was noted until 800°C (Figure 115, center), when most of the crystal had become colorless with a small area of

blue remaining in the interior. It was left at 800°C for an additional 4 hours after which time the blue portion in the interior of the crystal could still be seen. Increasing the annealing temperature to 1000°C gave the completely colorless crystal on the right of Figure 115.

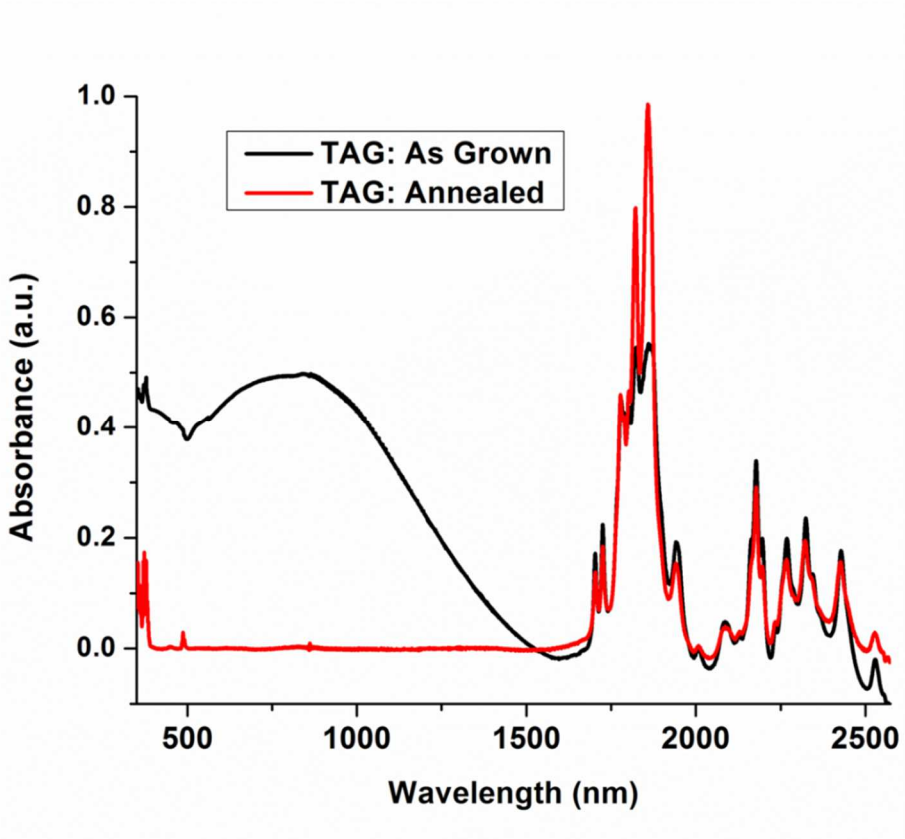

Figure 116. Absorption before annealing shows a broad band in the visible region (top, black). This band is gone after annealing (bottom, red).

The absorption spectrum in Figure 116 shows the absorbance of the as-grown, blue crystal with a broad, featureless absorption band below about 1500 nm and down into the visible region (black line). After annealing, the colorless crystal gave a spectrum

that is lacking this broad, visible band, retaining only the Tb^{3+} f-f transitions above 1600 nm (red line). There is also small absorption peak in the visible region near 500 nm, which is responsible for its light tan color. The overall effect is to grow a high quality single of mixed valent TAG. Heat treating of this crystal results in thermal reduction of all Tb ions to Tb^{3+} to produce a phase-pure TAG crystal containing only Tb^{3+} ions.

In an attempt to protect the seed from falling off of the ladder and to speed up

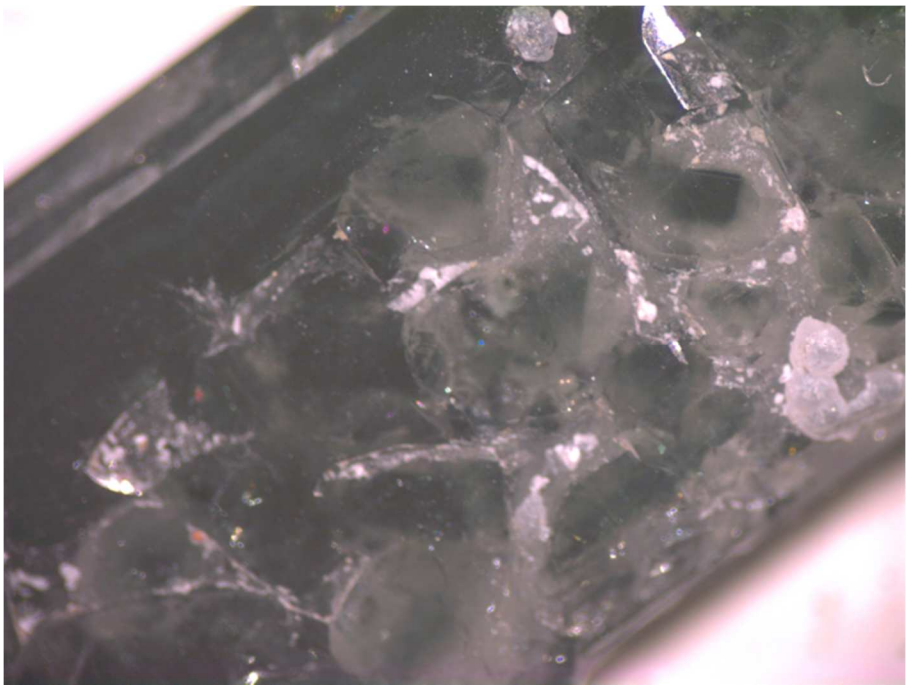

Figure 117. Increasing the thermal gradient to 600°C – 640°C gave a weight gain of 158% with portions of uncontrolled growth, but large regions of very good quality, colorless growth.

growth the temperature gradient was widened by lowering the growth zone to 600°C from 610°C. A growth duration of 27 days produced the crystal in Figure 117 that had a weight gain of 158%. The initial growth appears to be blue followed by the internal

attachment of colorless SN crystals and finally covered by colorless growth of much better quality.

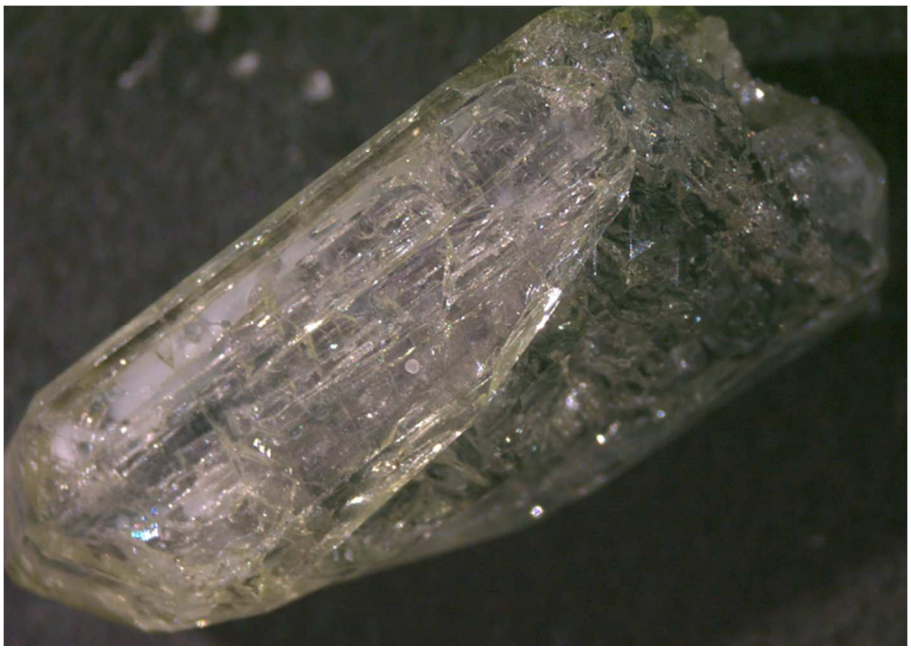

Figure 118. Out of control growth of TAG with blue internal growth covered by colorless growth.

In the initial attempt to grow TAG, the seed had fallen off the ladder into the feedstock and this might have been the actual cause of slow growth and not the result of a thermal gradient that was too narrow, as originally thought. Using this assumption, the gradient was widened back to 610°C – 640°C in part to reproduce the previous experiment. This would also confirm if instead of speeding up the growth it actually needed to be slowed down. Using the same reaction conditions, the crystal in Figure 118 resulted, with a 187% weight gain. This crystal again shows internal blue growth with a moderate degree of cracking, but also a significant amount of straw-colored outer growth. This confirmed that growth did not need to be sped up rather slowed down for greater

control. To try to slow down the growth, the thermal gradient was narrowed to 625°C – 640°C. A growth duration of 13 days produced the crystal in Figure 119 resulting in a

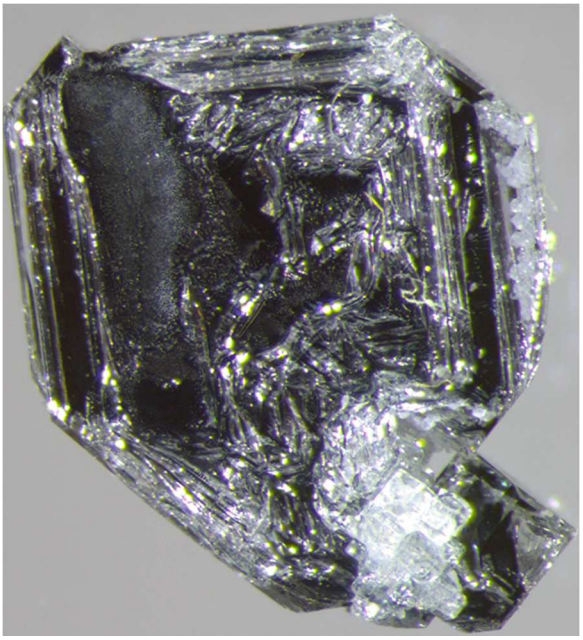

Figure 119. Clear, colorless portions around the edges imply that TAG can grow in the right hydrothermal environment.

weight loss of almost 12%, yet with obvious growth, supporting the notion that the seed crystal was regularly undergoing significant back-dissolve. Furthermore, because this growth was again blue, annealing was still required.

It was for this reason that a pure Tb^{3+} oxide component was targeted using a precipitation method similar to pre-doping feedstock components presented in Chapter 2. Dissolution of Tb_4O_7 using HNO_3 with subsequent precipitation into NH_4OH produced a white powdered precipitate. After drying, though, the powder started to turn a light tan color as the temperature was raised during calcination and was identical to that of Tb_4O_7

after complete calcining at 1000°C implying that it had fully oxidized back to its mixed valence state.

Again, the exact identity of this white feedstock is not known, but likely is an oxide of Tb^{3+}. This dried but not calcined, white powder from the above precipitation was used as the Tb source as a component with sapphire and a 2M K_2CO_3 mineralizer a 30°C gradient (610°C – 640°C) for 19 days. While there was a 38% weight loss overall, it was the first time that the growth was a yellow, straw color with no trace of blue in the tube.

To reduce the amount of back-dissolve while keeping the growth slow and controlled, the absolute temperature was lowered to 605°C – 610°C while using Tb_4O_7. A 14 day growth period resulted in the best quality growth to date of straw-colored growth everywhere except directly around the drill hole, which was still blue.

In summary, the use of Tb_4O_7 seemed to give poor-quality growth that was simply too fast to provide high quality growth. Future work will require smaller thermal gradients, overall lower temperatures or lower concentration of mineralizer to improve the quality of the growth. When mixed valent Tb_4O_7 is used as a feedstock the new growth of TAG is blue or partly blue indicating the presence of a measurable amount of Tb^{4+} in the lattice. This mixed valent ion can be reduced to all Tb^{3+} by annealing at 1000˚C. The use of the white powdered feedstock (presumably Tb_2O_3 or another species with no Tb^{4+}, although no additional tests were done to confirm this) gave significantly slower yellow to tan growth. It is a viable candidate for feedstock component because its

use resulted in growth with no blue color and additional investigation into its identity would be beneficial.

Lower temperatures seem to encourage Tb^{3+} over Tb^{4+} and prevent the mixed valence. A narrow gradient of 3°C for a few days slows down growth which leads to improved quality. Because when out-of-control growth occurred, it was close to the seed, or at the beginning of the run. In almost all cases good quality growth was occurring near the end of the growth cycle or on the outermost surfaces. Because of the poor quality followed by good quality that is often seen, it is likely that the 3°C gradient can be widened near the later stages of growth, speeding growth while maintaining control, increasing the rate of good quality crystal growth overall.

Maintaining a ΔT of 10°C but lowering the absolute temperatures is likely to increase epitaxial growth of single crystal onto the seed and decrease the occurrence of SN on the seed. While temperatures below 600°C run the risk of forming metal oxyhydroxides seen in other garnet systems such as YAG and LuAG, experimentation in this regime is likely to shed light on the optimization of this system. Lastly, clear evidence of the effect of lower mineralizer concentration was never attained. This lower molarity is another variable that could help moderate the environment bringing the system under better control.

Portions of high-quality TAG have been shown to grow in our hydrothermal system therefore it is possible to optimize the growth environment to maximize the

optical quality TAG that can be produced. This is in contrast to melt-based techniques that usually result in the TAP phase.

Co-doping YAG with Cr^{4+}/Ca^{2+} and Nd^{3+} for self Q-switching

In Chapter 2, the idea of pre-doping elements into a feedstock to better regulate the homogeneity of available feedstock was introduced and evidence of its effectiveness was offered in the form of elemental analysis of several points along its growth cross-section. In this chapter we extend this concept to a system involving a much more complex array of dopants in an attempt to highlight the power of this pre-doping method.

Chromium 4+ is a saturable absorber for the 1064 nm emission of Nd-doped lasers making a continuous-wave (cw) into a pulsed laser, or a Q-switched laser. The advantage of a pulsed laser as opposed to a cw laser is that the peak pulse power can be much greater than the average power of a cw laser. Unlike the simple pre-doping scenarios introduced in Chapter 2, where one 3+ ion is doped for another 3+ ion, though, the case of doping a 4+ ion into a garnet is a bit more complex. Adding the lasing ion Nd3+ into this system further complicates the doping scheme.

Co-doping two or more different elements into a crystal can introduce a lot of new variables especially in the case of Cr^{4+}/Nd^{3+} and it is more complex than simply adding both Cr and Nd. When the chromium is doped into the lattice during growth, it is likely all in the 3+ state, which is a pale green color. In order to allow for its eventual oxidation into the 4+ state, however, a charge compensating ion must also be inserted into the lattice during its growth. In this system, Ca^{2+} with its crystal radius of 1.26Å is a good

choice for both YAG and possibly LuAG, although it has not been explicitly tested here. It is easily inserted during growth into the garnet lattice at the Y site, whose host ions, Y and Lu, have 8-coordinate crystal radii of 1.159Å and 1.117Å respectively.

During growth, Ca^{2+} goes into a Y-site along with a charge-compensating oxygen vacancy. Nd^{3+} goes into the Y-site without the need for a vacancy, while Cr^{3+} goes mainly into the Al octahedral site[108] (0.53Å) in the 3+ state evidenced by the light green color. Careful post-growth annealing in an open-air furnace for several hours induces the Cr^{3+} to move to the tetrahedral Al-site (0.675Å) and to be oxidized to the 4+ state as evidenced by the color change from pale green to a deep to light brown color. It is not possible to detect the presence of Ca^{2+} in the lattice before annealing just by looking at it, however, but we offer evidence of its incorporation in the brown color that is evident. It is only possible for the green Cr^{3+} to turn to the brown 4+ state in the presence of Ca^{2+}. We can, thus, take the color change as evidence that the Ca^{2+} is, in fact, present.

Control of the dopant becomes especially important at the very low concentrations used in this type of a system, on the order of 0.3% for Cr. If dopants are distributed non-homogeneously throughout the crystal, uneven heating during laser operation can lead to a destruction of the crystal. The more complex a system gets, though, the harder it can become to control their concentrations. As we shall see in the next section, the use of individual dopant components does not necessarily result in the homogeneous distribution of all dopants throughout the growth.

Growth from components

As is often the case, it is usually best to start simple, so in this case components were used in the initial attempts to grow Cr/Ca, Nd:YAG. Because we have successfully used the pre-doped component Nd:Y_2O_3 several times before, use of it here as the source of Nd^{3+} was not expected to present any problems. Ca^{2+} and Cr^{3+} were added as components from $CaCl_2$ and $CrCl_3$, respectively, to target 0.1 % Ca and a matched 0.1% Cr doping. Along with the appropriate amount of crushed sapphire, 5 mL of 2M K_2CO_3

Figure 120. As-grown doped YAG on YAG seed. The pale green color indicates the presence of Cr^{3+} and the light pink is indicative of Nd^{3+}.

mineralizer was added. Twenty days' growth including a slow gradient widening to improve seed/interface quality produced a weight gain of almost 36% of excellent quality doped YAG crystal (Figure 120).To prepare the crystal for annealing to the brown, Cr^{4+} state, both ends were cut off being careful to remove any trace of the silver hang-wire that can be seen still imbedded in the crystal on the far left of the image. A view through one of the cut ends of the crystal in Figure 121 (left) shows the green color with the YAG seed barely visible diagonally through the center. After complete annealing at 1000°C

overnight, however, the resulting crystal on the right shows something unexpected. The dark brown color localized at the interface, again, indicative of the presence of Ca^{2+}, implies a much greater concentration of Cr^{4+} there relative to the rest of the new growth. Subsequent crystals grown by the same method showed the same phenomenon. There is no reason to believe that the Cr^{3+} was being unevenly distributed, as evidenced in Figure 13 left, that shows and even green coloring throughout and the fact that Cr-doping alone using the same component had never previously presented a problem. For this reason,

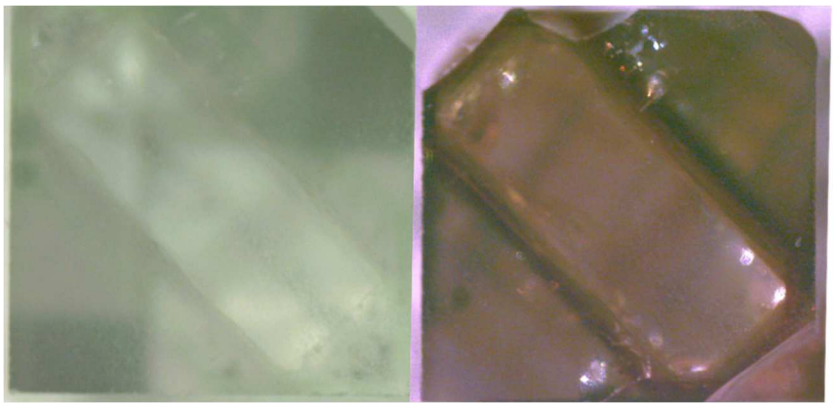

Figure 121. Ca/Cr,Nd:YAG crystal as-grown (left) and after annealing (right) reveals uneven doping.

attention was turned to the Ca-component, which is only present in extremely small quantities in the feedstock, around 10 mg. The logical conclusion was that the Ca^{2+} was being distributed unevenly, pooling at the interface at the beginning of the growth cycle.

Coprecipitation of a Ca,Cr:Y_2O_3 feedstock

The coprecipitation technique introduced in Chapter 2 was shown to be an effective method of producing a pre-doped feedstock that gave better control of dopants. The same technique was modified and used in the preparation of various precursors in the

investigation into the growth of grossular in Chapter 4. An alternative component was presented in the previous section to prepare a pure 3+-valence species of terbium oxide. The same principle is used here in a novel way to prepare a doubly-doped metal oxide feedstock for the growth of Ca^{2+}/Cr^{4+}, Nd^{3+}:YAG.

Because the targeted doping percentage of Nd is much higher, at around 2 at.%, and the fact that we had already demonstrated our ability to reliably produce and use Nd:Y_2O_3 feedstock, the focus was turned to the Cr^{3+}/Ca^{2+} doping issue to see if they could both be co-doped into the Y_2O_3 component to better regulate their availability.

Because of the difference in stable oxidation states, it was unknown whether Ca^{2+} could be doped into the Y_2O_3 lattice. To test this, a 50% Ca:Y_2O_3 feedstock was targeted for two reasons. First because if 50% (or some significant amount) doping could be accomplished then the amounts that would ultimately be necessary should certainly be possible, which are on the order of 1% or less. The second reason to target such a high level was to try to get doping amounts that would be reliably detectable by elemental analysis.

In the coprecipitation reaction $CaCl_2$ dissolved in water and Y_2O_3 dissolved in HNO_3 were precipitated into a NH_4OH solution as previously described, resulting in a dense, white precipitate. The wet powder was allowed to settle and then carefully decanted and rewashed until the pH was neutral. The isolated powder was dried and calcined as described. The powder pattern of a calcined sample in Figure 122 was a

perfect match to database Y_2O_3. Analysis by EDX, however, showed no Ca in the sample.

Although an explicit investigation into the exact nature of the precipitate(s) was not performed, it is probable that it is at least slightly soluble in water. The motivation behind this precipitation was the metathesis reaction and solubility rules. The double-displacement reaction between aqueous $CaCl_2$ and Y_2O_3 in HNO_3 predicts that the possible insoluble products formed will be Ca-doped or undoped Y_2O_3, YO(OH), and $Y(OH)_3$ and $Ca(OH)_2$ which is slightly soluble in water, ~1.73 g/L. With enough water washing, chloride, nitrate, ammonium and hydroxide ions can all be completely rinsed

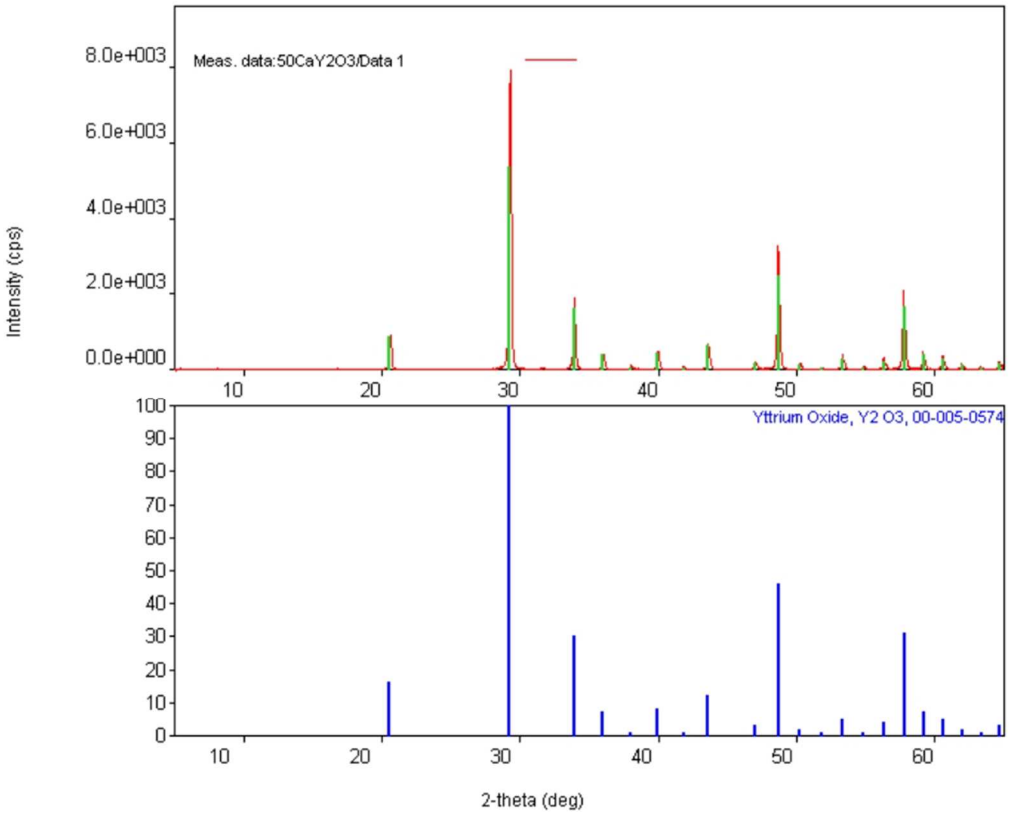

Figure 122. The coprecipitate using NH_4OH as precipitating agent showed a powder match to Y_2O_3.

from the supernatant. In cases where insufficient rinsing was used, Cl^- was detected in the elemental analysis. Unfortunately, because calcium hydroxide is slightly soluble, it too can be washed completely from the precipitate. Analysis by both differential scanning calorimetry (DSC) and EDX could be used to elucidate further the nature of the precipitate. It is noted that in most cases when we attempted pre-doping the laser-active lanthanides into an oxide component, use of NH_4OH as the precipitating agent worked well to create a heavy, well-separated precipitate. This does not appear to be the case, however, when Ca is being used.

A precipitate based on $CaCO_3$ was targeted because its solubility in water is only ~$6X10^{-3}$ g/L at 20°C, much less than for $Ca(OH)_2$ and it should be sufficiently insoluble to withstand washing and be available during the calcination process to be ultimately doped into Y_2O_3 during its formation. For this reason, and aqueous solution of $(NH_4)_2CO_3$ was used as a precipitating agent.

Following analogous reasoning, while the calcium salt likely formed by precipitation by a $(NH_4)_2CO_3$ solution is not completely insoluble either, it is sufficiently insoluble to allow adequate rinsing of the precipitate while leaving most of the calcium in the solid. A new powder was prepared using the same starting materials but precipitated into an $(NH_4)_2CO_3$ solution made from about 300 mL of water and enough ammonium carbonate to a pH of at least 13. A few more grams were added to ensure enough CO_3^{2+} would be available during the precipitation, and the pH was periodically monitored throughout. The precipitate was dense, but gel-like and did not settle readily. Vacuum

filtration was used to wash the precipitate until its pH was neutral. It was then dried and calcined as usual. Its powder pattern was a perfect match to database Y_2O_3, but EDX analysis of the material this time showed an equal 50/50 ratio of Ca/Y (to within 0.7%) for two separate areas of powder analyzed. It appeared that Ca could successfully be doped into the Y_2O_3 lattice. Next, we tried to co-dope both Ca and Cr into Y_2O_3.

This modified protocol was used to prepare co-doped Ca/Cr:Y_2O_3 feedstock using the same starting materials plus $CrCl_3$ dissolved in water as the source of Cr, targeting a 25% : 25% : 50% ratio of Ca:Cr:Y in the final doped Y_2O_3. The powder pattern of this co-doped material was a good match to database Y_2O_3, but its EDX analysis showed a significant decrease in the amount of Ca in the final product – a 20% : 28% : 52% ratio of elements (Ca:Cr:Y) for two separate areas of powder tested. The exact cause of this discrepancy is unknown, but possibly related to the solubility issues just discussed. This is likely the case because in each analysis of powders produced in this way, Ca appears to be affected the most is consistently found in lower amounts than targeted.

Because all of the Cr will ultimately be oxidized to the 4+ state, it is important that there be at least an equal molar ratio of Ca to Cr present in the lattice to begin with. The feedstock just discussed is calcium-poor and would not allow for complete oxidation of the Cr-species. Control of the amount of calcium in the final product can easily be accomplished, however, by adding additional calcium at the outset, though, targeting an amount of Ca that is in excess with respect to Cr. For example, in subsequent attempts to create a feedstock with reasonable doping levels for the intended application, (about 1 %

Cr-doping) we targeted a Ca-doping of 5 times in excess of Cr, or 5% Ca-doping. The coprecipitation method described above with $(NH_4)_2CO_3$ as the precipitant was used targeting a 5% Ca and 1% Cr doping. After complete washing, drying and calcining, a sample was taken for EDX which gave an analysis of 3.47% Ca-doping and 0.98% Cr-doping. The percentage of Cr was very close to the 1% targeted and, although a significant reduction is noted in the amount of Ca, it was still in excess of Cr. It is not known the maximum amount of calcium that can be substituted into a garnet host or what the ramifications of doing so might be.

It should also be noted that while we use pre-doped feedstocks regularly with good results, the few attempts here to dope all three components, Ca, Cr, and Nd into a single Y_2O_3 component never resulted in a feedstock in which the presence of all three elements could be detected in appropriate amounts. While this should be possible in principle and may warrant further investigation, ultimately the use of a combination of $Ca^{2+}/Cr^{3+}:Y_2O_3$ plus $Nd:Y_2O_3$ powdered feedstocks gave the best results. A detailed summary of the preparation of pre-doped $Ca^{2+}/Cr^{3+}:Y_2O_3$ is given in the summary of the preparation of pre-doped Ca^{2+} / Cr^{3+} :Y_2O_3 section below.

The feedstock just described (3.47% Ca, 0.98% $Cr:Y_2O_3$) was used in conjunction with pre-doped 4% $Nd:Y_2O_3$ in a 1:1 weight ratio along with the usual crushed sapphire and 5 mL of 2M K_2CO_3 mineralizer with the usual temperature gradient of 610°C / 640°C for 21 days.

Keeping in mind that, even though the Cr is calculated initially as a percentage of Y_2O_3 in that doped component, it will ultimately reside in an aluminum site, and its doping-percentage becomes a percentage of Al rather than Y. Using the combination of feedstocks mentioned, the final YAG doping percentages *calculated* were 1.74% Ca (w.r.t Y), 0.6% Cr (w.r.t Al), 2% Nd doping of the final YAG crystal. In such cases where the doping percentages are not straightforward, it might make more sense to report it as a number density of the entire crystal and can be is easily converted using its unit cell information or physical density, depending on which is known with greater certainty.

Figure 123. A co-doped YAG crystal grown from Ca/Cr:Y_2O_3 plus Nd:Y_2O_3 feedstock before annealing (left) and after (right). Absence of dark ring around the interface implies there has been a more homogeneous doping.

After the embedded silver wire was cut from the end of the crystal, an additional cross-sectional piece was cut just below that and is the sample in Figure 123. This slab still had material that had grown around the drill-hole which can be seen on the right of that figure. The undoped YAG seed is barely visible horizontally in the center of the as-grown crystal (left) and (ignoring the brown portion through the center vertically) the same seed can be clearly seen in the picture after annealing on the right. The presence of Cr^{3+} can be seen on the left of Figure 123 in the pale green color. The darker brown of the

Cr^{4+} is also apparent in the picture on the right. What is most significant in the picture, though, is the lack of dark ring at the interface implying that a more homogeneous doping has occurred.

In summary, introduction of the charge-compensating Ca^{2+} ion into the garnet lattice during growth does not appear to occur homogeneously when added as a simple $CaCl_2$ component. Pre-doping the Ca into a metal oxide component, such as Y_2O_3, results in a more homogeneous distribution of Ca during growth allowing for the eventual oxidation of nearby Cr^{3+} to the brown Cr^{4+} that is desired. The coprecipitation method from Chapter 2 can be modified by precipitating into a $(NH_4)_2CO_3$ solution rather than NH_4OH resulting in a pre-doped component with its Ca-content largely intact. Use of the feedstock prepared as described appears to result in more homogeneous doping of the final components, as indicated by the even coloration after annealing.

Targeted levels of all three dopants, Nd, Ca, and Cr can be achieved by varying amounts of Ca/Cr:Y_2O_3, Nd:Y_2O_3, and undoped Y_2O_3. While a suitable triply-doped metal oxide component containing all necessary ions was never prepared, it could ultimately be the best component and is worth further consideration.

Summary of the preparation of pre-doped Ca^{2+} / Cr^{3+}:Y_2O_3

Co-doped Ca^{2+} / Cr^{3+}:Y_2O_3 can be prepared in an analogous way to the other pre-doped components described in Chapter 2 with a few modifications. A powder with a targeted doping of $(Ca_{0.25}Cr_{0.25}Y_{0.5})_2O_3$ was made starting with 3 g of Y_2O_3 and enough water to make a thin slurry. This was dissolved in a minimum amount of HNO_3 with heat

and stirring until completely clear. Separate aqueous solutions of 3.54 g $CrCl_3 \cdot 6H_2O$ and 1.47 g of $CaCl_2$ were made with a minimum of water. These solutions were combined with the cooled HNO_3 solution and set to stir without heat while the precipitating agent was prepared.

An aqueous solution of about 300 mL $(NH_4)_2CO_3$ was made by adding 300 mL of DI water to a liter beaker along with several grams of $(NH_4)_2CO_3$. This was set to vigorously stir on a stir-plate without heat. The prepared solution from above was introduced very slowly using a 5 mL syringe giving sufficient time to fully precipitate. Periodic pH-monitoring of $(NH_4)_2CO_3$ solution was done to ensure that the solution remained basic enough to continue to immediately precipitate all metals as they were introduced (at least 13). If the pH was noted to be decreasing, a few more grams of $(NH_4)_2CO_3$ were added and dissolved easily. After precipitation of all metals, the stirring was discontinued and the bluish-purple, gel-like precipitate was allowed to settle. Depending on the thickness and the willingness of the precipitate to settle, a few methods can be used to wash and isolate the wet purple powder.

A thick gel can be isolated by separating the precipitate and supernatant into several balanced centrifuge tubes. Cold-temperature centrifugation works best to separate the precipitate pellets but is not necessary. A few minutes at a medium speed was sufficient to separate the precipitate and the supernatant and the liquid was poured away. More water was then added to each tube and sonicated until a well-separated powder

resulted. This process was repeated until the pH was at or near 7. The wet powder was then scooped out of the tubes and placed in a crucible for calcining.

A heavier, denser precipitate can best be isolated by repeated washing followed by vacuum filtration. The process of settling, decanting, and rewashing to a neutral pH that worked well for the pre-doping discussed in Chapter 2 is not recommended in this case because of the slight solubility of Ca-containing species. It appears that the longer the precipitate is in contact with water, the greater the chance it will be washed completely from the powder. As a result effort should be given to minimizing contact time.

Index of refraction tuning for waveguides

In Chapter 2 it was described how the lattice size of LuAG would expand when doped with an ion of larger radius like Ga in order to better match that of a surrogate seed. A series of coprecipitate feedstocks for the growth of Ga:LuAG (where Ga is doped into the Al sites) was prepared and the shifting of the peaks in their powder pattern was offered as proof that this expansion had, in fact, occurred. In addition to Ga having a larger crystal radius than Al, it is also more than twice as massive as Al and this has some important ramifications in terms of refractive index modifications.

The intensity of a beam of coherent light can be degraded by the refractive loss (Figure 124). Each time a beam encounters an interface both reflection and refraction of the beam occur. Snell's law relates the angles of incidence to the indices of refraction

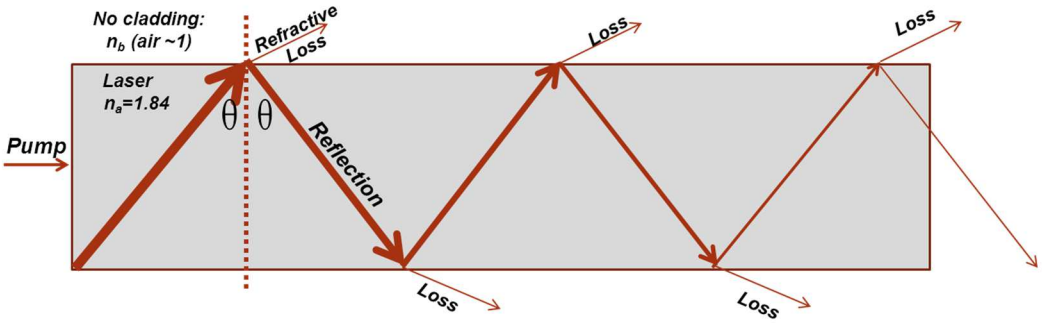

Figure 124. The refracive loss at each interface combines to degrade the intensity of the exiting beam.

(Equation 1). In this example, n_a is the refractive index of the gain medium and θ_1 is the angle of incidence and n_b is the refractive index of the medium at the interface (air) and θ_2 is the angle of reflection. Rearranging Snell's law to Equation 2, we see that the angle of refraction can be affected by changing the refractive index of the cladding, depicted in Figure 125.

$$\textbf{\textit{Equation 1}}: n_b \sin\theta_1 = n_a \sin\theta_2$$

$$\textbf{\textit{Equation 2}}: n_b = \frac{1}{n_a} \sin\theta_{crit}$$

When the index of refraction of the laser crystal (n_a) is close to that of the cladding (n_b) the refracted part goes directly through without much change of direction,

(Figure 125, left). As n_b gets smaller with respect to n_a (Figure 125, center two) the refracted part gets bent more toward the gain medium. We can also surmise from the equation that the index of the cladding must be lower than that of the laser crystal or the refracted part would be bent in the wrong direction, or away from the laser. When equation 2 is fulfilled the refracted part of the beam gets reflected back completely and is then confined to the laser gain medium as total internal reflection (TIR) is achieved (Figure 125, right).

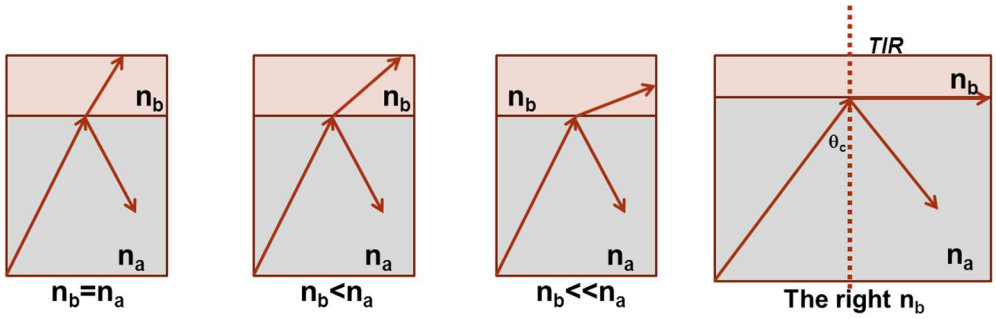

Figure 125. Controlling the refractive index of the cladding can guide the beam back into the gain medium reducing the refractive loss.

We have little control over the critical angle because it is a product of the dimensions of the crystal but there is some control we have over the refractive indices of both the laser crystal and the cladding. By tuning the refractive index of the cladding a waveguide can be created thus reducing these types of losses.

We have shown how doping with Ga can manipulate the properties of a crystal in two ways, to expand the lattice of an epitaxial layer to better fit a surrogate seed in Chapter 2 and in this chapter to increase the index of refraction to reduce refraction losses

at the interface using a cladding as a waveguide. These are just two examples of ways we can tune the properties of a crystal

CHAPTER NINE

CONCLUSION

Crystals are one of Nature's most amazing creations. Crystals are not only beautiful, but some have very useful properties, such as hardness, toughness, transparency and high heat-conductivity. They have found uses ranging from grinding grits, like alumina, all the way to high-tech applications in high-power lasers, like ruby or garnets. One such garnet is not found in nature but can be grown in a lab, borrowing nature's hydrothermal growth method. This thesis explores the use of the hydrothermal technique to grow high quality single crystals of a variety of refractory oxides including various members of the garnet family and lutetia (Lu_2O_3). In addition a number of doped analogs of these hosts were prepared and detailed absorption spectroscopy was performed in order to obtain the initial data necessary for high power laser applications.

YAG is ubiquitous in the laser industry and the ability to grow it and its lutetium analogue LuAG, hydrothermally has some important benefits over more traditional, melt-based methods. The significantly lower temperatures required by the hydrothermal method mitigate a lot of the detrimental high-temperature effects that are often seen in crystals grown by other methods. Indeed, it has been shown that materials that do not have an adequate growth route to high quality single crystals by any other method have been grown hydrothermally. Despite this promise of improved quality and the versatility offered by epitaxial coating, crystals grown hydrothermally are much less common. The ability to grow these crystals gives us a route to study their properties in detail.

It is evident in some of the figures in this thesis, though, that the growth parameters of LuAG are not yet optimized and there is still a long way to go in perfecting its growth so crystals of doped LuAG might become as ubiquitous as YAG. There are still many unanswered questions regarding LuAG, though. It is not clear what the maximum possible doping of LuAG for the various dopant ions, due to the fact that the lattice parameter of LuAG is less than YAG. This will have to be determined experimentally in the future. In addition, detailed thermal conductivity measurements of a wide variety of dopants and concentrations are unknown for LuAG due to the unavailability of suitably doped crystals. To develop the potential use of LuAG as a host for high temperature laser applications, such data is absolutely essential and again must be determined experimentally. Fortunately the work in this thesis provides the groundwork to enable these experiments to be carried out.

In addition to the versatility we have shown in growing a wide variety of laser hosts hydrothermally with an array of dopants, we have shown an added element of control in their doping by using prepared feedstock that combines both dopant and component into a single feedstock. Use of this feedstock has been shown to increase the homogeneity of distribution of the dopant throughout the crystal during growth. This homogeneity can be hard to achieve with melt-methods, but is very important, as laser crystals with uneven doping can lead to uneven heating during operation. This can result in the complete destruction of the crystal. The ability to prepare premade doped feedstocks adds considerable versatility to the growth of new potential laser crystals.

Doped YAG can be easily grown by both melt methods and by the hydrothermal method and has been thoroughly studied. The ease of growth of YAG is one of the reasons for its popularity. LuAG, however, has better properties for laser applications like an even greater thermal conductivity, density, and splitting of energy levels, which leads to a greater pumping efficiency. LuAG is much more difficult to grow, in part to its higher melting point, leaving this promising material relatively under-studied. We have shown the ability to not only easily grow these crystals, but to dope them with a wide variety of dopants including all of the naturally-occurring lanthanides, giving us a convenient route to their growth and study.

The ability to grow doped lutetia hydrothermally additionally highlights the benefits of hydrothermal growth because high-purity lutetia cannot be grown by standard melt methods. Its melting point is exceptionally high (ca. 2500˚C) which precludes most standard melt methods and leads to considerable strain and defects even when it can be grown. The benefits due to the increase in favorable properties of lutetia over YAG and even LuAG cannot be understated and the ability to easily grow doped lutetia opens the door to an area that has largely been ignored. We have demonstrated high-quality growth of a wide variety of doped lutetia of sufficient size and quality to give good cryogenic absorption data. These crystals are of sufficient quality to do a wide range of other testing, such as thermal conductivity measurements, dopant maximization, and room-temperature emission measurements and at cryogenic temperatures.

One of the reasons that continued study of these crystals is so important is that it is not always possible to predict their physical and spectroscopic properties with certainty. During laser use, for example, the shifting of an absorption band even by a small amount could be the difference between a crystal with excellent heat management capabilities and one with poor performance. This is true especially for lasers operating at very low temperatures and testing under these conditions is crucial. For these reasons a detailed analysis of the ultra-high resolution absorption spectrum of doped lutetia was carried out. A number of dopants were investigated including Nd, and Dy but the most detailed investigation was undertaken for Yb doped materials. This is due to the fact that Yb shows the most promise for high power laser application. In particular focus was paid to spectroscopy performed at cryogenic temperatures since the high power laser development of Yb-doped crystals has significant advantages at cryogenic temperatures. In addition detailed spectroscopy at cryogenic temperatures is severely lacking for most of these systems.

The demand for very high power lasers has always existed, but they still remain far from their routine development. One of the reasons for this is that the waste heat generated at such laser power would quickly destroy the crystal under current designs. Cryogenically cooled lasers are a step in the right direction in that they remove heat in two ways – by heat-exchange with the cryogenic fluid and in an increase in the thermal conductivity of the crystal itself. The properties of the crystal change at low temperatures, though making study of lasers crystals at low temperature a particularly important area of research.

Along with the demand of higher and higher power lasers, the world demands smaller and smaller technology. Solid-state lasers offered a significant decrease in the size of lasers compared to some of the first gas lasers, but even laser crystals can be further miniaturized. We have shown proof-of-concept of a coating method that not only coats outer surfaces of crystals but is also able to smoothly internal surface. This would, in effect "grow a crystal smaller." With the strategic preparation of a seed crystal, intricate architectures could be obtained that might require several growth runs by a different method to be accomplished in a single pass. Using this coating method we can create single crystals with multi-functional capabilities.

Continued study of hydrothermally grown crystals is important because there are still so many unanswered questions. While the goal of this thesis was to answer questions, the fear is that it may have asked more than it answered.

References

(1) Cavern of Crystal Giants. www.ngm.nationalgeographic.com (August 25, 2015)
(2) Coutures, J. P.; Rand, M. H., *Pure Appl. Chem.* **1989,** *61*, 1461-1482.
(3) Discovery of the Czochralski Method. www.janczochralski.com (March 19, 2015),
(4) Twisp, Czochralski Process. In *Inkscape*, Czochralski_Process.svg#/media/File:Czochralski_Process.svg, Ed. 2015.
(5) Brice, J. C.; Rudolph, P., Crystal Growth. In *Ullmann's Encyclopedia of Industrial Chemistry*, Wiley-VCH Verlag GmbH & Co. KGaA: 2000.
(6) Nelson, H., *J. Cryst. Growth* **1974,** *27*, 1-5.
(7) Ferrand, B.; Chambaz, B.; Couchaud, M., *Opt. Mater.* **1999,** *11*, 101-114.
(8) Markov, I. V., *Crystal Growth for Beginners*. 2 ed.; World Scientific Publishing Co.: Hackensack, 2003.
(9) Einstein, A., *Physikalische Zeitschrift* **1917,** *18*.
(10) Townes, C. H. Production of Electromagenetic Radiation. 2879439, January 28, 1958.
(11) Maiman, T. H., *Nature* **1960,** *187*, 493-494.
(12) Atherton, L. J.; Payne, S. A.; Brandle, C. D., *Annu. Rev. Mater. Sci.* **1993,** *23*, 453-502.
(13) Hudson Institute of Mineralogy. http://www.mindat.org/min-1651.html (August 22, 2015),
(14) Geller, S., *Z. Kristallogr.* **1967,** *125*, S1-S47.
(15) Geusic, J. E.; Marcos, H. M.; Van Uitert, L. G., *Appl. Phys. Lett.* **1964,** *4*, 182-184.
(16) Griebner, U.; Petrov, V.; Petermann, K.; Peters, V., *Opt. Express* **2004,** *12*, 3125-3130.
(17) Li, L.; Cao, X.-q.; Zhang, Y.; Guo, C.-x., *Trans. Nonferrous Met. Soc. China* **2012,** *22*, 373-379.
(18) McMillen, C.; Thompson, D.; Tritt, T.; Kolis, J., *Cryst. Growth Des.* **2011,** *11*, 4386-4391.
(19) Mix, E. Crystal Growth, Spectroscopy, and Laser Properties of Yb -Doped Sesquioxides. Ph.D Dissertation, University of Hamburg, 1999.
(20) Peters, R.; Kränkel, C.; Petermann, K.; Huber, G., *Opt. Express* **2007,** *15*, 7075-7082.
(21) Peters, V. Growth and Spectroscopy of Ytterbium-Doped Sesquioxides. Ph.D. Dissertation, University of Hamburg, Hamburg, 2001.
(22) Peters, V.; Bolz, A.; Petermann, K.; Huber, G., *J. Cryst. Growth* **2002,** *237*, 879-883.
(23) Peters, V.; Mix, E.; Fornasiero, L.; Petermann, K.; Huber, G.; Basun, S. A., *Laser Phys.* **2000,** *10*, 417-421.
(24) Sanghera, J.; Kim, W.; Baker, C.; Villalobos, G.; Frantz, J.; Shaw, B.; Lutz, A.; Sadowski, B.; Miklos, R.; Hunt, M.; Kung, F.; Aggarwal, I., *Opt. Mater.* **2011,** *33*, 670-674.

(25) Seeley, Z. M.; Kuntz, J. D.; Cherepy, N. J.; Payne, S. A., *Opt. Mater.* **2011,** *33*, 1721-1726.
(26) Shi, Y.; Chen, Q. W.; Shi, J. L., *Opt. Mater.* **2009,** *31*, 729-733.
(27) Wang, L.; Huang, H.; Shen, D.; Zhang, J.; Chen, H.; Wang, Y.; Liu, X.; Tang, D., *Opt. Express* **2014,** *22*, 19495-19503.
(28) Zhang, H.; Yang, Q.; Lu, S.; Shi, Z., *Opt. Mater.* **2012,** *34*, 969-972.
(29) Peters, R.; Krankel, C.; Fredrich-Thornton, S. T.; Beil, K.; Petermann, K.; Huber, G.; Heckl, O. H.; Baer, C. R. E.; Saraceno, C. J.; Sudmeyer, T.; Keller, U., *Appl. Phys. B: Lasers Opt.* **2011,** *102*, 509-514.
(30) LuAG Data Sheet. http://www.scientificmaterials.com/downloads/LuAG.pdf (May 10, 2013)
(31) Bass, M., *Handbook of Optics* Second ed.; McGraw Hill: 1995; Vol. 2.
(32) Shannon, R., *Acta Crystallographica Section A* **1976,** *32*, 751-767.
(33) Dieke, G. H.; Crosswhite, H. M., *Appl. Opt.* **1963,** *2*, 675-686.
(34) Moore, C. A., *J. Lumin.* **2015**.
(35) McMillen, C. D.; Kolis, J. W., *Philos. Mag.* **2012,** *92*, 2686-2711.
(36) McMillen, C. D.; Mann, M.; Fan, J.; Zhu, L.; Kolis, J. W., *J. Cryst. Growth* **2012,** *356*, 58-64.
(37) Puttbach, R. C.; Monchamp, R. R.; Nielsen, J. W., *Hydrothermal Growth of $Y_3Al_5O_{12}$*. Pergamon: Oxford, 1967; p 569-571.
(38) Denton, A. R.; Ashcroft, N. W., *Phys. Rev. A* **1991,** *43*, 3161-3164.
(39) Gorbenko, V.; Krasnikov, A.; Nikl, M.; Zazubovich, S.; Zorenko, Y., *Opt. Mater.* **2009,** *31*, 1805-1807.
(40) Kmetec, J. D.; Kubo, T. S.; Kane, T. J.; Grund, C. J., *Opt. Lett.* **1994,** *19*, 186-188.
(41) Aggarwal, R. L.; Ripin, D. J.; Ochoa, J. R.; Fan, T. Y., *J. Appl. Phys.* **2005,** *98*, 103514-14.
(42) Burnett, J. H.; Kaplan, S. G.; Shirley, E. L.; Horowitz, D.; Josell, D.; Clauss, W.; Grenville, A.; Peski, C. V., *SPIE Proceedings* **2006**, OO-21.
(43) Kolb, E. D.; Laudise, R. A., *J. Cryst. Growth* **1975,** *29*, 29-39.
(44) Laudise, R. A.; Crocket, J. H.; Ballman, A. A., *J. Phys. Chem.* **1961,** *65*, 359-361.
(45) Laudise, R. A.; Kolb, E. D., *J. Am. Ceram. Soc.* **1962,** *45*, 51-53.
(46) Ferrand, B.; Daval, J.; Joubert, J. C., *J. Cryst. Growth* **1972,** *17*, 312-314.
(47) Ferrand, B.; Geynet, J.; Challeton, D.; Daval, J.; Joubert, J. C., *Mater. Res. Bull.* **1974,** *9*, 495-506.
(48) Baughman, R. J., *J. Cryst. Growth* **1991,** *112*, 753-757.
(49) Brown, D. C.; McMillen, C. D.; Moore, C.; Kolis, J. W.; Envid, V., *J. Lumin.* **2013,** *148*, 26-32.
(50) Sugiyama, M.; Fujimoto, Y.; Yanagida, T.; Totsuka, D.; Chani, V.; Yokota, Y.; Yoshikawa, A., *Radiat. Meas.* **2012**.
(51) Wang, X. D.; Xu, X. D.; Zang, T. C.; Ma, C. L.; Zhao, Z. W.; Xu, J., *J. Inorg. Mater.* **2010,** *25*, 435-440.
(52) Xu, X. D.; Wang, X. D.; Meng, J. Q.; Cheng, Y.; Li, D. Z.; Cheng, S. S.; Wu, F.; Zhao, Z. W.; Xu, J., *Laser Phys. Lett.* **2009,** *6*, 678-681.

(53) Sugiyama, M.; Fujimoto, Y.; Yanagida, T.; Yokota, Y.; Pejchal, J.; Furuya, Y.; Tanaka, H.; Yoshikawa, A., *Opt. Mater.* **2011,** *33*, 905-908.
(54) Moore, C. A.; McMillen, C. D.; Kolis, J. W., *Cryst. Growth Des.* **2013,** *13*, 2298-2306.
(55) Solomonov, V. I.; Orlov, A. N.; Spirina, A. V.; Konev, S. F.; Cholakh, S. O.; Luk'yashin, K. E., *Opt. Spectrosc. 117*, 908-913.
(56) Brenier, A.; Guyot, Y.; Canibano, H.; Boulon, G.; Ródenas, A.; Jaque, D.; Eganyan, A.; Petrosyan, A. G., *J. Opt. Soc. Am. B* **2006,** *23*, 676-683.
(57) Hart, D. W.; Jani, M.; Barnes, N. P., *Opt. Lett.* **1996,** *21*, 728-730.
(58) Duan, X.; Yao, B.; Li, G.; Ju, Y.; Wang, Y.; Zhao, G., *Opt. Express* **2009,** *17*, 21691-21697.
(59) Patel, D. N.; Reddy, B. R.; Nash-Stevenson, S. K., *Opt. Mater.* **1998,** *10*, 225-234.
(60) Zhao, T.; Shen, D.; Chen, H.; Yang, X.; Xu, X.; Zhou, D.; Xu, J., *Laser Phys.* **2011,** *21*, 1851-1854.
(61) Walsh, B. M.; Grew, G. W.; Barnes, N. P., *J. Phys. Chem. Solids* **2006,** *67*, 1567-1582.
(62) Gruber, J. B.; Hills, M. E.; Seltzer, M. D.; Stevens, S. B.; Morrison, C. A.; Turner, G. A.; Kokta, M. R., *J. Appl. Phys.* **1991,** *69*, 8183-8204.
(63) Kalaycioglu, H.; Sennaroglu, A.; Kurt, A.; Ozen, G., *J. Phys.: Condens. Matter* **2007,** *19*, 036208.
(64) Tiseanu, C.; Lupei, A.; Lupei, V., *J. Phys.: Condens. Matter* **1995,** *7*, 8477.
(65) Wu, C.; Ju, Y.; Li, Y.; Wang, Z.; Wang, Y., *Chin. Opt. Lett.* **2008,** *6*, 415-416.
(66) Setzler, S. D.; Francis, M. P.; Young, Y. E.; Konves, J. R.; Chicklis, E. P., *Selected Topics in Quantum Electronics, IEEE Journal of* **2005,** *11*, 645-657.
(67) Zhou, D.; Xu, X.; Xia, C.; Shen, D.; Cheng, S.; Li, D.; Di, J.; Zhao, Z.; Wu, F.; Xu, J., *J. Opt. Soc. Am. B* **2011,** *28*, 2543-2548.
(68) Setzler, S. D.; Snell, K. J.; Pollak, T. M.; Budni, P. A.; Young, Y. E.; Chicklis, E. P., *Opt. Lett.* **2003,** *28*, 1787-1789.
(69) Cherepy, N. J.; Kuntz, J. D.; Tillotson, T. M.; Speaks, D. T.; Payne, S. A.; Chai, B. H. T.; Porter-Chapman, Y.; Derenzo, S. E., *Nucl. Instrum. Methods Phys. Res., Sect. A* **2007,** *579*, 38-41.
(70) Diego Gatta, G., *Am. Mineral.* **2008,** *93*, 988 - 995.
(71) Gallagher, S. A.; McCarthy, G. J., *Mater. Res. Bull.* **1982,** *17*, 89-94.
(72) Gallagher, S. A.; McCarthy, G. J.; Smith, D. K., *Mater. Res. Bull.* **1977,** *12*, 1183-1190.
(73) Yokomori, Y.; Asazuki, K.; Kamiya, N.; Yano, Y.; Akamatsu, K.; Toda, T.; Aruga, A.; Kaneo, Y.; Matsuoka, S.; Nishi, K.; Matsumoto, S., *Scientific Reports* **2014,** *4*, 4195.
(74) WebMineral Dellaite Mineral Data. http://webmineral.com/data/Dellaite.shtml#.VhbCz27Vo6A (October 10, 2015),
(75) Collongues, R.; Lejus, A. M.; Theiry, J.; Vivien, D., *J. Cryst. Growth* **1993,** *128*, 986-990.
(76) Lejus, A. M.; Kahn-Harari, A.; Benitez, J. M.; Viana, B., *Mater. Res. Bull.* **1994,** *29*, 725-734.

(77) Lejus, A. M.; Vivien, D.; Collongues, R.; Saber, D.; Benitez, J. M. Neodymium-doped gehlenite crystal and laser using same. WO9301139A1, 1993.
(78) Viana, B.; Lejus, A. M.; Saber, D.; Duxin, N.; Vivien, D., *Opt. Mater.* **1994,** *3*, 307-316.
(79) Kaminskii, A. A.; Belokoneva, E. L.; Mill, B. V.; Sarkisov, S. E.; Kurbanov, K., *physica status solidi (a)* **1986,** *97*, 279-290.
(80) Henmi, C., *Mineralogical Journal* **1976,** *8*, 171-183.
(81) Henmi, C., *Mineralogical Journal* **1987,** *13*, 347-367.
(82) Veronesi, S.; Zhang, Y. Z.; Tonelli, M.; Agnesi, A.; Greborio, A.; Pirzio, F.; Reali, G., *Opt. Commun.* **2012,** *285*, 315-321.
(83) Dong, J.; Ueda, K.-i.; Kaminskii, A. A., *Opt. Lett.* **2007,** *32*, 3266-3268.
(84) Ogino, H.; Yoshikawa, A.; Lee, J.-H.; Nikl, M.; Solovieva, N.; Fukuda, T., *Opt. Mater.* **2004,** *26*, 535-539.
(85) Yang, P.; Deng, P.; Yin, Z., *J. Lumin.* **2002,** *97*, 51-54.
(86) Beil, K.; Fredrich-Thornton, S. T.; Tellkamp, F.; Peters, R.; Kränkel, C.; Petermann, K.; Huber, G., *Opt. Express* **2010,** *18*, 20712-20722.
(87) Mun, J. H.; Anis, J.; Andrey, N.; Akira, Y.; Tsuyoshi, K.; Hiromich, O.; Hiroyuki, S.; Minoru, I.; Yoshio, W.; Georges, B.; Tsuguo, F., *Jpn. J. Appl. Phys.* **2006,** *45*, 5885.
(88) Mun, J. H., *J. Ceram. Process. Res.* **2013,** *14*, 636-640.
(89) Grunberg, P.; Hufner, S.; Orlich, E.; Schmitt, J., *Physical Review* **1969,** *184*, 285-293.
(90) Seltzer, M. D.; Wright, A. O.; Morrison, C. A.; Wortman, D. E.; Gruber, J. B.; Filer, E. D., *J. Phys. Chem. Solids* **1996,** *57*, 1175-1182.
(91) Seki, M.; Kochurikhin, V. V.; Kurosawa, S.; Suzuki, A.; Yamaji, A.; Fujimoto, Y.; Wakahara, S.; Pejchal, J.; Yokota, Y.; Yoshikawa, A., *physica status solidi (c)* **2012,** *9*, 2255-2258.
(92) Sardar, D. K.; Bradley, W. M.; Yow, R. M.; Gruber, J. B.; Zandi, B., *J. Lumin.* **2004,** *106*, 195-203.
(93) Klimczak, M.; Malinowski, M.; Sarnecki, J.; Piramidowicz, R., *J. Lumin.* **2009,** *129*, 1869-1873.
(94) Bowman, S. R.; O'Connor, S.; Condon, N. J., *Opt. Express* **2012,** *20*, 12906-12911.
(95) Berent, M.; Rangelov, A. A.; Vitanov, N. V., *J. Opt. Soc. Am. A* **2013,** *30*, 149-153.
(96) Zheleznov, D.; Starobor, A.; Palashov, O.; Chen, C.; Zhou, S., *Opt. Express* **2014,** *22*, 2578-2583.
(97) Geho, M.; Sekijima, T.; Fujii, T., *J. Cryst. Growth* **2004,** *267*, 188-193.
(98) Dachraoui, H.; Rupp, R. A.; Lengyel, K.; Ellabban, M. A.; Fally, M.; Corradi, G.; KovÃ¡cs, L.; Ackermann, L., *Phys. Rev. B.* **2006,** *74*, 144104.
(99) Ganschow, S.; Klimm, D.; Reiche, P.; Uecker, R., *Cryst. Res. Technol.* **1999,** *34*, 615-619.
(100) Valiev, U. V.; Uzokov, A. A.; Rakhimov, S. A.; Gruber, J. B.; Nash, K. L.; Sardar, D. K.; Burdick, G. W., *J. Appl. Phys.* **2008,** *104*, 073903-5.
(101) Geho, M.; Sekijima, T.; Fujii, T., *J. Cryst. Growth* **2005,** *275*, e663-e667.

(102) Boal, D.; Grunberg, P.; Koningstein, J. A., *Phys. Rev. B: Condens. Matter Mater. Phys.* **1973,** *7*, 4757-4763.
(103) Ganschow, S.; Klimm, D.; Epelbaum, B. M.; Yoshikawa, A.; Doerschel, J.; Fukuda, T., *J. Cryst. Growth* **2001,** *225*, 454-457.
(104) Henderson, B.; Gallagher, H. G.; Han, T. P. J.; Scott, M. A., *J. Phys.: Condens. Matter* **2000,** *12*, 1927.
(105) Qiao, J.; Zhao, J.; Yang, K.; Zhao, S.; Li, Y.; Li, G.; Li, D.; Qiao, W.; Li, T.; Chu, H., *Jpn. J. Appl. Phys.* **2014,** *54*, 032701/1-032701/7.
(106) Feldman, R.; Shimony, Y.; Burshtein, Z., *Opt. Mater.* **2003,** *24*, 333-344.
(107) Feldman, R.; Shimony, Y.; Burshtein, Z., *Opt. Mater.* **2003,** *24*, 393-399.
(108) Tsai, C. N. Study of Enhancement of Cr^{4+} Concentration in $Y_3Al_5O_{12}$ Crystal Fiber Using Pre-growth Perimeter Deposition. Ph. D. Dissertation, Sun Yat Sen University, Taiwan, 2009.